

**INTEGRATED STRUCTURAL HEALTH  
MONITORING AND ENERGY HARVESTING  
POTENTIAL OF ADHESIVELY BONDED THIN PIEZO  
PATCHES OPERATING IN  $d_{31}$  MODE**

**NAVEET KAUR**



**DEPARTMENT OF CIVIL ENGINEERING  
INDIAN INSTITUTE OF TECHNOLOGY DELHI  
MAY 2015**

© Indian Institute of Technology Delhi (IITD), New Delhi, 2015

**INTEGRATED STRUCTURAL HEALTH  
MONITORING AND ENERGY HARVESTING  
POTENTIAL OF ADHESIVELY BONDED THIN PIEZO  
PATCHES OPERATING IN  $d_{31}$  MODE**

by

**NAVEET KAUR**

Department of Civil Engineering

**Submitted**

**in fulfilment of the requirements of the degree of**

**Doctor of Philosophy**

to the



**INDIAN INSTITUTE OF TECHNOLOGY DELHI**

**MAY 2015**



*Dedicated to my family and teachers  
for their support and guidance.*





## **CERTIFICATE**

This is to certify that the thesis titled “**INTEGRATED STRUCTURAL HEALTH MONITORING AND ENERGY HARVESTING POTENTIAL OF ADHESIVELY BONDED THIN PIEZO PATCHES OPERATING IN  $d_{31}$  MODE**” which is being submitted by **Ms. NAVEET KAUR** for the fulfilment of the requirements for the award of degree of **Doctor of Philosophy**, is a record of the student’s own work carried out at the **Indian Institute of Technology Delhi** under my supervision and guidance. The matter embodied in this thesis has not been submitted elsewhere for the award of any other degree or diploma.

**Dr. Suresh Bhalla**

Associate Professor

New Delhi

May, 2015

Department of Civil Engineering

Indian Institute of Technology Delhi



## **ACKNOWLEDGMENTS**

*As I sat down to write this note of gratitude, I can't help but think of what a wild and wonderful ride the journey of my doctorate has been. From the day one in the lab to the bunch of publications today, the destination, which I set out to achieve, has surely been mine but the journey has been supported by many. I am at a loss of words, to do justice to thank the quantum of support offered by **Prof. Suresh Bhalla** throughout. Be it the critical guidance on work or the encouragement to stay strong and motivated to execute all kinds of tasks required to complete the work, he has been my strongest anchor. A heartfelt thanks to him for giving me the immense freedom to design my work plan and for always being around to help, provide feedback and valuable mentoring. Thanks to the professor for being a kind fatherly figure to me.*

*I thank **Dr. Sumedha Moharana** for all the head-start she gave me in networking and pitching my work at various places and forums. I am equally grateful to the staff members of the Smart Structures and Dynamics Laboratory, who, with their immense cooperation and friendly attitude, made experiments as exciting initiatives to look forward to in routine. I cannot thank enough **Mr. Vinod, Mr. Deepak, Mr. Vijay and Mr. Sujit** who lent their prompt help in anything and everything I needed in the labs. I appreciate **Mr. Jaitley's** kind help from the bottom of my heart for providing the much required assistance in the interdisciplinary activities required for my research work. Working in laboratory would not have been that fun if it was not for amazing juniors like **Abhishek Pal, Kamal Patel and Ravi Shanker**, who contributed with their efforts in the experimental work. **Nikit and Neshan**, the work you guys did still makes me feel good about my initial days in the lab. Thanks a bunch for taking me on board in your work. And of course, I can't miss thanking **IIT Delhi** and especially the **Civil Engineering Department** for being a warm host for my work and providing me with all the required facilities including library, grants and laboratories. I would always remember this place as a warm nest which not only hosted me for my tenure here, but also provided a nurturing environment for my research ideas to bloom. My tenure here in campus would be surely a memorable part of my life.*

*Thanks **Anuj Parasher** and **Rajinder Deol** for all the uncountable laughters at our tea sessions. I would like to give a huge token of gratitude to **Prateek Negi** for being the best brainstorming partner. I would always remember the time spent with you on the discussions on science and astronomy. Your capability of visualizing the working of mathematical models helped me to understand and interpret my results better.*

*I'd be a great amiss if I don't acknowledge the role of my family whole throughout. To begin with, I'd like to thank **Harshdeep Rapal** for not just his patience to deal with my schedule but also for the positivity he kept filling in, which motivated me to push my limits as much as possible. Harsh, I think it takes more than just courage to be in long distance marriage and still making it all happening and beautiful, and I think nobody but only you have the capacity to do it. Thank you for being you and for always being around, without fail. Heartfelt thanks to **my parents and my in-laws** for continuous appreciation and understanding towards my work life. I hope the degree at the end and the work so far makes your hearts swell with pride.*

*I would like to thank **Neha Chaturvedi** for her consistent moral support as a family member throughout my tenure at IIT Delhi. I would also like to thank **Surabhi Yadav** and **Akshi Singla** for giving the perfect ending to my stay in IIT Delhi. Surabhi, your happy-go-lucky and go-getter attitude made the last leg of my PhD even more amazing and fun filled.*

*Last but the not the least, I would like to express my immense gratitude towards **God**. I don't think I would have been what I am today if it was not for his blessings. Baba Ji, please always keep me in the list of your much-loved children.*

**Naveet Kaur**

## **ABSTRACT**

Piezoelectric materials have so far proven their efficacy for both energy harvesting and structural health monitoring (SHM) individually. Piezoelectric ceramic (PZT) patches, operating in  $d_{31}$ -mode, are considered best for SHM. However, for energy harvesting, built up configurations such as stack actuators are more preferred. The main objective of this research was to explore the possibility of employing the same piezo sensor for SHM as well as energy harvesting on real-life civil structures such as bridges. Experiments have been carried out in the laboratory environment to measure the voltage and the power generated by PZT patches in surface bonded as well as embedded  $d_{31}$  configurations. In embedded form, the PZT patches have been considered in the form of concrete vibration sensor (CVS), operating in the normal axial strain ( $d_{31}$ ) mode. This packaged sensor (CVS), which is composite in nature, has better compatibility with the surrounding concrete and can withstand the harsh conditions typically encountered during casting. Analytical models have been developed based on Euler Bernoulli's theory for a beam under harmonic vibrations, using which the voltage output of a PZT patch, either surface bonded or embedded (CVS), can be determined duly considering the effects of shear lag and other losses associated with the bonding layers. Beam structure has been considered for modelling as well as lab experimentation owing to the energy harvesting potential offered by real-life bridges. Utilization of the same patch for energy harvesting as well as for SHM through a combination of the global vibration and the local EMI techniques has been experimentally demonstrated. The strength gain and the fatigue characteristics of the real-life sized RC beam have been duly investigated via the embedded CVS in laboratory. The experimental observations have been found to match with theoretical predictions. The performance of the CVS is compared with surface-bonded PZT patch. The typical

measured output power from a piezo sensor  $10 \times 10 \times 0.3$  mm has been determined to be in microwatt range.

Optimum parameters of PZT patches have been arrived at by performing detailed numerical investigations. A comprehensive parametric study to investigate the effect of various parameters such as PZT geometric parameters, adhesive layer thickness and bond stiffness, which is otherwise difficult to perform experimentally, has been done. A numerical model has been developed for a real-life sized simply supported beam instrumented with (a) surface bonded PZT sensor (SBPS), and (b) embedded PZT patch in form of concrete vibration sensor (CVS), and coupled field analysis has been performed for the two configurations through finite element method (FEM). The results have been compared with the existing analytical model as well as the experimental data and the comparison has been found satisfactory. Effect of varying load resistance across the PZT patch on the close circuit power generated by the patch has also been investigated. The investigations show that a piezo thickness lying between 0.3 mm and 1 mm ensures maximum yield for SBPS. For CVS, the thickness above 1 mm is somewhat more beneficial. In addition, covering the SBPS with a layer of epoxy is also beneficial.

A real-life flyover with span of length 25 m has been numerically modelled to estimate the dynamic strain levels and hence, the power that could be produced in real-life structures. The numerical study predicts a yield of  $2.2 \mu\text{W}$  from a typical city flyover. This aids to quantify the gap between the voltage generated by the PZT patches under specific conditions in lab environment and corresponding to the strain levels produced in real-life structures. Harvesting potential of the structural vibration energy by PZT sensors during idle time is experimentally demonstrated and this concept has been extended to

eight real-life bridges across the world, based on the validated analytical model. Effect of losses such as mechanical loss, dielectric loss and shear lag loss, on the real-life structure have been duly considered. Computations show that the power yield could range anywhere from less than a microwatt (RC bridges) to over 25  $\mu\text{W}$  (steel bridges). These figures correspond to power densities over 30  $\mu\text{W}/\text{cm}^{-3}$  and 800  $\mu\text{W}/\text{cm}^{-3}$ , respectively. The study reveals that the PZT patches could harvest enough energy in reasonable time in the idle state so as to enable intermittent operation of SHM system. Typically, it could take only a couple of seconds to scavenge enough energy to power commercially available A/D converters.

Proof-of-concept demonstration of normal plate type piezo in axial strain mode in place of commercial expensive transducers for energy harvesting from real-life civil structure has been the original aspect of this study. It is expected that the outcomes of this research will pave way for dual use of the ordinary piezo patch in SHM as well as energy harvesting.



## **TABLE OF CONTENTS**

<b>TITLE</b>	<b>PAGE NO.</b>
Certificate.....	i
Acknowledgements.....	iii
Abstract.....	v
Table of Contents.....	ix
List of Figures.....	xiii
List of Tables.....	xix
List of Symbols.....	xxi
List of Acronyms.....	xxv
 <b>CHAPTER-1 INTRODUCTION.....</b>	<b>1-10</b>
1.1 Background.....	1
1.2 Motivation.....	2
1.3 Piezo Sensors for Structural Health Monitoring (SHM) and Energy Harvesting.....	4
1.4 Research Objectives and Scope.....	9
1.5 Organization of thesis.....	10
 <b>CHAPTER-2 STATE-OF-THE-ART IN STRUCTURAL HEALTH MONITORING AND ENERGY HARVESTING.....</b>	<b>11-47</b>
2.1 Introduction.....	11
2.2 Evolution and Advances in Structural Health Monitoring.....	12
2.3 Piezoelectric Energy Harvesting: Theoretical and Practical Aspects.....	21
2.3.1 <i>Transduction Principle</i> .....	22
2.3.2 <i>Electro-mechanical Model for Resonating Piezoelectric Devices</i> .....	24
2.3.3 <i>Optimal Shapes of Secondary Structures</i> .....	27
2.3.4 <i>Piezoelectric Transducer Configurations for Energy Harvesting</i> .....	27
2.3.5 <i>Energy Harvesting Circuits</i> .....	28
2.3.6 <i>Strategies For Enhancing Performance of Energy Harvester</i> .....	29
2.3.6.1 Multi-Modal Energy Harvesting.....	29
2.3.6.2 Frequency Pumping.....	30
2.3.6.3 Self-Tuning.....	31
2.3.6.4 Wide-Bandwidth Transducers.....	32

<b>TITLE</b>	<b>PAGE NO.</b>
2.3.7 <i>Practical Applications of Piezoelectric Energy Harvesting</i> .....	32
2.4 Evolution and Recent Advances in Energy Harvesting Using Piezo Sensor.....	33
2.5 Critical Literature Review: Identification of Research Gaps.....	44
2.6 Research Objectives, Scope and Original Contributions.....	46
<b>CHAPTER-3 FEASIBILITY OF ENERGY HARVESTING FROM THIN SURFACE BONDED PIEZO PATCHES: MODELLING AND EXPERIMENTATION.....</b>	<b>49-75</b>
3.1 Introduction.....	49
3.2 Energy Harvesting by Surface Bonded PZT Patch: Analytical Modelling	50
3.3 Laboratory Experimentation.....	55
3.3.1 <i>Experimental Set-Up</i> .....	55
3.3.2 <i>Determination of Calibration Constant for In-House Piezo Force-Sensor</i> .....	57
3.4 Comparison of Analytical and Experimental Results.....	62
3.4.1 <i>Mechanical Loss</i> .....	65
3.4.2 <i>Dielectric Loss</i> .....	65
3.4.3 <i>Shear Lag Loss</i> .....	66
3.5 Energy Harvesting: Power Measurement Across the PZT Patch....	69
3.6 Possibility Of Battery Charging Using Energy Harvested From PZT Patch.....	73
3.7 Summary and Concluding Remarks.....	74
<b>CHAPTER-4 ENERGY HARVESTING POTENTIAL OF EMBEDDED PIEZO PATCHES: MODELLING AND EXPERIMENTATION.....</b>	<b>77-104</b>
4.1 Introduction.....	77
4.2 Energy Harvesting From Embedded Concrete Vibration Sensor: Analytical Modelling.....	78
4.2.1 <i>Details of Concrete Vibration Sensor</i> .....	78
4.2.2 <i>Development of Coupled Electro-Mechanical Model</i> .....	80
4.2.3 <i>Comparison of Voltage Response of Embedded and Surface-Bonded PZT Patches</i> .....	88
4.3 Comparison with Experiment.....	90
4.4 Energy Harvesting Potential of Embedded CVS.....	99
4.5 Summary and Concluding Remarks.....	104

TITLE	PAGE NO.
<b>CHAPTER-5 PROOF-OF-CONCEPT DEMONSTRATION OF ENERGY HARVESTING AND STRUCTURAL HEALTH MONITORING USING EMBEDDED CVS..</b>	<b>105-126</b>
5.1 Introduction.....	105
5.2 Short Term Monitoring of RC Beam Using CVS.....	105
5.2.1 <i>Global Vibration Technique</i> .....	106
5.2.2 <i>Electro-Mechanical Impedance (EMI) Technique</i> .....	110
5.3 Long Term Monitoring of RC Beam Using Embedded CVS.....	114
5.3.1 <i>Global Vibration Technique</i> .....	115
5.3.2 <i>Electro-Mechanical Impedance (EMI) Technique</i> .....	119
5.4 Proof-of-Concept Demonstration of Energy Harvesting for SHM Using Embedded CVS.....	123
5.5 Summary and Concluding Remarks.....	125
<b>CHAPTER-6 ENERGY HARVESTING USING THIN PZT PATCHES SURFACE BONDED/EMBEDDED IN REAL-LIFE STRUCTURES: AN EXTENDED STUDY.....</b>	<b>127-140</b>
6.1 Introduction.....	127
6.2 Energy Harvesting From Typical City Flyover: Semi Analytical Study..	127
6.3 Extension to Existing Real-life Bridges/ Flyovers.....	135
6.3.1 <i>Steel Bridges</i> .....	135
6.3.2 <i>RC Bridges</i> .....	136
6.3.3 <i>Computation of Charging Period</i> .....	137
6.4 Summary and Concluding Remarks.....	140
<b>CHAPTER-7 NUMERICAL INVESTIGATIONS ON ENERGY HARVESTING FROM ADHESIVELY BONDED THIN PZT PATCHES IN SURFACE BONDED/ EMBEDDED CONFIGURATIONS.....</b>	<b>141-172</b>
7.1 Introduction.....	141
7.2 Numerical Modelling.....	142
7.3 Model Validation.....	146
7.4 Numerical Energy Harvesting Investigations.....	150
7.4.1 <i>Effect of External Load Resistance</i> .....	151
7.4.2 <i>Effect of Piezo and Bond Thicknesses</i> .....	156
7.4.3 <i>Effect of Piezo's Plan Dimensions</i> .....	160

<b>TITLE</b>	<b>PAGE NO.</b>
<i>7.4.4 Effect of Shear Modulus of Adhesive.....</i>	164
<i>7.4.5 Effect of Adhesive Covering on Surface Bonded PZT Sensor.....</i>	165
<i>7.4.6 Effect of Adhesive Covering on EMI Signature.....</i>	167
<b>7.5 Summary and Concluding Remarks.....</b>	<b>170</b>
<b>CHAPTER-8 CONCLUSIONS AND RECOMMENDATIONS.....</b>	<b>173-178</b>
8.1 Introduction.....	173
8.2 Research Conclusions and Contributions.....	174
8.3 Recommendations for Future Work.....	177
<b>AUTHOR'S PUBLICATIONS.....</b>	<b>179</b>
<b>AUTHOR'S INVITED LECTURES.....</b>	<b>183</b>
<b>REFERENCES.....</b>	<b>185</b>
<b>APPENDIX A</b> MATLAB Program for determination of amplitude of vibration of simply supported beam under sinusoidally varying concentrated load.....	201
<b>APPENDIX B</b> Design calculations for determination of ultimate moment carrying capacity, $M_u$ , of RC beam.....	203
<b>APPENDIX C</b> Design calculations for determination of stiffness of spring used in inertial-type shaker.....	205
<b>APPENDIX D</b> Design calculations for compensating effect of temperature on PZT parameters.....	209
<b>APPENDIX E</b> Invention Disclosure: Abstract .....	211
<b>AUTHOR'S CURRICULUM VITAE.....</b>	<b>213</b>

## LIST OF FIGURES

<b>FIGURE</b>	<b>CAPTION</b>	<b>PAGE NO.</b>
1.1	(a) Behaviour of PZT patch under direct effect..... (b) Behaviour of PZT patch under converse effect..... (c) A typical commercial PZT patch (PI Ceramic, 2014)..... (d) PZT patch with conventional 1, 2 and 3 axis.....	7 7 7 7
1.2	Operating modes (a) $d_{33}$ -mode and (b) $d_{31}$ -mode of piezoelectric transducer (Priya and Inman, 2009).....	9
2.1	(a) A typical structure under interrogation by EMI technique..... (b) A PZT patch surface-bonded to a structure..... (c) Liang's 1D impedance model for system shown in (b).....	17 17 17
2.2	Hierarchy of main energy harvesting technologies (Calio et al., 2014).....	21
2.3	(a) Monocrystal (b) Polycrystal (Calio et al., 2014) .....	23
2.4	(a) Polarization (b) Surviving polarity (Calio et al., 2014) .....	24
2.5	Mass-spring-damper-piezo model (Williams and Yates, 1996) .....	24
2.6	Power of the piezoelectric generator as a function of the electrical damping ratio (Calio et al., 2014) .....	26
2.7	Variation of strain along the length for various shapes of cantilevers (Calio et al., 2014) .....	27
2.8	Block diagram for the energy harvesting circuit (Priya and Inman, 2009) .....	29
2.9	Enhancing energy harvesting efficiency through increase of frequency (Priya and Inman, 2009).....	30
2.10	Self-tuning double cantilevered harvester (Eichhorn et al., 2011).....	31
2.11	Schematic and results of energy harvesting shoe (Kymmissis et al., 1998). (a) External view of shoe..... (b) Location of piezo sensors..... (b) Typical power vs time.....	37 37 37
2.12	Energy harvesting “eel” concept (Ocean Power Technologies, Inc. 2014).....	40
2.13	A prototype of sensor node with piezoelectric energy harvester (Microstrain, Inc., 2007) .....	42
2.14	Bio-inspired bi-stable structure (Kim and Kim, 2013) .....	43
3.1	Principle of integrated SHM and energy harvesting.....	50
3.2	(a) Free body diagram of beam under concentrated load..... (b) Variation of excitation load with respect to time..... (c) Strain distribution of beam with PZT patch at centre.....	51 51 51
3.3	Experimental set up for voltage measurement across PZT patch.....	56
3.4	Function generator with amplifier.....	57

<b>FIGURE</b>	<b>CAPTION</b>	<b>PAGE NO.</b>
3.5	Portable dynamic shaker along with Dytran force-sensor and piezo force-sensor.....	58
3.6	Data acquisition system for PZT patch at top flange and piezo force-sensor.....	59
3.7	Oscilloscope with PCB box.....	59
3.8	Calibration constant with varying operating frequencies.....	60
3.9	Comparison of the experimental and theoretical amplitudes for different damping values.....	63
3.10	Comparison of the experimental and theoretical voltage.....	64
3.11	Comparison of experimental and theoretical voltage incorporating the effect of losses ( $h$ : thickness of PZT patch).....	68
3.12	(a) Measuring equipment set up for power quantification. .... (b) Simple Circuit employed for power measurement.....	70
3.13	Plot showing area under the curve of power and time.....	72
3.14	Variation of $P_{\text{Peak}}$ , $P_{\text{RMS}}$ and $P_{\text{avg}}$ with varying forcing frequency.....	72
4.1	(a) Dynamic load acting on a RC beam housing a CVS. <i>Strain distribution across depth is also shown</i> ..... (b) Variation of excitation load with respect to time.....	79
4.2	Optical image showing different layers of CVS.....	79
4.3	(a) A PZT patch embedded inside concrete beam and bonded using adhesive layer..... (b) Deformation in bonding layer and PZT patch embedded in concrete beam.....	81
4.4	Theoretical comparison of voltage generated by embedded and surface PZT patch considering mechanical, dielectric and shear lag loss.....	90
4.5	RC beam (a) before casting and (b) during casting.....	91
4.6	(a) RC beam showing reinforcement, embedded CVS and notch for damage..... (b) Detail of reinforcement(cross-section) ( <i>refer Figure 7.1 for Section 2-2</i> ) .....	92
4.7	Complete experimental set up with CVS location.....	93
4.8	(a) Contact type shaker; (b) inertial-type Shaker; schematic diagram of inertial-type shaker showing (c) elevation; (d) View 1-1 and (e) View 2-2 ( <i>units in 'mm'</i> ).....	94
4.9	Voltage generated by surface bonded and embedded CVS at location 11 varying with time for four cases namely case (a) to case (d). .....	97
4.10	(a) Overall set up for power quantification..... (b) Details of energy quantification circuit.....	100

<b>FIGURE</b>	<b>CAPTION</b>	<b>PAGE NO.</b>
4.11	Variation of $P_{\text{Peak}}$ , $P_{\text{RMS}}$ and $P_{\text{avg}}$ with varying forcing frequency (a) Shaker and PZT patch at centre and (b) Shaker and PZT patch at an offset of 600 mm from centre.....	101
5.1	Cross-section and front view of the notch showing undamaged and different states of damage [ <i>see this figure in conjunction with Figure 4.5</i> ]. .....	106
5.2	Experimental set-up for obtaining curvature mode shape of the RC beam showing (a) element numbers and (b) data acquisition system.....	108
5.3	(a) Comparison of curvature mode shape and (b) corresponding damage index, for undamaged and three damaged states. ....	109
5.4	Experimental set-up for local EMI technique done using AD5933 ( <i>a low-cost alternative of conventional LCR meter</i> ). ....	111
5.5	Comparison of typical conductance ( $G$ ) signature acquired for States 1 to 4 using (a) AD5933 and (b) LCR meter.....	112
5.6	Variation of RMSD of conductance plots for various elements corresponding to States 2 to 4 acquired using (a) AD5933 and (b) LCR meter.....	113
5.7	FFT voltage with varying frequency depicting natural frequency ( $f_n$ ) and damping of concrete beam. ....	116
5.8	Three cases considered for comparing natural frequency of concrete beam, (a) Contact type shaker, with impact excitation (b) Inertial-type shaker, with impact excitation (c) Inertial-type shaker, shaker induced sweep excitation (5 Hz to 70 Hz). ....	116
5.9	FFT voltage with varying frequency depicting natural frequency ( $f_n$ ) for three different cases mentioned in Figure 5.8. ....	117
5.10	(a) Accelerometer placed over the inertial-type shaker..... (b) FFT voltage for inertial-type shaker alone with varying frequency.....	118
5.11	Variation of natural frequency with increasing number of days.....	119
5.12	Experimental set-up for acquiring EMI signatures of embedded CVS.....	120
5.13	The equivalent system plots of (a) real part ( $x'$ ) and (b) imaginary part ( $y'$ ) of mechanical impedance for a parallel spring-damper combination varying with frequency. ....	121
5.14	Variation of equivalent stiffness with increasing number of days for (a) curing period and (b) after curing period. ....	121
5.15	Variation of equivalent stiffness with increasing number of days with and without considering temperature effects on PZT parameters. ....	122

<b>FIGURE</b>	<b>CAPTION</b>	<b>PAGE NO.</b>
5.16	(a) Full-wave bridge rectifier circuit used for storing energy in capacitor..... (b) Equivalent circuit for the energy harvesting circuit shown in (a)..... (b) Charging and discharging voltage across capacitor.....	124 124 124
6.1	(a) Cross section of the flyover (obligatory span) and (b) cross girder (typical) ( <i>All dimensions are in mm</i> ).....	128
6.2	Plan of the flyover ( <i>All dimensions are in mm</i> )..	129
6.3	FE model of flyover (single span) in SAP2000 software.	130
6.4	(a) 1Lane(L) Class A: longitudinal and transverse placement of vehicle wheel loads..... (b) 2L Class A: transverse placement of vehicle wheel loads..... (c) 3L Class A: transverse placement of vehicle wheel loads..... (d) 1L Class 70R: longitudinal and transverse placement of vehicle wheel loads..... (e) 1L Class 70R + 1L Class A: transverse placement.....	131 131 131 131 131
6.5	Deformation pattern of the central node of the deck for 3 <sup>rd</sup> load case: 3L Class A ( <i>focusing on dynamic component</i> ) .....	133
7.1	Experimental set-up showing RC beam considered in present study with embedded CVS and SBPS (covered with adhesive) at its mid point.....	143
7.2	(a) Isometric view of RC beam with PZT patch surface bonded at midpoint..... (b) RC beam with an enlarged view to show embedded PZT patch....	144 144
7.3	(a) Isometric view of free PZT patch restrained at top and bottom central node..... (b) Electrical boundary conditions of free PZT patch.....	147 147
7.4	Comparison of numerical (a) conductance and (b) suscetance signature of a free PZT patch with analytical and experimental results.....	148
7.5	Comparison of (a) numerical and (b) experimental voltage generated by SBPS and embedded CVS in the RC beam.....	150
7.6	Load resistance attached across the (a) SBPS and (b) embedded CVS.....	152
7.7	RMS power for varying load resistance across (a) SBPS and (b) embedded CVS.....	152
7.8	Variation of (a) maximum power and (b) power corresponding to load resistance, $R_L = 10 \text{ M}\Omega$ generated by SBPS and embedded CVS with varying piezo thickness.....	153
7.9	RMS voltage varying with load resistance across (a) SBPS and (b) embedded CVS. ....	154

FIGURE	CAPTION	PAGE NO.
7.10	RMS current varying with load resistance across (a) SBPS and (b) embedded CVS. ....	155
7.11	Voltage generated by (a) SBPS and (b) embedded CVS, with constant adhesive bond layer thickness ( $t_s$ ); and (c) ratio of voltage generated by perfectly bonded embedded CVS and SBPS for varying piezo thickness ( $h$ ).....	157
7.12	Voltage generated by (a) SBPS and (b) embedded CVS with varying piezo thickness ( $h$ ) for adhesive bond layer thickness ( $t_s$ ) in a fixed ratio of ' $h$ '. .....	159
7.13	(a) Voltage generated by SBPS with varying piezo size ( $L_p \times L_p$ ) for different piezo thickness ( $h$ ), [ <i>adhesive thickness, <math>t_s = 0.15</math> mm</i> ].....	162
	(b) Voltage generated by embedded CVS with varying piezo size ( $L_p \times L_p$ ) for different piezo thickness ( $h$ ), [ $t_s = 0.15$ mm].....	162
	(c) Voltage generated by SBPS with varying piezo size ( $L_p \times L_p$ ) for different piezo thickness ( $h$ ), [ $t_s = h/10$ ]. .....	162
	(d) Voltage generated by embedded CVS with varying piezo size ( $L_p \times L_p$ ) for different piezo thickness ( $h$ ), [ $t_s = h/3$ ]......	162
7.14	(a) Voltage generated by SBPS with varying piezo thickness ( $h$ ) for different areas of PZT patch ( $L_p \times L_p$ ), [ <i>adhesive thickness, <math>t_s = 0.15</math> mm</i> ]......	163
	(b) Voltage generated by embedded CVS with varying piezo thickness ( $h$ ) for different areas of PZT patch ( $L_p \times L_p$ ), [ $t_s = 0.15$ mm].....	163
	(c) Voltage generated by SBPS with varying piezo thickness ( $h$ ) for different areas of PZT patch ( $L_p \times L_p$ ), [ $t_s = h/10$ ]. .....	163
	(d) Voltage generated by embedded CVS with varying piezo thickness ( $h$ ) for different areas of PZT patch ( $L_p \times L_p$ ), [ $t_s = h/3$ ]......	163
7.15	(a) Voltage generated by SBPS with varying shear modulus ( $G_s$ ) of adhesive for different adhesive thickness, [ <i>piezo thickness, <math>h = 0.3</math> mm</i> ]. .....	165
	(b) Voltage generated by embedded CVS with varying shear modulus ( $G_s$ ) of adhesive for different adhesive thickness, [ $h = 0.3$ mm]. .....	165
7.16	(a) Voltage generated by SBPS for varying piezo thickness with and without cover of adhesive layer over its top. ....	167
	(b) Ratio of voltage generated by embedded CVS and SBPS for varying piezo thickness with and without cover of adhesive layer over its top.....	167
7.17	Experimental set-up for acquiring EMI signatures of surface bonded PZT patches.....	168

---

<b>FIGURE</b>	<b>CAPTION</b>	<b>PAGE NO.</b>
7.18	Comparison of conductance and susceptance signatures with and without protective layer over the sensors for surface bonded PZT patch at (a) location 9, (b) location 10 and (c) location 11 .....	169

## LIST OF TABLES

TABLE	CAPTION	PAGE NO.
1.1	Difference between SHM, condition assessment and non-destructive evaluation (Bhalla, 2014).....	4
2.1	Bulk transducer structures for energy harvesting (Priya and Inman, 2009).....	28
2.2	Comparison of energy sources (Roundy, 2003).....	38
2.3	Energy harvesting demonstrated capabilities (Paradiso and Starner, 2005).....	38
3.1	Properties of I-section beam.....	55
3.2	Properties of PZT patch (PI Ceramic, 2014) and bond layer.....	64
3.3	Values of key parameters associated with shear lag effect.....	68
3.4	Experimental values of voltage, current and power for varying forcing frequencies.....	73
4.1	Properties of RC beam.....	89
4.2	Properties of PZT patch (PI Ceramic, 2014) and bond layer.....	89
4.3	Voltage generated by surface bonded and embedded CVS for four cases.....	98
4.4	Experimental values of voltage, power and current for varying forcing frequencies with shaker at centre.....	102
4.5	Experimental values of voltage, power and current for varying forcing frequencies with shaker at an offset of 600 mm from centre.....	102
4.6	Power generated by the embedded CVS at different locations when the shaker was positioned at centre of the beam .....	103
5.1	Charging cycles for different circuits for various applications .....	124
6.1	Peak vibration amplitudes and corresponding voltage and power for five load cases ( $t_s$ : bond layer thickness; $h$ : PZT patch thickness).....	134
6.2	Voltage and power generated by the surface bonded PZT patch under vibrations experienced at the mid span of existing real-life steel bridges.....	138
6.3	Voltage and power generated by the embedded CVS under vibrations experienced at the mid span of existing real-life RC bridges.....	139
7.1	Properties of PZT patch (PI Ceramic, 2014) and bond layer.....	145



## LIST OF SYMBOLS

$a$	Amplitude of vibration of beam
$A_{st}$	Area of tensile reinforcement
$b$	Width of RC beam
$B$	Susceptance
$c$	Equivalent damping
$(C_F)_{exp}$	Experimental calibration constant for piezo force-sensor
$(C_F)_{th}$	Theoretical calibration constant for piezo force-sensor
$C$	Capacitance of piezo sensor
$C_a$	Calibration constant for accelerometer
$C_b$	Curvature of beam
$C_n$	Generalized damping
$d$	Depth of neutral axis
$d'$	Distance of the centre line of PZT patch from neutral axis of beam
$[d]$	Third order piezoelectric strain coefficient tensor
$D$	Overall depth of beam
$D'$	Equivalent overall depth of beam( $=D-2t_c-2t_s-h$ )
$D_3$	Charge density
$[D_e]$	Electric displacement vector
$E$	Young's modulus of elasticity
$E_3$	Electric field along direction 3
$EI$	Flexural rigidity of beam
$EI_g$	Flexural rigidity of girder of flyover
$f$	Operating frequency of dynamic shaker
$f_a, f_b$	Forcing frequencies at which the amplitude is $1/\sqrt{2}$ times the resonant amplitude
$f_{br}$	Natural frequency of bridge
$f_{ck}$	Characteristic strength of concrete
$f_n$	Resonance frequency
$f_{sh}$	Natural frequency of vibration of inertial-type shaker
$f_y$	Characteristic strength of reinforcement in the RC beam
$F$	Force
$g$	Acceleration due to gravity
$G$	Conductance
$G_k^u$	Undamaged conductance value
$G_k^d$	Damaged conductance value
$G_s$	Shear modulus of elasticity of bonding layer

$h$	Thickness of PZT patch
$i$	Instantaneous current flowing in power measuring circuit
$i_L$	Current flowing in circuit with load resistance across PZT patch
$i_{\text{peak}}$	Maximum current flowing in power measuring circuit
$i_{\text{RMS}}$	RMS current flowing in power measuring circuit
$I$	Second moment of inertia of beam
$k$	Equivalent stiffness
$k_{31}$	Coupling coefficient of the PZT patch
$(K_b)_S, (K_b)_E$	Correction factor for the shear lag effect in bond layer for surface bonded and embedded PZT patch, respectively
$K_n$	Generalized stiffness
$K_p$	Correction factor due to Poisson's effect
$(l_{\text{eff}})_E$	Effective length of embedded PZT patch
$L$	Length of beam
$L_p$	Length of PZT patch
$\bar{m}$	Mass per unit length of beam
$m_{P1}, m_{P2},$ $m_{P3}, m_{P4}$	Mass of additional four mass plates in inertial shaker
$m_t$	Mass of top plate in inertial shaker
$M$	Bending moment at any section of the beam
$M_n$	Generalized mass
$M_u$	Ultimate load carrying capacity of RC beam
$n$	Number of modes
$p(x,t)$	Forcing function
$p_o$	Amplitude of dynamic load
$P$	Instantaneous power generated by PZT patch
$P_{\text{avg}}$	Average power generated by PZT patch
$P_n$	Generalized force
$P_{\text{peak}}$	Maximum power generated by PZT patch
$P_{\text{RMS}}$	RMS power generated by PZT patch
$Q$	Total charge across PZT patch
$q_n$	Generalized displacement
$R_1, R_2$	Resistance used in power measuring circuit
$R$	Resistances measured by AD5933
$R_D$	Dynamic magnification factor
$R_L$	Load resistance across PZT patch
$[S]$	Second order strain tensor
$(S_1)_S, (S_1)_E$	Strain in the topmost fibre of beam with surface-bonded and embedded PZT patch, respectively

$S_2$	Strain in the bottom-most fiber of the beam
$s_{11}^E$	Elastic compliance of PZT patch corresponding to 11 axis
$S_b$	Strain in RC beam
$S_p$	Strain in PZT patch
$S_q^*$	Circuit sensitivity
$t_c$	Depth of PZT patch in embedded CVS from surface of concrete beam
$(t_s)_S, (t_s)_E$	Thickness of bond layer for surface bonded and embedded PZT patch, respectively
$T_3$	Stress in direction '3' (thickness of patch)
$T_p$	Axial stress in PZT patch
$u(x,t)$	Displacement amplitude of dynamic vibration
$u_p$	Displacement at the interface between PZT patch and bond layer
$u_b$	Corresponding displacement at interface between bond layer and beam
$(u_{st})_o$	Static deflection of beam at centre
$(u_{st})_{peak}$	Peak deflection of beam at centre
$U$	Total energy generated by PZT patch
$V_1$	Voltage across PZT patch in power measuring circuit
$V_2$	Voltage across Resistance ' $R_2$ ' in power measuring circuit
$V_a$	Voltage output across accelerometer
$V_F$	Voltage across piezo force-sensor
$V_{FFT}$	FFT amplitude of voltage
$V_L$	Voltage across load resistance attached to PZT patch
$(V_p)_S (V_p)_E$	Voltage across the terminals of surface bonded and embedded PZT patch, respectively
$(V_p^M)_S, (V_p^M)_E$	Voltage generated by surface bonded and embedded PZT patch, respectively, considering mechanical loss
$(V_p^S)_S, (V_p^S)_E$	Voltage generated by surface bonded and embedded PZT patch, respectively, considering shear lag loss
$w_b$	Width of beam
$w_p$	Width of PZT patch
$x$	Displacement
$x'$	Real component of mechanical impedance
$\ddot{x}$	Acceleration
$X$	Reactance measured by AD5933
$(X_{eff})_S, (X_{eff})_E$	Effective length fraction of the surface bonded and embedded PZT patch, respectively
$y'$	Imaginary component of mechanical impedance
$y$	Beam deflection

$Y_o$	Amplitude of vibration
$\overline{Y^E}$	Complex young's modulus of elasticity of the PZT patch at constant electric field
$(Y_{eff})_S, (Y_{eff})_E$	Effective width fraction of surface bonded and embedded PZT patch, respectively
$Z$	Mechanical impedance of the structural system,
$Z_a$	Mechanical impedance of the PZT patch
$\zeta$	Damping Ratio
$\zeta_e$ and $\zeta_m$	Transducer and mechanical damping ratio
$\omega$	Operating angular frequency
$\omega_n$	Natural angular frequency
$\phi_n$	$n^{\text{th}}$ mode shape
$\theta$	Phase angle
$\overline{\epsilon_{33}^T}$	Complex electric permittivity (in direction '3') at constant stress
$\zeta_E$	Strain lag ratio for embedded PZT patch
$(\xi_E)_{L_p/2}$	Strain lag ratio at the ends of embedded PZT patch
$\sigma_b$	Bending stress of beam at its extreme top fibre
$\kappa$	Wave number.
$\eta$	Mechanical loss factor of the PZT material
$\eta_{cE}$	Compliance matrix loss factor
$\eta_s$	Structural loss factor
$\delta$	Dielectric loss factor of PZT material
$\nu$	Poisson's ratio
$\rho$	Density
$\tau$	Interfacial shear stress
$\Gamma_S$	Shear lag parameter for surface bonded PZT patch
$\Gamma_E$	Modified shear lag parameter for embedded PZT patch
$\gamma$	Shear strain in bond layer

## **LIST OF ACRONYMS**

AC	Alternative Current
CVS	Concrete Vibration Sensor
CVEH	Concrete Vibration Energy Harvester
c/c	Centre to centre distance
DAQ	Data Acquisition system
DC	Direct Current
DI	Damage Index
EMI	Electro-Mechanical Impedance
FFT	Fast Fourier Transformation
FRF	Frequency Response Function
LCR	Inductance Capacitance Resistance
NASA	National Aeronautics and Space Administration
NDT&E	Non-destructive Testing and Evaluation
PA	Power Amplifier
PVDF	Polyvinylidene Fluoride
PZT	Lead Zirconate Titanate (Piezoelectric Ceramic)
RC	Reinforced Concrete
RF	Radio Frequency
RMS	Root Mean Square
RMSD	Root Mean Square Deviation
SBPS	Surface Bonded PZT Sensor
SHM	Structural Health Monitoring
SMIS	Shuttle Modal Inspection System
SOI	Silicon on Insulator
SSDL	Smart Structures and Dynamic Laboratory
UDL	Uniformly Distributed Load



# **Chapter 1**

## **INTRODUCTION**

### **1.1 BACKGROUND**

Structural health monitoring (SHM) is currently attracting huge research funding across the world. Experts have identified SHM as one of the top ten technologies having the potential of driving the global economy (Majcher, 2011). SHM, especially for large civil structures, needs a mega network of sensors distributed throughout the structure. Powering these sensors is a critical issue. It either requires a distributed network of wiring or warrants installation of individual batteries, both of which call for huge investment. Fortunately, the power requirement of the sensors generally is low, ranging from micro to milli watts, and reducing further day by day. This has catalysed research efforts to explore the possibility of employing renewable energy sources to power the sensors. The use of piezoelectric materials to act as generators for converting the vibrational energy of structures into electrical energy is one such possibility being explored rigorously over the last three decades. Piezoelectric ceramic (PZT) patches, operating in  $d_{31}$ -mode, are considered best for SHM. However, for energy harvesting, built up configurations such as stack actuators are somewhat more preferred. The main objective of this thesis is to explore the potential of employing the same piezo sensor, operating in  $d_{31}$ -mode, for SHM as well as energy harvesting on real-life structures.

## 1.2 MOTIVATION

All structures are subjected to slow and continued deterioration, caused by several factors, such as environmental degradation, fatigue, excessive loads, vehicle impacts and prolonged extensive usage. Even a minor incipient damage carries the potential to grow out of proportion, culminating in collapse, thereby leading to disruption of services and/or loss of life and property. Whereas a car costing few thousand of dollars only is well equipped with sophisticated sensors, which continuously monitor its operational performance, the civil engineers, on the contrary, seldom check, validate, or evaluate the performance of their designed structures after construction. External loads due to construction, occupancy, vehicle movement, blast/ impact, and the associated stresses and deflections along with structural response, if monitored for occurrence of damages, the process is called as *structural health monitoring* (SHM).

Over the past few decades, piezo sensors have already established their niche in detecting, locating and estimating the severity levels of damage occurring in mechanical and structural systems. Employing these sensors for energy harvesting along with SHM has attracted researchers after the recent advent of modern low power consuming electronic circuits. *Energy harvesting* is converting the ambient energy (sunlight, thermal gradient, human motion and body heat, structural vibrations and ambient radio-frequency energy) into useful forms for direct/ future use. For the research covered in this thesis, mechanical vibrations of the structures are considered as the ambient source for energy. Mechanical vibrations ( $300 \mu\text{W}/\text{cm}^3$ ) and air flow ( $360 \mu\text{W}/\text{cm}^3$ ) are today the most attractive alternatives for energy harvesting (Park et al., 2008). The advances in the wireless technology and low power electronics like micro electro-mechanical systems (MEMS)

have resulted in intensified research in this area during the recent years. Das (2014) has estimated a \$ 823.8 million market for piezoelectric energy harvesters by 2023, with several thousand of developers involved throughout the value chain. There are two common modes utilized for piezoelectric energy harvesting:  $d_{33}$ -mode (stack actuators) and  $d_{31}$ -mode. In  $d_{33}$ -mode, the direction of the applied stress (force) and the generated charges (voltage) is the same (thickness), while in  $d_{31}$ -mode, stress is applied in the axial direction but the charges (electric voltage) are developed in perpendicular (thickness) direction. This thesis explores the possibility of stand-alone PZT patches operating in  $d_{31}$ -mode for energy harvesting alongside SHM. The  $d_{31}$ -mode is considered here because the corresponding excitation is more easily achieved by environmental sources in civil structures (Ramsey and Clark, 2001, Mateu and Moll, 2005). Further, the main focus of this thesis is civil structures, where plate type piezo patches are more preferred owing to their suitability for SHM.

Although extensive research in the field of energy harvesting using piezoelectric sensors can be found in literature, the integrated use of these sensors both for SHM and energy harvesting is new in its kind. Possibility of energy harvesting using the  $d_{31}$ -mode, which is generally employed for SHM, has not yet been explored in depth on civil structures. This configuration provides an advantage of being simple and most natural excitation from ambient sources. Additionally, it adequately serves for SHM, either based on the electro-mechanical impedance (EMI) technique, or the global vibration technique based on strain mode shape, or a combination of the two (Shaker et al., 2011). The prime objective of this thesis is to explore the possibility of both energy harvesting and SHM from surface bonded/ embedded PZT patches operating in the  $d_{31}$ -mode.

### 1.3 PIEZO SENSORS FOR STRUCTURAL HEATH MONITORING (SHM) AND ENERGY HARVESTING

In specific technical terms, SHM is defined as the measurement of the operating and the loading environment and the critical responses of a structure to track and evaluate the symptoms of operational incidents, anomalies, and/ or deterioration or damage indicators that may affect operation, serviceability, or safety reliability (Aktan et al., 2000). Another definition (Kessler et al., 2002), states that SHM denotes a reliable system with ability to detect and interpret adverse changes in the structure due to damage and normal operation. In most general terms, SHM implies acquisition, validation and analysis of technical data to facilitate the life cycle management decisions. The difference between SHM, condition assessment and non-destructive evaluation is explained in Table 1.1.

**Table 1.1:** Difference between SHM, condition assessment and non-destructive evaluation (Bhalla, 2014).

Structural Health Monitoring (SHM)	Condition Assessment	Non-Destructive Evaluation
Implies continuous monitoring	Periodic one-time establishment of current conditions of the structure	Evaluation of the properties of a material, component or system as and when needed (not in continuous manner), without subjecting it to damage.
To diagnose onset of anomalies in structural behaviour and performance	To check the fitness of the structure for a particular purpose	To detect specific flaw. Example: Ultrasonic, magnetic-particle, dye penetration, radiography, eddy currents, etc.
Broad and all inclusive scope	Subset of SHM	NDE may aid in SHM/ condition assessment

SHM is important for critical structures owing to following reasons:

- (a) To timely detect structural damages and take remedial actions
- (b) To ensure design validation, since structural design is often based on parameters affected by statistical variation and uncertainties.
- (c) Evaluation of structure after major retrofitting during design life.
- (d) To provide an alternative to conventional visual inspection, this is time as well as cost ineffective.
- (e) By monitoring of external loads, stress distributions and deflections, SHM can enable better understanding structural behaviour.

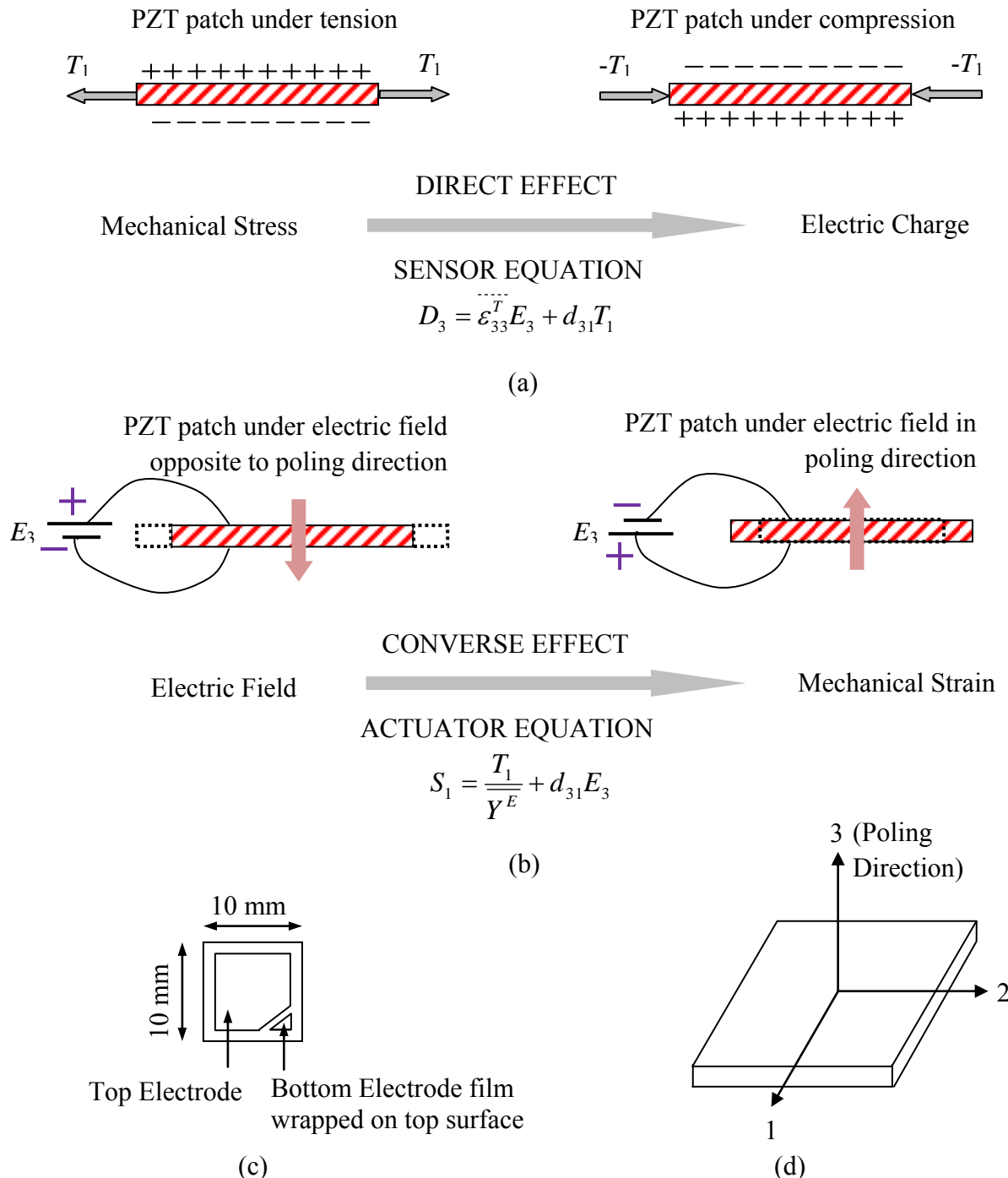
SHM has now been very well recognized as a crucial element of the overall structural management (Bhalla, 2004; Shanker et al., 2010 and Talakokula et al., 2014). However, it has not become a part of the codal provisions yet, though it is occasionally included in the contract now days, especially for critical structures such as long span bridges. No detailed cost-benefit analysis is available which can facilitate both the end user as well as the performer to decide upon the most effective method to be opted for SHM. It still lacks in certification, which is need of the day, since it is the age of the so called *brand*, no process is considered *authentic* without certification.

The sensors employed for the SHM are broadly divided into two major categories (a) Conventional sensors (b) Sensors based on smart materials. Electrical strain gauge, vibrating wire strain gauges, and accelerometers are few widely used sensors which can be categorized under conventional sensors. *Smart materials* are defined as the materials having the ability to change their physical properties in a specific manner due to a certain specific type of stimulus input (Rogers, 1988). Some of the commercially available smart materials are piezoelectric materials, shape memory alloys, electro-rheological fluids,

optical fibres and magneto-strictive materials. The work presented in this thesis is based on piezoelectric materials, often referred to as piezo sensors. Piezo sensors are available in two commercial forms: (a) Ceramics such as Lead Zirconate Titanate (PZT) (b) Polymers such as Polyvinylidene Fluoride (PVDF). Ceramics have higher strength and stiffness, however, they are somewhat brittle and hence not compliant with curved surfaces. They are suitable both as sensors as well as actuators. On the other hand, polymers are characterized by lesser strength and stiffness but are ductile and possess shape conformability. The piezo patches exhibit two special effects due to the phenomenon of piezoelectricity. They generate surface charges in response to a mechanical stresses applied in the plane of the patch, this phenomenon is called the '*direct effect*'. Conversely, they undergo mechanical deformations in response to an electric field applied across their thickness, which is known as the '*converse effect*'. Sensor applications are based on the direct effect, and actuator applications are based on the converse effect. The direct and converse effects exhibited by piezoelectric materials are explained with the help of the diagram and the equations presented in Figure 1.1. The constitutive relations (Sirohi and Chopra, 2000) for piezoelectric materials are

$$\begin{bmatrix} D_e \\ S \end{bmatrix} = \begin{bmatrix} \bar{\epsilon}^T & d^T \\ d & \bar{s}^E \end{bmatrix} \begin{bmatrix} E \\ T \end{bmatrix} \quad (1.1)$$

where,  $[D_e]$  (3×1) (C/m<sup>2</sup>) is the electric displacement vector,  $[S]$  (3×3) is the second order strain tensor,  $[E]$  (3×1) (V/m) is the applied external electric field vector and  $[T]$  (3×3) (N/m<sup>2</sup>) is the second order stress tensor. Accordingly,  $\bar{\epsilon}^T$  (F/m) is the second order dielectric permittivity tensor under constant stress,  $[d]$  (C/N) is the third order piezoelectric strain coefficient tensors and  $\bar{s}^E$  (m<sup>2</sup>/N) the fourth order elastic compliance tensor under constant electric field.



**Glossary:**

$D_3$ : the electric displacement over the PZT patch;  $E_3$ : Electric field in direction '3';  $T_1$ : Axial stress in direction '1';  
 $S_1$ : Strain in direction '1';  $d_{31}$ : Piezoelectric strain coefficient;  $\bar{\epsilon}_{33}^T$ : Complex electric permittivity (in direction '3') at constant stress;  $\bar{Y}^E$ : Complex Young's Modulus of elasticity corresponding to direction '1' at constant electric field

**Figure 1.1:** (a) Behaviour of PZT patch under direct effect.  
 (b) Behaviour of PZT patch under converse effect.  
 (c) A typical commercial PZT patch (PI Ceramic, 2014).  
 (d) PZT patch with conventional 1, 2 and 3 axis.

The most common application of the piezo sensor is strain measurement using the direct effect. The most striking unconventional application of piezo patches in the recent years has been in the form of the EMI technique. In this technique, unlike the conventional sensors, piezo sensors do not directly measure the physical parameters such as stresses, strains etc. Rather, they are capable of extracting a signature of the host structure to which they are bonded/ embedded by which damage detection can be done by comparing it with the signature acquired in the pristine stage (baseline signature). Typically, the PZT patch is electrically excited at ultrasonic frequencies (30-400 kHz) and its admittance measured as a function of frequency forms a diagnostic signature of the structure, any deviation of which provides an indication of damage.

As pointed earlier, the process of extracting energy from the environment or from a surrounding system, converting it to useable electrical power for direct use or stored for future use is known as *energy harvesting* (Park et al., 2008). Energy harvesting eliminates the requirement of running wires for operating electronics and thus the need of frequent replacement of batteries is also taken care of.

The two common modes utilized for piezoelectric energy harvesting namely, the  $d_{33}$ -mode (stack actuators) and the  $d_{31}$ -mode are illustrated in Figure 1.2. As pointed earlier, the research presented in this thesis explores the possibility of stand-alone PZT patches operating in  $d_{31}$ -mode. The  $d_{31}$ -mode is considered here because the corresponding excitation is more easily achieved by environmental sources in civil structures.

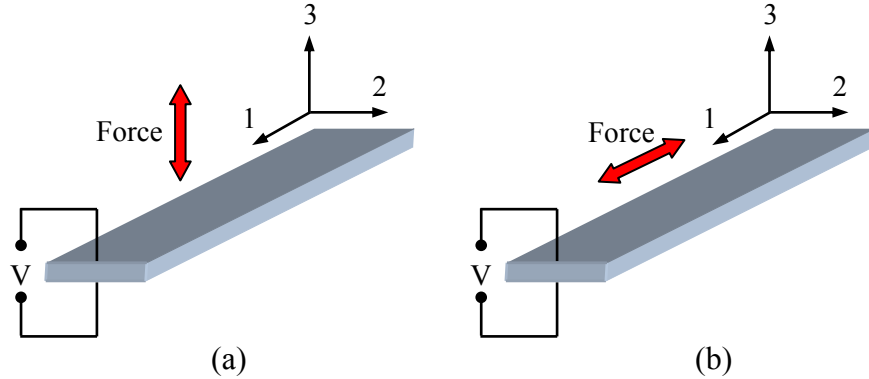


**Figure 1.2:** Operating modes (a)  $d_{33}$ -mode and (b)  $d_{31}$ -mode of piezoelectric transducer (Priya and Inman, 2009).

#### 1.4 RESEARCH OBJECTIVES AND SCOPE

So far, the piezo sensors have been independently employed for SHM and energy harvesting. Keeping in view the background given above, it is justified to pursue the present study to develop a conceptual framework which can integrate the two functions using same PZT patch. The main objective of this thesis is to investigate the potential of utilizing the **same PZT patch for SHM as well as energy harvesting employing axial strain actuation ( $d_{31}$ ) mode**. It is envisaged that in the *idle stage*, when SHM is not being performed, the PZT patch will be used for harvesting energy from the mechanical vibrations. In the *SHM stage*, the harvested energy will be utilized for performing SHM of the same structure. Secondary objectives of this research include developing and validating analytical and numerical models suitable for computation of harvestable energy from the piezo patches operating in  $d_{31}$ -mode, either in surface bonded or embedded configurations, including the **effect of losses** such as the mechanical loss, the dielectric loss and the shear lag loss and to extend the analytical model to real-life structures. Other objective includes performing detailed parametric studies to work out the optimum size and parameters of the patches from energy harvesting considerations. Use of normal plate

type piezo in axial strain mode in place of commercial expensive transducers for energy harvesting has been the innovative aspect of this study.

## 1.5 ORGANIZATION OF THESIS

The thesis is divided into eight chapters including the present introduction chapter. Important tables and figures have been presented wherever relevant. Chapter 1 covers the background and the overall idea of SHM and energy harvesting using piezo sensors. It also justifies the present study and further emphasizes the objectives of the work. Chapter 2 provides the summarized literature review of energy harvesting and SHM using piezo sensors. Chapter 3 provides the details of the modelling and experiments related to energy harvesting through piezo sensors in the surface-bonded configuration. Chapter 4 extends the model to piezo sensors in form of the embedded concrete vibration sensor (CVS) in RC structures for SHM and energy harvesting. Chapter 5 covers the proof-of-concept demonstration of combined energy harvesting and SHM using same PZT patch in  $d_{31}$ -mode. In this chapter long term and short term health monitoring of a real-life sized simply supported beam have also been covered. Chapter 6 extends the energy harvesting potential of the surface-bonded/ embedded CVS to real-life structures. It covers a semi-analytical modelling of a typical flyover and extending the proposed analytical models (derived in Chapter 3 and Chapter 4) to eight real-life existing bridges. Chapter 7 is based on numerical simulation to perform parametric study in order to achieve optimum parameters of PZT patch for energy harvesting. Chapter 8 summarizes the study and furnishes important conclusions that have been drawn based on the study. Originality of the work and new contributions are highlighted. Also, recommendations for further research are included in this chapter. Finally, author's publications and references followed by appendices have been provided at the end.

## **Chapter 2**

# **STATE-OF-THE-ART IN STRUCTURAL HEALTH MONITORING AND ENERGY HARVESTING**

### **2.1 INTRODUCTION**

During the past few decades, piezo sensors have established their niche in detecting, locating and estimating the severity levels of structural damage via the global vibration as well as the local EMI techniques. Employing these sensors for energy harvesting along with SHM has attracted researchers after the recent advent of modern low power consuming electronics. The area of energy harvesting has ample scope of advancement in future, and hence, the recent upsurge in the research in this field is more than justified. Advances in wireless technology and low power electronics like micro electro-mechanical systems (MEMS) devices have resulted in intensified research in this area in the recent years. In the SHM set-up, ideally, uninterrupted power supply should be available for the entire span of the sensor to circumvent battery replacement. Hence, enormous amount of financial and intellectual efforts are being investigated in this field currently. Das (2014) has estimated a \$ 823.8 million market for piezoelectric energy harvesters by 2023, with several hundred developers involved throughout the value chain. Wireless sensors, embedded in inaccessible locations of the structures, from where retrieval is difficult, need to have a self-sustaining power source. Conventionally, batteries have been used for this purpose but they need to be substituted with alternate power sources that can allow longevity in terms of power availability. Else, frequent battery replacement would prove unfeasible as well as uneconomical. Hence, for a sustainable solution to the problem, the power available from various renewable sources

needs to be tapped and stored. Ideally, the power back up should be available for the entire life span of the sensor implying continuous tapping of energy. Sensors equipped with energy harvesters have the versatility of being placed in the most inaccessible locations like bridges, aerospace installations, ships etc. to provide vital information on a wide variety of issues like operational, environmental and structural conditions.

## **2.2 EVOLUTION AND ADVANCES IN STRUCTURAL HEALTH MONITORING**

Due to the development of newer reliable algorithms, miniaturization and cost reductions of digital computing hardware, SHM is increasingly being implemented on real-life structures. It has received considerable attention in the technical literature and a brief summary of the developments in this technology over the last 40 years is presented below.

The oil industry has been instrumental in making considerable efforts to develop vibration based damage identification methods for offshore platforms during the 1970s and the 1980s (Farrar and Worden, 2007). The common methodology adopted by the oil industry was to numerically simulate candidate damage scenarios, examine the changes in resonant frequencies due to damage, and correlate these changes with those measured on a platform. However, this method had various practical problems. These included measurement difficulties caused by platform machine noise, instrumentation difficulties in hostile environments, changing mass caused by marine growth, varying fluid storage levels, temporal variability of foundation conditions and the inability of the wave motion to excite the higher vibration modes. In combination, these issues prevented the adaptation of the simulation based SHM approach for offshore platforms. Due to these problems, this approach was gradually abandoned in the early 1980s.

In the late 1970s and the early 1980s, the aerospace community began to consider the use of vibration-based damage identification in combination with the development of the space shuttle (Farrar and Worden, 2007). The National Aeronautics and Space Administration (NASA) has implemented the idea on its current space station and future reusable launch vehicle designs. The shuttle modal inspection system (SMIS) was developed to identify fatigue damage in components such as control surfaces, fuselage panels and lifting surfaces. The damaged parts, which are covered by the thermal protection system, have been successfully located by the SIMS. Since 1987, all the orbiter vehicles have been periodically subjected to SMIS testing. Boller and Buderath (2007) provide a more detailed discussion of SHM applied to aerospace structures.

The civil engineering community began showing interest in vibration-based damage assessment of bridge structures and buildings since the 1900s (Farrar and Worden, 2007). The primary features, which have been widely used to identify damage in bridge structures include the modal properties and the related parameters, such as the mode shape curvature and the dynamic flexibility matrix indices. Several experiment-based structural assessments of the bridges have been conducted before and after upgrading works, including strengthening, through the subsequent model updating (Brownjohn et al., 2003). Moyo et al. (2004) reported the application of extreme value statistics to estimate bridge live loads using strain measurements. Monitoring programs on different highway bridges originating from a range of requirements related to calibration of numerical models and long-term tracking of performance have been summarized Brownjohn et al. (2005) to draw out lessons relevant to the future development of SHM ‘systems’. Variability in environmental and operating conditions and specifically, the physical size of structure, present significant challenges to real-life bridge monitoring.

Regulatory requirements in Asian countries, which mandate that the companies that construct the bridges periodically certify their structural health, are driving current research and commercial development of bridge SHM systems (Farrar and Worden, 2007).

SHM techniques are divided into two major categories: (a) Global techniques (b) Local/Non-destructive evaluation (NDE) techniques. *Global techniques*, which essentially involve measurement of the overall structural response, are further sub-divided into two types: (i) global dynamic techniques (ii) global static techniques. In *global dynamic techniques*, the structure is subjected to low frequency excitations, of the order of 1-100 Hz. From the structural modal response, the first few mode shapes and their corresponding natural frequencies are extracted. Many ‘quick’ algorithms have been proposed to locate and quantify damage in simple structures (mostly beams) from the measured natural frequency and the mode shape data; such as the change in curvature mode shape method (Pandey et al., 1991), the change in stiffness method (Zimmerman and Kaouk, 1994), the change in flexibility method (Pandey and Biswas, 1994) and the damage index method (Stubbs and Kim, 1994). The main drawback of these techniques is that they rely on a relatively small number of low order modes, which, being global in character, are not very sensitive to the localized incipient damages (Bhalla and Soh, 2004a). This shows that the global parameters (on which these techniques heavily rely) are not significantly altered by the localized/incipient damages. Hence, these techniques are insensitive to local or incipient damages. Another limitation of these techniques is that measurement at low frequencies may get contaminated by ambient vibrational noise, which also happens to be in the low frequency range, typically less than 100 Hz. The *global static techniques*, such as the static displacement response technique (Banan et al.,

1994) and the static strain measurement technique (Sanaye and Saletnik, 1996), involve the measurement of the displacements (or strains) at specified points under the action of static forces applied at same or other specified locations. The main limitation of the static response techniques is that their application on real-life-sized structures is not practically feasible. Further, the application of large loads to cause measurable deflections (or strains) requires huge machinery and power input. As such, the static technologies are not considered amenable to practical application.

Contrary to the global techniques, the *Local/ NDE techniques* rely on the localized interrogation of structures for detection and localization of structural damage. These techniques are best to use when approximate damage location is known *a-priori*. Popular techniques under this category are ultrasonic wave propagation, acoustic emission, eddy currents, impact echo testing, magnetic field methods, electrical methods, dye penetrant testing and X-ray radiography. Detailed description of these methods can be found in literature (Mark and George, 2000-2003; McCann and Forde, 2001). The main limitation of the above NDE techniques is that they may render the structure unavailable during the interrogation and perform optimally under specific conditions only. In most of the techniques, a probe needs to be physically moved around the structure to record the data, which is not only tedious but may demand the removal of finishes or covers such as false ceilings. As such, these techniques work best only for specific industrial applications, where the user has some idea about the possible damage location.

The *Electro-mechanical impedance* (EMI) technique is an interface between the global dynamic techniques and the local NDE technique described above. The transducers used for the EMI technique are patches made of piezoelectric materials like PZT, and can act

as both sensors and actuator simultaneously and eventually as mechatronic impedance transducers (MIT) due to their direct and converse effect capabilities. In the EMI technique, a PZT patch is surface bonded on a structure using high strength adhesive and subjected to an alternating voltage excitation from an impedance analyzer/ LCR meter [Figure 2.1(a)], sweeping through a particular frequency range, generally a subset of 30–400 kHz. At a given frequency, the patch actuates the structure and the structural response is in turn sensed and measured in terms of the electro-mechanical admittance of the patch, consisting of the real and the imaginary components, the conductance, and the susceptance, respectively. In this manner, frequency plots, termed conductance and susceptance signatures, are generated across the specified frequency range. Figure 2.1(b) shows the idealized connection between the PZT patch and the host structure, as a link element connected to the structure at its ends. The PZT patch-host structure system can be equivalently represented by mechanical impedance ( $Z$ ), connected to an axially vibrating thin bar, as shown in Figure 2.1(c). In this figure,  $l$  is the half-length;  $w$  is the width and  $h$  is the thickness of the PZT patch. Electric field (by LCR meter) is acting in direction ‘3’, which causes dynamic axial vibrations of the patch in direction ‘1’. The two end points of the patch can be assumed to encounter equal mechanical impedance  $Z$  (from the host structure) due to negligible mass and stiffness of PZT patch. Under these conditions, the patch invariably has nodal point at the centre [Figure 2.1(b)], irrespective of its location on the host structure (Bhalla, 2004). The governing one-dimensional wave equation for the generic system comprising one half of the patch and the structure [Figure 2.1(c)], was first solved by Liang et al. (1994) using the impedance approach. Using Liang’s generic derivation, the following expression can be written for the complex electro-mechanical admittance  $\bar{Y}$  (inverse of electrical impedance), of the coupled system shown in [Figure 2.1(c)]

$$\bar{Y} = 2\omega j \frac{wl}{h} \left[ \bar{\varepsilon}_{33}^T + \left( \frac{Z_a}{Z + Z_a} \right) d_{31}^2 \bar{Y}^E \left( \frac{\tan \kappa l}{\kappa l} \right) - d_{31}^2 \bar{Y}^E \right] \quad (2.1)$$

where,  $d_{31}$  is the piezoelectric strain coefficient,  $\bar{Y}^E$  the complex Young's modulus of the PZT patch at constant electric field,  $\bar{\varepsilon}_{33}^T$  the complex electric permittivity of the PZT material at constant stress,  $Z$  the mechanical impedance of the structural system,  $Z_a$  the mechanical impedance of the PZT patch,  $\omega$  the angular frequency and  $\kappa$  the wave number. It may be noted here that a factor of 2 appears in this equation (contrary to Liang's original derivation) to take care of the full length of the patch as against half length in the case of the original derivation of Liang.

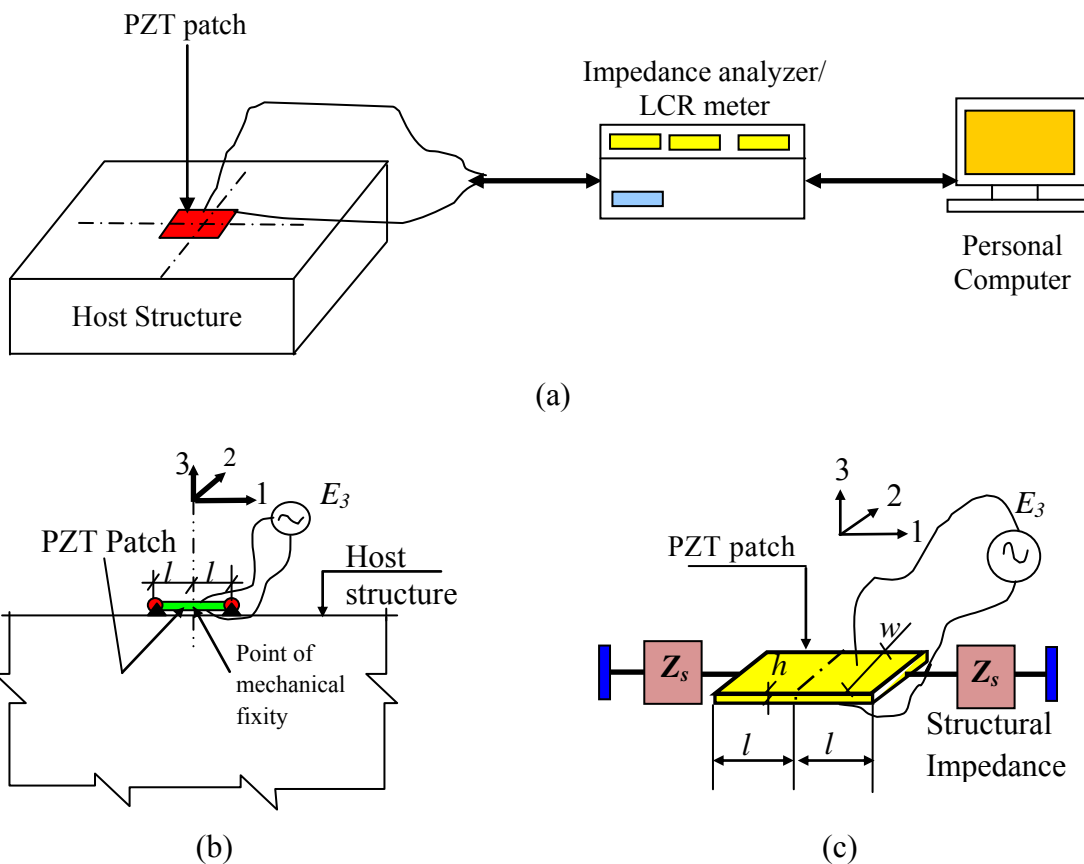


**Figure 2.1:** (a) A typical structure under interrogation by EMI technique.  
 (b) A PZT patch surface-bonded to a structure.  
 (c) Liang's 1D impedance model for the system shown in (b).

The mechatronic coupling represented by Eq. (2.1) is utilized for damage detection in the EMI technique. The structural mechanical impedance  $Z$  in this equation is a function of the structural parameters, i.e. the stiffness, the damping and the mass. Any damage to the structure will cause these parameters to change, and hence alter the drive point mechanical impedance  $Z$ . Consequently, as can be observed from Eq. (2.1), the electro-mechanical admittance,  $\bar{Y}$ , will undergo change, and this serves as an indicator of the state of health of the structure. Measuring  $Z$  directly may not be feasible practically, but  $\bar{Y}$  can be easily measured by using an electrical impedance analyzer/ LCR meter. The measured admittance is a complex quantity consisting of real and imaginary parts, the conductance ( $G$ ) and the susceptance ( $B$ ); respectively, and its unit is Siemens ( $\text{ohm}^{-1}$ ). During the initial years of the EMI technique, the imaginary part was regarded to have a weak interaction with the structure (Sun et al., 1995). The real part, on the other hand, was regarded to actively interact with the structure and was, therefore, preferred in SHM applications. A plot of  $G$  over a sufficiently wide band of frequency serves as a diagnostic signature of the structure and is called the conductance signature. Bhalla and Soh (2003) advocated using both  $G$  and  $B$  to extract components of  $Z$  for improved structural identification and damage diagnosis.

The EMI technique has far greater sensitivity to damage than the global techniques. Yet, it is not as cumbersome to implement on large structures as the local NDE techniques. The piezoelectric transducers are bonded non-intrusively on the structure, have negligible weight, exhibit negligible effect of ageing and demand low power consumption (Park et al., 2000). Use of an array of such transducers omits the requirement of damage location to be known a priori (Soh et al., 2000; Park et al., 2001). The limited sensing area of the PZT patches aids in isolating the effects of far field changes, including boundary

conditions. The PZT transducers are permanently bonded to the structure and can be interrogated without removal of any finishes. Several other advantages of these transducers like low-cost, fast dynamic response, long term durability and competitive performance, negligible ageing, immunity to noise, render them preferable for autonomous SHM.

Some prominent developments in the field of EMI technique reported during the last one and a half decade are briefly covered here. Giurgiutiu et al. (2002) combined the EMI technique with wave propagation approach for crack detection in aircraft components. Lim et al. (2006) presented a new method for structural identification and SHM using the EMI technique without demanding any prior information about the structure. Hey et al. (2006) investigated important practical issues concerning the implementation of EMI based SHM and proposed a new interrogation algorithm utilizing sensor multiplexing to optimize the interrogation time of the sensors. Yang et al. (2008) simulated the PZT-structure interaction at the high frequencies (up to 1000 kHz) through FEM using ANSYS 8.1. Their studies proved that FEM could serve as an excellent alternative to the experimentation in investigations involving the EMI technique. Bhalla et al. (2009) presented a simplified impedance model incorporating shear lag effect into the electro mechanical admittance signatures for both 1D and 2D cases. This culminated into a closed form solution, circumventing the necessity of preparing a model of the host structure or the bond layer. More accurate models of piezo-bond-structure interaction have also come up in the recent years (Bhalla and Moharana, 2012; Moharana and Bhalla, 2014). Shanker et al. (2010) proposed the simultaneous application of the EMI and the global dynamic techniques using the same set of PZT sensor patches for SHM. The combined approach was demonstrated to be more sensitive, reliable and cost effective in

detecting damage ranging from incipient to severe types in the civil structures. In global dynamic technique, PZT patch act as sensor only. Hence, the integrated technique suggested by Shanker et al. (2010, 2011) substituted expensive accelerometers by low-cost PZT patches. The experimental undamaged and damaged mode shapes could be directly obtained, circumventing any numerical modelling of structure. It was shown that damage detection, localization and severity assessment can be done more optimally using the global techniques after the damage has reached ‘moderate’ levels. Bhalla et al. (2012) presented a new approach for fatigue life assessment of bolted steel joints using the equivalent stiffness determined by the surface bonded piezo-impedance transducers. The most promising feature of the EMI technique, when employed through the extraction of structural mechanical impedance, is that it circumvents determination of the actual stiffness of the component. The equivalent stiffness is more than sufficient in characterizing the damage completely. Anamdas and Yang (2012) reported a practical investigative case study involving monitoring of excavation support structures using piezo sensors.

Recently, a number of developments have been reported in the literature concerning the electronics aspects of the EMI technique. Overly et al. (2008) successfully demonstrated the operation of the miniature impedance chip AD 5933 (Analog Devices, 2014) in wireless mode in conjunction with WID 2.0 (Atmel, 2014). Hoja and Lentka (2009) showed the limitations of using AD5933 in the proposed manufacturer’s configuration. In order to eliminate the limitations, the researchers proposed a new solution of using two AD5933 microsystems. Margo et al. (2013) proposed the AD5933 chip as an alternative bio-impedance measurement approach for embedded applications operating in the four electrode configuration.

### 2.3 PIEZOELECTRIC ENERGY HARVESTING: THEORETICAL AND PRACTICAL ASPECTS

Due to miniaturization of sensors, tremendous increase in their demand and development of the low power consuming electronics, energy harvesting has attracted the researchers worldwide. Energy harvesting materials and systems constitute a promising research area and are currently undergoing rapid growth. Components and devices at micro to macro scales, covering materials, electronics and integration are some of the latest developments witnessed by the industry. A wide spectrum of applications are being researched for energy harvesters, including distributed wireless sensor nodes for SHM, recharging the batteries of layered systems, embedded and implanted sensor nodes for medical applications, self-powered unmanned aerial and ground vehicles, security systems and monitoring of type pressure in automobiles, to name a few. Numerous product prototypes and the rising number of publications in the field clearly indicate the importance of the area. The hierarchy of main energy harvesting technologies is shown in Figure 2.2 (Calio et al, 2014).

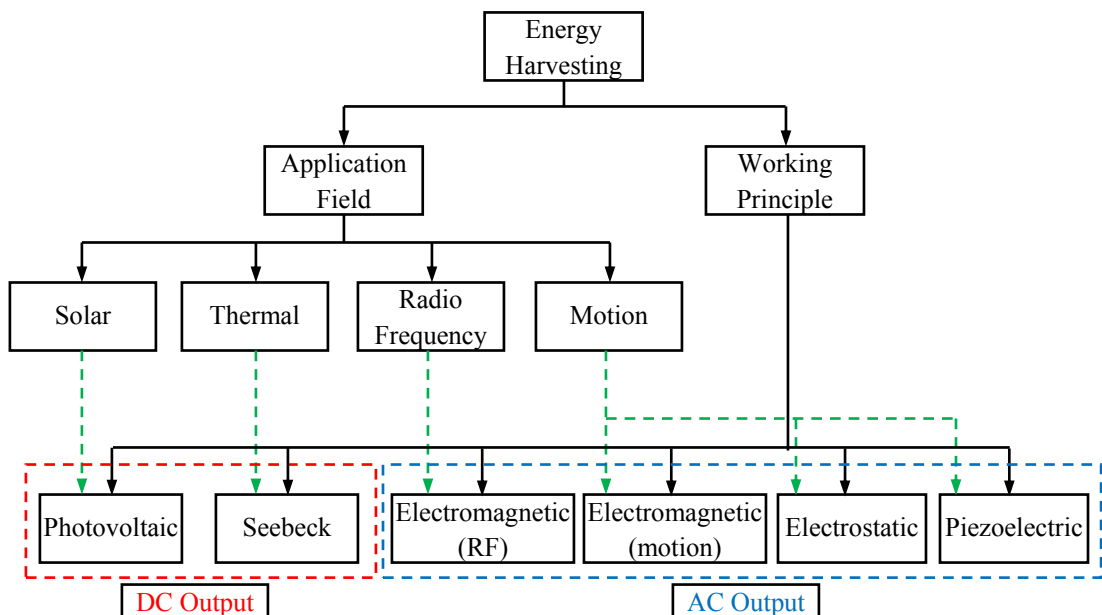


**Figure 2.2:** Hierarchy of main energy harvesting technologies (Calio et al., 2014).

The energy harvesting technologies are divided on two basis, (a) field of application and (b) working principle. This section of the thesis will be focusing specifically on piezoelectric motion based harvesting techniques. Among available motion based harvesting techniques, piezoelectric transduction offers higher power densities (Roundy et al., 2003) in comparison to electrostatic transduction (which, in addition, needs an initial polarization). Also, piezoelectric technologies are better suited than electromagnetic ones for MEMS implementation, because of the limitations in the miniaturization of magnets with the current constraints pertaining to state-of-the-art in micro fabrication processes (Beeby et al., 2006; Calio et al., 2014).

The piezoelectric energy harvesters possess various advantages over conventional renewable sources of energy such as wind and solar energy harvesting. The easy installation and low maintenance required by the piezoelectric harvesters renders them cost effective and appropriate for end product in the market. Another advantage is that they do not require vast area of public space for their operation and at the same time they are not restricted to any specific climate, weather, time of the day or geographic locations. Specifically configured piezoelectric energy harvesters provide the additional advantage of converting the host structure into a “smart” structure by providing the real time data assessment of the structure (Wray, 2008). Following subsections cover various theoretical and practical aspects pertinent to piezoelectric energy harvesting.

### **2.3.1 Transduction Principle**

The word ‘piezo’ is derived from the Greek word for pressure. The piezoelectric effect, first discovered by Jacques and Pierre Curie in 1880, essentially converts mechanical strain into electric current or voltage. Conversely, a voltage applied across the crystal

causes strain in the crystal. This phenomenon is based on the fundamental structure of a crystal lattice. Many crystalline structures have a charge balance with negative and positive polarization, which being randomly distributed, neutralize themselves along the imaginary polar axis (Calio et al., 2014). However, when an external stress is applied onto the crystal mesh, this charge balance gets disturbed and the energy is transported by electric charge carriers, creating a current in the crystal. Conversely, an external charge input will create an imbalance in the neutral charge state, causing mechanical stress internally. There is a close correlation between piezoelectricity and the crystal symmetry. The piezoelectric effect is observed in crystals without centre of symmetry, and the relationship can be explained in terms monocrystal and polycrystalline structures, as illustrated in Figure 2.3. In a monocrystal [Figure 2.3(a)], since the polar axes of all of the charges are uni-directional, they exhibit symmetry, even if it is sub divided into smaller pieces. On the other hand, a polycrystal [Figure 2.3(b)] is characterized by different regions within the material with different polar axes. It is asymmetrical because there is no point at which the crystal could be cut that would leave the two remaining pieces with the same resultant polar axes (Calio et al., 2014). The polycrystal is heated to a transition temperature called as Curie point along with strong electric field in order to impart the piezoelectric effect. The molecules move more freely (Figure 2.4) and the electric field forces the dipoles to rearrange in accordance with the external field due to the heat.

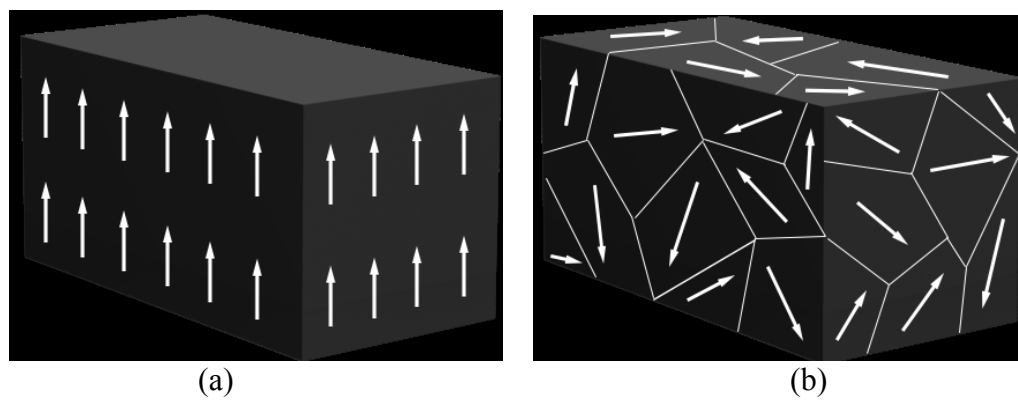


**Figure 2.3:** (a) Monocrystal (b) Polycrystal (Calio et al., 2014)



**Figure 2.4:** (a) Polarization (b) Surviving polarity (Calio et al., 2014).

### 2.3.2 Electro-mechanical Model for Resonating Piezoelectric Devices

Piezoelectric transducers are frequently used in inertial generators. When external load is applied on any structure, its vibrations cause mechanical strain in the piezo transducers attached to them. Piezoelectric materials provide transduction, utilizing the mechanical strain occurring within them. Inertial generators can be described as a second order mass-spring-damper system (Priya and Inman, 2009; Ferrari et al., 2008; Erturk and Inman, 2008; Williams and Yates, 1996), with a piezoelectric element connected parallel to the damper (Lefeuvre et al., 2006), as shown in Figure 2.5.

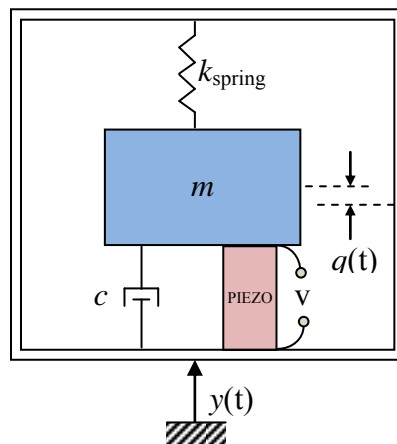


**Figure 2.5:** Mass-spring-damper-piezo model (Williams and Yates, 1996).

The system is governed by the following equation of motion:

$$m\ddot{q}(t) + c\dot{q}(t) + kq(t) = -m\ddot{y}(t) \quad (2.2)$$

where  $m$ ,  $c$  and  $k$  are the seismic mass, the damping coefficient and the stiffness, respectively. Referring to Figure 2.5, the generator housing vibrates with absolute instantaneous displacement  $y(t) = Y_0 \sin(\omega t)$ , the relative displacement of the seismic mass with respect to the housing being  $q(t)$ . The transducer contributes additional damping to the vibrating mass due to the conversion of the mechanical energy to the electrical energy. The damping coefficient  $c$  comprises of both the mechanical losses and the coefficient based on energy conversion, namely,  $c_m$  and  $c_e$ , respectively. The total stiffness of the spring accounts to the spring stiffness ( $k_{\text{spring}}$ ) and the piezoelectric stiffness ( $k_{\text{piezo}}$ ). This is a good approximation as long as the structure vibrates with small displacements and the mechanical behaviour of the motion remains linear (Calio et al., 2014). Such a system is characterized by a natural or resonant angular frequency,  $\omega_n$ , given by

$$\omega_n = \sqrt{\frac{k}{m}} \quad (2.3)$$

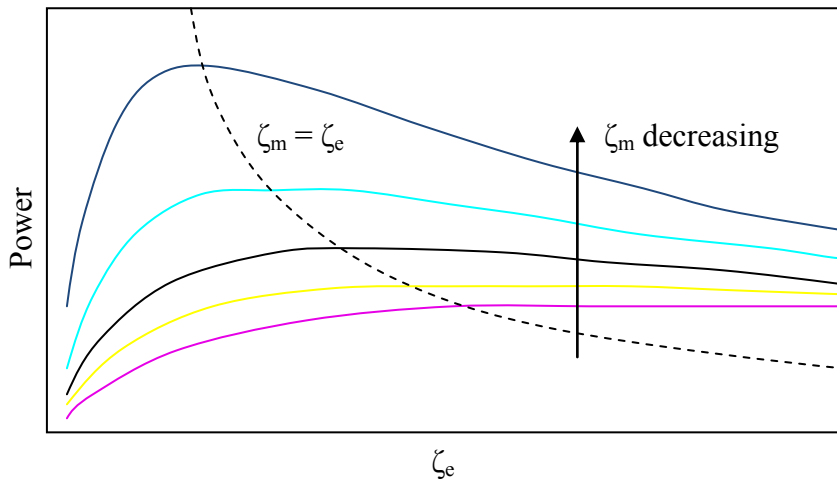
In practical cases,  $\omega_n$  has to be designed to match the expected ambient excitation angular frequency ( $\omega$ ) for maximum energy extraction from the transducer. The power ( $P$ ) that can be harvested from the transducer is given by (Beeby et al., 2006; Williams and Yates, 1996)

$$P = \frac{m\zeta_e Y_o^2 \left( \frac{\omega}{\omega_n} \right)^3 \omega^3}{\left[ 1 - \left( \frac{\omega}{\omega_n} \right)^2 \right]^2 + \left[ 2(\zeta_m + \zeta_e) \frac{\omega}{\omega_n} \right]^2} \quad (2.4)$$

where,  $\zeta_e$  and  $\zeta_m$  are the transducer and the mechanical damping ratio, respectively.  $Y_o$  is the amplitude of vibration. For resonance, ( $\omega = \omega_n$ ) the power ( $P_{\max}$ ) generated by the transducer, which is the maximum possible harvestable power, is given by

$$P_{\max} = \frac{m\zeta_e Y_o^2 \omega_n^3}{4(\zeta_m + \zeta_e)^2} \quad (2.5)$$

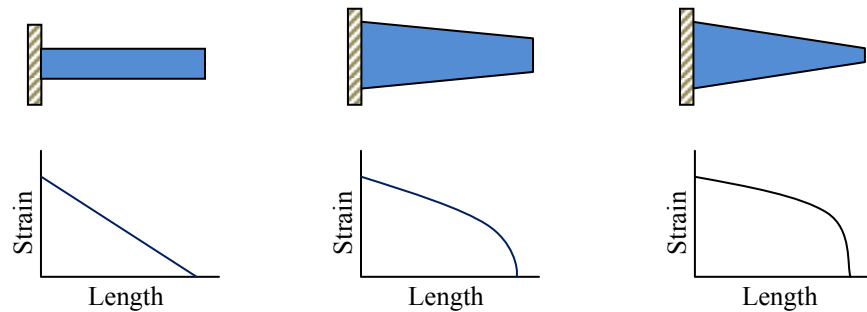
Figure 2.6 shows the typical variation of the harvested power as function of the electrical and mechanical damping. It can be observed that a higher mechanical damping tends to flatten out the power curve. From the figure, it can also be concluded that the power output reaches its maximum when the electrical damping is equal to the mechanical damping (Roundy et al. 2003; Calio et al., 2014).



**Figure 2.6:** Power of the piezoelectric generator as a function of the electrical damping ratio (Calio et al., 2014).

### 2.3.3 Optimal Shapes of Secondary Structures

In rectangular cantilever type harvesters, excessive mechanical strain at the grounded point (near clamping) of the oscillator is often a problem. In order to prevent overstrain, alternative mechanical structures were investigated by several researchers (Mateu and Moll, 2005a; Roundy et al., 2005; Baker et al., 2005; Goldschmidtboeing and Woias, 2008). This was achieved by fabricating new possible shapes, such as triangle/ trapezoid, as illustrated in Figure 2.7. These shapes are characterized by more uniform distribution of the strain along the length of the structure and also allow loading the device with higher excitation, thereby increasing the harvested energy density. Using a deep reactive ion etching on a Silicon on insulator (SOI) wafer, Marzencki et al. (2007) developed a MEMS cantilever as a part of the European VIBration Energy Scavenging (VIBES) project. They studied the possibility of introducing two angles of curvature at the beginning and the end of the beam (before the mass) in order to reduce the overstrain.

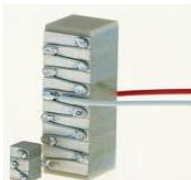
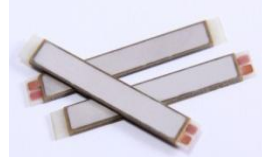
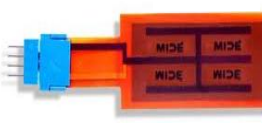


**Figure 2.7:** Variation of strain along the length for various shapes of cantilevers (Calio et al., 2014).

### 2.3.4 Piezoelectric Transducer Configurations for Energy Harvesting

Significant progress has been witnessed in the design and fabrication of piezoelectric transducer structures for energy harvesting. Various designs, which are promising for energy harvesting application, can now be easily procured from commercial sources, are listed in Table 2.1.

**Table 2.1:** Bulk transducer structures for energy harvesting (Priya and Inman, 2009).

Transducer Products	Company/ Characteristics	
	Key Supplier	Characteristics
<b>Multilayer/Stack</b> 	Morgan Electro-ceramics, APC International.	Low frequency (~10Hz), suitable under large uniaxial stress, easy mounting.
<b>Macro Fiber Composite (MFC)</b> 	Smart Material.	Flexible, both $d_{33}$ and $d_{31}$ -modes are possible, low strain high frequency application, large area coverage, can be used as a bimorph element.
<b>Bimorphs</b> 	APC International.	Resonance frequency can be tuned in the range of 5-100 Hz, used in various configurations such as cantilever, end-end clamped, etc.
<b>Quick Pack</b> 	Mide Technologies	Similar to bimorphs, but easier in mounting, wide bandwidth, widely used in cantilever configuration.

### 2.3.5 Energy Harvesting Circuits

A simple energy harvesting circuit consists of a diode rectifier [alternate current (AC) to direct current (DC) convertor], a DC–DC converter and a storing device, which could be a battery or a super capacitor, as shown in Figure 2.8. A DC-DC converter is an electronic circuit which converts a source of DC from one voltage level to another. The addition of DC–DC converter results in higher yield of power (Priya and Inman, 2009).

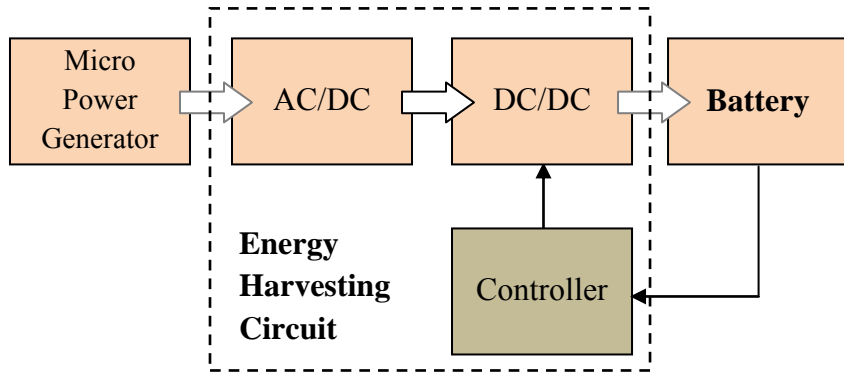


**Figure 2.8:** Block diagram for the energy harvesting circuit (Priya and Inman, 2009).

### 2.3.6 Strategies for Enhancing Performance of Energy Harvester

This subsection provides few strategies, as suggested by Priya and Inman (2009), which can enhance the performance of the piezoelectric energy harvesters. These methods have already been used in the past; however they still require the attention of researchers for serving the purpose efficiently.

#### 2.3.6.1 Multi-modal Energy Harvesting

The concept of multi-modal energy harvesting is fairly new and is based on the fact that multiple sources of energy can be effectively utilized simultaneously from the available environmental sources. This concept further helps to improve upon the existing system by using a combination of following ideas (i) two or more energy harvesting schemes can be synergized such that they complement each other e.g. combining electromagnetic and piezoelectric energy harvesting mechanisms (Poulin et al., 2004) (ii) in any given scenario, multiple energy sources, such as solar, wind, and vibration, may be available for energy harvesting.

### 2.3.6.2 Frequency Pumping

Another method to increase the power harvested by piezoelectric transducers is to enhance the ratio of the frequency of the piezo to that of the source, i.e.  $f_{\text{piezo}}/f_{\text{source}} > 1$ . In general, the operating frequency of the microgenerator is much higher than the usual vibration frequency (5–100Hz) of the machines, aircraft, ship hulls and deck. A higher efficiency can be obtained, if the source vibration frequency can be modified before being applied to the piezoelectric transducer. This method is used to design piezoelectric windmills (Figure 2.9), where each bimorph goes through 5Hz oscillation for source frequency of 1Hz (Priya and Inman, 2009). In this arrangement, two magnets sandwich the tip of the bimorphs, which in turn interact with 10 magnets mounted on the vanes in alternating polarities, in turn forcing the bimorphs to go through five cycles for every rotation of the vanes (Priya and Inman, 2009).

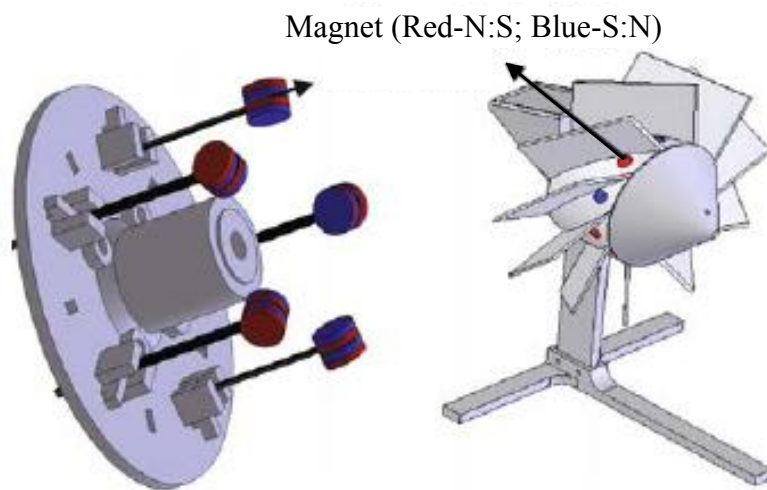


**Figure 2.9:** Enhancing energy harvesting efficiency through increase of frequency (Priya and Inman, 2009).

### 2.3.6.3 Self-Tuning

An energy harvester that can optimize itself in terms of its power output in virtually any vibration environment is highly desirable. An approach based on non-linearity of the piezoelectric material was proposed by Nayfeh and Mook (1995). It is well known that change in stiffness has a bearing on the applied electrical voltage, which in turn has an effect on the resonance. The applied voltage has an inverse effect on the resonance frequency of the piezoelectric harvester, which is in turn related to the elastic non-linearity. The shift in the resonance frequency with increasing excitation can be represented by an empirical response relationship proposed by Nayfeh and Mook (1995). Recently, Eichhorn et al. (2011) have developed a self tuning double cantilevered harvester using PZT patches both for harvesting and actuation. It consists of a two beam device with three arms, as shown schematically in Figure 2.10.

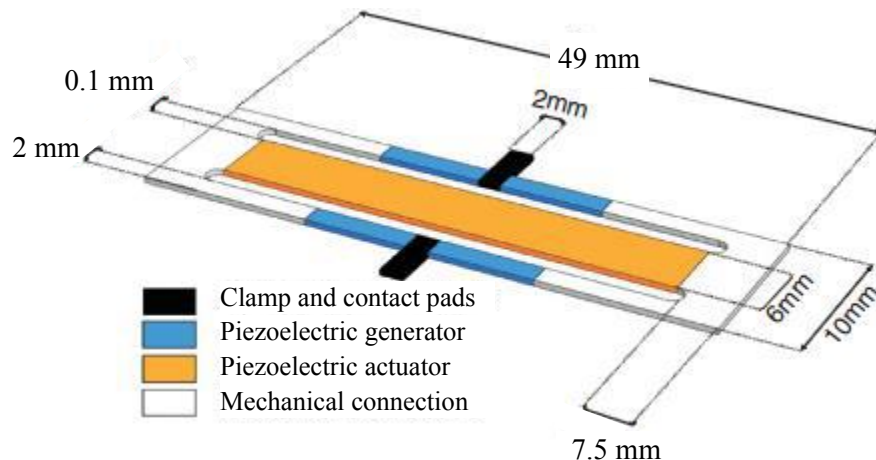


**Figure 2.10:** Self-tuning double cantilevered harvester (Eichhorn et al., 2011).

#### **2.3.6.4 Wide-Bandwidth Transducers**

The overall efficiency of an energy harvester can be increased by harvesting power across varying vibration inputs. Narrow bandwidth is the primary problem of the current energy harvesters. Significant drop in power levels produced is noticed, even due to minute deviations from the resonating frequency of the structure, which is a major point of concern. It must be pointed out here that several simple schemes can be designed to achieve a wide-bandwidth operation, but most of these have a common fundamental drawback that power density decreases with even slight departure from the structure's resonance frequency. Recent research is focused on developing transducer structures that exhibit multiple closely resonances which are closely spaced (Priya and Inman, 2009).

#### **2.3.7 Practical Applications of Piezoelectric Energy Harvesting**

Possible interesting applications of piezoelectric energy harvesting enunciated by Artfuldodger (2014) are:

(a) **Exercise Bicycle:**

Several gyms, notable in Portland and a few other places, are powered by a combination of piezoelectric set ups and generators filled on stationary bikes, where individuals generate power while performing exercise.

(b) **Shoe sole power generator:**

The armed forces toyed with the idea of incrementing piezoelectric harvesters in soldiers' boots to power radios and other portable electronic gear. This turned out to be infeasible with the current technology due to the extra weight and discomfort of the setup. However, future miniaturization might make this feasible.

(c) **Human activity based generator:**

- (i) Several nightclubs, mostly in Europe, have already begun to power their strobes and stereos using the force of hundreds of people pounding on piezoelectric lined dance-floors.
- (ii) Special flooring tiles embedded with piezoelectric sensors have been installed in Tokyo Station, Japan (Ratnasari, 2014) for energy harvesting. 400,000 people using Tokyo station on an average day, according to East Japan Railway, are able to generate sufficient energy to light up electronic signboards.

(d) **Side Walk Power Generator:**

Piezoelectric crystal arrays can possibly lie underneath sidewalks, stairwells, and other high traffic areas to power street lights. The city of Toulouse, France, after inspiration from a nightclub in Rotterdam, Netherlands, has begun investigating the installation of energy-absorbing sidewalk panels that would harvest pedestrian energy to power the street lights (Fox, 2014).

## **2.4 EVOLUTION AND RECENT ADVANCES IN ENERGY HARVESTING USING PIEZO SENSORS**

The history of energy harvesting dates back to the use of windmills, watermills and passive solar systems in the ancient times. People have searched and implemented ways to store the energy from heat and vibrations for many decades. One driving force behind the search for new energy harvesting devices is the desire to power sensor networks and mobile devices without batteries. Energy harvesting is also motivated by a desire to address the issue of climate change and global warming. Today's power harvesting

systems are scavenging energy from a wider variety of sources, and researchers are finding innovative applications like energy harvesting to power wireless networks. The world's oldest windmills are a Persian windmill, with vertical sails made of bundles of reeds or wood, attached to the central vertical shaft by horizontal struts. In these windmills, usually an asymmetry is created by screening half the rotor with a wall in order to utilize the drag forces for driving the rotor (Gasch and Twele, 2012). The Chinese drag wheels (dating back to approximately 1000 AD) were also based on vertical axis using asymmetry, created by sails, to rotate out of the wind on their way "back" (König, 1976). However, in contrast to the Persian mills, they had the typical advantage of the motion about vertical axis which utilized the wind independent of its direction (Gasch and Twele, 2012). The existing technology of horizontal axis based watermills in Western Europe since the third century BC (Tomlinson, 1976), encouraged the development of horizontal axis windmills in Europe. In the ancient times, the wind mills and the watermills were used for grinding, sawing, cutting etc. In 1970s, when the first energy crunch was felt, these technologies attracted the researchers' interest for power scavenging. Sun and wind have always been the predominant sources of scavenged/waste or free energy. Their success and what had been learned from them inspired the researchers to scale down energy harvesting from macro (1950-1990) to the micro level (1990 onwards). As a result, the girth of energy harvesting has expanded beyond just wind and sun to include movement, heat, mechanical vibration, RF, and others, as mentioned previously (Chao, 2012).

With the beginning of the 21<sup>st</sup> century, there began a new era of low-power energy harvesting characterized by a short but dynamic history. The ability to reduce the power requirements of portable devices by orders of magnitude, during just the last ten years,

has made formerly unthinkable waste energy sources realistic for the next generation of portable and remote devices. While low-power harvested energy has been in its early stage since the late 1990's, it was not until about ten years ago that the first generation of low-power energy-harvesting devices emerged. They were designed to harvest micro power primarily from photovoltaic or piezoelectric sources. The major application was their use as backup sources to charge circuits (Chao, 2012).

It has now been three decades since the researchers first showed interest in the studies of energy harvesting by piezoelectric materials in biological environment (Hausler and Stein, 1984). They claimed that the mechanical energy released during the respiration of a mongrel dog could be transferred to the electrical energy using a piezoelectric PVDF film and a converter. In the demonstration experiment, the piezoelectric material was fixed to the ribs of the dog and a peak voltage and power of 18V and  $17\mu\text{W}$ , respectively, was produced by the motions of the ribs during the spontaneous breathing. Though piezoelectric energy harvesting has been thoroughly investigated since the late 1990s, it still remains an emerging technology and critical area of interest. Energy harvesting application fields have so far mainly focused on low power devices due to their limited transduction efficiencies (Mitcheson et al., 2008). Several review articles published on the topic covering wide variety of mechanisms and techniques are available in literature such as Priya (2007); Anton and Sodano (2007); Beeby et al. (2006); Roundy and Wright (2004) and Sodano et al. (2004a).

Umeda et al. (1996) quantified the amount of energy when a steel ball impacts against a piezoelectric plate. An equivalent circuit model was used to predict the energy while modifying the various associated parameters to arrive at the best combination of the

parameters. It was concluded that as the mechanical quality factor (reciprocal of internal friction) of the piezo material increased, the electro-mechanical coupling coefficient increased and the dielectric loss decreased, thereby enhancing the overall efficiency.

Starner (1996) performed calculations for a piezoelectric device mounted inside a shoe. As per their study, approximately 67 W of power is lost during an average person (weighing 68 kg) walking at brisk pace (two steps per second with the foot moving 5 cm vertically). In their experiments, 8.4 W of power could be harvested, resulting in a conversion efficiency of 12.5 %. Kymmissis et al. (1998) developed a piezoelectric system that was capable of harvesting the energy lost during walking and then channelized this energy to power up a radio transmitter (refer Figure 2.11). The set systems or devices employed included a piezoceramic thunder actuator located in the heel of the shoe and a multilayer PVDF foil laminate patch located in the sole of the shoe. As a part of the study, it was noticed that the peak power approached 20 mW for the PVDF stave while it was 80mW for the piezoelectric actuator. Although, the average power generated from both the systems was significantly low, in the range of 1 mW and 2 mW respectively, owing to slow excitation, as shown in figure, both the piezo devices could easily produce enough energy to power up a transmitter that could send a 12-bit RFID code in every 3-6 steps while walking.

Similar investigation into the use of piezo electric materials for energy harvesting from the motion of humans or animals was carried out by Ramsey and Clark (2001). They specifically studied the ability to power up an *in vivo* MEMS application. Here, a square plate driven by the blood pressure was used to provide energy and proved capable of powering the electronics involved, if used intermittently.

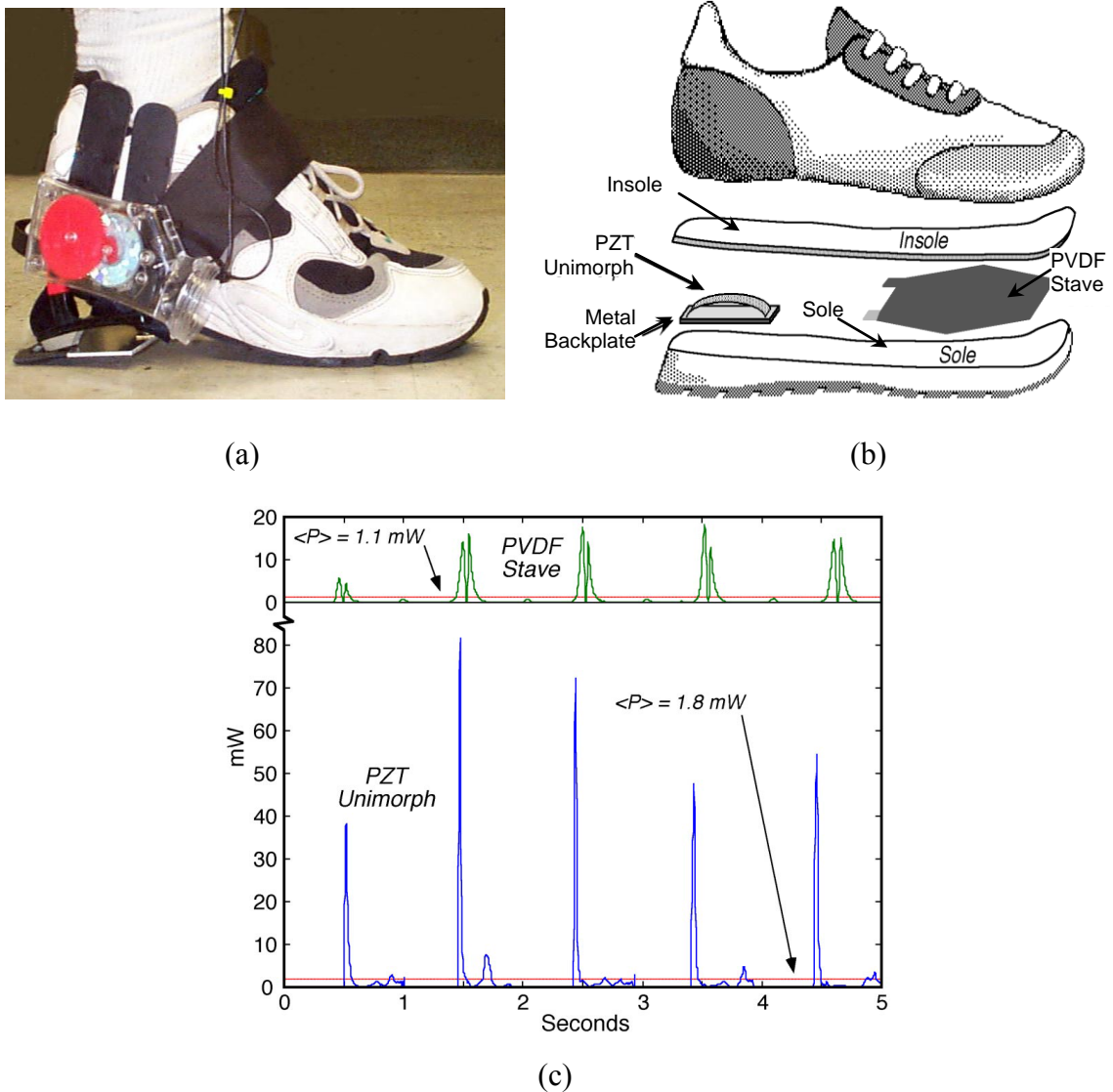


**Figure 2.11:** Schematic and results of energy harvesting shoe (Kymmissis et al., 1998).

- (a) External view of shoe
- (b) Location of piezo sensors
- (c) Typical power vs time

Energy density of the available and the possible portable energy sources have been compared for one and ten year lifetimes in Table 2.2 (Roundy, 2003). Roundy concluded that for a device whose desired life time is in the range of one year or lesser, a battery alone is sufficient. A device with a longer service life, essentially, should be better equipped with an energy harvesting solution for optimum performance. Paradiso and

Starner (2005) elaborated the capability of different sources for energy harvesting (refer Table 2.3). It may be noted that the suggestion made by Paradiso and Starner (2005) is in slight variance to that of Roundy (2003) in terms of vibrational generators.

**Table 2.2:** Comparison of energy sources (Roundy, 2003).

		<b>Power Density (<math>\mu\text{W}/\text{cm}^3</math>) 1 Year Lifetime</b>	<b>Power Density (<math>\mu\text{W}/\text{cm}^3</math>) 10 Year Lifetime</b>	<b>Source of Information</b>
Scavenged Power Sources	Solar (Outdoors)	15,000 – direct sun 150 – cloudy day	15,000 – direct sun 150 – cloudy day	Commonly Available
	Solar (Indoors)	6 – office desk	6 – office desk	Roundy (2003)
	Vibrations	200	200	Roundy et al. (2003)
	Temperature Gradient	15 @ 10°C gradient	15 @ 10°C gradient	Stordeur and Stark (1997)
	Shoe Inserts	330	330	Starner (1996)
Energy Reservoirs	Batteries (non-rechargeable Lithium)	45	3.5	Commonly Available
	Batteries (rechargeable Lithium)	7	0	
	Nuclear Isotopes (Uranium)	$6 \times 10^6$	$6 \times 10^5$	

**Table 2.3:** Energy harvesting capabilities (Paradiso and Starner, 2005).

<b>Energy Source</b>	<b>Performance</b>
Ambient light	100 mW/cm <sup>2</sup> (directed towards bright sun) 100 $\mu\text{W}/\text{cm}^2$ (illuminated office)
Vibrational micro generators	4 $\mu\text{W}/\text{cm}^3$ (human motion – Hz) 800 $\mu\text{W}/\text{cm}^3$ (machines – kHz)
Ambient airflow	1 mW/cm <sup>2</sup>
Push buttons	50 $\mu\text{J}/\text{N}$
Hand generators	30 W/kg
Heel strike	7 W potentially available (1 cm deflection at 70 kg per 1 Hz walk)

Roundy et al. (2003) studied the availability of low level vibrations as a power source for wireless sensors. Roundy used two piezoelectric patches attached to a steel cantilevered beam which was designed to harvest mechanical energy from vibrations. The piezoelectric material achieved a  $70 \mu\text{W}/\text{cm}^3$  power density, corresponding to an excitation force designed to stimulate the vibration of an operating microwave oven.

Another useful example of energy harvesting is that of the ‘eel’ concept developed by Ocean Power Technologies Inc. (2014). The system extracts energy from the flow of a fluid in confined or unconfined space. Generating systems are eel-like structures made from PVDF films. The ‘eels’ are scalable in size and have a capacity to generate few milli watts to few watts of power depending on size of the system and velocity of flow. The concept is illustrated in Figure 2.12.

Sodano et al. (2005) and Park et al. (2008) estimated the power output from a piezoelectric cantilever auxiliary structure attached to an automobile compressor. A  $40 \times 62 \text{ mm}$  cantilever was able to charge a  $40 \text{ mAh}$  button cell battery in one hour. The development of an accurate analytical model to estimate the power output from the piezoelectric transducers and the need to understand the effects of related components, such as the mechanical and the electrical loads and electrical circuits, has received considerable attention by energy harvesting researchers. As such, numerous efforts on analytical modelling and analysis of piezoelectric energy harvesting can be found in the literature [Park et al., 2008; duToit et al., 2005; Sodano et al., 2004b; Lu et al., 2004; Twiefel et al., 2006; Roundy and Wright, 2004; Kim et al., 2005; Sohn et al., 2005; Goldfarb and Jones, 1999].



**Figure 2.12:** Energy harvesting “eel” concept (Ocean Power Technologies Inc., 2014).

Interestingly, Goldfarb and Jones (1999) explained that the basic problem with harvesting electrical power using the piezoelectric transducers is that the vast majority of the energy produced is stored inside the transducers and eventually returned back to the excitation source. Therefore, minimizing the amount of energy stored inside the transducers would lead to maximize its efficiency of power generation. An analytical model was proposed by Goldfarb and Jones (1999) and it was found that at frequencies above 100 Hz, the efficiency of the stack actuator is substantially reduced. Maximum efficiency was obtained at a 5 Hz, which is much lower than the first mechanical and electromechanical resonance frequency of the stack. Although the piezoelectric stack configuration utilizes higher electromechanical coupling mode ( $d_{33}$ ) compared to that of the patch configuration ( $d_{31}$ ), the  $d_{31}$  configuration holds more advantages in energy conversion because the excitation is more easily achieved by environmental sources (Park et al., 2008; Ramsey and Clark 2001; Mateu and Moll, 2005b).

Mohammadi et al. (2003) and Churchill et al. (2003) used piezo fibres and succeeded in harvesting 120 mW from a  $34 \times 11 \times 5.85$  mm plate and 7.5 mW from  $130 \times 13 \times 0.38$  mm

beam, respectively. duToit et al. (2005) summarized several experimental and analytical results of energy harvested with varying sizes of the piezoelectric elements. The power generation ranges between  $1 \mu\text{W}$  to few milli watts with size of the piezoelectric elements varying from micro ( $0.01 \text{ cm}^3$ ) to macro ( $75 \text{ cm}^3$ ) scales. Different energy harvesting schemes with varying mass, size and input frequency spectra were employed by the above researchers for their experiments. Additionally, the host structures on which harvesters were installed varied in numerous aspects. In order to compare the efficiencies of different energy harvesting systems, the researchers recommended fixing the parameters to ensure realistic comparison. The power density ( $\text{W/cm}^3$  or  $\text{W/kg}$ ) and the efficiency parameter were suggested as a good indicator for comparison.

Poulin et al. (2004) presented a comparative study of the electromagnetic and the piezoelectric energy. These researchers suggested that the energy generated by the piezoelectric system is sufficient enough for microsystems because of somewhat higher power density. They recommended electromagnetic systems for medium-scale applications.

To achieve higher efficiency, it is necessary to match the resonance frequency of the transducer with the most distinct frequency of the vibration source (Park et al., 2008). It was concluded by Cornwell et al. (2005) that the power generation from a piezoelectric element typically increases by a factor of 25 when the frequency of the harvesting device and that of the structure are well tuned to each other. The optimization of the transducer setup and geometry is one of the most challenging tasks during the design, but till now it has received relatively very less attention from researchers.

Microstrain Inc., (2007) developed the prototype of piezoelectric-based energy harvester, shown in Figure 2.13. In this device, the sensor node is equipped with temperature and humidity sensors with wireless telemetry. It is claimed that the piezoelectric harvester can produce up to 2.7 mW of instant power at 57 Hz vibration (Park et al., 2008).

Kim et al. (2011) examined the piezoelectric effects on various loading conditions for the possibility of harvesting energy from bridges. The test results were compared with the well-known analytical formulations such as the pin force model, the enhanced pin force model and the Euler-Bernoulli model. The Euler–Bernoulli model is found to provide the most accurate estimation for the piezoelectric modules attached on the bridges.

Kim and Kim (2013) proposed a bio-inspired device designed to mimic the auditory hair bundle structure (Figure 2.14). The auditory structure is responsible to stimulate the brain with electrical signals in response to the oscillations due to acoustic pressure forces generated by any broadcasted sound. It mechanically amplifies the activities of the hair cells, owing to negative stiffness (Platus, 1991), which conveys a bi-stable behavior. The proposed device is composed of a four bar structure, linked by thin spring steel flexural joints. A piezoelectric cantilever can be placed on the coupler link (Calio, 2014).



**Figure 2.13:** A prototype of sensor node with piezoelectric energy harvester (Microstrain Inc., 2007).

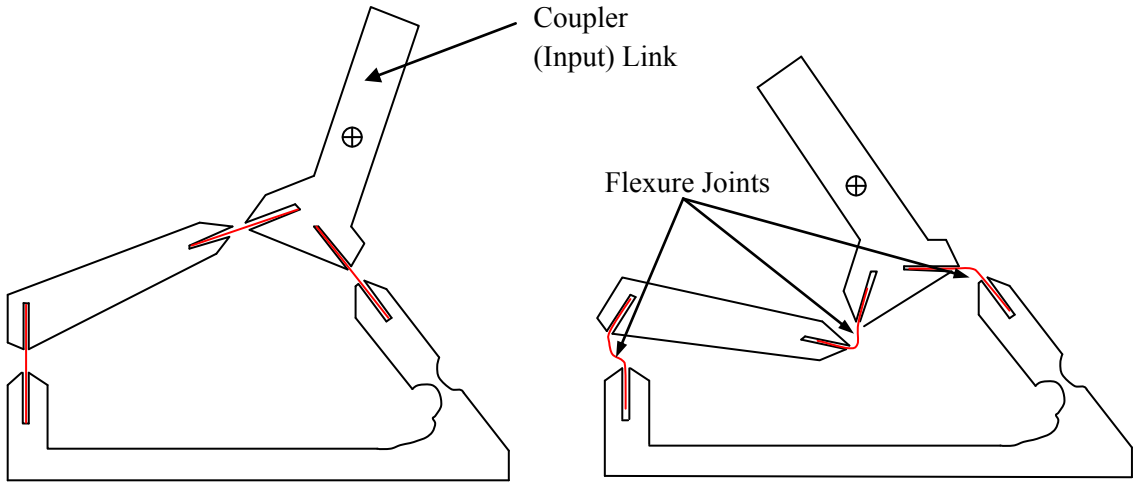


**Figure 2.14:** Bio-inspired bi-stable structure (Kim and Kim, 2013).

Although the piezoelectric effect is inherently related to axial elongations, several alternate device configurations such as transforming a rotatory excitation into a longitudinal strain have been proposed recently (Oliver et al., 2002; Priya 2007; Myers et al., 2007; Tien and Goo, 2010; Khaligh et al., 2010; Bressers et al., 2011; Khameneifar et al., 2011; Gu and Livermore, 2012; Khameneifar et al., 2013; Pillatsch et al., 2013; Karami et al., 2013; Calio et al., 2014). Pillatsch et al. (2013) developed a harvester composed of a fixed piezoelectric beam and an eccentric proof mass free to rotate, similar to the Seiko Kinetik watch. This device was able to harvest up to  $43 \mu\text{W}$  at 2 Hz and  $20 \text{ ms}^{-2}$  of acceleration when tested on an upper human limb during a running task. Two configurations of wind turbine, both consisting of a circular array of cantilever beams clamped below a windmill, were proposed by Karami et al. (2013). Movement of the windmill, which was equipped with repulsive magnets, caused mechanical vibrations in these beams.

More recently, Dagdeviren et al. (2014) employed PZT ribbons to harvest energy from movements of heart, lung and diaphragm. The harvester was mounted onto a flexible

membrane, which was further integrated with a bridge rectifier and a rechargeable battery. It was observed that a stack of five PZT sheets was able to harvest a power density  $1.2 \mu\text{W}/\text{cm}^2$ , which was sufficient to operate a cardiac pacemaker. Development of such a system would help in avoiding risks of surgical procedures to replace the depleted batteries of implantable devices, as pacemaker, neural stimulators, etc.

Delebarre et al. (2012) developed an integrated method utilizing vibration power harvesting and SHM in a dual mode for aerospace application. They demonstrated the application on a small aluminium plate  $500 \times 300 \times 3$  mm in size, instrumented with surface bonded piezoelectric power harvesters, and excited by an electromechanical shaker. The power measurement demonstrated the ability of the piezoelectric SHM sensors to harvest power over an extended frequency range normally observed in aircrafts. However, the specimen size adopted by the researchers was too small to emulate a real-life system. At most, it represented a miniature aerospace structure. The research work presented in this thesis on the other hand, has gone much beyond, to investigate the concept on real-life structures, both steel and RC. The next section elaborates further by pointing out specific research gaps which have been duly addressed in the present thesis.

## **2.5 CRITICAL LITERATURE REVIEW: IDENTIFICATION OF RESEARCH GAPS**

Following gaps areas stem out from the comprehensive literature review presented in the preceding sections of the Chapter:

1. Enormous research has already been done in the field of piezoelectric energy harvesting and SHM individually. However, integrated use of the same sensors, both for SHM and energy harvesting has not been investigated in depth.

2. Most of the energy harvesting approaches proposed so far employ especially built stack type or other similar piezo-configurations in addition to deploying secondary structures. Potential of energy harvesting using axial strain actuation ( $d_{31}$ ) mode of simple type PZT patches has not been explored yet for real-life civil engineering structures. Such configuration carries the advantage of being simple and most natural form of excitation from ambient sources. In addition, this can also serve for SHM, either using the EMI technique or global vibration technique based on strain mode shape.
3. Additionally, employing this integrated application for real-life structures and/ or estimation of possible power yield from such configuration has also been not experimentally attempted till date.
4. No investigating study could be found in literature exploring the potential of embedded piezo sensors for energy harvesting. The embedded configuration offers several advantages, such as protection to the piezo element, space saving and freedom from maintenance. Exploring the  $d_{31}$  effect for energy harvesting from embedded sensors in RC structures has also not been explored yet.
5. No detailed parametric studies have been reported in the literature on the dependence of power on various parameters of the PZT patches, especially with regard to  $d_{31}$  configuration.

The above points provide the motivation for the research being reported in this thesis. Particular emphasis has been paid to PZT patches bonded to the real-life civil structures in axial actuation ( $d_{31}$ ) mode using adhesive bond layer, both in surface-bonded as well as embedded configurations. Based on these gaps, the next section outlines the objectives, scope and original contributions stemming out from the research presented in this thesis.

## 2.6 RESEARCH OBJECTIVES, SCOPE AND ORIGINAL CONTRIBUTIONS

Piezo sensors have been independently employed for SHM and energy harvesting. Keeping in view the background given above, it is justified to pursue the present study to develop a conceptual framework which can integrate the two functions using same PZT patch. The specific objectives addressed in this thesis are:

1. To investigate the potential of utilizing the **same PZT patch for SHM as well as energy harvesting employing axial strain actuation ( $d_{31}$ ) mode for civil structures.** It is envisaged that in the *idle stage*, when SHM of the structure is not being performed, the PZT patch will be used for harvesting energy from the mechanical vibrations. In the *SHM stage*, the energy harvested through the PZT patch will be utilized for performing SHM of same structure.
2. To evaluate and compare the performance of surface-bonded and embedded PZT patches from energy harvesting considerations. For both configurations, suitable analytical models extendable to real-life structures are necessary.
3. To develop and validate analytical and numerical models suitable for computation of harvestable energy from this piezo patches operating in  $d_{31}$ -mode, either in surface bonded or embedded configurations. For surface-bonded configuration, the investigations are necessary for real-life RC as well as steel structures.
4. To carry out detailed parametric studies to work out the optimum size and parameters of the patches from energy harvesting considerations.
5. To quantify **effect of losses** such as the mechanical loss, the dielectric loss and the shear lag loss for piezo patches on the real-life structures in detail for both surface-bonded as well as embedded configurations.
6. To estimate potential harvestable energy in real-life structures based on the developed analytical/ numerical models.

This research is the first systematic and comprehensive effort to propose an integrated approach in which the same PZT patch can be used both for energy harvesting as well as SHM utilizing strain actuation ( $d_{31}$ ) mode for civil structures. The specific original contributions budding out from this research are:

1. For the first time, proof-of-concept experimental demonstration has been provided to employ the same PZT patch for SHM as well as energy harvesting.
2. Energy harvesting has been explored through simplest structural configuration, without any secondary structure. The thesis has explored the axial strain actuation ( $d_{31}$ ) mode. Although  $d_{33} > d_{31}$  (for thin PZT patch), however, the patch configuration ( $d_{31}$ ) is simpler and more natural way of being excited in civil structures. It additionally offers ample opportunities for SHM.
3. Analytical models have been proposed and validated for power output from surface-bonded and embedded PZT sensors duly considering the effect of adhesive bond layer.
4. Proof-of-concept extensions have been made on real-life sized structures in contrast to very small size specimens investigated by prior researchers.
5. Effect of losses such as, mechanical loss, dielectric loss and shear lag loss, on the real-life structure has been systematically investigated and quantified in detail.
6. Optimum size and parameters of PZT patches which are suitable for both SHM and energy harvesting are arrived at through numerical investigations.

It is expected that the outcomes of this research will pave way for the dual use of the ordinary low cost piezo patches in SHM as well as energy harvesting. The forthcoming chapters present the research work undertaken in detail.



## **Chapter 3**

# **FEASIBILITY OF ENERGY HARVESTING FROM THIN SURFACE BONDED PIEZO PATCHES: MODELLING AND EXPERIMENTATION**

### **3.1 INTRODUCTION**

This chapter presents the development of basic analytical model and experimental study involving surface bonded PZT patches operating in the  $d_{31}$ -mode for energy harvesting. The  $d_{31}$ -mode is explored for the possibility of energy harvesting from the PZT patch owing to its well established suitability for SHM, by means of either the global vibration or the local EMI technique. The principle of integrated SHM and energy harvesting is illustrated in Figure 3.1. The structure is assumed to be operating in two states, idle state and SHM state. During the *idle state* (when SHM is not being performed), the PZT patches will harvest the energy and store it in an appropriate storage device, such as a battery or a capacitor. In the *SHM state*, the same stored energy will be utilized for the SHM of the host structure by the same PZT patch, either in the global mode (standard vibration techniques) or the local mode (EMI technique) or both. It is assumed that the total duration of the SHM state will be very small as compared to the idle state. In the study covered in this chapter, the voltage and the power generated by a PZT patch surface bonded in the  $d_{31}$ -mode on a simply supported laboratory steel beam are measured experimentally. A coupled PZT-bond-structure electro-mechanical model is developed for determining the voltage output across the patch under harmonic vibrations duly considering the losses associated with the PZT patches. The losses associated with the PZT patch, namely the mechanical damping, the electrical damping and the shear lag are included and rigorously quantified.

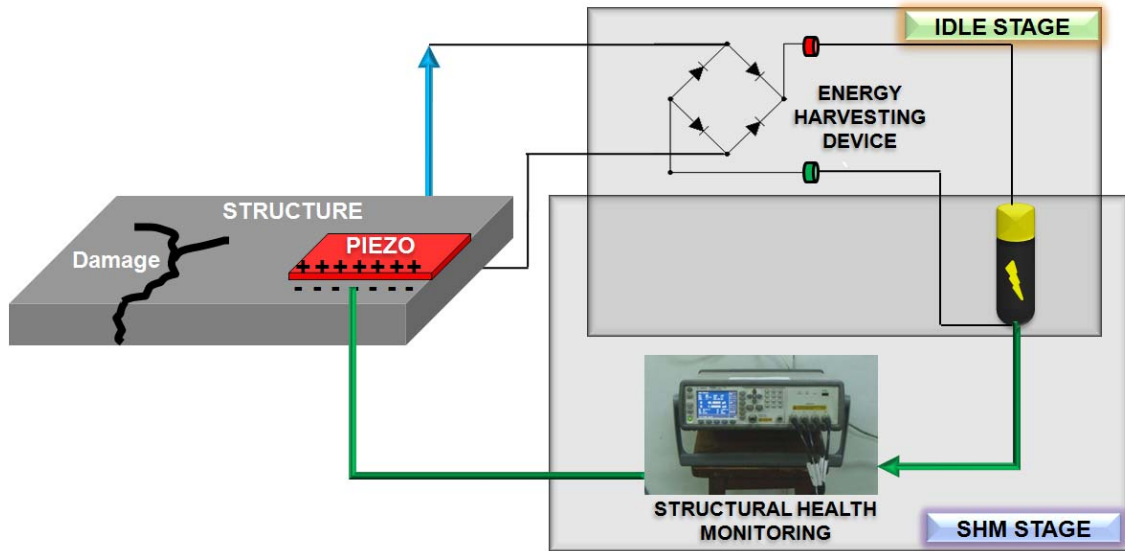


**Figure 3.1:** Principle of integrated SHM and energy harvesting.

### 3.2 ENERGY HARVESTING BY SURFACE BONDED PZT PATCH: ANALYTICAL MODELLING

A coupled electro-mechanical analytical model is derived here for estimation of the voltage generated by a PZT patch surface bonded on a simply supported beam. This structure is chosen because of the high vibration energy harnessing potential offered by bridges. The free body diagram and the strain distribution of the simply supported beam considered for the model are shown in the Figure 3.2. Here,  $S_1$  is the strain produced in the topmost fibre and  $D$  is the overall depth of the beam. The beam is assumed to be under a concentrated load at the centre, varying sinusoidally with time with an operating frequency  $\omega$ . The amplitude of vibration has been determined using a MATLAB program based on mode superposition theory (Chopra, 2007), listed in Appendix A. A close form relation has been established between the voltage generated by the PZT patch and the amplitude of vibration of beam and the excitation force as well.

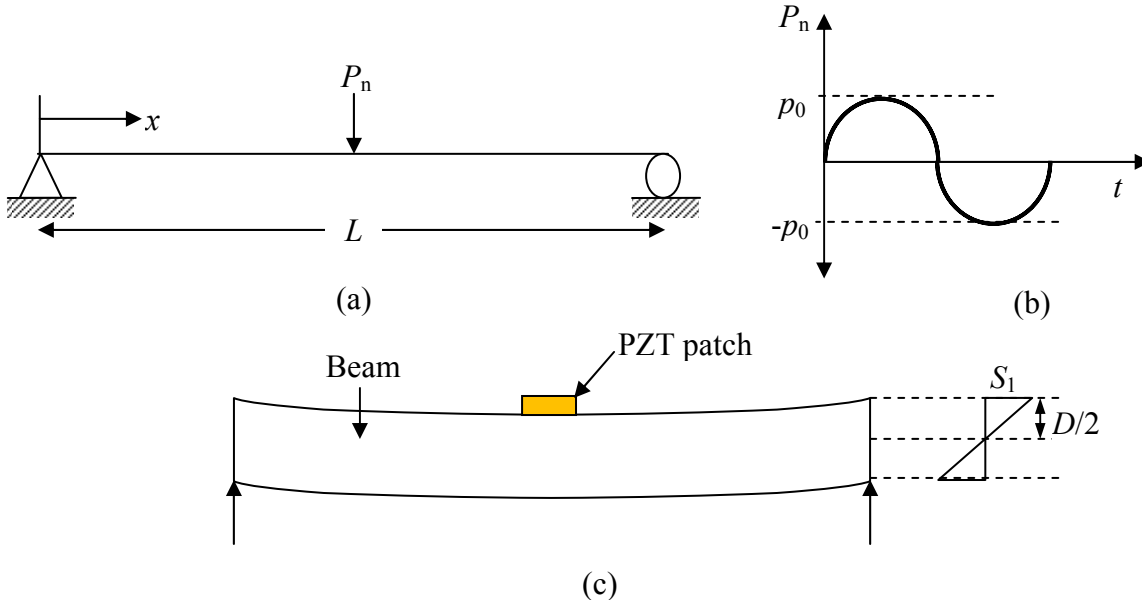


**Figure 3.2:** (a) Free body diagram of beam under concentrated load.  
 (b) Variation of excitation load with respect to time.  
 (c) Strain distribution of beam with PZT patch at centre.

The dynamic equation of motion for the simply supported beam with generalized mass (\$M\_n\$), stiffness (\$K\_n\$) and damping (\$C\_n\$) under the generalized force (\$P\_n\$), producing generalized displacement (\$q\_n\$) is given by,

$$M_n \ddot{q}(t) + C_n \dot{q}(t) + K_n q(t) = P_n(t) \quad (3.1)$$

where, \$M\_n\$, \$K\_n\$ and \$P\_n\$ are respectively, given by,

$$M_n = \frac{\bar{m}L}{2} \quad (3.2)$$

$$K_n = \frac{n^4 \pi^4 EI}{2L^3} \quad (3.3)$$

and

$$P_n = \int_0^L p(x, t) \phi_n(x) dx \quad (3.4)$$

where, \$\bar{m}\$ is the mass per unit length, \$EI\$ the flexural rigidity and \$L\$ the length of the beam. For a harmonically varying concentrated load acting at centre (\$x=L/2\$) of the beam

[as shown in Figure 3.2(b)] under an excitation frequency  $\omega$ , the forcing function  $p(x,t)$  is given by,

$$p(x,t) = \begin{cases} p_o \sin \omega t & x = L/2 \\ 0 & 0 < x < L/2 \\ 0 & x > L/2 \end{cases} \quad (3.5)$$

Where,  $p_o$  is the force amplitude. The natural frequency ( $\omega_n$ ) and the mode shape ( $\phi_n$ ) of the simply supported beam respectively are given as,

$$\omega_n = \frac{n^2 \pi^2}{L^2} \sqrt{\frac{EI}{m}} \quad (3.6)$$

$$\phi_n(x) = \sin \frac{n\pi x}{L} \quad (3.7)$$

Substituting the mode shape  $p(x,t)$  and  $(\phi_n)$  from Eqs. 3.5 and 3.7 respectively in Eq. 3.4, the generalized force  $P_n$  becomes,

$$P_n = p_o \sin \omega t \sin \left( \frac{n\pi}{2} \right) \quad (3.8)$$

The steady state solution (Chopra, 2007) of the governing differential equation [Eq. (3.1)] is given by,

$$q_n(t) = (u_{st})_o R_D \sin(\omega t - \theta) \quad (3.9)$$

where,  $(u_{st})_o$  denotes the static deflection of the beam at the centre,  $R_D$  the dynamic magnification factor and  $\theta$  the phase angle, respectively given by

$$(u_{st})_o = \frac{P_n}{K_n} \quad (3.10)$$

$$R_D = \frac{1}{\sqrt{[1 - (\omega/\omega_n)^2]^2 + [2\zeta(\omega/\omega_n)]^2}} \quad (3.11)$$

and  $\theta = \tan^{-1} \left[ \frac{2\zeta(\omega/\omega_n)}{1 - (\omega/\omega_n)^2} \right]$  (3.12)

where,  $\zeta$  denotes the damping ratio and  $\omega$  and  $\omega_n$  respectively, denote the operating and the natural frequency. The amplitude,  $u(x,t)$  of the dynamic vibration of the beam, considering  $n$  number of modes, is given by,

$$u(x,t) = \sum_{i=1}^n \phi_i(x) q_i(t) \quad (3.13)$$

Using Euler's beam theory, the moment ( $M$ ) at any section of the beam can be expressed in terms of its flexural rigidity ( $EI$ ), strain ( $S_1$ ) in its top fibre and the depth of the neutral axis ( $d$ ) as

$$\frac{M}{EI} = \frac{S_1}{d} \quad (3.14)$$

For a beam with uniform cross-section, the beam curvature  $C_b$  is given by the second derivative of the beam deflection ( $y$ ) (Nechibvute et al., 2011) as

$$C_b = \frac{d^2 y}{dx^2} = \frac{M}{EI} \quad (3.15)$$

For extreme fibre of the beam ( $d=D/2$ ), following relation between strain ( $S_1$ ) and the curvature ( $C_b$ ) can be derived from Eqs. (3.14) and (3.15),

$$S_1 = \frac{d^2 y}{dx^2} \times \frac{D}{2} \quad (3.16)$$

Further, from the fundamental bending theory of beam, the deflection ( $y$ ) of a simply supported beam at a distance  $x$  from the support, under concentrated load at the centre, can be expressed in terms of the peak deflection ( $a$ ), at the centre as

$$y = \frac{4a}{L^3} \left( \frac{3xL^2}{4} - x^3 \right) \quad (3.17)$$

The above equation is valid for both static as well as dynamic excitation condition. The curvature of the beam can be obtained by double differentiation of the deflection with respect to distance, that is

$$\frac{d^2y}{dx^2} = -\frac{24ax}{L^3} \quad (3.18)$$

The potential difference  $(V_p)_S$  across the terminals of the PZT patch of thickness  $h$ , surface bonded at the top of the beam, is given by (Shanker et al., 2011),

$$(V_p)_S = \left( \frac{d_{31} h \overline{Y^E}}{\varepsilon_{33}^T} \right) S_1 = S_q^* S_1 \quad (3.19)$$

where, the subscript ‘ $S$ ’ signifies the surface-bonded configuration,  $d_{31}$  is the piezoelectric strain coefficient,  $\overline{Y^E} = Y^E (1 + \eta j)$  the complex Young’s modulus of elasticity of the PZT patch at constant electric field,  $\overline{\varepsilon_{33}^T} = \varepsilon_{33}^T (1 - \delta j)$  the complex electric permittivity (in direction ‘3’) at constant stress, (with  $j = \sqrt{-1}$ ) and  $S_q^*$  denotes the circuit sensitivity. In these expressions,  $\eta$  and  $\delta$  denote the mechanical loss factor and the dielectric loss factor of the PZT material, respectively. From Eqs. (3.16), (3.18) and (3.19), the voltage  $(V_p)_S$  produced by the PZT patch surface bonded at the centre of the beam ( $x = L/2$ ) is,

$$(V_p)_S = \left( \frac{6d_{31} h \overline{Y^E} D}{\varepsilon_{33}^T L^2} \right) u(x, t) \Big|_{peak} \quad (3.20)$$

where,  $u(x, t) \Big|_{peak}$ , which is substituted in place of ‘ $a$ ’ in Eq. (3.18), can be determined by Eq. (3.13). Using Eqs. (3.9), (3.10) and (3.13), the relation between the voltage  $(V_p)_S$  generated by the surface bonded PZT patch and the generalized excitation force  $P_n$  can be determined as,

$$(V_p)_S = \left( \frac{6d_{31} h \overline{Y^E} D}{\varepsilon_{33}^T L^2} \right) \sum_{i=1}^n \left[ \left( \frac{\phi_i(x)}{K_i} R_D \sin(\omega t - \theta) \right) P_i \right]_{x=L/2} \quad (3.21)$$

### 3.3 LABORATORY EXPERIMENTATION

#### 3.3.1 Experimental Set-Up

Experiments were carried out in the laboratory environment to measure the voltage and the power generated by a surface bonded PZT patch resulting from the vibrations of the host structure. A simply supported I-section beam, with the properties as listed in Table 3.1, was chosen as the host structure. The complete experimental set-up is shown in Figure 3.3. A commercially available PZT patch of  $10 \times 10 \times 0.3$  mm size, conforming to grade PIC 151 (PI Ceramic, 2014) was surface bonded on the top flange, at the centre of the beam, using two part araldite epoxy adhesive. The shear modulus of elasticity of the bonding layer is considered to be 1 GPa (Moharana and Bhalla, 2014). Figures 3.4 to 3.7 show the various components in detail, as explained below.

The beam was excited using LDS V406 series portable dynamic shaker. A function generator (Agilent 33210A) was employed to generate an electrical signal, which was amplified by a power amplifier (LDS PA500L) and transmitted to the shaker, which converted it into a mechanical force (Figure 3.4). Pure harmonic signal was applied with frequency ( $f$ ) ranging between 10 to 100 Hz at a step interval of 10 Hz, with an amplitude of 5 V. An accelerometer (PCB 352C34 with a sensitivity of 100 mV per g) was attached on the top flange at the centre of the beam along with the PZT patch in order to measure acceleration amplitude (Figure 3.5).

**Table 3.1:** Properties of steel I-section beam.

Property	Unit	Value
Span, $L$	m	3.2
Section	m	Flange: $0.070 \text{ m} \times 0.006 \text{ m}$ Web: $0.133 \text{ m} \times 0.004 \text{ m}$
Flexural rigidity modulus, $EI$	N-m <sup>2</sup>	$1.017 \times 10^6$
Mass per unit length, $\bar{m}$	kg/m	12.91
Poison's ratio of beam, $\nu$	-	0.3

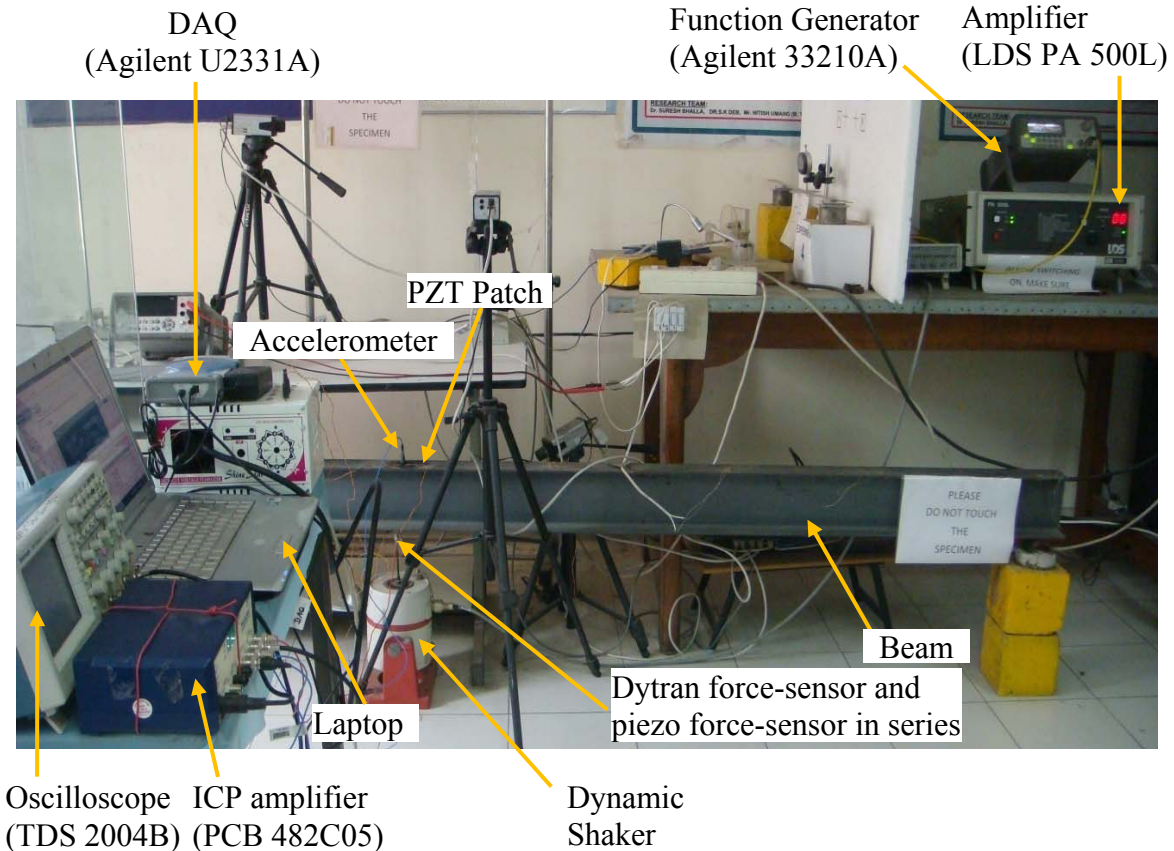


**Figure 3.3:** Experimental set up for voltage measurement across PZT patch.

The *amplitude of vibration (a)* of the beam under concentrated load at centre varying sinusoidally was experimentally measured using the accelerometer and compared with the theoretical amplitude values. The accelerometer is calibrated to express the acceleration in terms of the output voltage ( $V_a$ ), which is directly proportional to the acceleration. As per the calibration constant ( $C_a = 98 \text{ ms}^{-2}\text{V}^{-1}$ ) of the accelerometer, 100 mV measured by accelerometer corresponds to 1 g ( $= 9.8 \text{ ms}^{-2}$ ). Under harmonic excitation, the displacement,  $x$  and the acceleration,  $\ddot{x}$  are related by

$$\ddot{x} = -\omega^2 x \quad (3.22)$$

Therefore, the displacement amplitude can be deduced from the output voltage ( $V_a$ ) across the accelerometer by

$$a = \frac{V_a C_a}{\omega^2} \quad (3.23)$$

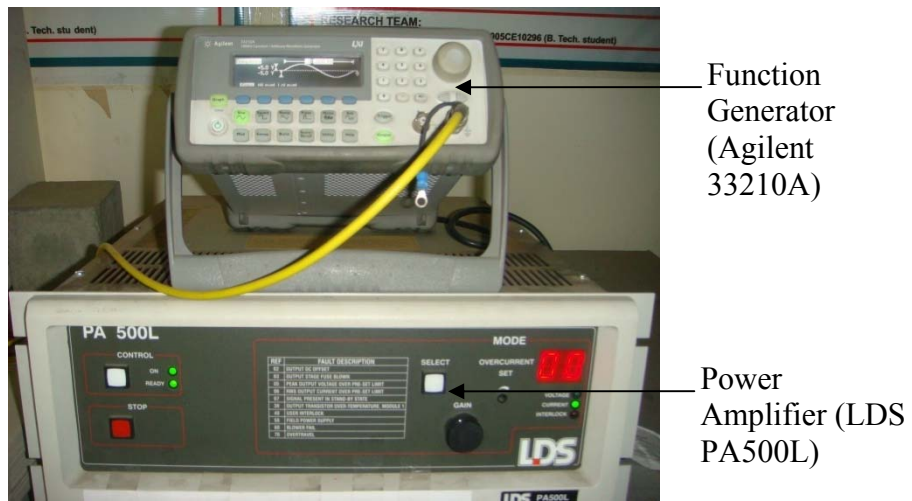


**Figure 3.4:** Function generator with amplifier.

A force-sensor (Dytran 1051V4) was attached in between the stringer and the beam (Figure 3.5) on its bottom flange to measure the mechanical force transferred from the shaker to the beam. The force-sensor is ICP type and requires a signal conditioner cum amplifier. An additional piezo force-sensor was sandwiched between the Dytran force-sensor and the bottom flange of the beam (Figure 3.5). The Dytran force-sensor is a precalibrated sensor to measure force. The piezo force-sensor, on the other hand, is an in-house sensor fabricated by sandwiching a PZT patch between two aluminium plates, as shown in Figure 3.5 (Aggarwal, 2009). The next section covers the determination of the calibration constant for the in-house force sensor.

### 3.3.2 Determination of Calibration Constant for In-House Piezo Force-Sensor

The in-house force sensor was fixed in series with the Dytran force-sensor in order to calibrate it with respect to Dytran force-sensor. It provides a cost-effective and less cumbersome alternative over the Dytran force-sensor with no requirement of signal conditioner. The voltage was measured across the PZT patch (bonded at the top surface of

the beam centre) and the piezo force-sensor using Agilent U2331A data acquisition (DAQ) system (Agilent, 2014) simultaneously, controlled by a laptop (Figure 3.6). The accelerometer and the Dytran force-sensor were connected to an oscilloscope (Tektronix, TDS 2004B) through ICP amplifier (PCB 482C05) for data acquisition (Figure 3.7).

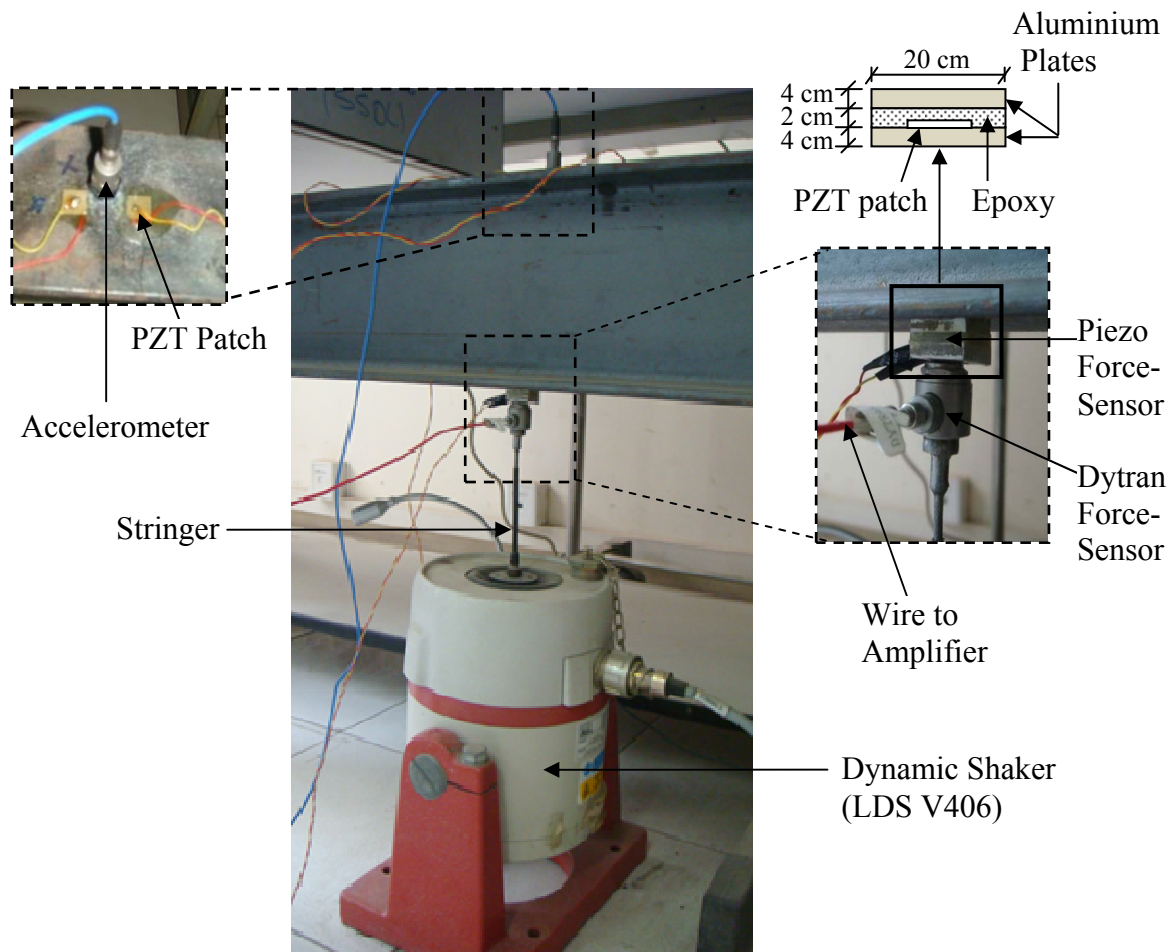


**Figure 3.5:** Portable dynamic shaker along with Dytran force-sensor and piezo force-sensor.

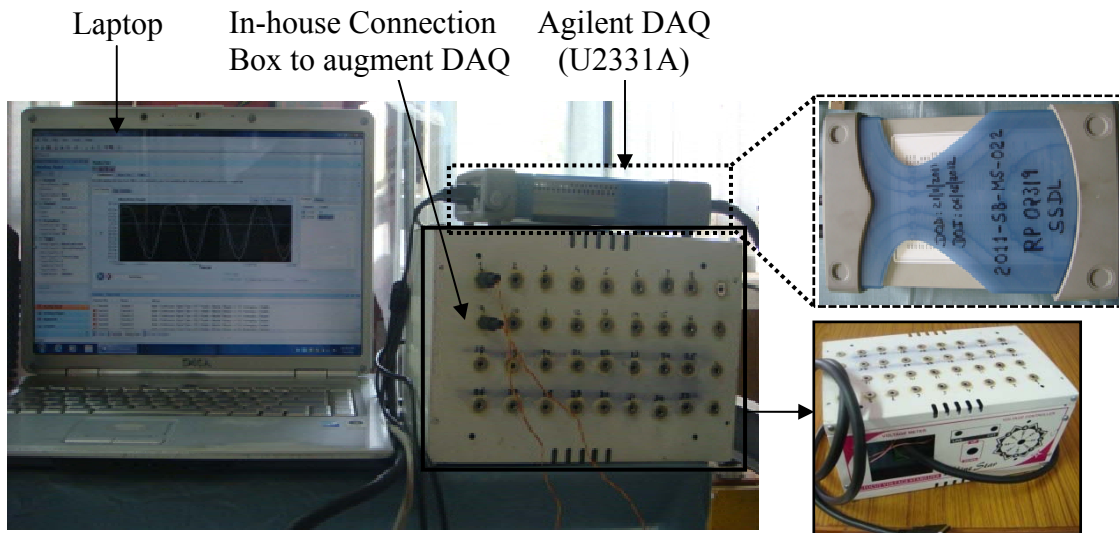


**Figure 3.6:** Data acquisition system for PZT patch at top flange and piezo force-sensor.

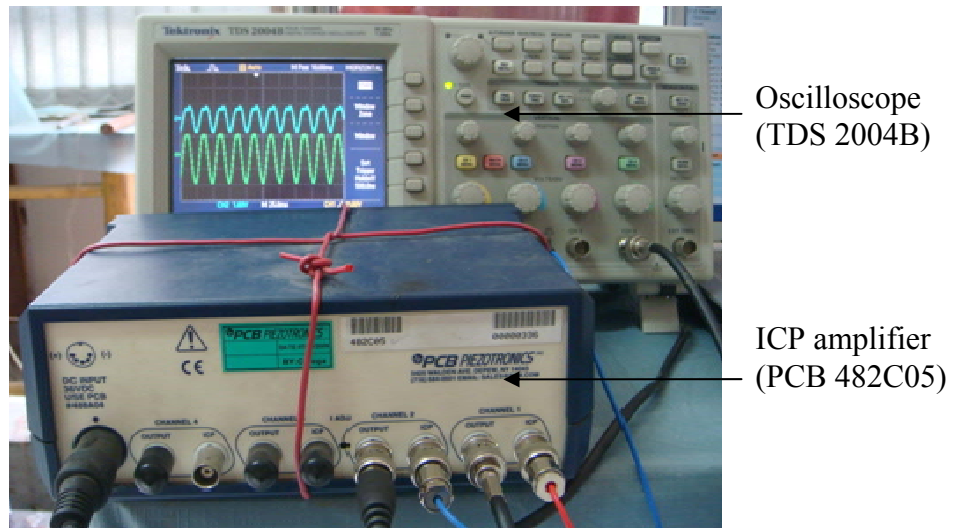


**Figure 3.7:** Oscilloscope with PCB box.

The in-house piezo force-sensor (Figure 3.5) was calibrated with respect to the Dytran force-sensor for the measurement of force transferred to the beam through the shaker. The two sensors were installed in series (Figure 3.5) to ensure equal force transmission. As per the manufacturer's data sheet, the Dytran force-sensor has a calibration constant of 100.2 lb/V (445.124 N/V). Using this calibration constant, the force exerted on the Dytran force-sensor was determined corresponding to the voltage measured by it. Sinusoidal

force with frequency varying from 10 to 100 Hz was applied through the shaker (Figure 3.5). The excitation frequency was varied monotonically at a step interval of 10 Hz. Since same force was transmitted in both the sensors, the experimental value of calibration constant ( $C_F$ ), for piezo force-sensor was easily determined. The values of  $C_F$  corresponding to varying operating frequencies are shown in Figure 3.8. It can be observed that the value of  $C_F$  remains almost constant with increasing frequency for the considered range of frequency, especially beyond 50 Hz. The average experimental value of  $C_F$  was determined as 21.3 N/V.

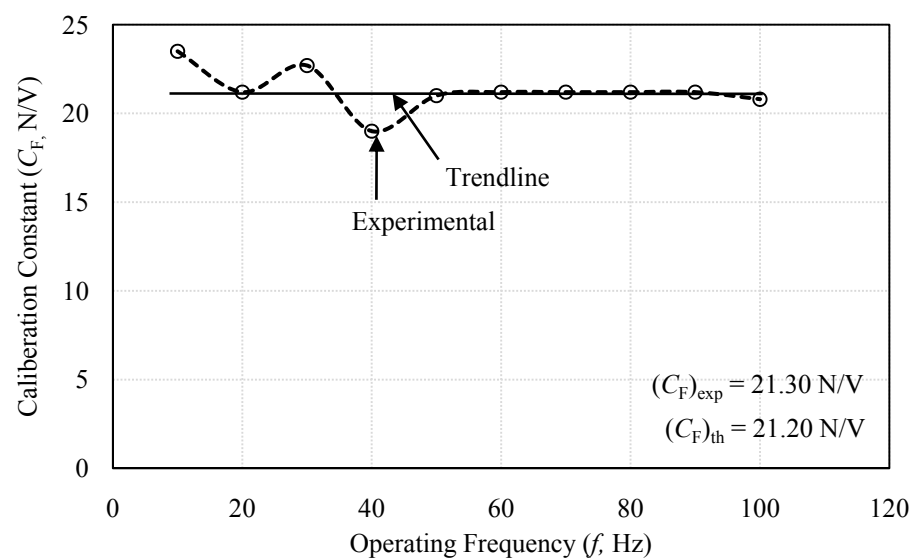


**Figure 3.8:** Calibration constant with varying operating frequencies.

For comparison, the theoretical value of  $C_F$  can be derived from the basic theory of piezoelectricity follows. The charge density ( $D_3$ ) can be obtained for no external elastic field i.e. ( $E_3 = 0$ ) in terms of  $T_3$ , the stress in direction ‘3’ (Figure 2.1) as

$$D_3 = d_{33} T_3 \quad (3.24)$$

where,  $d_{33}$  is the relevant piezoelectric strain coefficient. From the theory of parallel plate capacitors, the total charge ( $Q$ ) developed across the piezo sensor is the product of the capacitance ( $C$ ) and the voltage ( $V_F$ ) across it, that is,

$$Q = CV_F \quad (3.25)$$

$$\text{or } D_3 L_p^2 = CV_F \quad (3.26)$$

where,  $L_p$  denotes the length of the PZT patch. The capacitance ( $C$ ) can be expressed as (Halliday et al., 2008)

$$C = \frac{\epsilon_{33}^T L_p^2}{h} \quad (3.27)$$

The total force acting on the patch is given by

$$F = T_3 L_p^2 \quad (3.28)$$

From the Eqs. (3.24) to (3.27) and  $T_3 = F/L_p^2$ , the calibration constant ( $C_F$ ) of the piezo force-sensor, which is the ratio of force ( $F$ ) to voltage ( $V_F$ ), is given by

$$(C_F)_{th} = \frac{F}{V_F} = \frac{\epsilon_{33}^T L_p^2}{d_{33} h} \quad (3.29)$$

Using the values given in Table 3.2, the theoretical  $C_F$  was determined as 21.20 N/V, which is very close to the average value of 21.3 N/V obtained experimentally (Figure 3.8). Thus, the in-house piezo force-sensor has been successfully developed as an a cost-effective alternative over the commercial force-sensor.

### **3.4 COMPARISON OF ANALYTICAL AND EXPERIMENTAL RESULTS**

The physical properties of the beam used in the MATLAB program are listed in Table 3.1. In the present case, first twenty modes were superimposed for obtaining the theoretical amplitude of vibration. The experimental damping ( $\zeta$ ) was measured as 4.63% using the half-power band width method (Chopra, 2007) as given by

$$\zeta = \frac{f_b - f_a}{2f_n} \quad (3.30)$$

Here,  $f_b$  and  $f_a$  are the forcing frequencies at which the amplitude is  $1/\sqrt{2}$  times the resonant amplitude corresponding to resonance frequency ( $f_n$ ). Three different values, 3%, 4.63% and 10%, of damping ratio ( $\zeta$ ) were considered in the model.

On comparison of the experimental and theoretical amplitudes, it was observed that the theoretical first natural frequency was somewhat higher than the experimental one. This could be attributed to the variability associated with the physical properties of beam considered for theoretical calculations. Model updating of the structure was done by fine tuning the  $EI$  value so as to match the theoretical and the experimental frequencies. The comparison of the experimental and theoretical amplitudes for different damping ratios after model updating is shown in Figure 3.9. It can be observed that the experimental and the theoretical amplitudes are agreeable for  $\zeta = 4.63\%$ . The difference in the peak values can be attributed to several experimental factors such as partial fixity conditions and possible dislocation of the load from the centre of the beam.

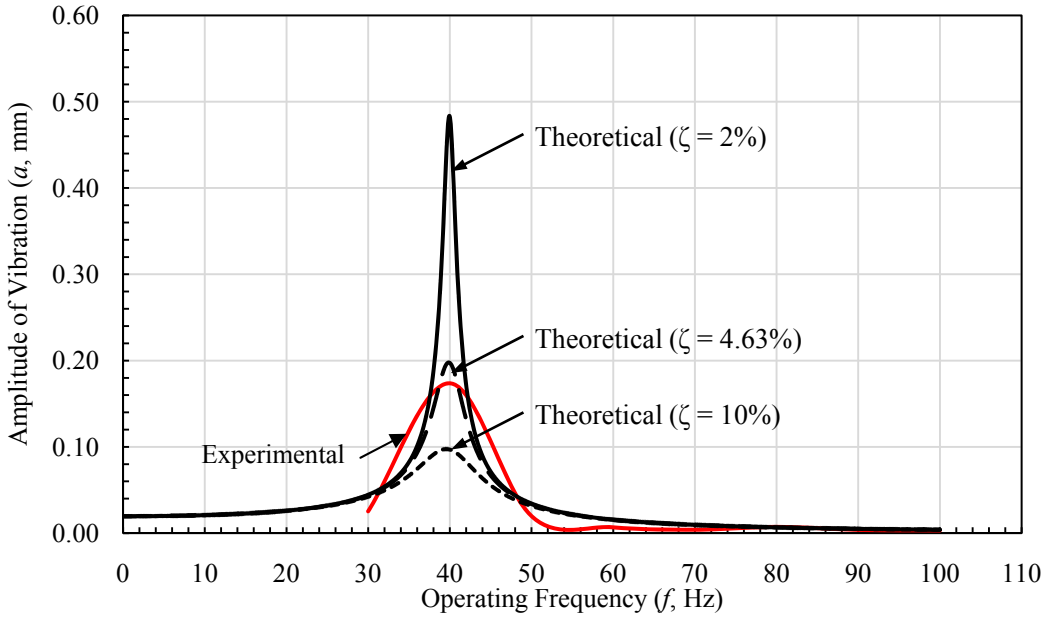


**Figure 3.9:** Comparison of the experimental and theoretical amplitudes for different damping values.

Eq. 3.21 was used for estimation of the output voltage generated by the PZT patch. The properties of the PZT patch listed in Table 3.2 were considered. The mechanical loss factor ( $\eta$ ) and the dielectric loss factor ( $\delta$ ) were neglected (considered later in detail) for simplicity. The comparison of the theoretical and the experimental results is shown in Figure 3.10. It can be observed from the figure that unlike the displacement amplitudes, the experimental and the theoretical peak voltages show significant deviation. The discrepancy in the peak voltage can be attributed to reasons such as the effect of the bond layer and the loss ratios,  $\eta$  and  $\delta$ . A small deviation in the material supplied by the manufacturer (Table 3.2) could also be possible. In order to improve the prediction of the model, effect of different types of losses associated with PZT materials were considered, namely, the mechanical loss, the dielectric loss and the shear lag loss (due to interaction of PZT material with the host structure through the adhesive layer). These losses are considered in the following sub-sections in detail.

**Table 3.2:** Properties of PZT patch (Bhalla, 2004; PI Ceramic, 2014) and bond layer.

Property	Unit	Value
PZT Size, $L_p \times w_p$	$\text{m}^2$	$0.010 \times 0.010$
Thickness of PZT patch, $h$	m	$3.000 \times 10^{-4}$
Piezoelectric Strain Coefficient, $d_{31}$	$\text{m/V}$	$-2.100 \times 10^{-10}$
Young's Modulus, $Y^E$	$\text{N/m}^2$	$6.667 \times 10^{10}$
Piezoelectric Strain Coefficient, $d_{33}$	$\text{m/V}$	$5.000 \times 10^{-10}$
Electric Permittivity, $\epsilon_{33}^T$	Farad/m	$2.124 \times 10^{-8}$
Mechanical Loss Factor, $\eta$		0.0325
Dielectric Loss Factor, $\delta$		0.0224
Poisson's Ratio, $\nu$		0.3000
Shear Modulus of bond layer, $G_s$	$\text{N/m}^2$	$1.000 \times 10^9$
Thickness of bond layer, $t_s = \frac{h}{2}, \frac{h}{5}, \frac{h}{20}$	m	$1.5 \times 10^{-4},$ $6.0 \times 10^{-5},$ $1.5 \times 10^{-5}.$

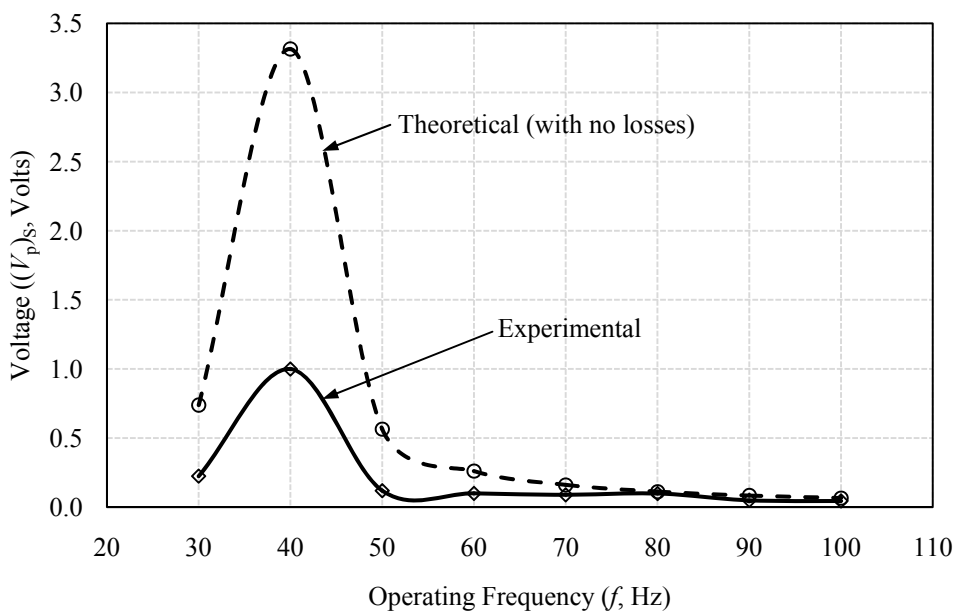


**Figure 3.10:** Comparison of the experimental and theoretical voltage.

### 3.4.1 Mechanical Loss

The mechanical loss occurs due to the heat generated in the PZT patch owing to the internal mechanical friction and the hysteresis effect. It can be accounted by using complex Young's Modulus  $\overline{Y^E} = Y^E(1 + \eta j)$  [Eq. (3.20)]. Considering the value of  $\eta$  as per Table 3.2 (but ignoring the dielectric loss) the voltage given by Eq. (3.20) gets transformed as

$$(V_p^M)_S = \left[ \frac{6d_{31}hY^ED}{\varepsilon_{33}^T L^2} \right] u(x, t)|_{\text{peak}} (1 + \eta j) \quad (3.31)$$

where, the superscript ' $M$ ' signifies that the expression considers the mechanical loss. The absolute value of the voltage,  $|(V_p^M)_S|$  generated by the surface bonded PZT patch, duly considering the mechanical loss, can be determined as,

$$|(V_p^M)_S| = \left[ \frac{6d_{31}hY^ED\sqrt{1 + \eta^2}}{\varepsilon_{33}^T L^2} \right] u(x, t)|_{\text{peak}} \quad (3.32)$$

### 3.3.2 Dielectric Loss

The dielectric loss occurs due to the heat generated in the PZT patch during the dielectric effect. It can be incorporated by using complex  $\overline{\varepsilon_{33}^T} = \varepsilon_{33}^T(1 - \delta j)$  for the calculation of voltage [Eq. (3.20)]. Considering the dielectric loss ( $\delta$ ) as per Table 3.2 (but ignoring  $\eta$ ), the voltage given by Eq. (3.20) gets transformed as,

$$(V_p^D)_S = \left[ \frac{6d_{31}hY^ED}{\varepsilon_{33}^T L^2(1 + \delta^2)} \right] u(x, t)|_{\text{peak}} (1 + \delta j) \quad (3.33)$$

where, the superscript ‘D’ signifies that the expression considers the dielectric loss. The absolute value of voltage,  $|V_p^D|_S$  generated by the surface bonded PZT patch, duly considering the effect of the dielectric loss, can thus be expressed as,

$$|V_p^D|_S = \left[ \frac{6d_{31}hY^E D}{\varepsilon_{33}^T L^2 \sqrt{1 + \delta^2}} \right] u(x, t)_{\text{peak}} \quad (3.34)$$

### 3.3.3 Shear Lag Loss

The piezo transducers are bonded to the surface of the host structures using an adhesive (such as epoxy), which forms a permanent finite thickness interfacial layer between the structure and the patch (Bhalla, 2004). The phenomenon of the difference in the strains of the PZT patch and the host structure is called as *shear lag effect* (Bhalla, 2004; Bhalla and Soh, 2004b; Bhalla and Moharana, 2012). Shear lag effect takes into account the interaction between the PZT patch and the host structure by considering the mechanical deformation of the thin bond layer. The parameter  $\Gamma_s$  (unit  $\text{m}^{-1}$ ), given by the following equation, is called the *shear lag parameter*.

$$\Gamma_s^2 = \left\{ \frac{G_s}{Y^E t_s h} + \frac{L_p D^2 G_s}{4EI t_s} \right\} \quad (3.35)$$

where,  $G_s$  denotes the shear modulus of elasticity of the bond layer,  $t_s$  the thickness of the bond layer,  $L_p$  the length of the PZT patch,  $Y^E$  the Young’s modulus of elasticity of PZT the patch,  $h$  the thickness of the patch,  $D$  the overall depth of the beam and  $EI$  the flexural rigidity of the beam. The voltage  $(V_p^s)_S$  generated by the PZT patch bonded on a beam surface duly considering the effect of shear lag is given by (Sirohi and Chopra, 2000)

$$(V_p^S)_S = K_p (K_b)_S S_q^* S_1 \quad (3.36)$$

where, the superscript ‘*S*’ signifies that the expression considers the shear lag loss,  $(K_b)_S$  is the correction factor for the shear lag effects in the bond layer,  $K_p$  the correction factor due to Poisson’s effect and  $S_q^*$  the circuit sensitivity, as given by Eq. (3.19). The value of  $(K_b)_S$  is independent of the material properties of the sensor and depends only on its geometry and the properties of the adhesive layer.  $K_p$  and  $(K_b)_S$  are respectively given by,

$$K_p = \left( 1 - \nu \frac{d_{31}}{d_{32}} \right) \quad (3.37)$$

and

$$(K_b)_S = (X_{eff})_S (Y_{eff})_S \quad (3.38)$$

where,  $\nu$  is the Poisson’s ratio of the host structure material. Incidentally,  $d_{31} = d_{32}$  for the PZT patch used in the present set of experiments. It should be noted that the shear lag effect has been considered in the longitudinal direction only (along the plane of bending of beam). Hence, the effective width fraction  $(Y_{eff})_S$  has been considered as unity. The effective length fraction  $(X_{eff})_S$  for surface bonded PZT patch can be determined as (Bhalla and Soh, 2004b)

$$(X_{eff})_S = 1 - \frac{\tanh \Gamma(L_p/2)}{\Gamma(L_p/2)} \quad (3.39)$$

Using Eqs. (3.16), (3.18) and (3.36), following expression can be derived for determining the voltage generated by PZT surface bonded at the centre of the simply supported beam, duly considering the shear lag loss,

$$(V_p^S)_S = \frac{6D}{L^2} K_p (K_b)_S S_q^* u(x, t)|_{peak} \quad (3.40)$$

Based on the parameters listed in Table 3.2,  $K_p$  was worked out to be 0.7 and  $S_q^*$  equal to  $1.977 \times 10^5$  V. The parameters related to shear lag effect are listed in Table 3.3

corresponding to various thicknesses of the bond layer. The effect of considering all the three losses (mechanical, dielectric and shear lag) individually is shown in Figure 3.11. It can be observed that the mechanical and the dielectric losses do not contribute much to the theoretical amplitudes. This is due to the fact that the values of  $\eta$  and  $\delta$  are too small to result in any major variation in the values of voltages,  $(V_p^M)_S$  and  $(V_p^D)_S$  [see Eqs. (3.32) and (3.34)]. It can be observed that with increase in bond layer thickness, the predicted theoretical voltage reduces significantly. Hence, shear lag loss effect is identified as the major contributor of voltage loss from the plot. Shear lag effect is incorporated for varying thicknesses of the adhesive bond layer (note that  $h$  is the thickness of the PZT patch).

**Table 3.3:** Values of key parameters associated with shear lag effect.

Property	Thickness of bond layer ( $t_s$ )		
	$h/2$	$h/5$	$h/20$
Shear lag parameter, $\Gamma_s$ (cm <sup>-1</sup> )	577.35	912.87	1825.74
Effective length fraction, $(X_{eff})_S$	0.656	0.781	0.890
$(K_b)_S$	0.656	0.781	0.890

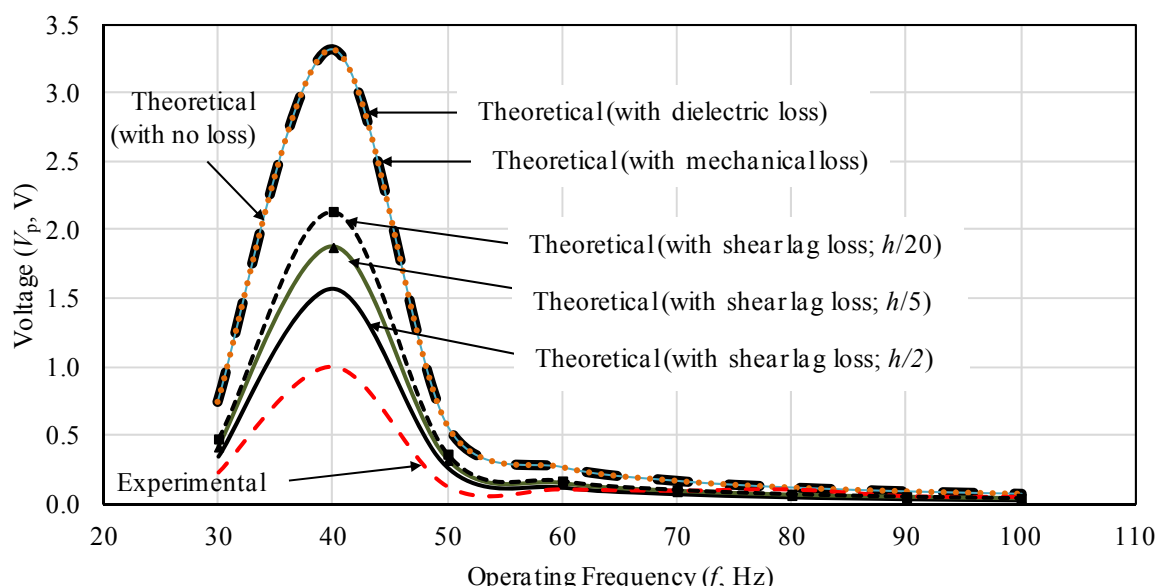


**Figure 3.11:** Comparison of experimental and theoretical voltage incorporating the effect of losses ( $h$ : thickness of PZT patch).

The actual thickness of bond layer was measured to be 0.15mm ( $=0.5h$ ) experimentally, for which reasonable match can be noted between the theoretical and the experimental plots. From the significant contribution of bond layer, it can be concluded that effect of shear lag must be taken into account in the electro-mechanical coupling model, whereas the mechanical and dielectric losses can be neglected.

### **3.5 ENERGY HARVESTING: POWER MEASUREMENT ACROSS THE PZT PATCH**

This section deals with the measurement of the power generated by the surface-bonded PZT patch. The experimental setup and the loading were similar to the voltage measurement set-up described in the previous section, except that it was supplemented by the addition of a simple circuit shown in Figure 3.12. The PZT patch acts as the source of the voltage generation ( $V_1$ ), which was indirectly measured by the Agilent U2331A DAQ via the in-house circuit. This circuit takes into consideration the fact that the electrical impedance of the PZT patch is very high, as a result of which the electric current ( $i$ ) flowing through the circuit will be extremely small, possibly in microampere range. Such a small order current is practically very difficult to be measured accurately in the laboratory. Hence, instead of measuring the current directly, the voltage ( $V_2$ ) was measured via the circuit (Figure 3.12), and finally the current determined using  $i = V_2/R_1$ . Thus, the power ( $P$ ) generated by the PZT patch is given by,

$$P = i^2(R_1 + R_2) \quad (3.41)$$

The external force was applied harmonically as before and the frequencies were varied from 20 Hz to 90 Hz. The value of the load resistances ( $R_1 = 494.7\text{ k}\Omega$  and  $R_2 = 471.66\text{ k}\Omega$ ) were chosen based on the maximum power transfer theorem (Kuphaldt, 2007).

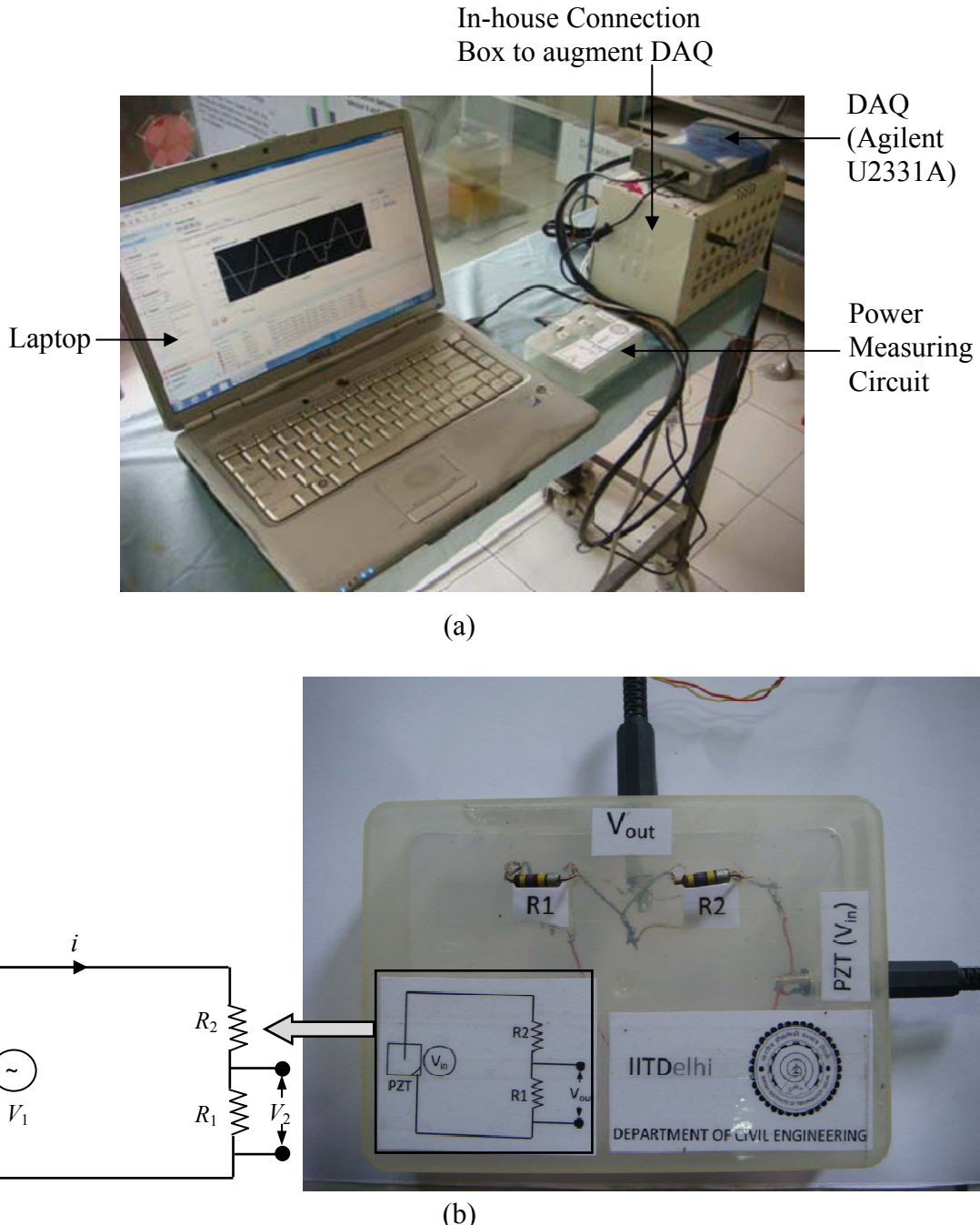


**Figure 3.12:** (a) Measuring equipment set up for power quantification.  
(b) Simple circuit employed for power measurement

The *maximum power transfer theorem* states that the maximum amount of power is dissipated by load impedance when it is equal to the impedance of the network supplying the power. It becomes important to understand the concept of *impedance matching* before proceeding further. If the impedance of the load and the source are not comparable, the

source would tend to dissipate more than its fair share of power in the form of heat, trying to drive the low impedance load. Transformers are used to match these mismatched impedances in electronic circuits, though not employed in the present work. Use of transformers (step-up / step-down) to satisfy the maximum power transfer theorem in this capacity is called as impedance matching. This can be well understood by considering the example of multiple-speed bicycle, in which the purpose of the “gears” is to impedance-match the rider's legs to the riding conditions, so that they always spin the crank at the optimum speed, which is about 60 to 90 revolution per minute (Kuphaldt, 2007). For the present set up, the impedance of the PZT patch was measured as  $1.39 \text{ k}\Omega$ . Since, operating frequency is very low, we expect the reactive component of PZT patch to be negligible. Hence, in order to achieve near maximum power transfer, the resistances  $R_1$  and  $R_2$  were chosen such that  $(R_1+R_2)$  has same order of magnitude as the PZT patch.

The current ( $i$ ) and the power ( $P$ ) derived before [Eq. (3.41)], represent the instantaneous values. The root mean square (RMS) values of the current and power were respectively determined as

$$i_{RMS} = 0.707 i \quad (3.42)$$

$$P_{RMS} = i_{RMS}^2 (R_1 + R_2) \quad (3.43)$$

Figure 3.13 shows the variation of power with time. The total energy ( $U$ ) generated by the PZT patch was determined by integrating the power ( $P$ ) with respect to time ( $t$ ), that is, the area under the curve (Figure 3.13). Using Eq. (3.41), the total energy from time  $t=0$  to time  $t=t_1$  can be expressed as

$$U = \int_0^{t_1} P dt \quad (3.44)$$

or

$$U = \int_0^{t_1} i^2 (R_1 + R_2) dt \quad (3.45)$$

The average power ( $P_{avg}$ ) based on the energy generated ( $U$ ) was determined as

$$P_{avg} = \frac{U}{t_1} \quad (3.46)$$

The variation of three different forms of power,  $P_{peak}$ ,  $P_{RMS}$  and  $P_{avg}$ , with varying forcing frequency (20 Hz to 90 Hz) is shown in Figure 3.14. It can be observed that the maximum power (in all forms) is achieved at the first natural frequency ( $f_n = 40\text{Hz}$ ) of the vibrating structure (here, steel beam) when it experiences maximum deflection. The detailed results are presented in Table 3.4 corresponding to various frequencies. It can be noted that a maximum RMS power of  $0.27 \mu\text{W}$  ( $9 \mu\text{W}/\text{cm}^3$ ) could be successfully harnessed.

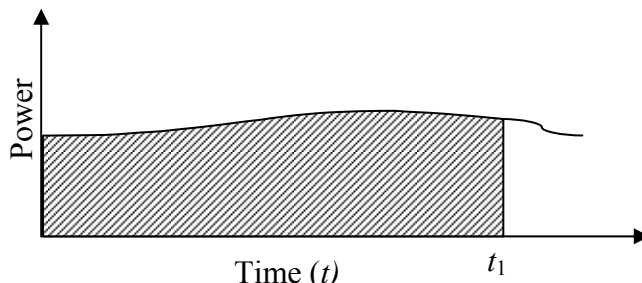


**Figure 3.13:** Plot showing area under the curve of power and time.

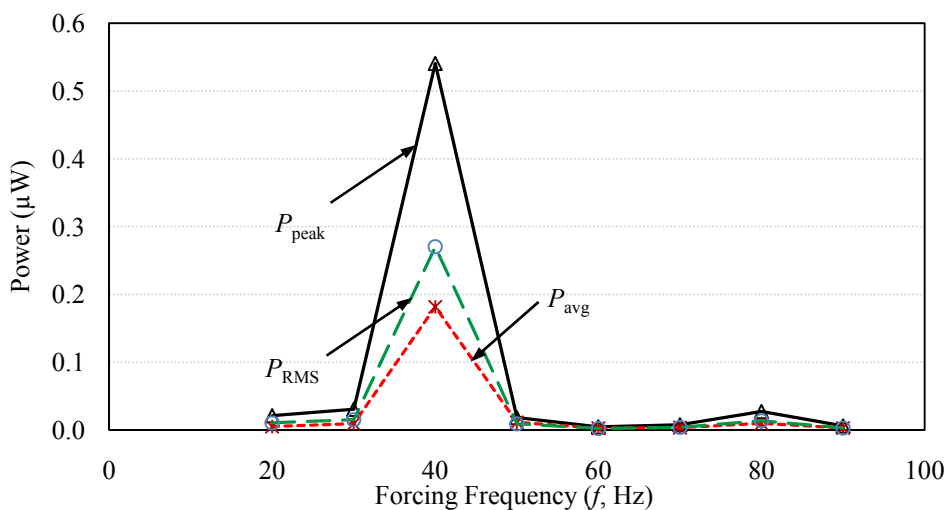


**Figure 3.14:** Variation of  $P_{peak}$ ,  $P_{RMS}$  and  $P_{avg}$  with varying forcing frequency.

**Table 3.4:** Experimental values of voltage, current and power  
 for varying forcing frequencies.

Freq (Hz)	Voltage (V)	Current ( $\mu$ A)		Power ( $\mu$ W)		
		$i_{\text{peak}}$	$i_{\text{RMS}}$	$P_{\text{peak}}$	$P_{\text{RMS}}$	$P_{\text{avg}}$
20	0.073	0.148	0.104	0.021	0.011	0.0049
30	0.088	0.178	0.126	0.031	0.015	0.0092
<b>40</b>	<b>0.37</b>	<b>0.748</b>	<b>0.529</b>	<b>0.541</b>	<b>0.270</b>	<b>0.1816</b>
50	0.068	0.137	0.097	0.018	0.009	0.0111
60	0.034	0.069	0.049	0.005	0.002	0.0026
70	0.044	0.089	0.063	0.008	0.004	0.0035
80	0.083	0.168	0.119	0.027	0.014	0.0097
90	0.039	0.079	0.056	0.006	0.003	0.0028

### 3.6 POSSIBILITY OF BATTERY CHARGING USING ENERGY HARVESTED FROM PZT PATCH

*Amp-hour* is a unit of battery energy capacity, equal to the amount of continuous current multiplied by the discharge time that a battery can supply before exhausting its internal store of chemical energy (Kuphaldt, 2007). A battery with a capacity of 1 amp-hour should be able to continuously supply a current of 1 amp to a load for exactly 1 hour, or 2 amps for 1/2 hour, or 1/3 amp for 3 hours, etc., before becoming completely discharged. Therefore, the amp-hour relationship is an ideal approximation of battery life. The amp-hour rating is trusted only near the specified current or time-span given by the manufacturer. Such a rating cannot be extrapolated for very high currents or very long time durations accurately. Hence, on the basis of above background, the following relation can be written for calculating the charge/discharge time (Kuphaldt, 2007):

$$\text{Charge/discharge time (in hours)} = \frac{\text{Amp hour rating}}{\text{Continuous current (in Amp)}} \quad (3.47)$$

Chip type electric double layer capacitors, specifically, CPH3225A and CP3225A, product by Seiko Instrument Inc. (2014), have nominal battery capacity of  $4.6\mu\text{Ah}$  and  $4.5\mu\text{Ah}$  respectively. Using the Eq. (3.47), it can be concluded that piezo sensor with  $i_{\text{RMS}}$

of 0.529  $\mu$ A (Table 3.4) is capable of charging the chip type capacitor in 8.5 hours, which can provide a power back up for various devices and super small size power supply for portable phones such as smart phones, tablets, and cellular phones, personal computers, IC card, game machine, handy terminal, video camera and various other kinds of small appliance. This time is reasonable from practical considerations.

### **3.7 SUMMARY AND CONCLUDING REMARKS**

This chapter has presented the feasibility of energy harvesting using thin surface-bonded PZT patch operating in the  $d_{31}$ -mode. Experiments have been carried out in the laboratory environment to measure the voltage and the power generated by a PZT patch in surface bonded condition. Amplitude of vibration for the beam was determined theoretically and compared with experiment. A coupled electro-mechanical model has been derived and validated with experimental measurements. The losses associated with the PZT patch were quantified. The experimental voltage showed a reasonable match with the theoretical prediction after incorporating losses, especially the shear lag loss. The size of the host structure (beam length= 3.2 m) considered in this study is considerably larger than those available in literature (Park et al., 2008; Sodano et al., 2005; Mohammadi et al., 2003 and Churchill et al., 2003). It can be estimated that two day operation of energy extraction is sufficient enough to scavenge energy sufficient enough to drive AD5933 circuit (Analog Devices, 2014) for one time data acquisition/operation for SHM. It is also found that the shear lag effect significantly affects the output voltage and should be as small as practically possible for maximum efficiency. The paper has focused on using the normal piezos in place of commercial expensive transducers for energy harvesting in the strain mode. This piezo will act as energy harvester when not in use and shall carry out SHM utilizing its own energy harvesting. Chapter 6 extends the coupled electro-

mechanical model developed in this chapter to estimate power levels achievable in real-life bridges.

With increase in size (area) of piezo sensor, its energy harvesting capacity is expected to increase; however, its suitability for SHM will reduce owing to (a) increase of shear lag effect (Bhalla and Moharana, 2012) and (b) reduction in sensing area. For the same area of host structure, small distributed sensors will enable larger more sensing area in overall, as compared to single large sized sensor. The Chapter 7 of this thesis investigates these issues in a comprehensive manner so as to arrive at an optimum size and parameters suitable for both SHM and energy harvesting. The results of the present chapter have been published in the Kaur and Bhalla (2014).

The next chapter will extend the model to concrete vibration sensor (CVS) embedded inside the reinforced concrete (RC) structures.



## **Chapter 4**

# **ENERGY HARVESTING POTENTIAL OF EMBEDDED PIEZO PATCHES: MODELLING AND EXPERIMENTATION**

### **4.1 INTRODUCTION**

This chapter covers modelling, experimental verification and proof-of-concept experimental demonstration of energy harvesting from the PZT patch in the form of concrete vibration sensor (CVS), which is specifically designed for reinforced concrete (RC) structures (Bhalla and Gupta, 2007). CVS, which is a packaged sensor, is composite in nature, has better compatibility with surrounding concrete and can withstand the harsh conditions normally encountered in the RC structures. The analytical model presented in the previous chapter for surface-bonded PZT patch is extended to compute the power output from the embedded CVS, duly considering the effect of shear lag associated with the bonding layers. This aspect is much more complicated than the surface-bonded PZT patches and has not been attempted before. The analytical model is followed by experiments carried out in the laboratory environment to measure the voltage and the power generated by a CVS embedded in a life-sized (4 m) simply supported RC beam under harmonic excitations. The analytical model has been duly validated with the experimental results. The performance of the CVS is compared with surface-bonded PZT patch with regard to RC structures. Vibration energy harvesting potential of the PZT sensors during idle time is experimentally demonstrated.

## **4.2 ENERGY HARVESTING FROM EMBEDDED CONCRETE VIBRATION SENSOR: ANALYTICAL MODELLING**

This section outlines the details of the concrete vibration sensor (CVS) along with the thickness of the various layers constituting the CVS. The theoretical coupled electro-mechanical model for quantification of the voltage generated by the embedded CVS has also been described and validated here.

### **4.2.1 Details of Concrete Vibration Sensor**

CVS, shown in Figure 4.1(a), is a packaged sensor, designed especially for monitoring RC structures. CVS is composite in nature, has better compatibility with the surrounding concrete, and can withstand the harsh conditions typically encountered in the RC structures during casting. It has been developed in the Smart Structures and Dynamics Laboratory (SSDL), IIT Delhi (SSDL, 2014). It consists of a PZT sensor patch encapsulated in a proprietary configuration suitable for casting along with the structure, thereby permanently embedding the patch in the host RC structure. The packaging offers an additional advantage of protecting the sensing element against ambient environmental conditions, thereby enhancing its life expectancy. In this section, an analytical model is developed for determination of the voltage generated by the PZT patch embedded as CVS in a simply supported RC beam, with the configuration shown in Figure 4.1(a). The beam is assumed to be under a concentrated sinusoidal load ( $P_n$ ) at the centre, with an operating angular frequency ( $\omega$ ).

The optical image of the one diagonal half of the cross-section of the CVS was captured under the Leica M205C microscope to measure the thickness of all the layers, namely, the mortar, PZT patch and the two adhesive layers. Figure 4.2 shows a typical image of the

cross-section of the CVS showing different layers under the microscope. The thickness of the top and the bottom adhesive layers were measured to 0.671 mm and 3.411 mm, respectively. In the analytical model developed here, the average thickness of the top and bottom adhesive layer has been assumed equal (2.0 mm) on either side for simplification.

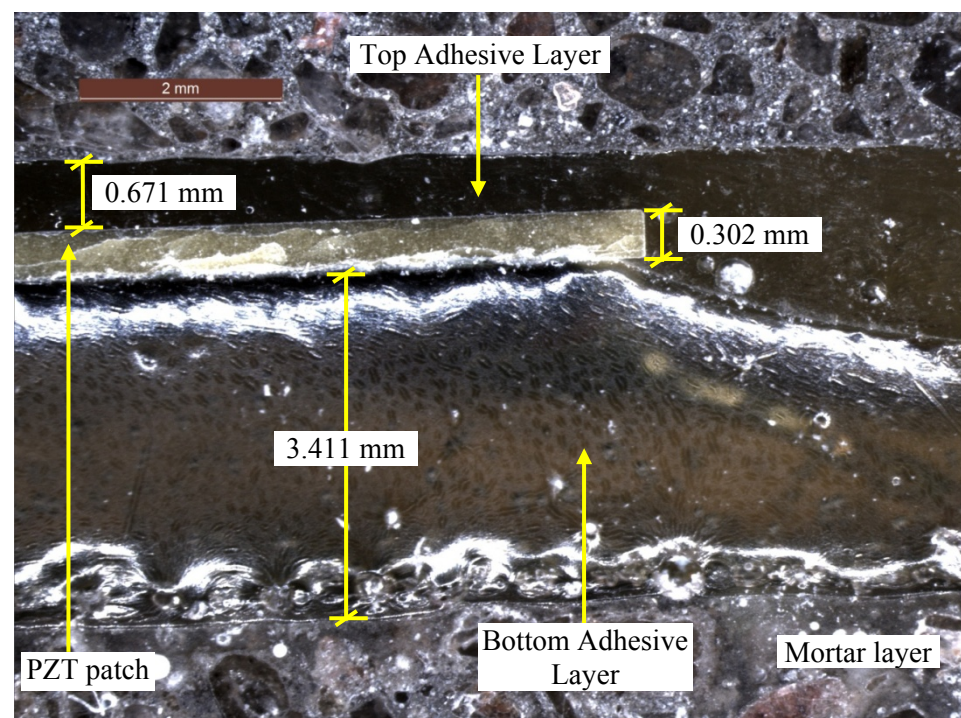
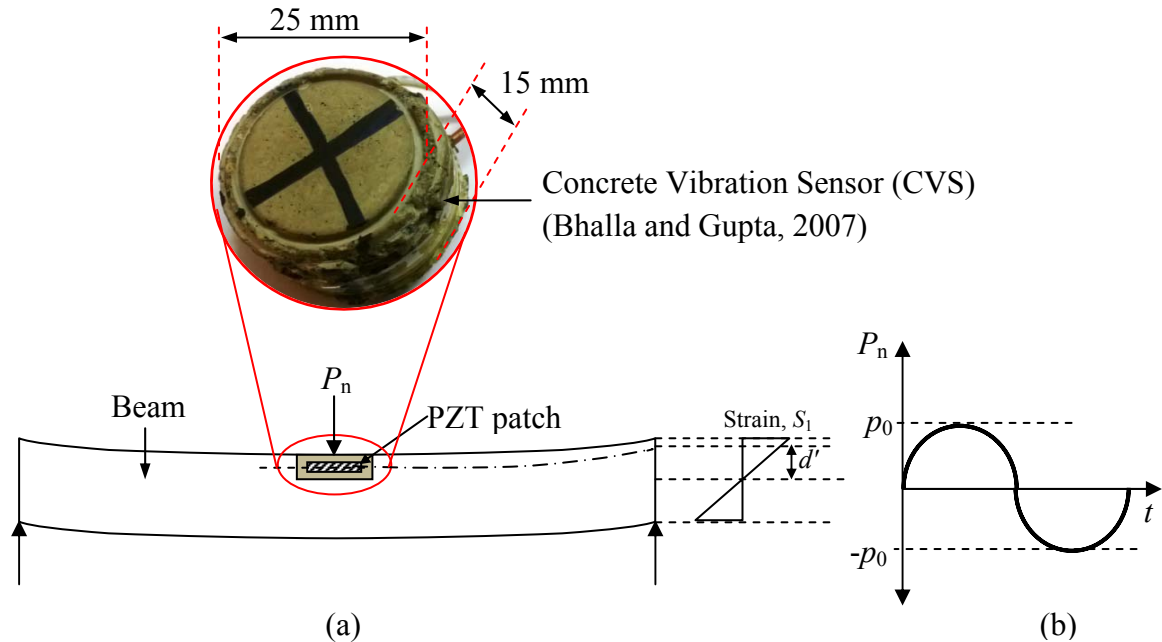


Figure 4.2: Optical image showing different layers of CVS.

#### 4.2.2 Development of Coupled Electro-Mechanical Model

The theoretical amplitude of the dynamic vibration of the beam, based on the developments presented in Chapter 3 (Eqs. 3.9, 3.10 and 3.13) considering first  $n$  modes, can be expressed as,

$$u(x,t)|_{peak} = \sum_{i=1}^n \left[ \left( \frac{\phi_i^{x|L/2}}{K_i} R_D \sin(\omega t - \theta) \right) P_i \right] \quad (4.1)$$

where,  $(\phi_n)$  denotes the mode shape and  $\omega_n$  the cyclic natural frequency,  $R_D$  the dynamic magnification factor,  $\theta$  the phase angle and  $P_n$  the generalized force, as explained in Chapter 3. However, The configuration of the embedded PZT patch [Figure 4.1(a)] is somewhat different from that of the surface bonded PZT patch earlier considered in Chapter 3. Here, the stress is transferred from the structure to the patch from the top, the bottom, as well as the side faces [Figure 4.1(a)], unlike the surface bonded configuration where only the bottom face solely interacts with the structure [see Figure 3.2(c)]. The potential difference  $(V_p)_E$  across the terminals of the embedded PZT patch of thickness  $h$ , undergoing an axial strain ( $S_1$ ) can be derived in line with Chapter 3 as,

$$(V_p)_E = \left( \frac{12d_{31}hY^E d'}{\varepsilon_{33}^T L^2} \right) \sum_{i=1}^n \left[ \left( \frac{\phi_i^{x|L/2}}{K_i} R_D \sin(\omega t - \theta) \right) P_i \right] \quad (4.2)$$

where,  $d'$  denotes the distance of the centre line of the PZT patch from the neutral axis (refer Figure 4.1). All other symbols have usual meanings as defined in Chapter 3. It may be noted that the above equation assumes perfect bonding between the PZT patch and the structure. The losses considered are only the mechanical and the dielectric losses, which are automatically accounted by the complex terms, namely, the Young's Modulus and the electric permitivitty. The prominent loss, however, is the shear lag loss due to the interaction of PZT patch with the host structure via the adhesive layer, which, unlike the

surface-bonded configuration, surrounds the patch from all sides. Based on the background covered in Chapter 3, the absolute value of the voltage,  $\left| \left( V_p^M \right)_E \right|$  and  $\left| \left( V_p^D \right)_E \right|$  generated by the embedded PZT patch including the effect of the mechanical loss and the dielectric loss, respectively, can be expressed as,

$$\left| \left( V_p^M \right)_E \right| = \left[ \frac{12d_{31}hY^E d' \sqrt{1+\eta^2}}{\varepsilon_{33}^T L^2} \right] u(x,t)_{peak} \quad (4.3)$$

and

$$\left| \left( V_p^D \right)_E \right| = \left[ \frac{12d_{31}hY^E d'}{\varepsilon_{33}^T L^2 \sqrt{1+\delta^2}} \right] u(x,t)_{peak} \quad (4.4)$$

where,  $u(x,t)_{peak}$  is given by Eq. (4.1).

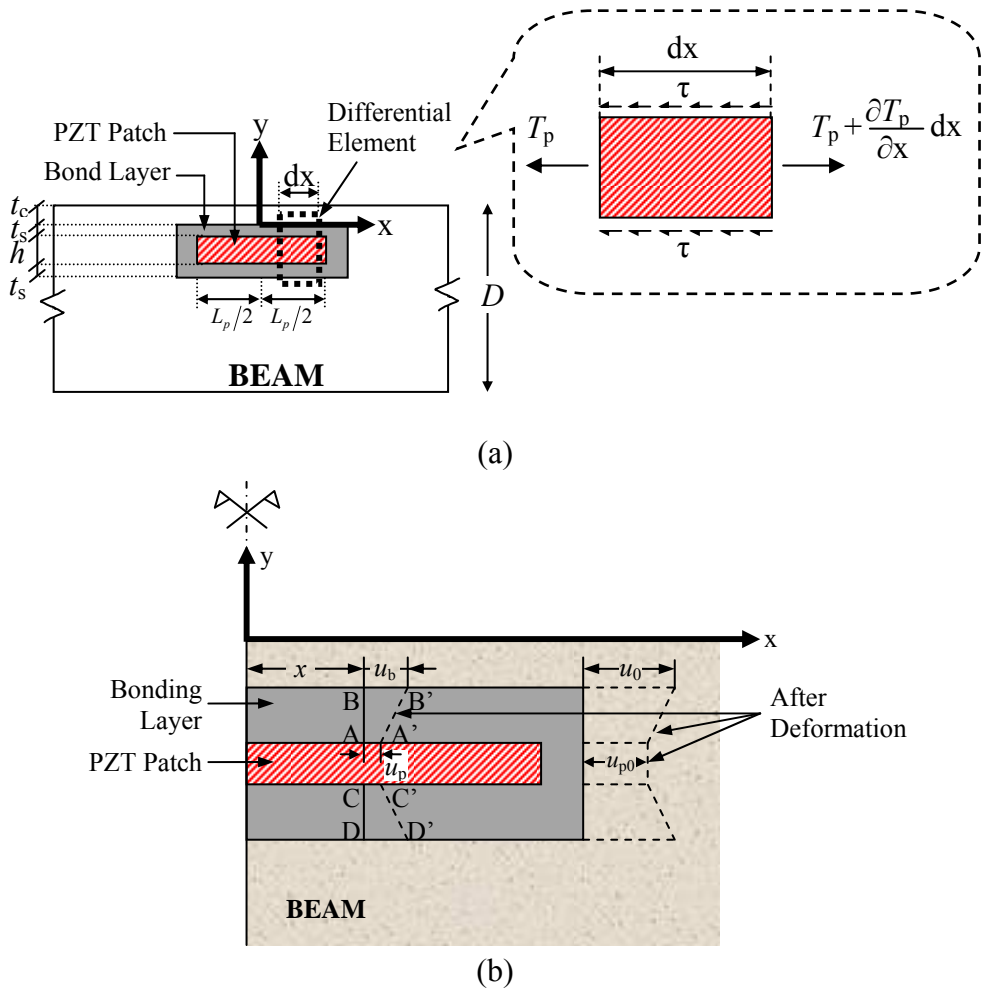


**Figure 4.3:** (a) A PZT patch embedded inside concrete beam and bonded using adhesive layer.

(b) Deformation in bonding layer and PZT patch embedded in concrete beam.

Figure 4.3 shows in detail the configuration of the embedded PZT patch. As can be observed, the PZT patch is encapsulated inside the CVS, which is in turn embedded inside the host structure. As pointed out above, unlike the surface bonded PZT patch (Sirohi and Chopra 2000; Bhalla and Soh 2004b), the adhesive (such as epoxy) in this case, forms a permanent finitely thick interfacial layer between the host structure and the PZT patch on all the four sides, which adds to the complication. In addition, the boundary conditions encountered at the two ends are different from the stress free conditions in the case of the surface-bonded patch. Here, a close form analytical solution is derived for the embedded PZT patch, duly considering the very difficult nature of the shear lag induced by the adhesive layer. Following assumptions, based on Sirohi and Chopra (2000) and Bhalla (2004), have been considered for the model:

- (i) The system is under quasi-static equilibrium.
- (ii) The beam is actuated in pure bending mode and the bending strain is linearly distributed across any cross section.
- (iii) The PZT patch is in a state of pure 1D axial strain only and no shear stress acts on it.
- (iv) The bonding layer is in a state of pure shear stress only, which is independent of ' $y$ '.
- (v) The stresses at the both ends of the embedded PZT sensor are equal and opposite in sign, that is, symmetry from the force consideration exists.
- (vi) Strain distribution is assumed uniform across the thickness of the patch.
- (vii) Plain strain condition exists within the piezo-bond-structure zone.

The typical configuration of the system is shown in Figure 4.3(a). The patch has a length  $L_p$ , width  $w_p$  and thickness  $h$ , while the bonding layer has a thickness of  $t_s$  (assumed equal on both top and bottom for ease of modelling), and the adhesive encasing PZT patch is

located at a depth  $t_c$  from the surface of the beam. The beam has an overall depth  $D$  and width  $w_b$ . Let  $T_p$  denote the axial stress in the PZT patch and  $\tau$  the interfacial shear stress [see Figure 4.3(a)]. Let  $u_p$  be the displacement at the interface between the PZT patch and the bond layer and  $u_b$  the corresponding displacement at the interface between the bond layer and the beam at a distance ‘ $x$ ’ from the centre of the patch. Considering the static equilibrium of the differential element of the PZT patch in the x-direction, as shown in Figure 4.3(a), we can derive, along the lines of Sirohi and Chopra (2000) and Bhalla and Soh (2004b)

$$2\tau = \frac{\partial T_p}{\partial x} h \quad (4.5)$$

where, a factor of two has crept in unlike the surface bonded case. The bending moment at any cross section of the beam, where the PZT patch is embedded, is given by

$$M = T_p w_p h (0.5D - t_c - t_s - 0.5h) \quad (4.6)$$

Further, using Euler Bernoulli’s beam theory, we can derive

$$M = -\sigma_b \left( \frac{I}{0.5D} \right) \quad (4.7)$$

where,  $\sigma_b$  is the bending stress in the beam at its extreme top fibre and ‘ $I$ ’ is the second moment of inertia of the beam cross-section. The negative sign signifies the fact that the sagging moment and the tensile stresses are considered positive. Comparing Eqs. (4.6) and (4.7), and solving, we get

$$-\sigma_b \left( \frac{I}{0.5D} \right) = T_p w_p h (0.5D - t_c - t_s - 0.5h) \quad (4.8)$$

$$\text{or } \sigma_b + \frac{T_p w_p h D}{4I} (D - 2t_c - 2t_s - h) = 0 \quad (4.9)$$

which can be compacted as

$$\sigma_b + \frac{T_p w_p h D D'}{4I} = 0 \quad (4.10)$$

where  $(D - 2t_c - 2t_s - h)$  has been substituted by  $D'$ . Differentiating with respect to  $x$ , and comparing with Eq. (4.5), we get

$$\frac{\partial \sigma_b}{\partial x} + \frac{w_p DD'}{4I}(2\tau) = 0 \quad (4.11)$$

From Figure 4.3(b), the shear strain ( $\gamma$ ) in the bond layer can be expressed as,

$$\gamma = \frac{u_b - u_p}{t_s} \quad (4.12)$$

Using Hooke's law,  $\sigma_b = ES_b$ ;  $T_p = Y^E S_p$  and  $\tau = G_s \gamma$ . Here,  $E$  and  $Y^E$  denote the Young's modulus of elasticity of the beam and the PZT patch (at zero electric field for the patch), respectively, and  $S_b$  and  $S_p$  respectively the corresponding strains and  $G_s$  the shear modulus of elasticity of the bond layer. Making these substitutions in Eqs. (4.5) and (4.11), followed by the substitution of Eq. (4.12), then differentiating with respect to  $x$ , we get Eqs. (4.13) and (4.14), respectively.

$$\frac{\partial^2 S_p}{\partial x^2} = \left( \frac{2G_s S_b}{Y^E h t_s} \right) \xi_E \quad (4.13)$$

$$\frac{\partial^2 S_b}{\partial x^2} = - \left( \frac{2G_s w_p DD' S_b}{4EI t_s} \right) \xi_E \quad (4.14)$$

where,

$$\xi_E = \left( 1 - \frac{S_p}{S_b} \right) \quad (4.15)$$

is the ***strain lag ratio*** for embedded PZT patch (note that subscript ' $E$ ' signifies 'embedded' configuration). The ratio  $\xi_E$  is a measure of the PZT patch's differential strain (patch being in embedded condition) relative to the strain in the host substrate surrounding the PZT patch, caused by the shear lag effect. Subtracting Eq. (4.13) from Eq. (4.14), we get

$$\frac{\partial^2 \xi_E}{\partial x^2} + \Gamma_E^2 \xi_E = 0 \quad (4.16)$$

where,

$$\Gamma_E^2 = 2 \left\{ \frac{G_s}{Y^E h t_s} + \frac{G_s w_p D D'}{4 E I t_s} \right\} \quad (4.17)$$

The parameter  $\Gamma_E$  (unit  $m^{-1}$ ) is the ***modified shear lag parameter*** for embedded PZT patch. Comparison with the corresponding governing differential equation for surface bonded patch (Sirohi and Chopra, 2000; Bhalla, 2004) reveals the presence of an additional factor of two. This implies better strain transfer as compared to surface-bonded configuration. The general solution for Eq. (4.16) can be written as,

$$\xi_E = A \cosh \Gamma_E x - B \sinh \Gamma_E x \quad (4.18)$$

where,  $A$  and  $B$  the constants to be determined from the boundary conditions. Since the PZT patch is embedded inside the concrete, hence, the shear lag ratio will be equal on the both the ends of the patch (i.e.  $\xi_E|_{x=+L_p/2} = \xi_E|_{x=-L_p/2} = (\xi_E)_{L_p/2}$ ). Further, contrary to the surface-bonded PZT patch, whose ends are stress-free, the ends of the PZT patch for CVS in the present configuration experience non-zero stress. Using Eq. (4.15) and assuming that at the ends of the patch, the stress in the beam ( $\sigma_b = E S_b$ ) will be same as the stress in the patch ( $\sigma_p = Y^E S_p$ ), we can derive that,

$$\xi_E|_{x=\pm L_p/2} = (\xi_E)_{L_p/2} = \left( 1 - \frac{E}{Y^E} \right) \quad (4.19)$$

Now, substituting the above equation in Eq. (4.18), we get

$$\text{At } x=+L_p/2; \quad (\xi_E)_{L_p/2} = A \cosh(\Gamma_E L_p / 2) - B \sinh(\Gamma_E L_p / 2) \quad (4.20)$$

$$\text{At } x=-L_p/2; \quad (\xi_E)_{L_p/2} = A \cosh(\Gamma_E L_p / 2) + B \sinh(\Gamma_E L_p / 2) \quad (4.21)$$

Solving Eqs. (4.20) and (4.21) for constants  $A$  and  $B$ , we get

$$A = \frac{(\xi_E)_{L_p/2}}{\cosh(\Gamma_E L_p / 2)} \text{ and } B = 0 \quad (4.22)$$

Substituting the values of constants  $A$  and  $B$  in Eq. (4.18), we get

$$\xi_E = (\xi_E)_{L_p/2} \frac{\cosh \Gamma_E x}{\cosh(\Gamma_E L_p / 2)} \quad (4.23)$$

Also, from Eqs. (4.15) and (4.23), the PZT patch to beam strain ratio can be derived as

$$\frac{S_p}{S_b} = 1 - (\xi_E)_{L_p/2} \frac{\cosh \Gamma_E x}{\cosh(\Gamma_E L_p / 2)} \quad (4.24)$$

In order to lump the overall effect of the shear lag into a single term, the effective/equivalent length  $(l_{eff})_E$  of the embedded PZT patch can now be derived as defined by Sirohi and Chopra (2000). It is that length which possesses a constant strain, equal to  $S_b$  (the strain on the beam surface), such that the patch produces the same voltage output as that of the same PZT patch with actual strain distribution. It is mathematically given by the area under the curve between  $(S_p/S_b)$  and  $(x/L_p)$  for half length of the patch, that is,

$$(l_{eff})_E = \int_{x=0}^{x=L_p/2} (S_p/S_b) dx \quad (4.25)$$

Substituting Eq. (4.24) into Eq. (4.25) and upon integrating, we can derive effective length fraction  $(X_{eff})_E$  for embedded PZT patch as

$$(X_{eff})_E = \frac{(l_{eff})_E}{L_p/2} = 1 - (\xi_E)_{L_p/2} \frac{\tanh(\Gamma_E L_p / 2)}{(\Gamma_E L_p / 2)} \quad (4.26)$$

The voltage  $(V_p^S)_E$  generated by the PZT patch embedded in the concrete beam, duly considering the effect of shear lag and Poisson's ratio and ignoring the mechanical and dielectric loss (which were shown to be negligible in Chapter 3), can be expressed as (Sirohi and Chopra, 2000)

$$(V_p^S)_E = K_p (K_b)_E S_q^* (S_1)_E \quad (4.27)$$

where,  $(S_1)_E$  denotes the longitudinal strain developed in the beam at the level of the embedded PZT patch,  $(K_b)_E$  the correction factor to take care of the shear lag effect in the bond layer,  $K_p$  the correction factor due to Poisson's effect and  $S_q^*$  the circuit sensitivity, representing the output voltage per unit strain input.  $K_p$ ,  $(K_b)_E$  and  $S_q^*$  are given by (Sirohi and Chopra, 2000),

$$K_p = \left(1 - \nu \frac{d_{31}}{d_{32}}\right) \quad (4.28)$$

$$(K_b)_E = (X_{eff})_E (Y_{eff})_E \quad (4.29)$$

$$S_q^* = \frac{d_{31} h Y^E}{\varepsilon_{33}^T} \quad (4.30)$$

where,  $\nu$  is the Poisson's ratio of the host structure material and  $d_{31}=d_{32}$  for the PZT patch used in the present set of experiments.  $(X_{eff})_E$  and  $(Y_{eff})_E$  are the effective length and width fractions for the embedded PZT patch, respectively, along length and width as expressed by Eq. (4.26), as in the case of the surface-bonded patch (Chapter 3). It may be noted that the value of  $(K_b)_E$  is independent of the material properties of the sensor, and is dependent only on its geometry and the properties of the adhesive layer. Ignoring the shear lag effect along the direction of the width of the PZT patch,  $(Y_{eff})_E$  can be considered as unity. On the lines of Eqs. (3.15), (3.16), (3.17) and (3.19), we can derive

$$(S_1)_E = \frac{12d'}{L^2} u(x, t)|_{peak} \quad (4.31)$$

From Eqs. (4.27) and (4.31), following final expression can be derived for the voltage generated by the embedded PZT patch, duly considering the shear lag and Poisson's effect

$$(V_p^S)_E = \frac{12d'}{L^2} K_p (K_b)_E S_q^* u(x, t)|_{peak} \quad (4.32)$$

#### 4.2.3 Comparison of Voltage Response of Embedded and Surface-Bonded PZT Patches

The voltage generated by a PZT patch,  $(V_p^S)_E$  embedded at the centre of a life-sized RC beam, subjected to a sinusoidal concentrated load, has been compared with that generated by a surface bonded PZT patch,  $(V_p^S)_S$  (derived in Chapter 3) at same location. The parameters of the RC beam and the PZT patch / bond layer for both the embedded and the surface bonded PZT patches are listed in Tables 4.1 and 4.2, respectively. The adhesive layer is assumed to consist of two part araldite epoxy adhesive with shear modulus of elasticity of 1 GPa (Moharana and Bhalla, 2012). The values of  $K_p$  and  $S_q^*$  were considered as 0.9 and  $1.977 \times 10^5$  V in accordance with Tables 4.1 and 4.2. The amplitude  $u(x, t)|_{peak}$  was computed in accordance with Eq. (4.1), considering damping ( $\zeta$ ) of 1.7% (determined experimentally using half-power band width method as explained in Chapter 7). The comparison of the voltage generated by the embedded and the surface PZT patches incorporating the effect of the mechanical, the dielectric and the shear lag loss determined theoretically with varying forcing frequency is shown in Figure 4.4. It may be noted that the values of  $\eta$  and  $\delta$  are so small that there is not much variation in the absolute values of the voltages,  $V_p^M$  and  $V_p^D$  [see Eqs. (3.32) and (3.34) for the surface bonded patches and Eqs. (4.3) and (4.4) for the embedded patch], for both the embedded and the surface bonded PZT patches. For comprehensive description, refer Sections 3.3.1 and 3.3.2 of Chapter 3.

It can be observed from Figure 4.4 that the theoretical voltage generated by the surface bonded PZT patch is somewhat higher than that of the embedded CVS at the same location. The ratio of the voltage generated by embedded CVS to the surface bonded PZT

patch  $(V_p)_E / (V_p)_S$  was found to be 0.79 theoretically at the frequency of 16.5 Hz, where peak is observed.

**Table 4.1:** Properties of RC beam.

Property	Unit	Value
Length, $L$	m	4.0
Cross-section, $D \times b$	$\text{m}^2$	$0.210 \times 0.160$
Density, $\rho$	$\text{kg}/\text{m}^3$	2500
Characteristic strength of concrete, $f_{ck}$	$\text{N}/\text{mm}^2$	40
Characteristic strength of reinforcement, $f_y$	$\text{N}/\text{mm}^2$	415
Flexural rigidity modulus (based on $f_{ck}$ ), $EI$	$\text{N}\cdot\text{m}^2$	$3.90 \times 10^6$
Mass per unit length, $\bar{m}$	$\text{kg}/\text{m}$	84
Ultimate load carrying capacity, $M_u$	kN-m	10.86
Poison's ratio of beam, $\nu$		0.20

**Table 4.2:** Properties of PZT patch (PI Ceramic, 2014) and bond layer.

Property	Unit	Value	
PZT Size, $L_p \times w_p$	$\text{m}^2$	$0.010 \times 0.010$	
Thickness, $h$	m	$3.000 \times 10^{-4}$	
Piezoelectric Strain Coefficient, $d_{31}$	$\text{m}/\text{V}$	$-2.100 \times 10^{-10}$	
Young's Modulus, $Y^E$	$\text{N}/\text{m}^2$	$6.667 \times 10^{10}$	
Compliance, $s_{11}^E$	$\text{m}^2/\text{N}$	$15.000 \times 10^{-12}$	
Electric Permittivity, $\epsilon_{33}^T$	Farad/m	$2.124 \times 10^{-8}$	
Shear modulus of elasticity of the bond layer, $G_s$	$\text{N}/\text{m}^2$	$1.0 \times 10^9$	
Depth of top of bond layer from the beam top surface, $t_c$	m	$6.0 \times 10^{-3}$	
Thickness of bond layer, $t_s$	Embedded CVS	$\text{m}$	$25 \times 10^{-4}$
	Surface Bonded PZT patch		
Shear lag parameter, $\Gamma$	Embedded CVS	$(\text{m}^{-1})$	365.305
	Surface Bonded PZT patch		
Effective length fraction, $X_{eff}$	Embedded CVS		0.637
	Surface Bonded PZT patch		

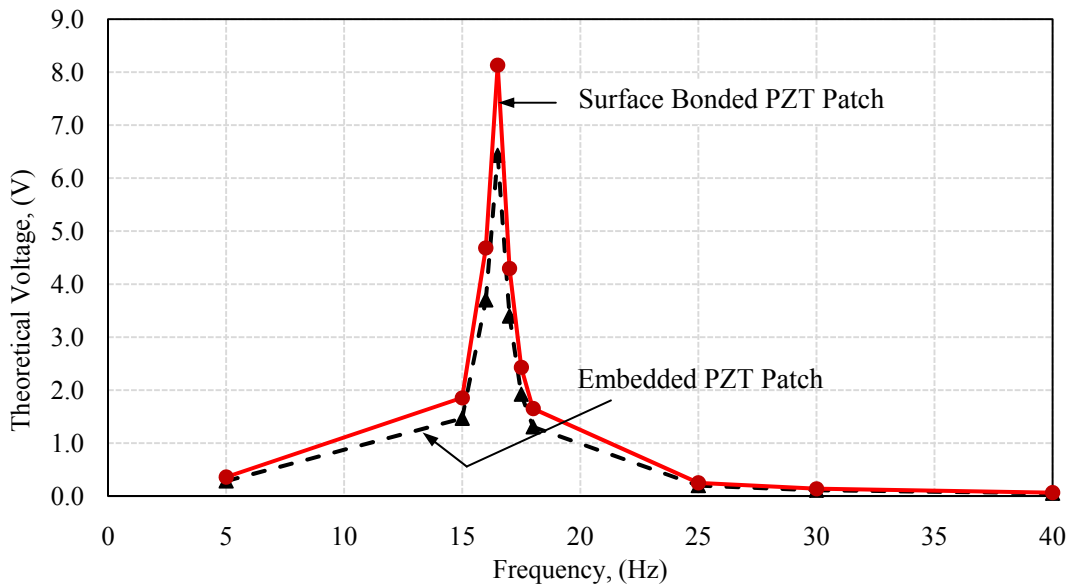


**Figure 4.4:** Theoretical comparison of voltage generated by embedded and surface PZT patch considering mechanical, dielectric and shear lag loss.

### 4.3 COMPARISON WITH EXPERIMENT

For comparison with the voltage obtained experimentally, a simply supported real-life sized (4 m long) RC beam, with properties as listed in Table 4.2, was chosen as the experimental host structure. The concrete of the beam confirmed to a self-compacting M40 grade with 30% fly ash. Ultimate load carrying capacity of the beam was determined to be 9.65 kN. Appendix B may be referred for the design calculations for the ultimate load carrying capacity,  $P_{\max}$  and the moment carrying capacity,  $M_u$ , of the beam. The RC beam is shown in Figure 4.5 (a) before casting and (b) during casting.

The schematic diagram of the beam showing the reinforcement and the location of the embedded CVS is shown in Figure 4.6. The beam consisted of two layers of 19 CVS each at top and bottom, flushing with the surface.

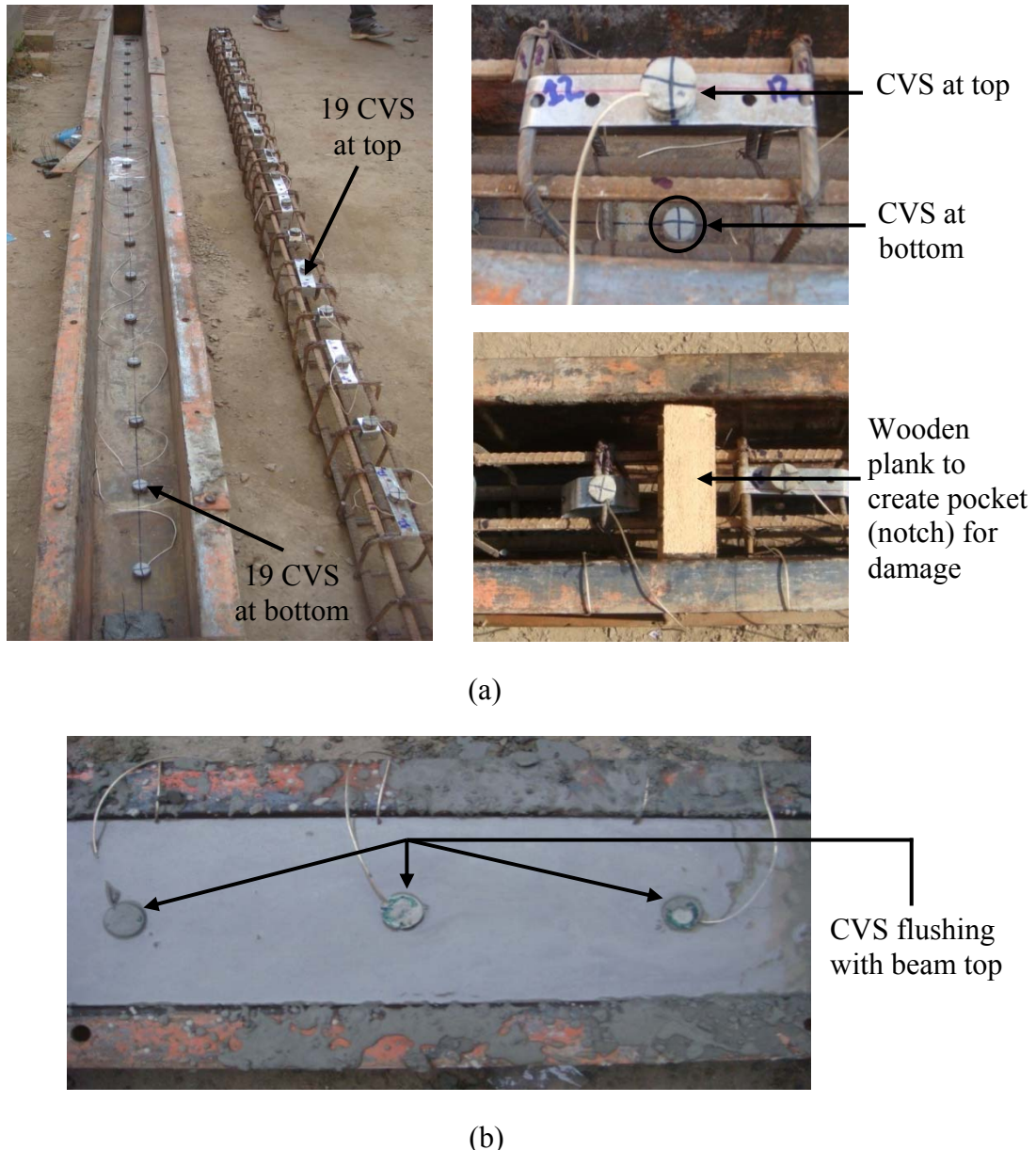


**Figure 4.5:** RC beam (a) before casting and (b) during casting.

The complete experimental set-up under excitation is shown in Figure 4.7. In addition to the CVS, three PZT patches were surface bonded on the top of the beam, first one at the centre (just above CVS 10) and other two at an offset of 195 mm to left and right each (above CVS 9 and CVS 11, respectively, see Figure 4.7). The thickness of the bond layer for the surface bonded PZT patches was maintained equal to 150  $\mu\text{m}$  with the help of two optical fibers while bonding the patch on the beam surface, as done earlier by Bhalla and

Soh (2004b). The top and the bottom thickness of the adhesive layer in the embedded CVS were found to 0.671 mm and 3.411 mm (Figure 4.2). For simplification, the average experimental thickness of the top and bottom adhesive layer was assumed equal (2.0 mm) on either side of the PZT patch. The beam was excited using LDS V406 series portable dynamic shaker. A function generator (Agilent 33210A) was used to generate an electrical signal, which was amplified by a power amplifier (LDS PA500L) and transmitted to the shaker, which converted the signal into mechanical force. Pure harmonic signal (sinusoidal in nature) was applied to the structure via the function generator. Sinusoidal signals, with different monotonic frequencies, at an excitation level of 5 V, were applied during the experiment. The output voltage across the PZT patches was measured using TDS 2004C oscilloscope (Tektronix, 2014).

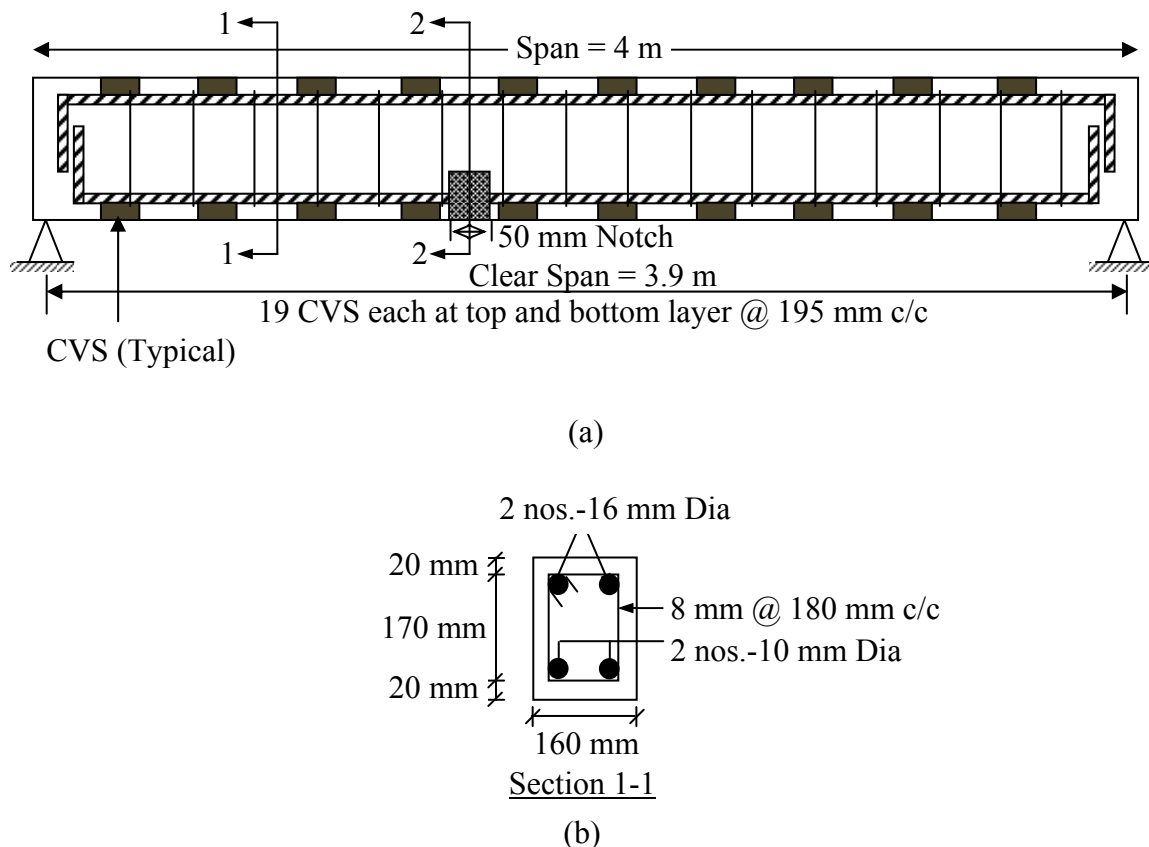


**Figure 4.6:** (a) RC beam showing reinforcement, embedded CVS and notch for damage.  
(b) Detail of reinforcement (cross-section) (*refer Figure 7.1 for Section 2-2*).

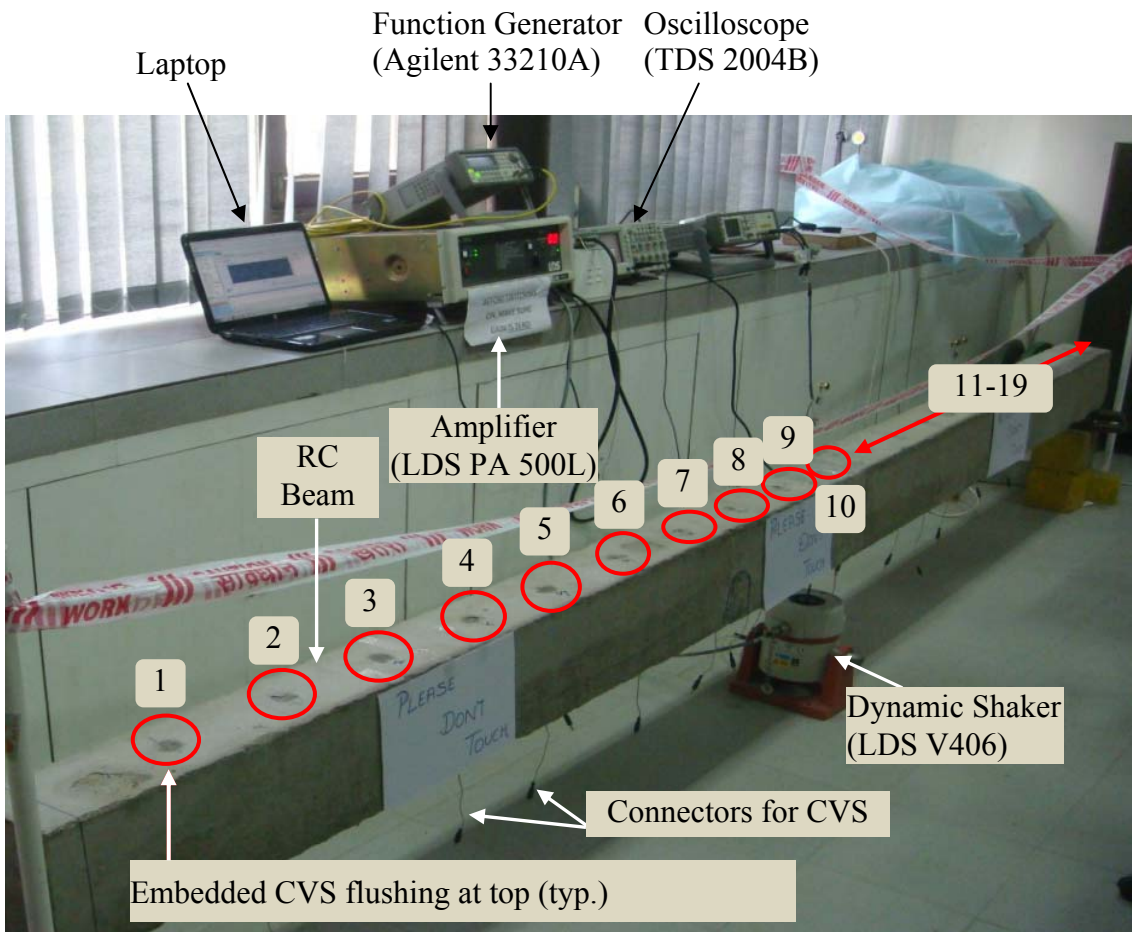


**Figure 4.7:** Complete experimental set up with CVS location.

In the initial stage, the experiments were conducted using contact type dynamic shaker (LDS V406), with the arrangement shown in Figure 4.8(a). However, due to the limitation of force the generated by the contact type arrangement, it was converted into inertial-type shaker using a simple rearrangement [Figure 4.8(b)], with the help of four springs and cover plates. The schematic diagram of the inertial-type shaker is shown in Figure 4.8(c)-(e) with all the essential details. The bottom and the mid plates were connected using four 16 mm diameter bolts to facilitate secure connection with the RC beam and also to allow the movement of the shaker along the length of the beam, whenever needed.

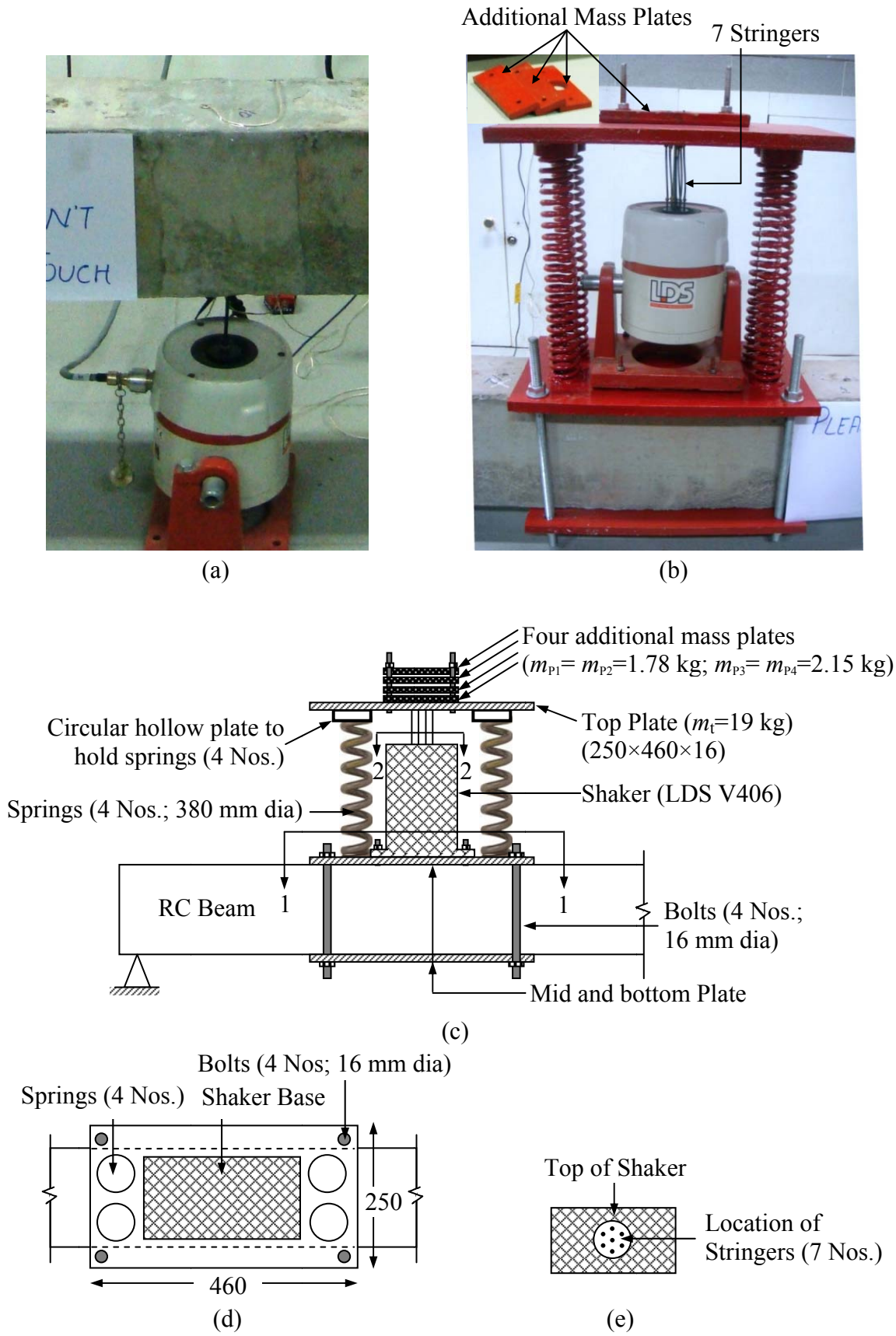


**Figure 4.8:** (a) Contact type shaker; (b) inertial-type Shaker; schematic diagram of inertial-type shaker showing (c) elevation; (d) View 1-1 and (e) View 2-2 (all dimensions in 'mm').

In arrangement explained above, the mechanical force generated by the LDSV406 shaker was transferred to the top plate via the seven stringers, as shown in Figure 4.8(e). The inertial force generated by the vibration of the top plate and the additional plates (which acted as the inertial mass) was finally transferred to the beam via the four springs. The detailed design calculations for the stiffness of the springs used in the inertial-type shaker are covered in Appendix C. The main advantage of this arrangement is that the force transmission can be controlled by varying the number of the additional mass plates at the top. The force generated was experimentally quantified by measuring the acceleration of the top plate of the shaker and multiplying it with the total mass of the top plates. In the present study, the force measured by an accelerometer attached at the top plate of inertial-type shaker was 75 N. The inertial shaker arrangement is capable of exerting force in excess of 110 N, much higher than the contact type shaker (refer Pal, 2013 for further details).

The output voltages generated by the surface bonded PZT patches and the embedded CVS were compared in four different cases illustrated in detail in Figure 4.9. These are briefly described below:

**Case (a):** Force applied by hitting an impact hammer, with the contact type shaker present [Figure 4.9(a)];

**Case (b):** Harmonic force applied by the contact type shaker, at 20 Hz frequency [Figure 4.9(b)];

**Case (c):** Force applied by inertial-type shaker, at 20 Hz frequency, [Figure 4.9(c)]; and

**Case (d):** Force applied by inertial-type shaker, with the frequency sweeping from 5 Hz to 70 Hz, within a duration of 4 seconds [Figure 4.9(d)].

For better understanding of the type of the signal applied and the voltage output observed in the sensors for above mentioned four cases, the typical overlapped voltage plots for the surface bonded and the embedded CVS at location 11 varying with time are shown in Figure 4.9 itself for all the four cases described above. The nature of the voltage signal clearly depicts the type of the force applied on the concrete beam. Various sets of readings were recorded for the above mentioned four cases. The voltages generated by the embedded CVS and the surface bonded sensors along with the average of the ratio  $(V_p)_E / (V_p)_S$  for the four cases and their subsequent sets of readings are listed in Table 4.3. For case (a), the voltage readings were recorded for both the surface bonded and the embedded sensors at location 9, 10 and 11, with the hammer hitting the beam at locations 1, 8, 12 and 19 (Refer Figure 4.7). The ratio  $(V_p)_E / (V_p)_S$  was experimentally determined and averaged for the four sets of readings. On the similar lines, in rest of the three cases, two sets of readings were recorded. Unfortunately, for case (d), because of the unexpected malfunctioning of the embedded CVS at locations 9 and 10, the comparison could be possible for location 11 only. Given the rigorous nature of the experiments and consistency observed in other results, trustworthy conclusions can be drawn even in the absence of the readings of the CVS at location 9 and 10 for case (d). The ratio  $(V_p)_E / (V_p)_S$ , when averaged over all the cases, comes out to be 0.967 (against 0.79 from theoretical analysis), which strengthens the conclusions deduced by the proposed analytical model and the related observation that the voltage generated by surface bonded sensor is higher than that of the embedded CVS. However, exceptions can be observed from the table in three sets of readings. Two of these sets (with average voltage ratios 1.39 and 1.82 at locations 10 and 11 respectively) were recorded by hitting the beam with hammer [Case(a)], which not only implied inconsistency of the applied force, but

possibly caused direct compression of the embedded patch (and hence involved  $d_{33}$  effect), leading to somewhat higher voltage.

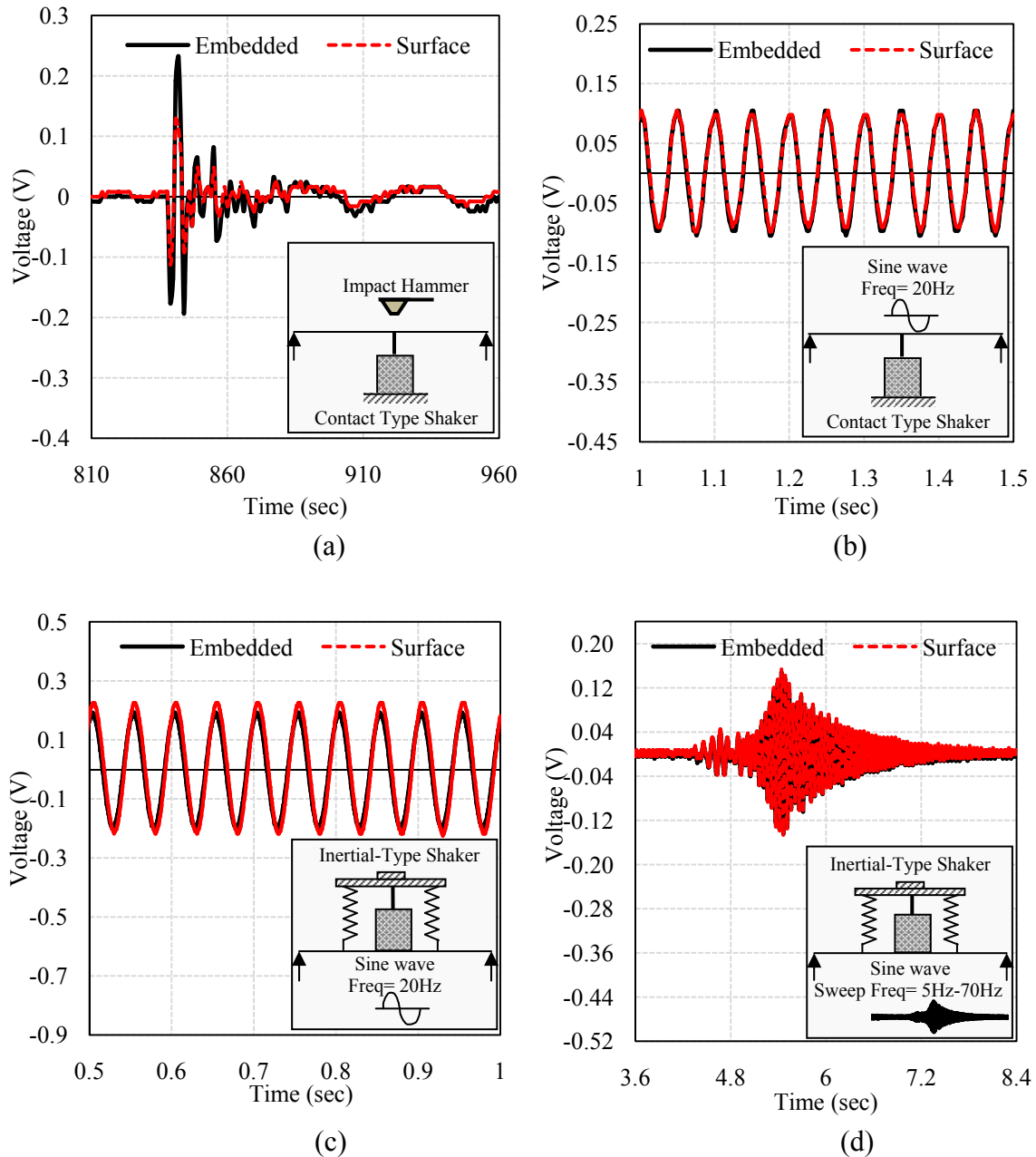


**Figure 4.9:** Voltage generated by surface bonded and embedded CVS at location 11 varying with time for four cases namely case (a) to case (d).

**Table 4.3:** Voltage generated by surface bonded and embedded CVS for four cases.

CVS Location	Voltage (V)	Case (a)				Case (b)		Case (c)		Case (d)	
		Hit 1	Hit 8	Hit 12	Hit 19	Set 1	Set 2	Set 1	Set 2	Set 1	Set 2
9	$(V_p)_E$	0.17	0.11	0.21	0.13	0.11	0.12	0.15	0.15	--	--
	$(V_p)_S$	0.24	0.18	0.31	0.19	0.19	0.18	0.37	0.37	--	--
	$\frac{(V_p)_E}{(V_p)_S}$	0.70	0.64	0.67	0.67	0.57	0.67	0.41	0.41	--	--
	<b>Average Ratio</b>	<b>0.67</b>				<b>0.62</b>		<b>0.41</b>		--	
10	$(V_p)_E$	0.21	0.14	0.16	0.18	0.14	0.13	0.19	0.19	--	--
	$(V_p)_S$	0.15	0.10	0.12	0.14	0.14	0.14	0.21	0.23	--	--
	$\frac{(V_p)_E}{(V_p)_S}$	1.37	1.50	1.33	1.35	0.96	0.95	0.91	0.85	--	--
	<b>Average Ratio</b>	<b>1.39</b>				<b>0.95</b>		<b>0.88</b>		--	
11	$(V_p)_E$	0.46	0.16	0.27	0.23	1.04	0.14	0.25	0.25	0.15	0.13
	$(V_p)_S$	0.22	0.10	0.16	0.13	0.98	0.13	0.26	0.26	0.15	0.14
	$\frac{(V_p)_E}{(V_p)_S}$	2.11	1.67	1.70	1.81	1.06	1.05	0.94	0.94	0.96	0.89
	<b>Average Ratio</b>	<b>1.82</b>				<b>1.06</b>		<b>0.94</b>		<b>0.93</b>	

In other cases [Case (b) to (d)] shaker was used to maintain the consistency in applied force. However, an exception can be observed here too for Case (b) at location 11, where the average ratio is 1.06. The possible reason is that the proximity of the sensor to the stinger in the contact type shaker configuration, which caused direct compression of the embedded CVS. Further, the possible reasons for the experimental voltage ratio (0.967) being higher than the theoretical value (0.79) are the idealized modelling of the shear lag effect in the theoretical analysis and the non-inclusion of possible localized 3D stress

effects. In ordinary flexural vibrations of beam type members with a surface bonded or embedded PZT patch, the patch is likely to undergo strain along its length (direction "1") leading to charge development along thickness (direction 3), which is the  $d_{31}$  effect. However, under special conditions, such as in the present experimentation, where especially the embedded patch is inadvertently subjected to strain in the thickness direction (axis "3") in addition to the length, additional charge is likely to be generated. Similar phenomena has been experienced in another related study (Bhalla and Deb, 2011), which leads to the generation of somewhat higher voltage in CVS than the theoretical prediction based on  $d_{31}$  effect only. In one isolated case of shaker excitation [case (c)], somewhat lower value (0.41) can be observed from Table 4.3. Possible reason could be that the mid base plate [refer Figure 4.8(c)] of the inertial-type shaker was touching the surface bonded sensor, thereby inadvertently inducing  $d_{33}$  effect in it and thus leading to bit higher value of the voltage in the surface bonded sensor in contrast to the previous exceptions. However, in most other cases, where the sensor was far from the loading system, the voltage ratio  $(V_p)_E / (V_p)_S$  lied in the range 0.67 to 0.94, implying consistency of the observations and hence strengthening the conclusions of the analytical model. The next section extends the experimental study to evaluate the energy harvesting potential of the CVS.

#### 4.4 ENERGY HARVESTING POTENTIAL OF EMBEDDED CVS

Experiments were performed in the laboratory for harvesting and storing the energy generated by the CVS embedded in the RC beam. The experimental set-up is similar to Figure 4.7. The power measurement was done for two different locations of the concentrated dynamic loads, (a) shaker at the centre of the RC beam (b) shaker at an

offset of 600 mm from the beam centre. The PZT patch in the form of the CVS, embedded inside the RC beam just below the shaker location was considered for power measurement. Electrical signal in form of sine waves with varying frequency was generated by the function generator, then amplified by the power amplifier (PA 500L) [Figure 4.10(a)] and further propelled to dynamic shaker (LDS V406), which transformed the signal into mechanical force. The excitation frequency was varied monotonically at a step interval of 2 Hz and 5 Hz, respectively, for the shaker locations at the centre and at an offset of 600 mm from the centre. The power generated by the PZT patch was measured via the oscilloscope and the simple in-house circuit shown in Figure 4.10(b) (Kaur and Bhalla 2014a). Here, the PZT patch acts as the source of voltage generation ( $V_1$ ). The value of load resistances,  $R_1 = 494.7 \text{ k}\Omega$  and  $R_2 = 471.66 \text{ k}\Omega$ , were chosen by trial and error such that these values are close to impedance of the source, here the PZT patch, for the reasons related to impedance matching, already outlined in Chapter 3.

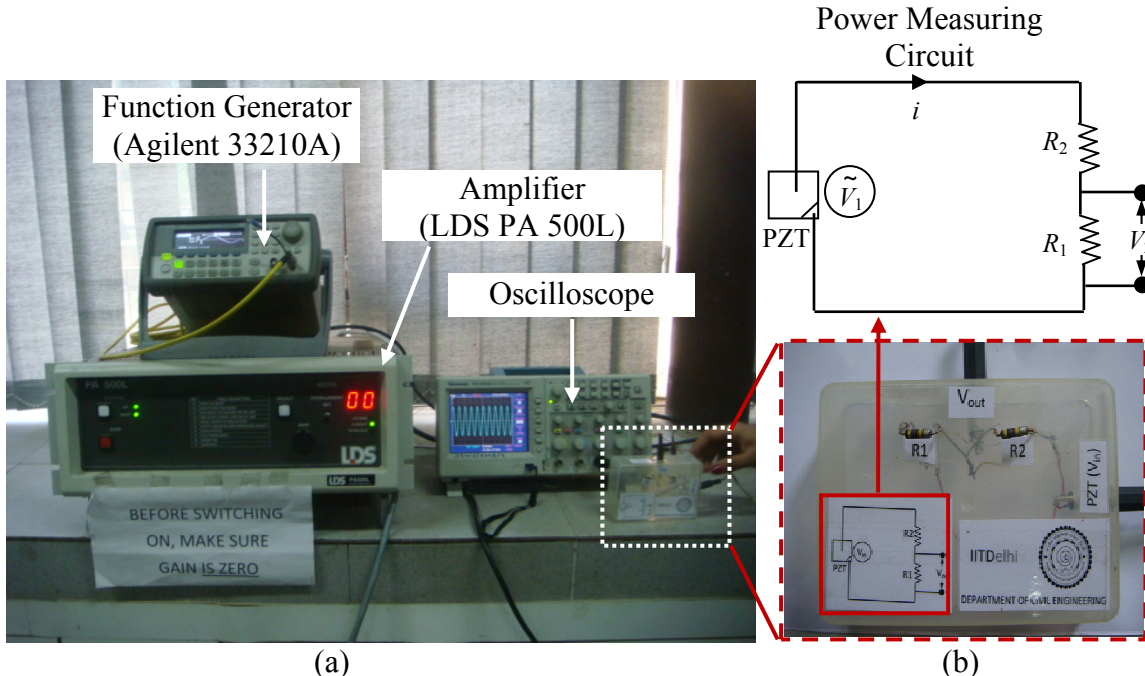


**Figure 4.10:** (a) Overall set up for power quantification.  
(b) Details of energy quantification circuit.

The variation of three different forms of power,  $P_{\text{peak}}$ ,  $P_{\text{RMS}}$  and  $P_{\text{avg}}$ , as explained in Chapter 3, with varying forcing frequency, is shown in Figure 4.11. The corresponding values are listed in Tables 4.5 and 4.6, respectively for shaker at centre and at an offset of 600 mm from centre. It can be observed that in first case (shaker at centre), maximum power (in all forms) is achieved at the first natural frequency ( $f_n = 19 \text{ Hz}$ ) of the vibrating structure (RC beam, here). In the second case (shaker at offset), maximum values are observed at an operating frequency of 20 Hz. This is due to adopting higher frequency interval (5 Hz) in latter case, resulting in missing the peak value in its close proximity. Also, it can be observed that higher modes of vibration were effectively captured (at a frequency of 75 Hz) in the latter case [Figure 4.11(b)]. This mode was missed out in the first case because the sensor location (centre of beam) was at the nodal point for second mode (Avitabile, 2001).

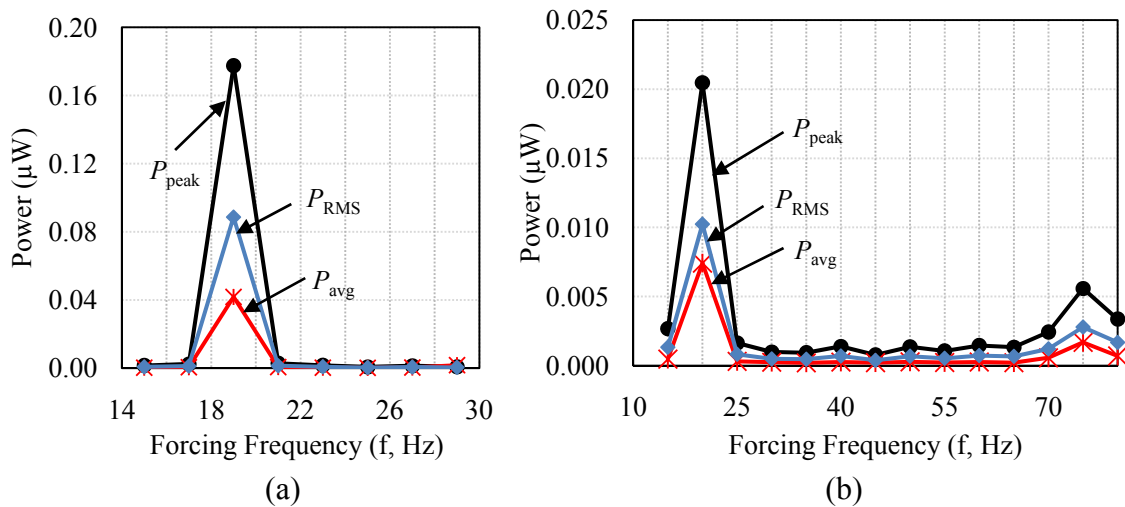


**Figure 4.11:** Variation of  $P_{\text{Peak}}$ ,  $P_{\text{RMS}}$  and  $P_{\text{avg}}$  with varying forcing frequency  
 (a) Shaker and PZT patch at centre and  
 (b) Shaker and PZT patch at an offset of 600 mm from centre.

**Table 4.4:** Experimental values of voltage, power and current for varying forcing frequencies with shaker at centre.

Freq (Hz)	Voltage (V)	Current ( $\mu\text{A}$ )		Power ( $\mu\text{W}$ )		
		$i_{\text{peak}}$	$i_{\text{RMS}}$	$P_{\text{peak}}$	$P_{\text{RMS}}$	$P_{\text{avg}}$
15	0.02	0.040	0.029	0.002	0.0003	0.001
17	0.025	0.051	0.036	0.002	0.0006	0.001
<b>19</b>	<b>0.212</b>	<b>0.429</b>	<b>0.303</b>	<b>0.177</b>	<b>0.0418</b>	<b>0.089</b>
21	0.027	0.055	0.039	0.003	0.0007	0.001
23	0.021	0.042	0.029	0.002	0.0003	0.001
25	0.014	0.028	0.020	0.001	0.0002	0.000
27	0.019	0.038	0.027	0.001	0.0004	0.001
29	0.015	0.030	0.021	0.001	0.0018	0.0004

**Table 4.5:** Experimental values of voltage, power and current for varying forcing frequencies with shaker at an offset of 600 mm from centre.

Freq (Hz)	Voltage (V)	Current ( $\mu\text{A}$ )		Power ( $\mu\text{W}$ )		
		$i_{\text{peak}}$	$i_{\text{RMS}}$	$P_{\text{peak}}$	$P_{\text{RMS}}$	$P_{\text{avg}}$
15	0.026	0.053	0.037	0.0027	0.0005	0.0013
<b>20</b>	<b>0.072</b>	<b>0.146</b>	<b>0.103</b>	<b>0.0205</b>	<b>0.0074</b>	<b>0.0102</b>
25	0.020	0.041	0.029	0.0016	0.0003	0.0008
30	0.016	0.032	0.023	0.0010	0.0002	0.0005
35	0.015	0.031	0.022	0.0009	0.0002	0.0005
40	0.019	0.038	0.027	0.0014	0.0003	0.0007
45	0.014	0.028	0.020	0.0008	0.0002	0.0004
50	0.019	0.038	0.027	0.0014	0.0003	0.0007
55	0.016	0.033	0.023	0.0011	0.0002	0.0005
60	0.019	0.039	0.027	0.0015	0.0003	0.0007
65	0.018	0.037	0.026	0.0013	0.0002	0.0007
70	0.025	0.050	0.035	0.0024	0.0006	0.0012
75	0.038	0.076	0.054	0.0056	0.0017	0.0028
80	0.029	0.059	0.042	0.0034	0.0007	0.0017

From Tables 4.4 and 4.5, the maximum power generated by the CVS embedded in the concrete is found to be  $0.177 \mu\text{W}$  (power density=  $5.9 \mu\text{W}/\text{cm}^3$ ) and  $0.02 \mu\text{W}$  (power density=  $0.67 \mu\text{W}/\text{cm}^3$ ), respectively for the CVS located at the centre of beam [Figure 4.11(a)] and another PZT patch at an offset of 600 mm from the centre [Figure 4.11(b)]. The maximum power generated by an embedded PZT patch is thus in the microwatt

range. Also, Table 4.6 provides an idea of the power generated by the embedded CVS at different locations when the shaker was positioned at the centre of the beam and operated at the natural frequency (19 Hz) of the beam. The maximum RMS power ( $0.09 \mu\text{W}$ ) was found to be at the centre of the beam corresponding to the CVS at location 11. As expected, the power drops as we move away from the centre of the beam towards the support. The normalized value of the power with respect to acceleration was computed to be  $0.027 \mu\text{W}/\text{ms}^{-2}$ , against  $0.046 \mu\text{W}/\text{ms}^{-2}$ , which was observed for the experimental steel beam with surface bonded PZT patch (Chapter 3). Although the power yield is lower than from typical steel structures, the results confirm that a CVS sensor embedded in RC structures possesses the potential for energy harvesting suitable for low power electronics. The embedded CVS has additional advantages that the sensor is unobtrusively encased inside the concrete and well protected against environmental degradation, thereby ensuring maintenance free operation and higher longevity. In addition, being packaged sensor, its installation is relatively simpler than surface bonded sensors, which requires a certain skill level from the user.

**Table 4.6:** Power generated by the embedded CVS at different locations when the shaker was positioned at centre of the beam.

CVS location	Power ( $\mu\text{W}$ )	
	$P_{\text{peak}}$	$P_{\text{RMS}}$
1	0.0008	0.0004
2	0.0137	0.0068
3	0.0268	0.0134
5	0.0386	0.0193
6	0.1074	0.0537
<b>11</b>	<b>0.1775</b>	<b>0.0887</b>
15	0.1074	0.0537
16	0.0137	0.0068
18	0.0034	0.0017
19	0.0002	0.0001

#### **4.5 SUMMARY AND CONCLUDING REMARKS**

This chapter has presented the feasibility of energy harvesting using specially designed embedded PZT patch (CVS) operating in the axial mode. Experiments have been carried out in the laboratory environment to measure the voltage and the power generated by a PZT patch embedded in life sized RC beam. A coupled electro-mechanical model for the embedded CVS duly incorporating the losses associated with the PZT patches, especially the shear lag loss, has been derived and validated with experimental measurements. Comparison of the voltage generated by the surface bonded PZT patch and the embedded CVS has been done analytically and validated experimentally. Comparison of the power generated by the surface bonded PZT patch and the embedded CVS suggests that the CVS is capable of generating power about 60% of its counterpart bonded in a steel structure, when subjected to same order of magnitude of acceleration. With the ongoing developments in electronics, as lesser power consuming circuits are emerging, it is believed that the energy scavenging time will drastically come down. The findings of this chapter have been converted into two journal publications: Kaur and Bhalla (2014) and Kaur et al. (2014).

The next chapter will present the proof-of-concept laboratory demonstration of energy harvesting and structural health monitoring (SHM) using the embedded CVS. Detailed SHM of the real-life sized RC beam, considered in this Chapter 4 via embedded CVS, will be presented.

## **Chapter 5**

# **PROOF-OF-CONCEPT DEMONSTRATION OF ENERGY HARVESTING AND STRUCTURAL HEALTH MONITORING USING EMBEDDED CVS**

### **5.1 INTRODUCTION**

This chapter presents the proof-of-concept demonstration of combined energy harvesting and SHM using the embedded CVS. Detailed SHM of the real-life sized RC beam, which was earlier considered in the Chapter 4, has been carried out via the embedded CVS. Three levels of damage, ranging from incipient to severe, have been correctly detected in the RC beam using a combination of the global vibration and the local EMI techniques under short term monitoring. Continuous long term monitoring of the strength gain and fatigue induced damage of the RC beam has also been investigated using the two techniques, commencing immediately after casting and continuing for 108 days.

### **5.2 SHORT TERM MONITORING OF REINFORCED CONCRETE (RC) BEAM USING CVS**

A comprehensive study involving SHM of the same RC beam, considered in Chapter 4 as test specimen, was carried out using embedded CVS. Controlled damage was induced by chipping off the concrete at a specific location [one third length of the beam, between CVS location 7 and 8 (refer Figure 4.6)] where a notch was created at the time of casting for controlled damage initiation (see Figure 5.1 for details). Curvature mode shape (global vibration technique) and conductance signatures (local vibration technique) of the CVS embedded in the RC beam were compared for the undamaged and the damaged states.

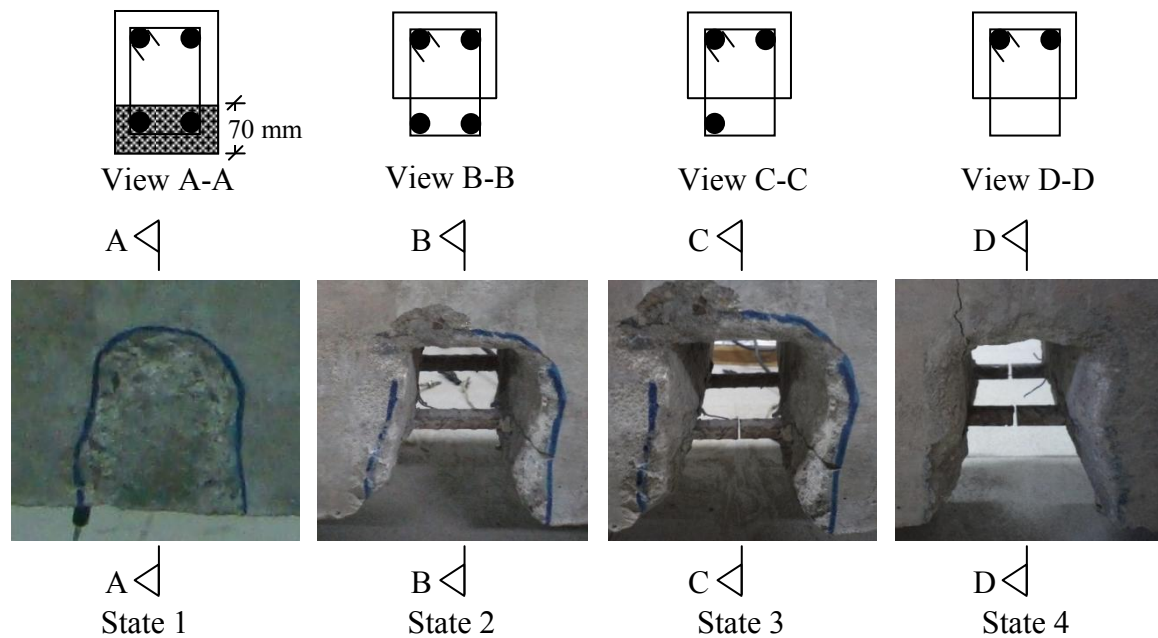


**Figure 5.1:** Cross-section and front view of the notch showing undamaged and different states of damage [see this figure in conjunction with Figure 4.5].

The damage was induced in three levels, resulting in four conditions, referred to as ‘State’ 1 to 4, as explained using Figure 5.1. Here, State 1 represents the undamaged condition. In State 2, concrete was chipped off from the notch to simulate incipient damage. For States 3 and 4, 50% and 100% of the bottom reinforcement was curtailed, respectively, so as to achieve moderate and severe damage conditions. Detailed observations of the application of the two techniques are covered in the following subsections.

### 5.2.1 Global Vibration Technique

The SHM of the beam was carried out using the global vibration technique by obtaining its curvature mode shape in the undamaged condition (State 1) and comparing it with the particular damaged state. The key feature of this approach is that the curvature mode shape is directly obtainable from the response of the PZT patches embedded near the

surface (Shanker et al., 2011). For this purpose, the PZT patches located at the top and bottom at a given section were connected in series. From fundamental of structural analysis, curvature  $C_b$  at a given point of beam can be derived as

$$C_b = (S_1 + S_2)/D \quad (5.1)$$

where  $S_1$  and  $S_2$  are the flexural strains at the top and the bottom fibres of the beam (see Figure 4.6), respectively and  $D$  is overall depth of beam. As evident from fundamentals of piezoelectricity, the voltage across PZT patch ( $V_p$ ) is proportional to the strain at the location of sensor on the beam. Hence, the combined voltage generated by the two CVS sensors (one each at top and bottom), when connected in series, can be derived as

$$V_p = S_q^*(S_1 + S_2) \quad (5.2)$$

where,  $S_q^*$  is the circuit sensitivity given by Eq. 4.30. From Eqs. (5.1) and (5.2), it can be concluded that the curvature ( $C_b$ ) of the beam at any point is proportional to the combined voltage ( $V_p$ ) generated by the PZT sensors located at the top and bottom of the beam and connected in series. The experimental set-up for obtaining the curvature mode shape is shown in Figure 5.2. Impact force was applied on the RC beam by hitting it with a wooden hammer at alternate CVS locations, the force being measured with Dytran force sensor mounted over the beam [see Figure 5.2(a)]. The voltage signal across the series connected CVS at locations 2, 4, 8,..,16 and 18 was acquired using the eight channel data logger QDA1008 (Quazar Technologies, 2014) controlled by a computer in two rounds of operation. The voltage response (frequency domain) was normalized with that of the applied force to obtain frequency response function (FRF).

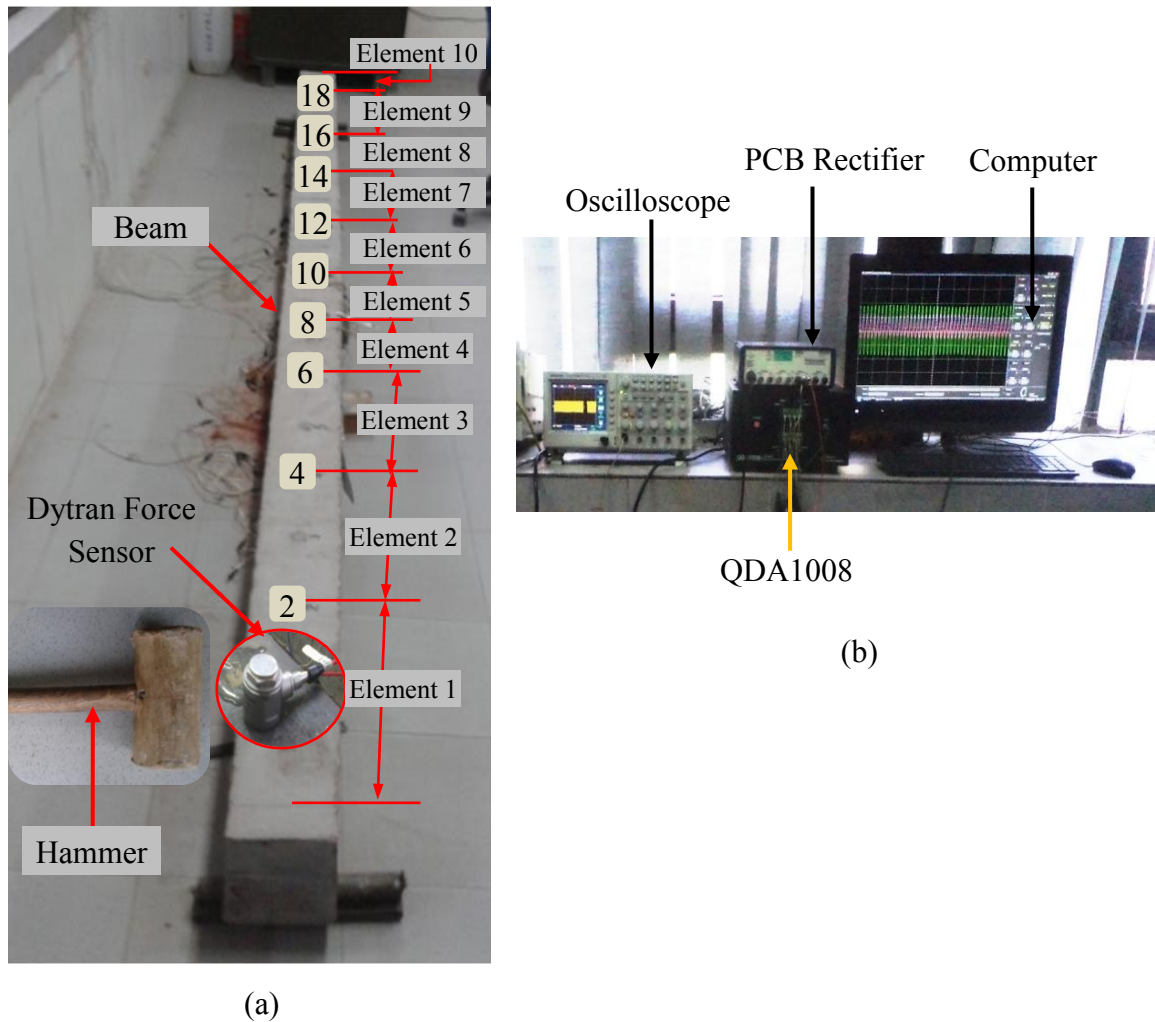


**Figure 5.2:** Experimental set-up for obtaining curvature mode shape of the RC beam showing (a) element numbers and (b) data acquisition system.

The curvature mode shapes for the undamaged and the damaged states were obtained by plotting the relative amplitudes (Pal, 2013; Shaker et al., 2011) of curvature along the length of the beam, as shown in Figure 5.3(a). The damage index for States 2 to 4 was computed for ten elements of the beam [situated between the alternate sensor locations, see Figure 5.2(a)] using the following relation (Talwar, 2011)

$$(DI)_i^j = \left| \left( \frac{(C_b)_n + (C_b)_{n+1}}{2} \right)_i^u - \left( \frac{(C_b)_n + (C_b)_{n+1}}{2} \right)_i^d \right| \quad (5.3)$$

where,  $j$  represents the damage state and  $i$  the element number between  $n^{\text{th}}$  and  $(n+2)^{\text{th}}$  sensor node location, where  $n$  varies as 2, 4, 6..,16 and 18. The variation of the damage index for the three damage states is shown in Figure 5.3(b). The damage location in this approach is identified as the element with maximum value of DI.

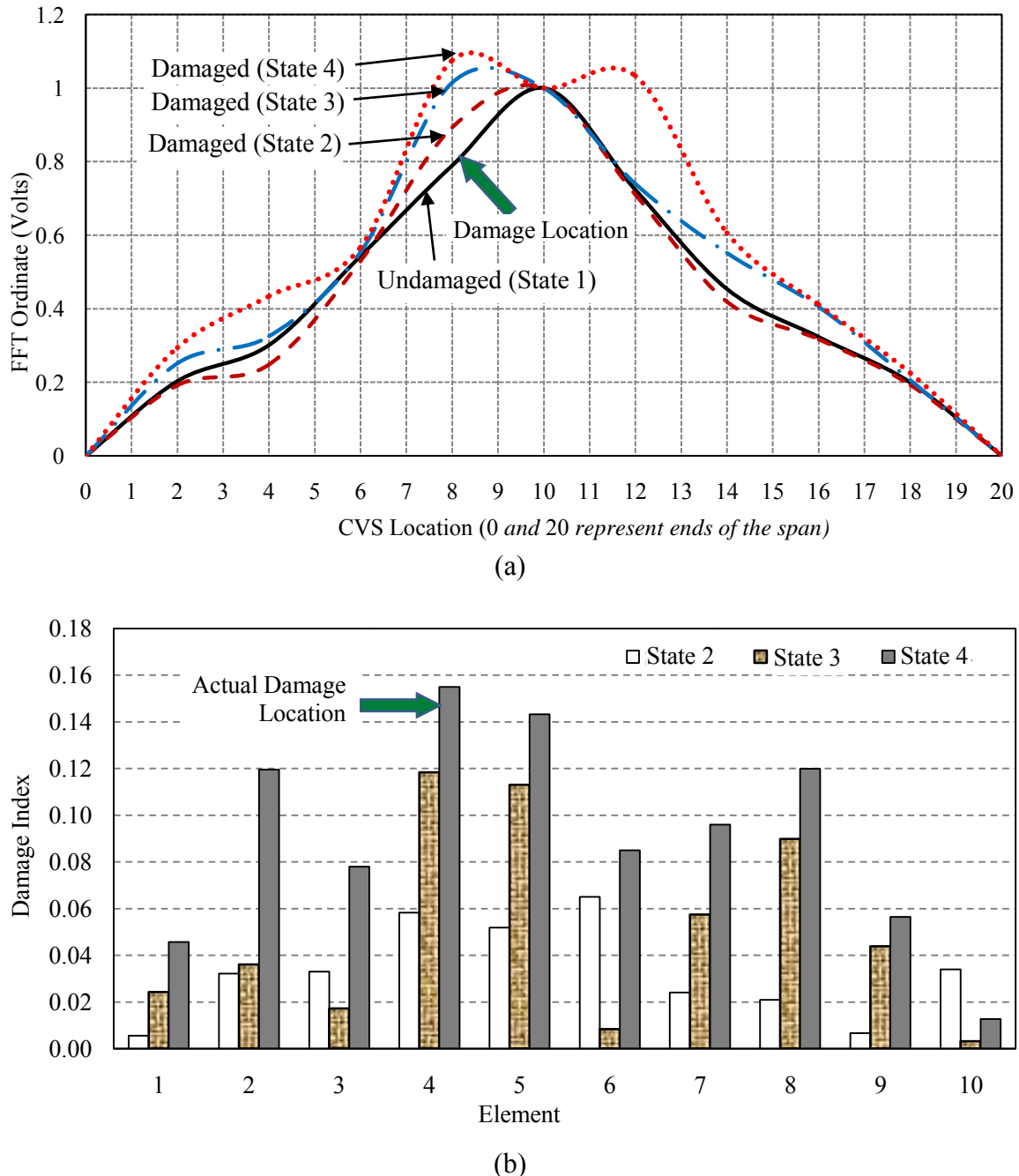


**Figure 5.3:** (a) Comparison of curvature mode shape and (b) corresponding damage index, for undamaged and three damaged states.

It can be observed from the figure that the damage has been correctly and effectively located using the CVS sensors for States 3 and 4, with maximum damage index value for the most severe damage (State 4). The error lies only with reference to State 2 (element 6 is identified as the damaged element instead of 4), in which case the level of the induced damage is incipient in nature. This is a well accepted fact for the global vibration technique (Shanker et al., 2011) and the short-coming is effectively overcome with the aid of the EMI technique, as described below.

### 5.2.2 Electro-Mechanical Impedance (EMI) Technique

The three levels of damage induced in the RC beam were also monitored via the EMI technique, which is the local vibration technique, typically operating in the high frequency (kilohertz) range. The EMI based conductance signature of the beam was acquired using the new cost effective and low power consuming miniature impedance analyzer AD5933 (Analog Devices, 2014) and verified using the conventional LCR meter, model E4980A (Agilent Technologies, 2014). The signature was acquired for all the 19 CVS located at top and the 19 at the bottom separately, using both the equipment. The experimental setup used for acquiring the EMI based conductance signature using AD5933 is shown in Figure 5.4. For the operation of AD5933, the frequency range 80-100 kHz was chosen by trial and error. The procedure for using AD5933 is based on the Shankar (2013). The calibration of the circuit was done as per manufacturer's manual (Analog Devices, 2014) before using it for the CVS sensors. The output of the circuit is in form of the real part (resistance,  $R$ ) and the imaginary (reactance,  $X$ ) part of impedance, from which the conductance ( $G$ ) value was determined as

$$G = \frac{R}{R^2 + X^2} \quad (5.4)$$



**Figure 5.4:** Experimental set-up for local EMI technique done using AD5933 (*a low-cost alternative of conventional LCR meter*).

Typical plots of the conductance for various states acquired using AD5933 and LCR meter are shown in Figures 5.5(a) and (b), respectively. Similar observations can be deduced from the both the figures with regard to the effect of the damage on conductance. Significant deviation in the conductance values can be observed even between State 1 (undamaged condition) and State 2 (incipient level of damage). As would be shown later, this facilitates clear cut identification of damage State 2, which was not correctly located using the global vibration technique, as shown in the previous sub-section. For locating the damage using the EMI technique, RMSD value was calculated for each sensor node using the following equation (Shanker, 2011)

$$RMSD(\%) = \sqrt{\frac{\sum(G_k^d - G_k^u)^2}{\sum(G_k^u)^2}} \times 100 \quad (5.5)$$

where,  $G_k^u$  denotes the undamaged conductance value and  $G_k^d$  the conductance value after damage for the  $k^{\text{th}}$  frequency. RMSD value for the  $i^{\text{th}}$  element (between  $n^{\text{th}}$  and  $(n+1)^{\text{th}}$  sensor node location) was calculated using,

$$RMSD_i = \frac{RMSD_n + RMSD_{n+1}}{2} \quad (5.6)$$

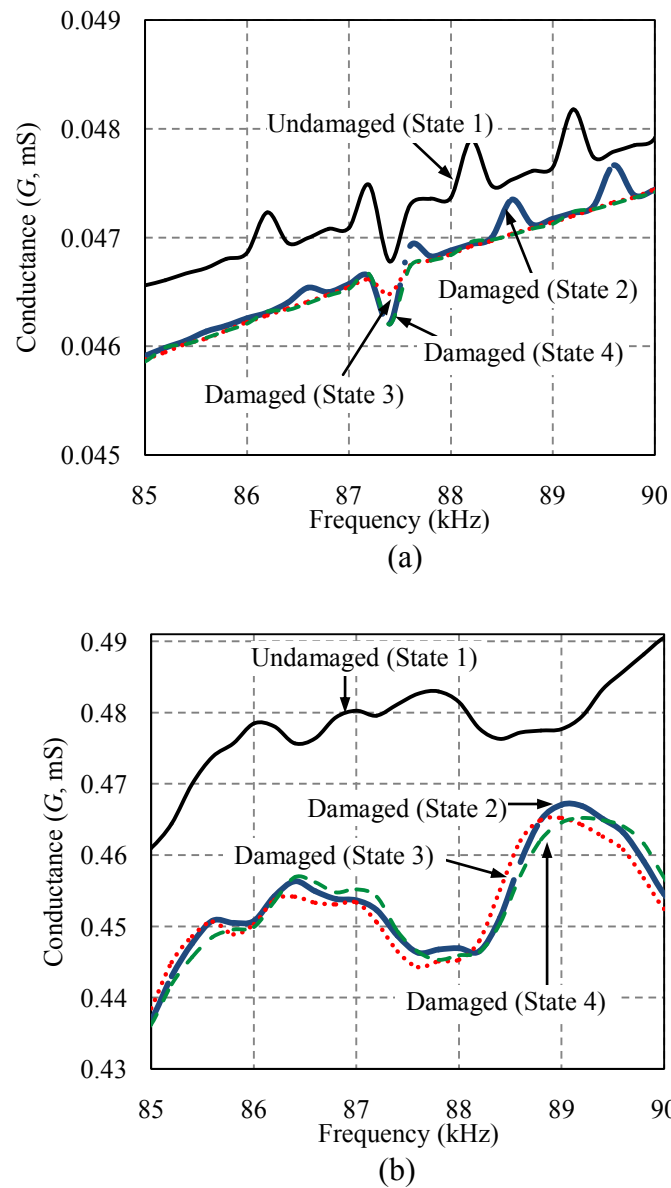


**Figure 5.5:** Comparison of typical conductance ( $G$ ) signature acquired for States 1 to 4 using (a) AD5933 and (b) LCR meter.

The RMSD values for the 20 elements of the beam corresponding to the three damage states are plotted for AD5933 and LCR meter in Figures 5.6(a) and (b), respectively. It can be observed from the figures that unlike the global vibration technique, the damage corresponding to all the three states has been effectively and correctly located. However, the difference in the magnitudes of the RMSD index corresponding to States 3 and 4 is not very high. This fact can also be well corroborated with Figure 5.5, where significant

shift in signature is observed for State 2 but not thereafter. Hence, as damage level grows from incipient to moderate, the higher levels of damage tend to became less and less distinguishable. Again, this is a well accepted fact for the EMI technique (Shanker et al., 2011) and therefore, makes a strong case for the integrated use of the global vibration and the EMI techniques.

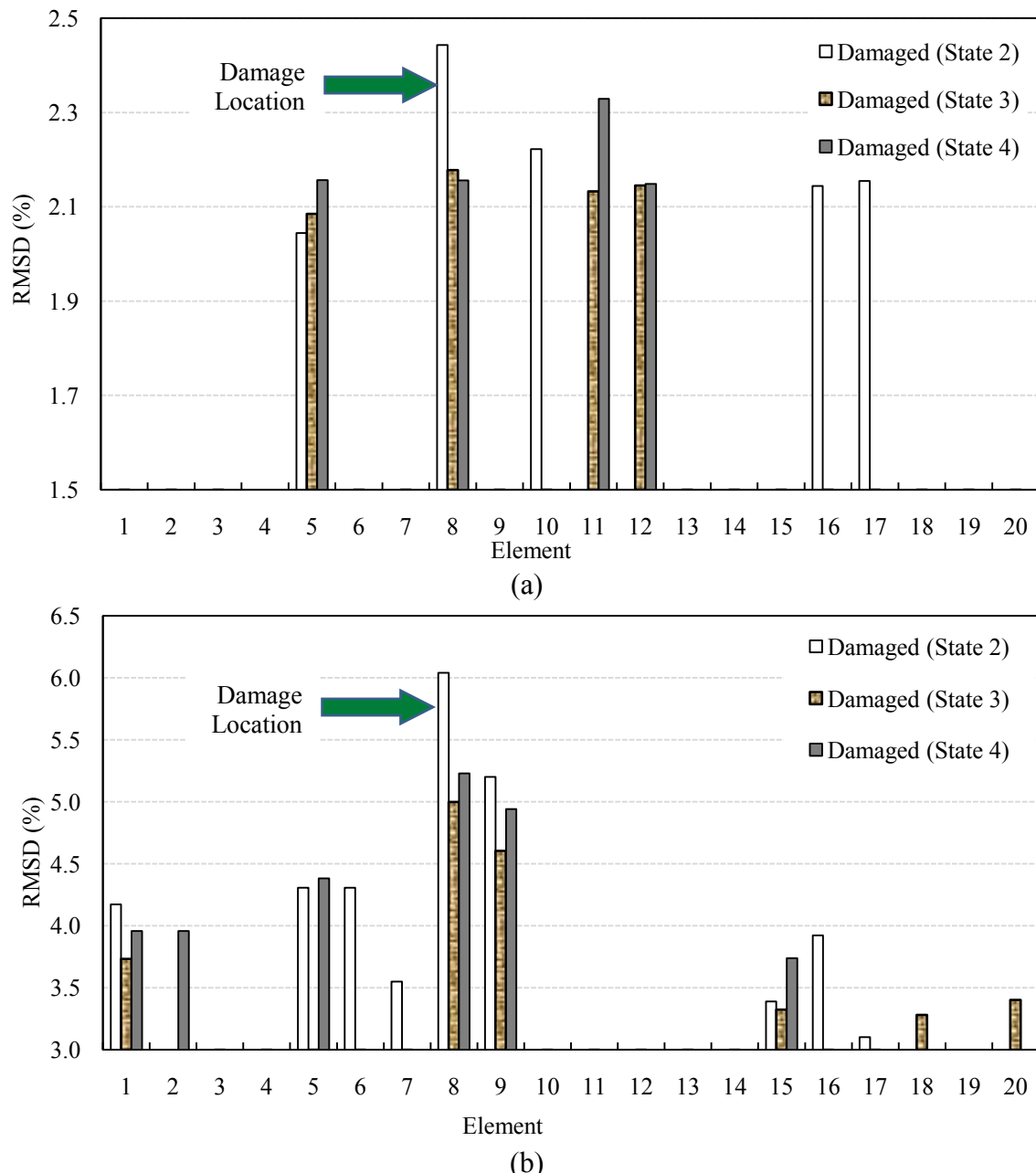


**Figure 5.6:** Variation of RMSD of conductance plots for various elements corresponding to States 2 to 4 acquired using (a) AD5933 and (b) LCR meter.

The global vibration technique could not effectively detect incipient level damage (State 2) which was easily detected by the EMI technique. Similarly, the EMI technique could not distinguish between moderate and severe damage, which was easily done by the global vibrational technique. Hence, the two techniques complement each other. The next section highlights the long-term monitoring of the RC beam subjected to sustained fatigue load using embedded CVS.

### **5.3 LONG TERM MONITORING OF RC BEAM USING EMBEDDED CVS**

Continuous long term monitoring of the *strength gain and fatigue characteristics* of the RC beam were first investigated using two techniques, namely, the global dynamic technique and the local EMI technique via the embedded CVS, commencing 14 days after casting and continuing for 108 days. This period can be divided into two intervals, I (14 to 40 days) and II (41 to 108 days). During interval-I, the shaker was operated as contact type shaker and placed underneath of the beam at the centre. It was operated in intermittent manner to determine the natural frequency of the beam and measure the peak voltage. No damage due to the operation of shaker was expected during interval-I. During interval-II, the contact type shaker was converted to inertial-type shaker. This weighed around 80 kg, was installed at the top of the beam (refer Chapter 4 and the following Section) and operated on daily basis at the natural frequency of the beam, applying  $1.368 \times 10^5$  cycles per day (overall  $9.303 \times 10^6$  cycles during interval II). The peak force exerted on the beam was measured as following subsections explain the procedures and results of both the techniques in detail.

### 5.3.1 Global Vibration Technique

In the global dynamic technique, the global characteristics, here the fundamental natural frequency and the damping ratio of the beam were monitored. These were determined by impact excitation. The Fast Fourier Transformation (FFT) amplitude of voltage readings ( $V_{FFT}$ ) against frequency for the 28<sup>th</sup> day after casting is shown in Figure 5.7. It can be observed from the figure that the experimental first fundamental frequency of the RC beam was 22.32 Hz on 28<sup>th</sup> day. The damping ratio was determined from the FFT plot using the half-power band method (Chopra, 2007), using Eq. (5.7),

$$\zeta = \frac{f_2 - f_1}{2f_n} \quad (5.7)$$

All the terms are well explained in Figure 5.7. The damping ratio was determined as 1.7%. Effect of conversion of the shaker from contact-type to inertial-type (40<sup>th</sup> day) on the natural frequency of the beam was also investigated. For this purpose, the natural frequency was measured experimentally by impact excitation when the shaker was (a) below the beam (contact type shaker) and (b) placed over the beam (inertial-type shaker). Also, in the latter configuration, both impact as well shaker based excitations were applied. The shaker applied a sweep signal with frequency sweeping from 5 Hz to 70 Hz in a duration of 4 seconds. The voltage readings were acquired for the CVS at location 11 (refer Figure 4.6) using the oscilloscope. The pictorial representation of the three cases, explained with complete experimental set-up, is shown in Figure 5.8.

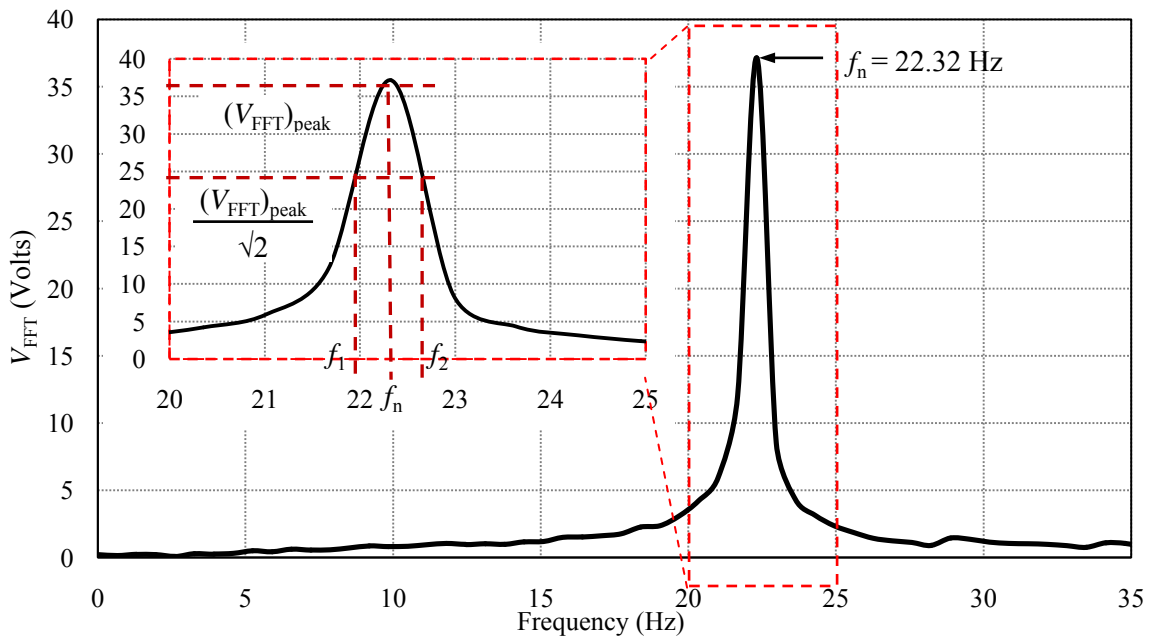


**Figure 5.7:** FFT voltage with varying frequency depicting natural frequency ( $f_n$ ) and damping of concrete beam.

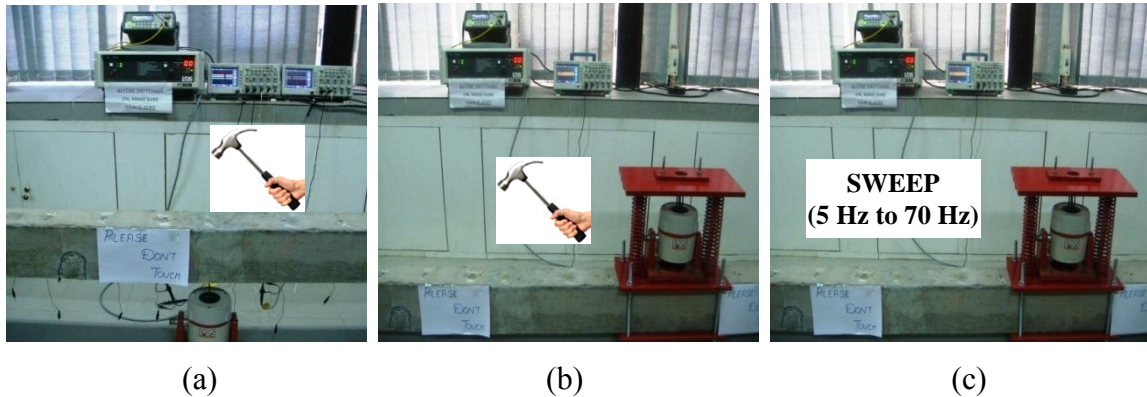


**Figure 5.8:** Three cases considered for comparing natural frequency of concrete beam,  
 (a) Contact type shaker, with impact excitation  
 (b) Inertial-type shaker, with impact excitation  
 (c) Inertial-type shaker, shaker induced sweep excitation (5 Hz to 70 Hz).

The FFT plots for the three cases are compared in Figure 5.9. In case (a), when the shaker was positioned under the beam, the natural frequency of the beam was measured to be 22.32 Hz (28<sup>th</sup> day after casting), which matched well with the theoretical value

( $f_n = 22.27$  Hz) of the first fundamental ( $n = 1$ ) natural frequency, determined with the parameters listed in Table 4.1 using the following equation (Chopra, 2007),

$$f_n = \frac{n^2 \pi}{2L^2} \sqrt{\frac{EI}{m}} \quad (5.8)$$

In case (b), when the contact type shaker was converted into an inertial-type and installed at the top of the beam, a reduction in natural frequency to  $f_n = 20.18$  Hz was observed, which can be attributed to the increase in the mass of the system due to addition of approximately 80 kg additional dead weight of the shaker system. In case (c), where a sweep signal was applied, an additional peak was observed at  $f_{sh} = 9.68$  Hz. This peak has emerged due to the resonance of the inertial-type shaker itself.

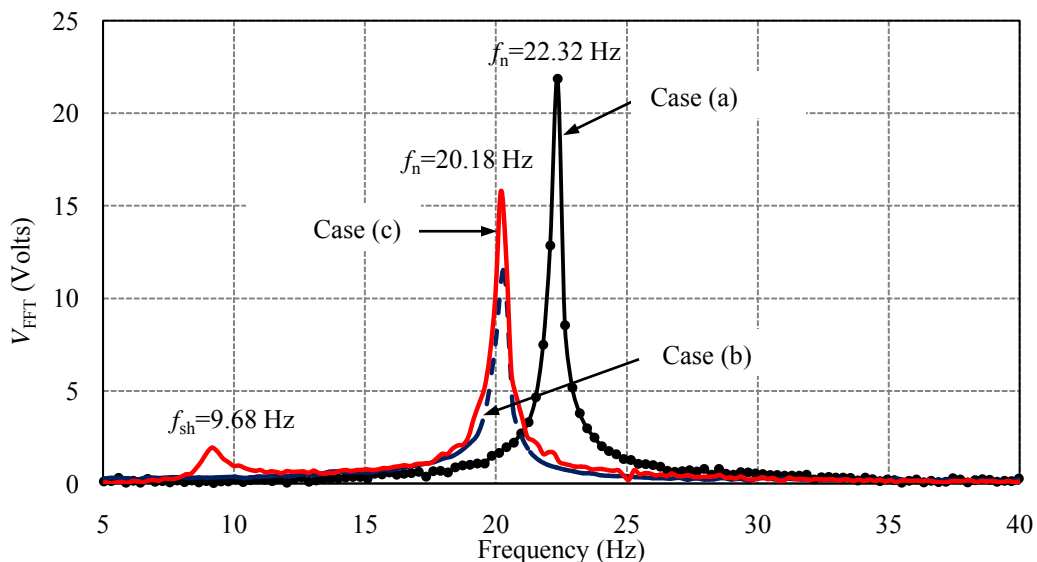
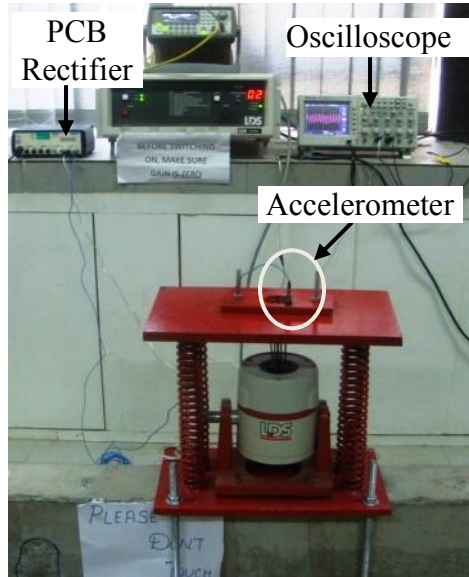
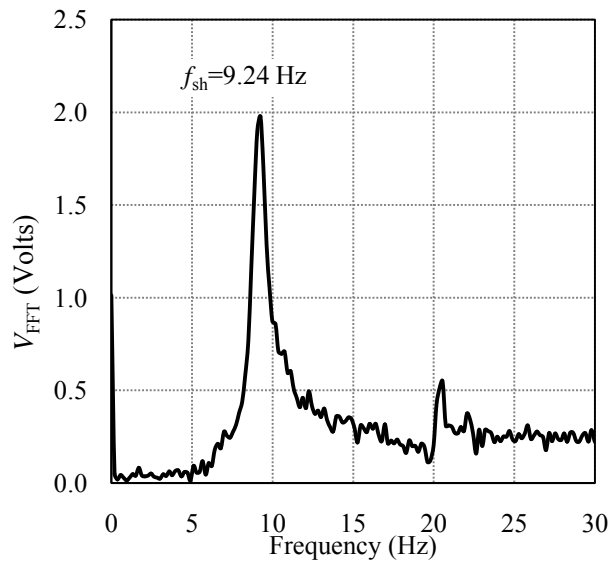


**Figure 5.9:** FFT voltage with varying frequency depicting natural frequency ( $f_n$ ) for three different cases mentioned in Figure 5.8.



(a)



(b)

**Figure 5.10:** (a) Accelerometer placed over the inertial-type shaker.  
 (b) FFT voltage for inertial-type shaker alone with varying frequency.

This outcome was further strengthened by individually measuring the natural frequency of inertial-type shaker, as shown in Figure 5.10. An accelerometer was attached on the top of the inertial-type shaker and its voltage output was measured using oscilloscope via PCB amplifier. The FFT of the voltage readings is shown in Figure 5.10(b). The occurrence of a distinct peak at a frequency of 9.24 Hz confirms the explanation that the new peak, which emerged in case (c) at 9.68 Hz (Figure 5.9), was due to the resonance of the inertial-type shaker itself at that frequency.

The variation of the natural frequency of the beam from the 20<sup>th</sup> day to the 108<sup>th</sup> day after casting at varying intervals of time is shown in Figure 5.11. It can be observed that natural frequency remained almost constant (22.32 Hz) till day 40. However, it started reducing during interval-II (day 40 to day 108) due to rigorous shaking of beam under fatigue loading, which ended up in micro structural damage in the form of micro-cracks and reduction in fatigue strength. In overall, the natural frequency reduced from 22.32 Hz on the 28<sup>th</sup> day to 16.5 Hz on the 108<sup>th</sup> day.

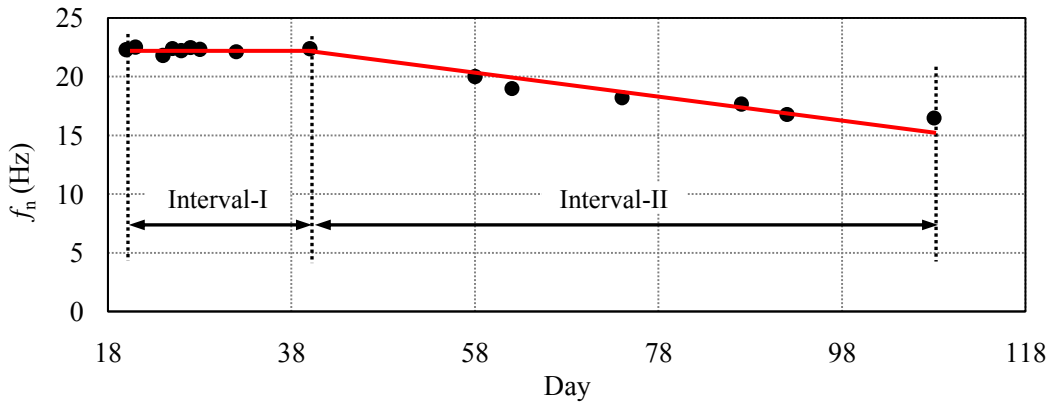


**Figure 5.11:** Variation of natural frequency with increasing number of days.

### 5.3.2 Electro-Mechanical Impedance (EMI) Technique

For the EMI technique, the equivalent stiffness of the beam was determined from admittance signatures of the typical CVS (here, at location 16). The equivalent stiffness is based on the experimentally observed trend of the real and the imaginary components of the mechanical impedance,  $x'$  and  $y'$ , respectively, extracted from the EMI signature. The experimental set-up shown in Figure 5.12 was employed to acquire the raw admittance signatures (conductance and susceptance) of the CVS at any random location (16, here) using the LCR meter for a frequency range of 50 kHz to 250 kHz, at an excitation voltage of 1 V (RMS). The equivalent stiffness was determined from the signatures of the CVS using the computational procedure outlined by Bhalla et al. (2012) and Talakokula et al. (2014). A close examination of the extracted impedance components in the frequency range 50-150 kHz suggested that the system behaviour was similar to a *Kelvin-Voigt* system [parallel spring-damper ( $k-c$ ) combination] for which

$$x' = c \quad \text{and} \quad y' = -\frac{k}{\omega} \quad (5.9)$$

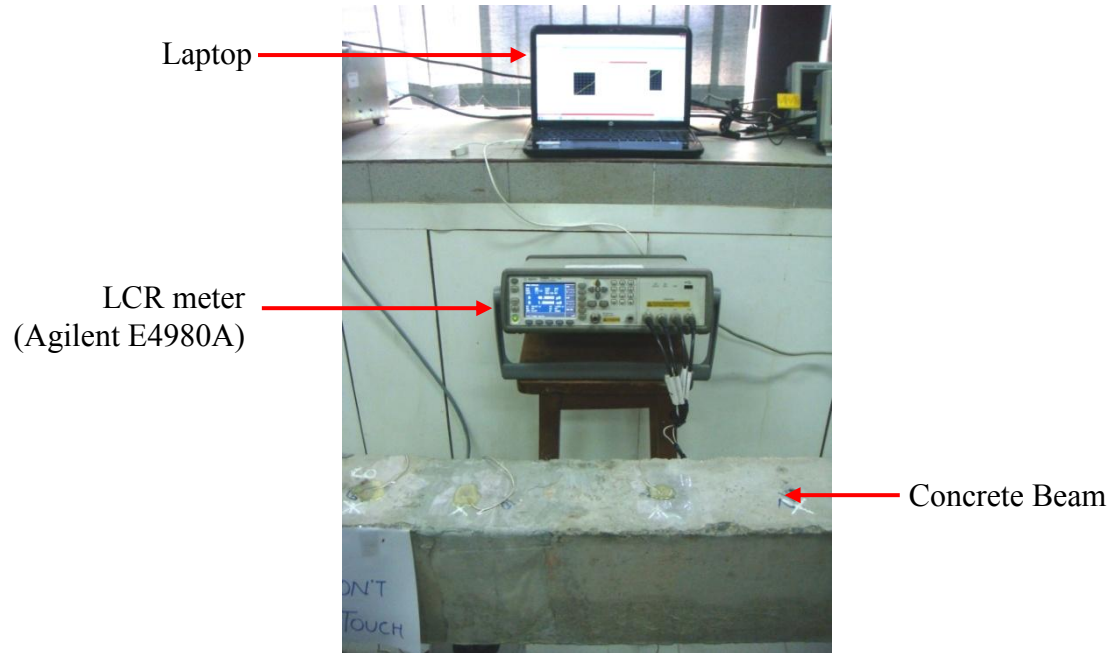


**Figure 5.12:** Experimental set-up for acquiring EMI signatures of embedded CVS.

Using Eq. (5.9) and the actual impedance plots, the average “equivalent” system parameters were worked as:  $c = 35 \text{ Ns/m}$  and  $k = 21.16 \text{ kN/m}$  for the 6<sup>th</sup> day after casting of the RC beam. The analytical plots of  $x'$  and  $y'$  obtained by these equivalent parameters match well with their experimental counterparts, as shown in Figure 5.13. Long term monitoring of the equivalent stiffness ( $k$ ) was done for the beam from the 6<sup>th</sup> day to 108<sup>th</sup> day after the casting. Initial period from day 6 to day 14 was designated as ‘curing period’. No external excitation was applied on the beam during this period. The equivalent stiffness exhibited an increasing trend, as observed from Figure 5.14(a) during the curing period, which is consistent with the expected increase of the physical stiffness. After this curing period, the equivalent stiffness became constant over the interval-I (day 14 to day 40) as can be observed from Figure 5.14 (b). During Interval II (day 40 to day 108), the equivalent stiffness parameter started exhibiting similar behaviour (reducing trend) as exhibited by the natural frequency (Figure 5.11). Rigorous shaking of beam

under fatigue loading ended up in micro structural damage in the form of micro-cracks and reduction in fatigue strength, which has been well captured by the reduction in the equivalent stiffness, identified using the embedded CVS. This is the first of its kind proof-of-concept application of the equivalent stiffness concept for monitoring fatigue in RC structures using the embedded PZT patch.

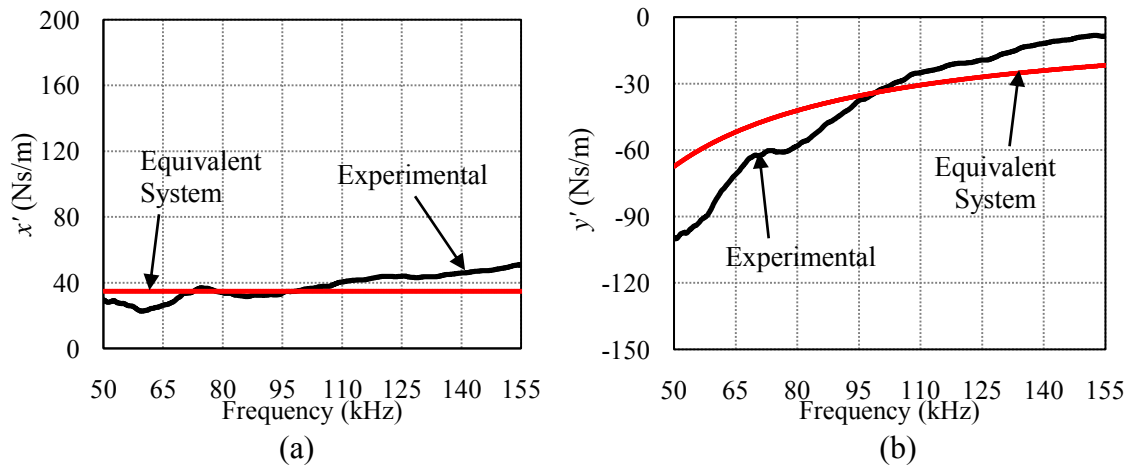


**Figure 5.13:** The equivalent system plots of (a) real part ( $x'$ ) and (b) imaginary part ( $y'$ ) of mechanical impedance for a parallel spring-damper combination varying with frequency.

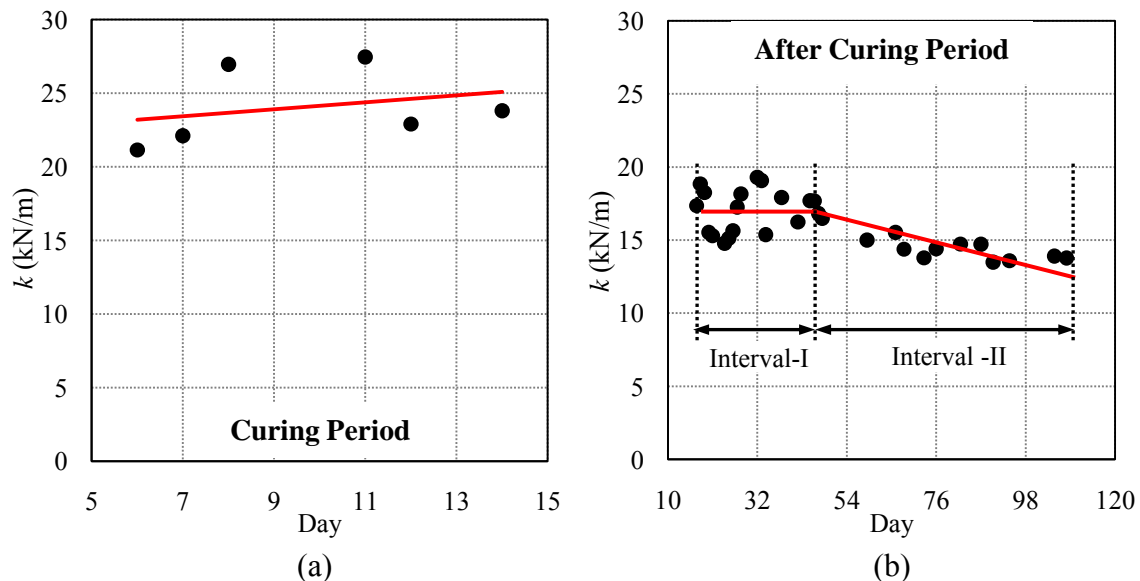


**Figure 5.14:** Variation of equivalent stiffness with increasing number of days for (a) curing period and (b) after curing period.

It should be mentioned here that there were temperature fluctuations during the experiment spanning over 108 days. The properties of the PZT materials are very much sensitive to temperature. The equivalent stiffness ( $k$ ) of the beam was updated by considering the updated value of electric permittivity ( $\epsilon_{33}^T$ ), incorporating the effect of temperature. Figure 5.15 shows the trend of ' $k$ ' with and without temperature compensation. The higher absolute value of the equivalent stiffness after incorporating temperature effects, confirms the fact that the effect of temperature should not be neglected during SHM applications. In overall, the equivalent stiffness underwent about 50% reduction on account of  $9.303 \times 10^6$  cycles. Hence, temperature effects must be taken into consideration while using PZT parameters for determining the equivalent stiffness of the concrete beam. The detailed procedure of applying temperature compensation is explained in Appendix D.

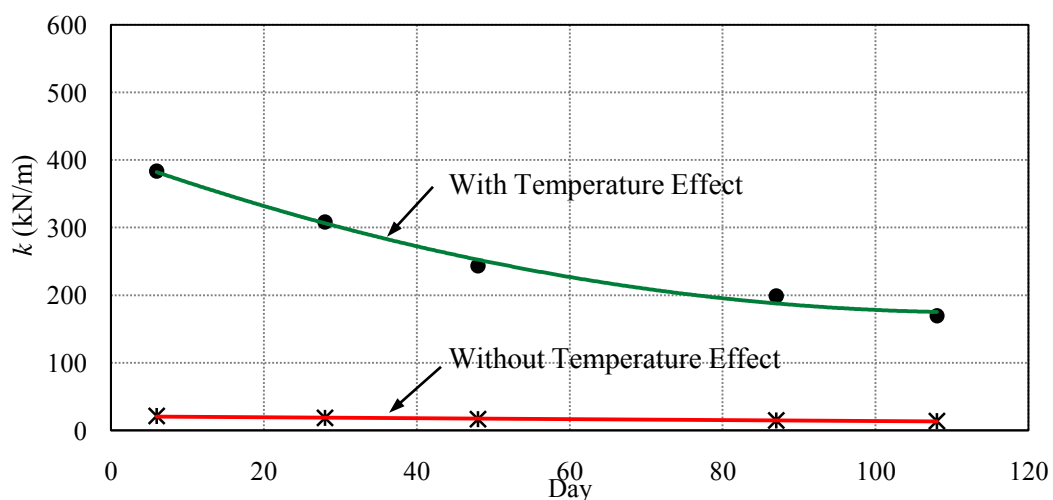


**Figure 5.15:** Variation of equivalent stiffness with increasing number of days with and without considering temperature effects on PZT parameters.

#### **5.4 PROOF-OF-CONCEPT DEMONSTRATION OF ENERGY HARVESTING FOR SHM USING EMBEDDED CVS**

The RC beam was subjected to a sinusoidal loading at a frequency of 16.5 Hz using the inertial-type shaker placed at the centre of the beam. It was operated at a frequency equal to the natural frequency of the beam to attain maximum deflection in the beam at the centre. The corresponding acceleration to attain maximum deflection, hence the maximum strain and voltage in the PZT patch, at the beam centre was measured to be  $3.14 \text{ ms}^{-2}$ . An energy harvesting circuit [shown in Figure 5.16(a)], consisting of a full wave bridge rectifier built of Zener diodes and a  $1000 \mu\text{F}$  capacitor, was employed for harvesting and storing the energy generated by the CVS embedded at location 11 in the RC beam. The variation of the voltage across the capacitor during its charging and discharging is shown in Figure 5.16(b). It can be observed that the capacitor was charged to a maximum voltage of 97 mV in 187 seconds. Using the relation,  $E_c = 1/2CV^2$ , the energy stored in the capacitor ( $E_c$ ) was computed as  $4.753 \mu\text{J}$ , from which it can be derived that a continuous harvesting for 15 days is sufficient for one time operation of AD5933 (Table 5.1), which requires an energy of 33 mJ for one time operation. Hence, SHM of the real-life structure can be performed twice a month using the same CVS for SHM and energy harvesting. Other low power consuming circuits available in market for various applications, which can also be powered using the embedded CVS, are summarized in Table 5.1. Hence, combined energy harvesting and SHM are feasible using embedded CVS. It can carry out energy harvesting during the idle time and can use this energy to carry out SHM after regular intervals.

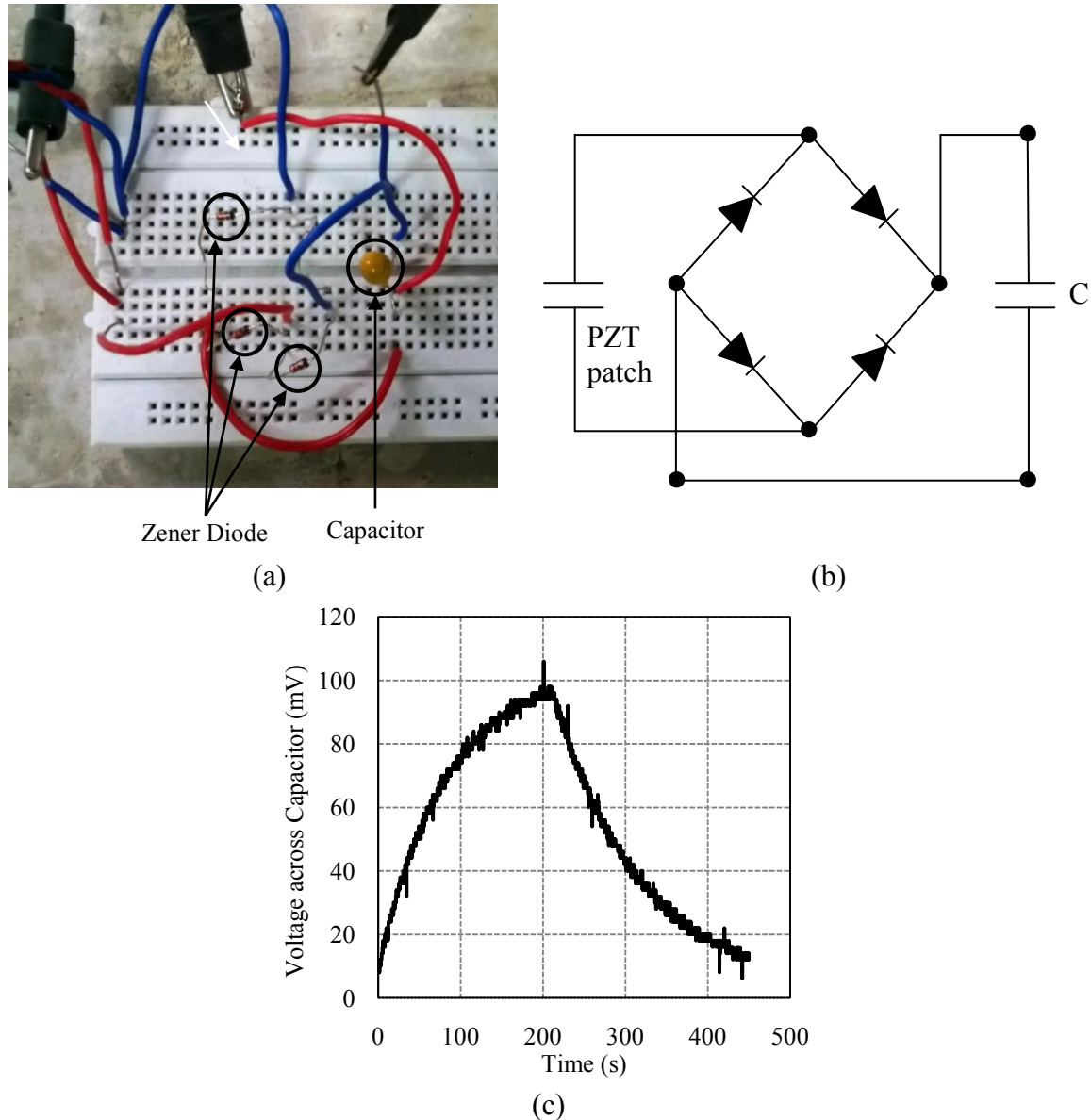


**Figure 5.16:** (a) Full-wave bridge rectifier circuit used for storing energy in capacitor.  
(b) Equivalent circuit for the energy harvesting circuit shown in (a).  
(c) Charging and discharging voltage across capacitor.

**Table 5.1:** Charging cycles time for different circuits for various applications.

Circuit / IC	Energy Required	Charging Cycles	Application
Typical A/D Convertor, TMP 112 (Texas Instruments, 2014)	$25.2 \mu\text{J}$	6	Industrial Application
RE46C800 (Microchip Technology, 2014)	3 mJ	631	CO/heat Detector
AD5933 (Analog Devices, 2014)	33 mJ	6943	SHM via EMI Technique

## 5.5 SUMMARY AND CONCLUDING REMARKS

This chapter has presented the proof-of-concept demonstration of combined SHM and energy harvesting using specially designed embedded PZT patch (CVS) operating in the axial mode. SHM via the global vibration technique and the local EMI technique of a 4m long simply supported RC beam has been performed using embedded CVS. It is concluded that the embedded CVS can effectively detect damage ranging from incipient to severe nature, using the global vibration and the local EMI technique when implemented in combination. The strength gain and the fatigue characteristics of the beam were successfully monitored using the embedded CVS. The monitoring was done by investigating the two aspects of the beam, the global parameters (natural frequency) and the local parameters (equivalent stiffness) of the beam. Long term continuous monitoring of the natural frequency and the equivalent stiffness of the RC beam for 108 days showed that both the natural frequency and equivalent stiffness remained constant for the ‘no loading’ period after curing. However, it started reducing after day 40 due to loss of the fatigue strength, thus proving suitability of CVS for fatigue damage monitoring. Experimental demonstration for harvesting and storage of energy has also been described. With the ongoing developments in electronics, as lesser power consuming circuits are emerging, it is believed that the necessary minimum energy scavenging time will drastically come down. Hence, using PZT patch in the form of CVS both for SHM and energy harvesting in real-life structures is expected to emerge as a new and useful contribution.

The next chapter will extend the coupled electro-mechanical model derived in this chapter and Chapters 3 to estimate the power generation capability of the surface bonded and the embedded PZT patches on real-life structures.



## **Chapter 6**

# **ENERGY HARVESTING USING THIN PZT PATCHES SURFACE BONDED/EMBEDDED IN REAL-LIFE STRUCTURES: AN EXTENDED STUDY**

### **6.1 INTRODUCTION**

This chapter extends the PZT-bond-structure coupled electro-mechanical models derived and validated in Chapters 3 and 4 to estimate the power generation capability of the surface bonded and the embedded PZT patches on real-life structures. Finite element (FE) modelling of a typical city flyover has been done using SAP2000 software to estimate the dynamic strain levels occurring in the real-life structures. The voltage and the power, which a PZT patch can produce corresponding to these strain values, has been computed using the electro-mechanical models. Further, based on the vibration data reported in the literature for eight typical existing real-life bridges/flyovers across the world, the power generated by a typical PZT patch in surface-bonded/ embedded configurations has been computed.

### **6.2 ENERGY HARVESTING FROM TYPICAL CITY FLYOVER: SEMI ANALYTICAL STUDY**

A typical city flyover with a span 25 m has been considered in the present study. Numerical modelling has been employed to determine the dynamic displacement of the bridge from which the harvestable power has been computed using the analytical model developed in Chapter 3. Hence, the approach is semi-analytical in nature. The elevation and the plan of the flyover are shown in Figures 6.1 and 6.2, respectively.

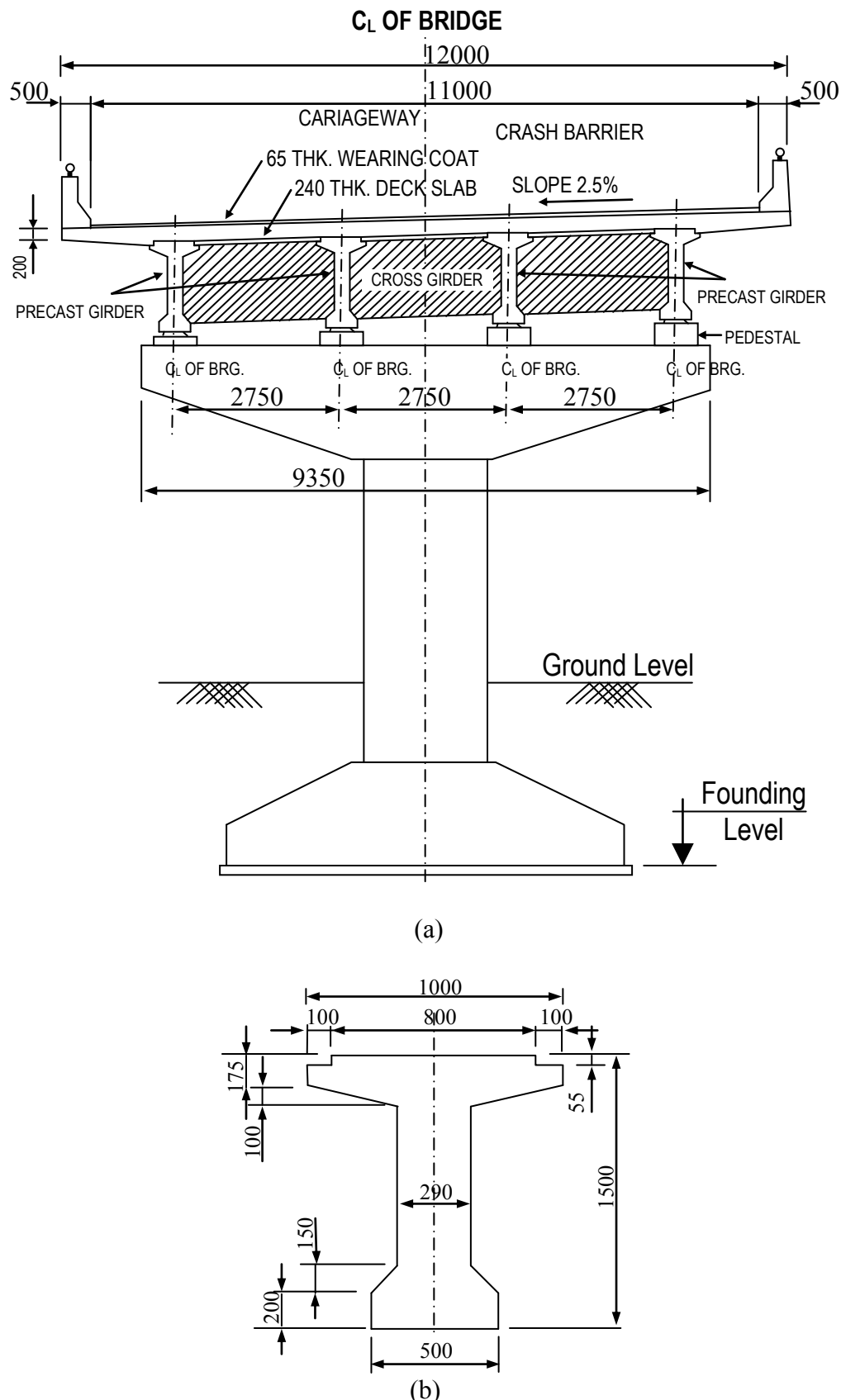


**Figure 6.1:** (a) Cross section of the flyover (mid span) and (b) cross girder (typical)  
(All dimensions are in mm).

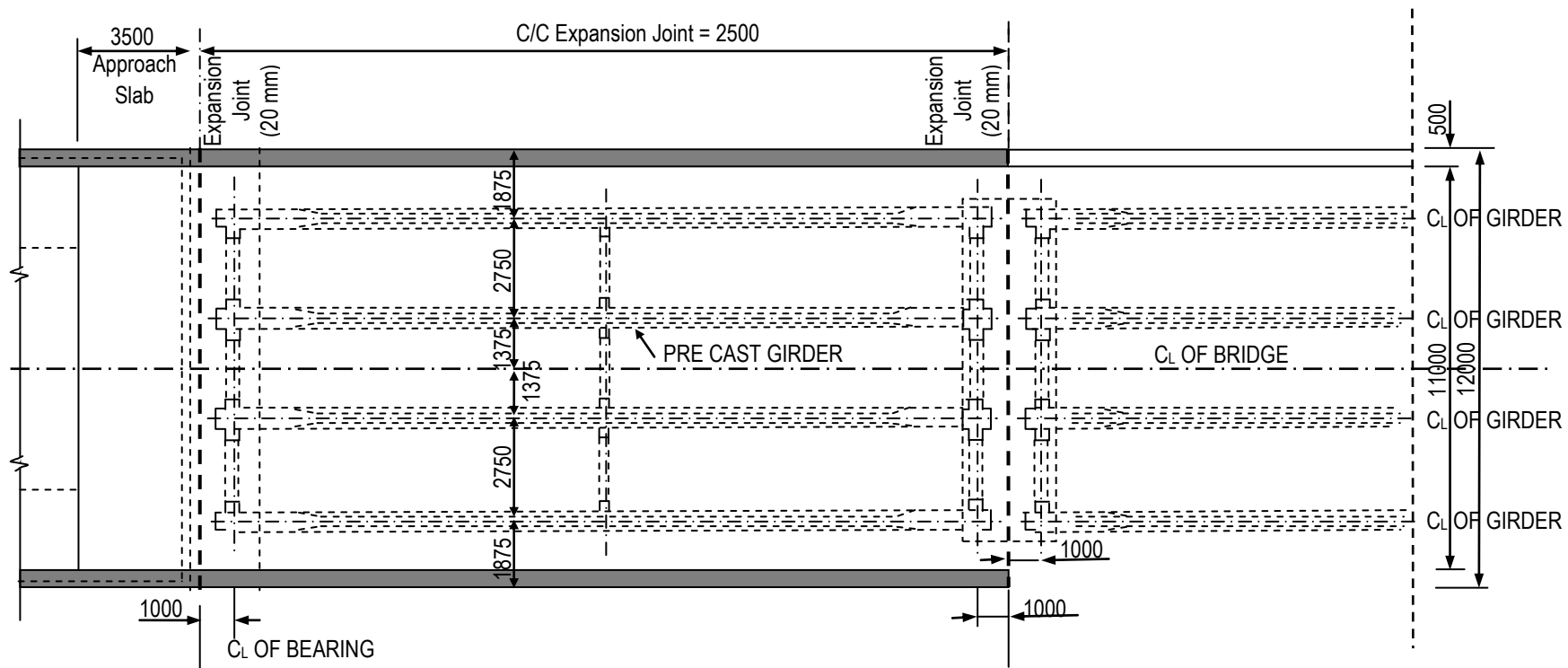


**Figure 6.2:** Plan of the flyover (All dimensions are in mm).

Special module of SAP2000 called '*Bridge Modeller*', specifically meant for the analysis of bridges/flyover, was used for the FE modelling. Out of the three spans making up the flyover, the central span with simply supported end conditions has been considered here for the analysis. Two lanes of 4 m width each were modelled for the vehicle movement. Vehicle loads as per IRC: 6 (2000) were applied on the flyover structure. The FE model consisted of concrete deck slab of 250 mm thickness, three vehicle lanes (IRC, 2000) and four concrete girders, located as shown in Figure 6.3. The ends of the span were considered simply supported. In accordance with IRC: 6 (2000), one lane of Class A together with one lane of Class 70R or 3 lanes of Class A were considered as the governing load combinations for the bridge. Accordingly, five different load cases resulted as depicted in Figure 6.4. An impact factor of 15% was considered for both Class A and Class 70R loading.

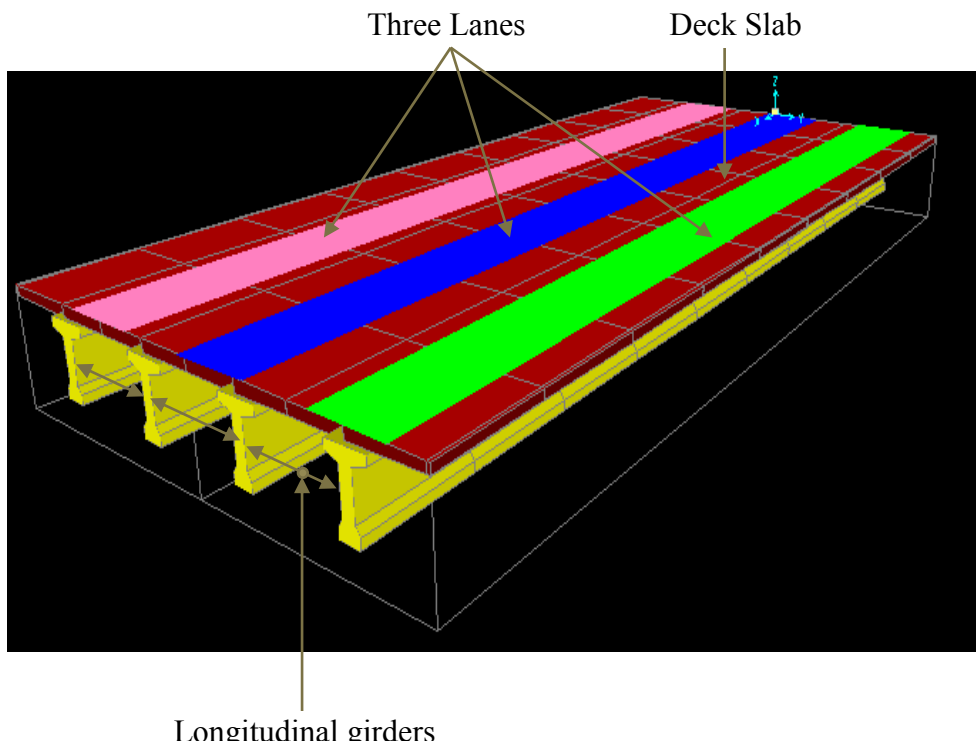


**Figure 6.3:** FE model of flyover (single span) in SAP2000 software.

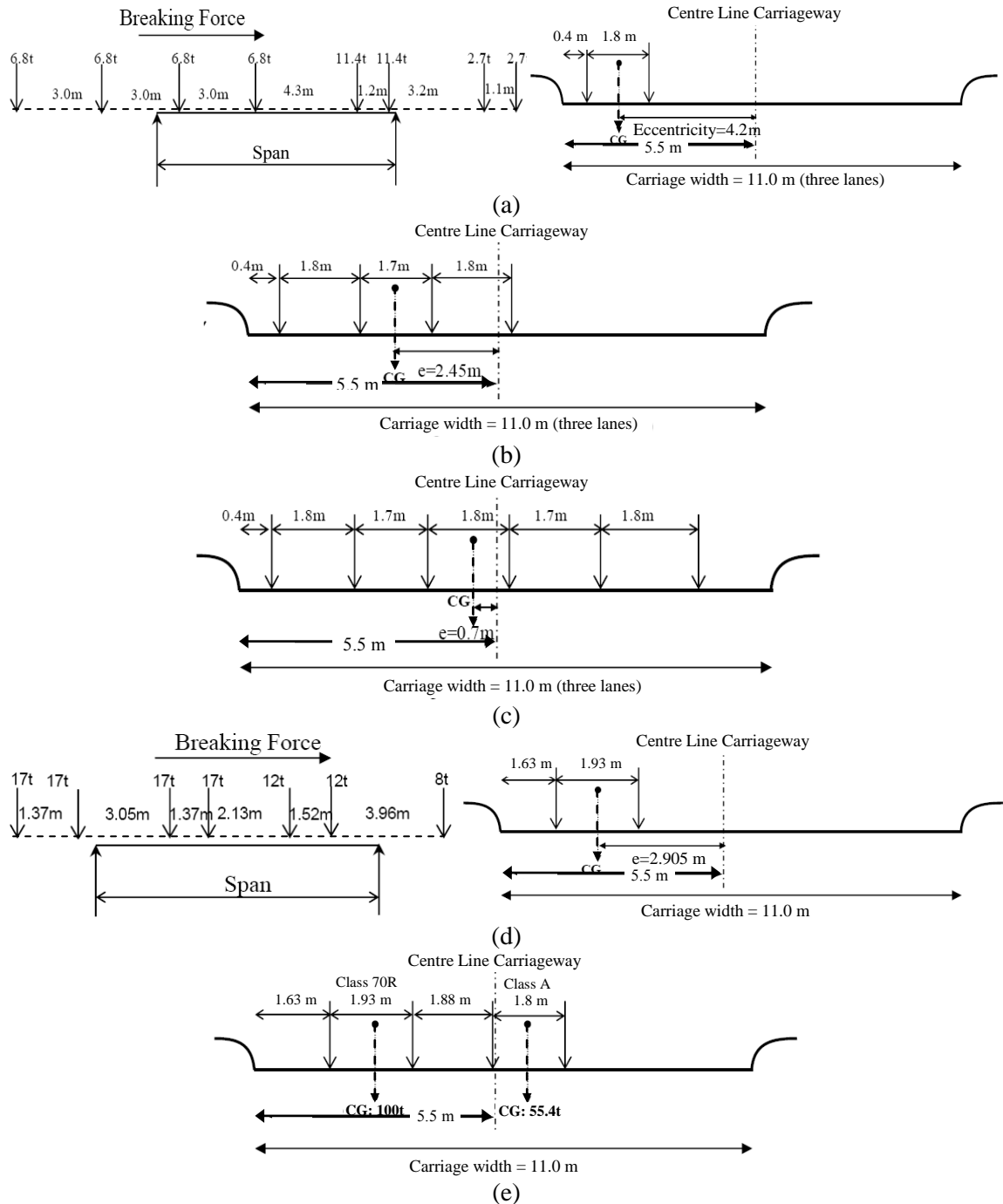


**Figure 6.4:** (a) 1Lane(L) Class A: longitudinal and transverse placement of vehicle wheel loads.  
 (b) 2L Class A: transverse placement of vehicle wheel loads.  
 (c) 3L Class A: transverse placement of vehicle wheel loads.  
 (d) 1L Class 70R: longitudinal and transverse placement of vehicle wheel loads.  
 (e) 1L Class 70R + 1L Class A: transverse placement.

Typical deformation vs time plot of the central node of the flyover for the 3<sup>rd</sup> load case [3L Class A, as depicted in Figure 6.4(c)] is shown in Figure 6.5. The response consists of static deflection (0-2 seconds) followed by the dynamic response resulting from recoil of the bridge after the vehicle has passed. The peak value here denotes the static deflection; however, for energy harvesting, dynamic amplitude is of greater interest, since PZT patch responds to dynamic strains only. Hence, filtering the static deformations, dynamic vibrations were extracted and shown enhanced in Figure 6.5. The differential displacement between the girders was ignored. Similar experimental observations have been reported by Niitsu and Iizuka (2014) during the real-time displacement measurement of road-bridges under traffic using digital image correlation method.

The dynamic displacement computed above was converted into dynamic strain and finally into the voltage across the PZT patch using the analysis presented in Chapter 3. However, in the place of Eq. 3.40 (which is valid for a point load acting at the centre of the beam), following equation, which is valid for uniformly distributed load, UDL (the vehicular loads considered here are closer to UDL) has been used for computing the voltage which a surface bonded PZT patch on flyover is expected to produce, considering the shear loss

$$(V_p^s)_s = \frac{4.8D}{L^2} K_p (K_b)_s S_q^* u(x, t)_{\text{peak}} \quad (6.1)$$

Here,  $u(x, t)_{\text{peak}}$  was determined from FEM unlike in the case of the steel beam considered in Chapter 3 where it was analytically computed. The flexural rigidity of girder ( $EI_g$ ) was determined to be  $4.438 \times 10^{10}$  Nm<sup>2</sup>. The thickness of the bond layer was assumed to be 0.15 mm (half the PZT patch's thickness). Additionally, a thickness of 0.3 mm (PZT patch's thickness) was considered for comparison purpose.

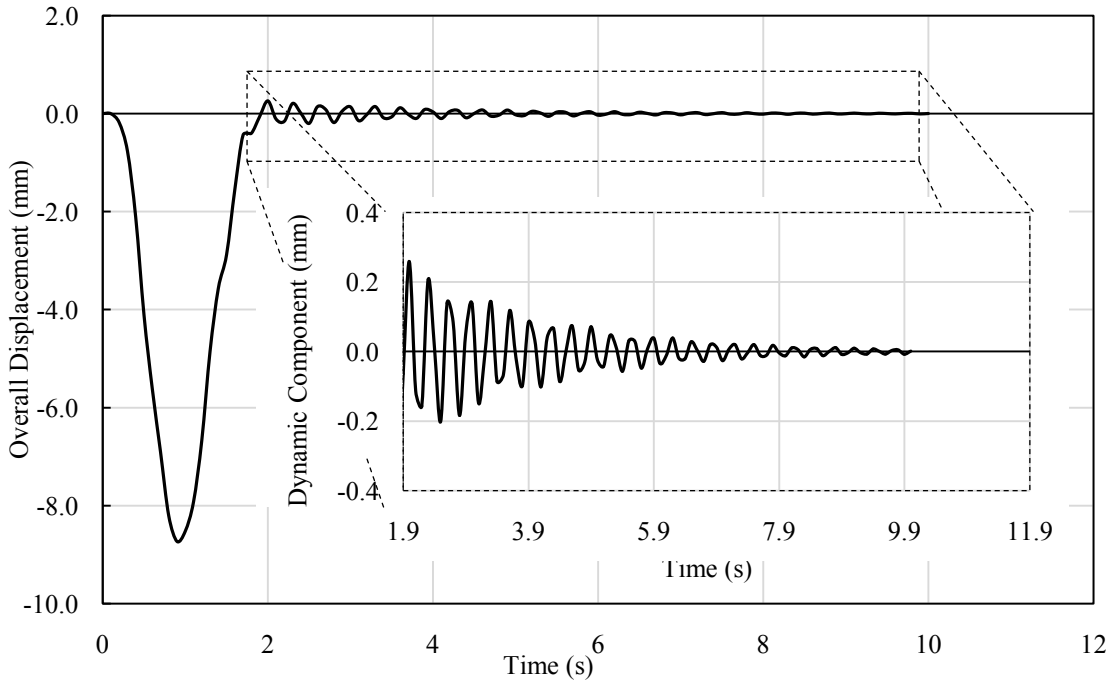


**Figure 6.5:** Deformation pattern of the central node of the deck for 3<sup>rd</sup> load case: 3L Class A (*focusing on dynamic component*).

The peak displacement amplitude, strain ( $S_1$ ), the corresponding voltage and the RMS power that the piezo is expected to produce based on the combined FE and analytical modelling presented here are summarized in Table 6.1. All computations correspond to  $R_1 = 494.7 \text{ k}\Omega$  and  $R_2 = 471.66 \text{ k}\Omega$  for the energy harvesting circuit covered in Chapter 3. From this table, it can be observed that maximum vibrations occur for the 4<sup>th</sup> load case: 1L Class 70R, with peak amplitude of 0.289 mm, strain ( $S_1$ ) of  $2 \times 10^{-5}$  and voltage of 2.305 V.

**Table 6.1:** Peak vibration amplitudes and corresponding voltage and power for five load cases ( $t_s$ : bond layer thickness;  $h$ : PZT patch thickness).

S. No.	Load Case	Peak Amplitude (mm)	Strain ( $\times 10^{-3}$ )	For $t_s=h/2$		For $t_s=h$	
				Voltage (V)	$P_{RMS}$ ( $\mu$ W)	Voltage (V)	$P_{RMS}$ ( $\mu$ W)
1	1L Class A	0.077	0.005	0.614	0.156	0.493	0.101
2	2L Class A	0.190	0.013	1.516	0.951	1.217	0.613
3	3L Class A	0.259	0.018	2.066	1.767	1.658	1.138
<b>4</b>	<b>1L Class 70R</b>	<b>0.289</b>	<b>0.020</b>	<b>2.305</b>	<b>2.199</b>	<b>1.851</b>	<b>1.417</b>
5	1L Class 70R +1L Class A	0.283	0.020	2.258	2.109	1.812	1.359

Based on the circuit (Figure 3.12), the power generated by the patch was determined as 2.199  $\mu$ W (power density= 73.3  $\mu$ W/cm<sup>3</sup>) for  $t_s= h/2$ , which is much greater than the power generated (0.270  $\mu$ W) by PZT patch on beam in the laboratory. With this power, the typical charging time for the chip type capacitor (CP3225A with battery capacity of 4.5  $\mu$ Ah) will be 2.04 hours (against 8.5 hours for the laboratory specimen), which provides good justification for the proposed usage of the PZT patch in the  $d_{31}$ -mode. For the case of  $t_s= h$ , the generated power worked out to be 1.417  $\mu$ W (power density= 47.23  $\mu$ W/cm<sup>3</sup>), for which the charging time will be 3.17 hours. Further, if the surface-bonded PZT patch is replaced by the CVS, the power yield would be 1.37  $\mu$ W (power density= 45.7  $\mu$ W/cm<sup>3</sup>), which would require a charging time of 3.27 hours.

In general, the PZT material shows very high compressive strength, typically over 500 MPa and it essentially exhibits a linear stress-strain relation up to strains as high as 0.006 (Cheng and Reece, 2001), which is far greater than the maximum strain (dynamic:  $2 \times 10^{-5}$  and static:  $6.5 \times 10^{-4}$ ) being produced in the girder during the vehicular movement. Hence the possibility of damage to PZT patches in the process of energy harvesting is very remote.

### **6.3 EXTENSION TO EXISTING REAL-LIFE BRIDGES/ FLYOVERS**

The dynamic vibrations, under traffic loads and ambient conditions, experienced by eight existing real-life bridges/ flyovers across the world, have been considered in this section for estimating power generation capability of surface-bonded/ embedded PZT patches. Based on the vibration data reported in the literature, the power generated by a surface bonded/ embedded CVS in these structures has been computed by extending the coupled electro-mechanical models presented in Chapters 3 and 4, respectively. In the following subsections, steel bridges have been considered for surface-bonded PZT patch and RC bridges for embedded CVS.

#### **6.3.1 Steel Bridges**

The four steel bridges/ flyovers considered in this study based on literature are listed in the Table 6.2 and investigated for power estimation from the surface bonded PZT patches. The specifications and the type of the loading considered for vibration response from these bridges are described in Table 6.2. The acceleration values reported in the literature were converted into displacement ( $a$ ) using,

$$a = \frac{\ddot{x}}{(2\pi f_{br})^2} \quad (6.2)$$

where,  $f_{br}$  is the natural frequency of the bridge. The estimated voltage generated by the PZT patch surface bonded on the steel bridges was calculated using the Eq. (3.40) for point load case. In the case of UDL, necessary modification represented by Eq. (6.1) was applied. The peak power ( $P_{peak}$ ) was computed using the basic electrical relations between voltage  $(V_p^s)_s$  and the resistance ( $R_1 = 494.7 \text{ k}\Omega$  and  $R_2 = 471.66 \text{ k}\Omega$ ) for the power measuring circuit described in Chapter 3, that is

$$P_{peak} = \frac{(V_p^S)_S}{R_1 + R_2} \quad (6.3)$$

From Table 6.2, it can be observed that the maximum power, which can be harnessed from the mechanical vibrations in steel bridges is 26.154  $\mu\text{W}$  (power density= 871.8  $\mu\text{W}/\text{cm}^3$ ), for the case Zuo et al. (2012). The minimum power was computed to be 0.0009  $\mu\text{W}$  (0.3  $\mu\text{W}/\text{cm}^3$ ) for the bridge considered by Moghimi and Ronagh (2008). The average peak power considering all listed cases works out to be 0.406  $\mu\text{W}$  (13.53  $\mu\text{W}/\text{cm}^3$ ). This corresponds to an RMS power of 0.287  $\mu\text{W}$ , which is of same order as the power generated by the surface-bonded PZT patch on the steel beam in the laboratory (Chapter 3).

### 6.3.2 RC Bridges

On the same lines, the voltage generated by a CVS embedded in four real-life RC bridges listed in Table 6.3 was estimated using the analytical model proposed in Chapter 4 [Eq. (4.32)]. Further, the power generated was computed using the relations derived from power measuring circuit in Chapter 4, with  $R_1 = 494.7 \text{ k}\Omega$  and  $R_2 = 471.66 \text{ k}\Omega$ , and listed in Table 6.3. It can be observed that the maximum power which can be achieved from the mechanical vibrations of the RC bridges comes out to be 0.171  $\mu\text{W}$  (power density= 5.7  $\mu\text{W}/\text{cm}^3$ ) for the case considered by Peigney and Siegert (2013). The average power resulting from all the four cases worked out to be 0.066  $\mu\text{W}$  (power density= 2.2  $\mu\text{W}/\text{cm}^3$ ). This is much less than the power estimated for the case of 25 m span city flyover considered in Section 6.2. As expected, RC bridges yield much less power than steel bridges owing to less pronounced vibrations due to their larger inertia as well as damping.

### 6.3.3 Computation of Charging Period

The estimated power can be harvested during the *idle state* using a capacitor, as described in Chapter 4, and utilized for SHM of the structure via same surface bonded/embedded CVS using AD5933 (Analog Devices, 2013), or any other equivalent circuit. Assuming that AD5933 consumes 33 mW of power (Analog Devices, 2013) for one time operation and considering the average power generated by the surface bonded/ embedded CVS in real-life bridge, it is estimated, that under traffic loads, a period of 21 minutes for steel bridges (for 26.1  $\mu$ W power) and 2.2 days for RC bridges (as CVS for 0.171  $\mu$ W power) will be needed for the thin piezo based harvester to harvest sufficient energy so as to operate AD5933 for one time signature acquisition. The harvesting times will be significantly less for other standard sensors. Low power consuming circuits like typical A/D convertor, such as TMP 112 (Texas Instruments, 2014) would warrant energy harvesting for 1 second and 2.5 minutes when powered by a surface bonded PZT patch on steel bridge and an embedded CVS in a RC bridge, respectively. These durations are quite realistic from practical considerations.

**Table 6.2:** Voltage and power generated by the surface-bonded PZT patch under vibrations experienced at the mid span of existing real-life steel bridges.

Paper Details	Bridge Details		Loading		Acceleration (m/s <sup>2</sup> )	Displacement (mm)	Micro Strain	Power (μW)				
Kim et al., 2004	Two-span steel bridge		Single Vehicle		0.65	1.344	10.3	1.186				
	Span Length	53 m	Weight Speed	196.03 kN 100 km/h								
	Width	11.4 m										
	Girder depth	3 m										
Ren and Peng, 2005	Three-span cable stayed bridge Qingzhou cable-stayed bridge on Ming River, China		Ambient Vibrations		0.045	22.121	1.947	0.0421				
	Span Length	605 m										
	Width	29 m										
	Girder depth	2.45 m										
Moghimi and Ronagh, 2008	Composite steel girder bridge Karkheh Dam, Khuzestan, Iran		Single Vehicle		0.0095	0.06	0.283	0.0009				
	Span Length	60.5 m	Weight Speed	400 kN 10 km/h								
	Width	12.5 m										
	Girder depth	2.5 m										
Zuo et al., 2012	Three-span steel bridge near football stadium at Texas Technical University, USA		Fully occupied with pedestrians <i>(considered as uniformly distributed load)</i>		0.25	9.919	48.5	26.154				
	Span Length	40 m										
	Width	3.66 m										
	Girder depth	2.5 m										
Natural Frequency ( $f_n$ )		0.799 Hz										

**Table 6.3:** Voltage and power generated by the embedded CVS under vibrations experienced at the mid span of existing real-life RC bridges.

Paper Details	Bridge Details		Loading		Acceleration (m/s <sup>2</sup> )	Displacement (mm)	Micro Strain	Power (μW)
Lee and Yhim, 2005	Two-span concrete box girder bridge Han River in Seoul, South Korea		Single Vehicle		--	0.50	3.033	0.075
	Span Length	60 m	Weight Speed	24 kN				
	Width	14.5 m		50 km/h				
	Girder Depth	3.67 m						
Ashebo et al., 2007	Three-span concrete skew box girder bridge Tsing Yi South, New Territories West, Hong Kong		5 trucks		--	--	1.5	0.018
	Span Length	23 m	Weight Speed	24.6 kN				
	Width	10.58 m		75 km/h				
	Girder Depth ( <i>mean</i> )	1.63 m						
Abdessemed et al., 2011	Three-span concrete bridge Oumazer River, Tipaza, west of Algiers		Ambient Vibrations		0.04	0.065	0.490	0.0019
	Span Length	40 m						
	Width	15 m						
	Girder Depth	1 m						
Peigney and Siegert, 2013	Three-span prestressed concrete bridge North of France		Traffic induced Vibrations		0.25	0.416	4.588	0.171
	Span Length	33 m						
	Width	10.5 m						
	Girder Depth	1 m						
	Natural Frequency	3.9 Hz						

## 6.4 SUMMARY AND CONCLUDING REMARKS

This chapter has extended the coupled electro-mechanical model for estimation of power generation by surface bonded/ embedded PZT patches, proposed in Chapters 3 and 4, respectively, to real-life bridges across the world. A typical city flyover has been modelled through FEM to determine the strain levels produced in the real-life structures. The peak vibration amplitude, the corresponding voltage and the RMS power that a surface-bonded PZT patch is expected to produce on the basis of the semi-analytical model is determined to be 0.289 mm, 2.305 V and 2.199  $\mu$ W, respectively. The study has been extended to eight real-life steel/ RC structures. It is estimated that a period of less than 21 minutes for steel bridges and about 2.2 days for RC bridges (as CVS) will be needed for the thin piezo based harvester to harvest sufficient energy so as to enable one time operation of AD5933, when using the EMI technique. With the ongoing developments in electronics, as lesser power consuming circuits are emerging, it is believed that the energy scavenging time will drastically come down. Hence, using PZT patch in surface-bonded condition or in the form of CVS for both SHM and energy harvesting is technically feasible.

The next chapter will cover comprehensive parametric studies involving surface-bonded and embedded CVS for energy harvesting through numerical simulation.

## **Chapter 7**

# **NUMERICAL INVESTIGATIONS ON ENERGY HARVESTING FROM ADHESIVELY BONDED THIN PZT PATCHES IN SURFACE BONDED/ EMBEDDED CONFIGURATIONS**

### **7.1 INTRODUCTION**

This chapter deals with the effect of adhesive bond on the energy harvested from thin piezoelectric ceramic (PZT) patches, either surface bonded or embedded inside RC structures. As seen in Chapter 4, the adhesive bond acts as an elastic medium facilitating the transfer of stresses and strains between the patch and the host structure and significantly influences the voltage generated across the patch and hence the power output. This chapter presents a numerical approach to perform a detailed parametric study to investigate the effect of various parameters such as PZT geometric parameters, adhesive layer thickness and bond stiffness on energy harvesting. A numerical model has been developed for a real-life sized simply supported beam instrumented with (a) surface bonded PZT sensor (SBPS), and (b) embedded PZT patch in form of concrete vibration sensor (CVS), and coupled field analysis has been performed for the two configurations. The results are compared with the existing analytical model as well as the experimental data. Effect of varying load resistance across the PZT patch, piezo and bond thicknesses, patch's plan dimensions, shear modulus of the adhesive and adhesive covering on the voltage close circuit power generated by the patch has also been investigated.

The next sections cover the details of the numerical model and the associated parametric study.

## 7.2 NUMERICAL MODELLING

A real-life sized RC beam shown in Figure 7.1, earlier investigated in Chapter 4, is again considered for numerical simulation in this chapter. The beam has a length of 4 m and cross-section of  $150 \times 210$  mm. Other related physical properties of the beam are listed in Table 4.1. The Rayleigh's damping coefficients ( $\alpha = 11.86 \text{ s}^{-1}$  and  $\beta = 1.1 \times 10^{-4} \text{ s}$ ) considered in the study correspond to a damping ratio of 5%. The Young's Modulus ( $E$ ) of concrete was considered as  $31.622 \times 10^9 \text{ N/m}^2$ . The numerical investigation of the power generated by the PZT patch was carried out for two configurations: (a) the surface bonded PZT sensor (SBPS) and (b) embedded, in form of CVS, both located at the top fibre of the beam at the midpoint, as shown in Figure 7.1. A 3D FE model of the beam was generated using the MEMS module of COMSOL 4.4 (COMSOL, 2014) FE software. The isometric view of the RC beam with the surface bonded and the embedded PZT patches is shown in Figure 7.2. For case (a), a  $10 \times 10 \times 0.3$  mm PZT patch was meshed on the top of the beam bonded with a 0.15 mm thick adhesive bond layer, as shown in Figure 7.2(a). For case (b), an identical PZT patch was meshed and sandwiched in between  $25 \times 25 \times 2$  mm adhesive layers on top and bottom, such that the top of the upper adhesive layer was under a clear concrete cover of 5 mm, as shown in Figure 7.2(b). The physical properties of the PZT patch and the adhesive bond layer in addition to those already covered in Table 4.2 are listed in Table 7.1. In FE modelling, the 'Piezoelectric Devices Interface' available under 'Solid Mechanics' has been utilized, which can simulate both the direct and the converse piezoelectric effects employing piezoelectric coupling via the strain-charge or stress-charge formulations. Here, the piezoelectric coupling has been done using the strain-charge form. The global Z direction is the poling direction of both the PZT patches. In FE modelling, both concrete as well as the adhesive are assumed to exhibit linearly elastic and isotropic behaviour. The reinforcement bars have been ignored

in the modelling, consistent with the acceptable norm of considering gross cross-section. The excitation of the beam in this study is well within the linear range as the dynamic force applied is very small (amplitude=75 N, see Chapter 4). Effect of hysteresis on piezo performance is also assumed to be negligible here due to the application of very small strain (Moharana and Bhalla, 2012).

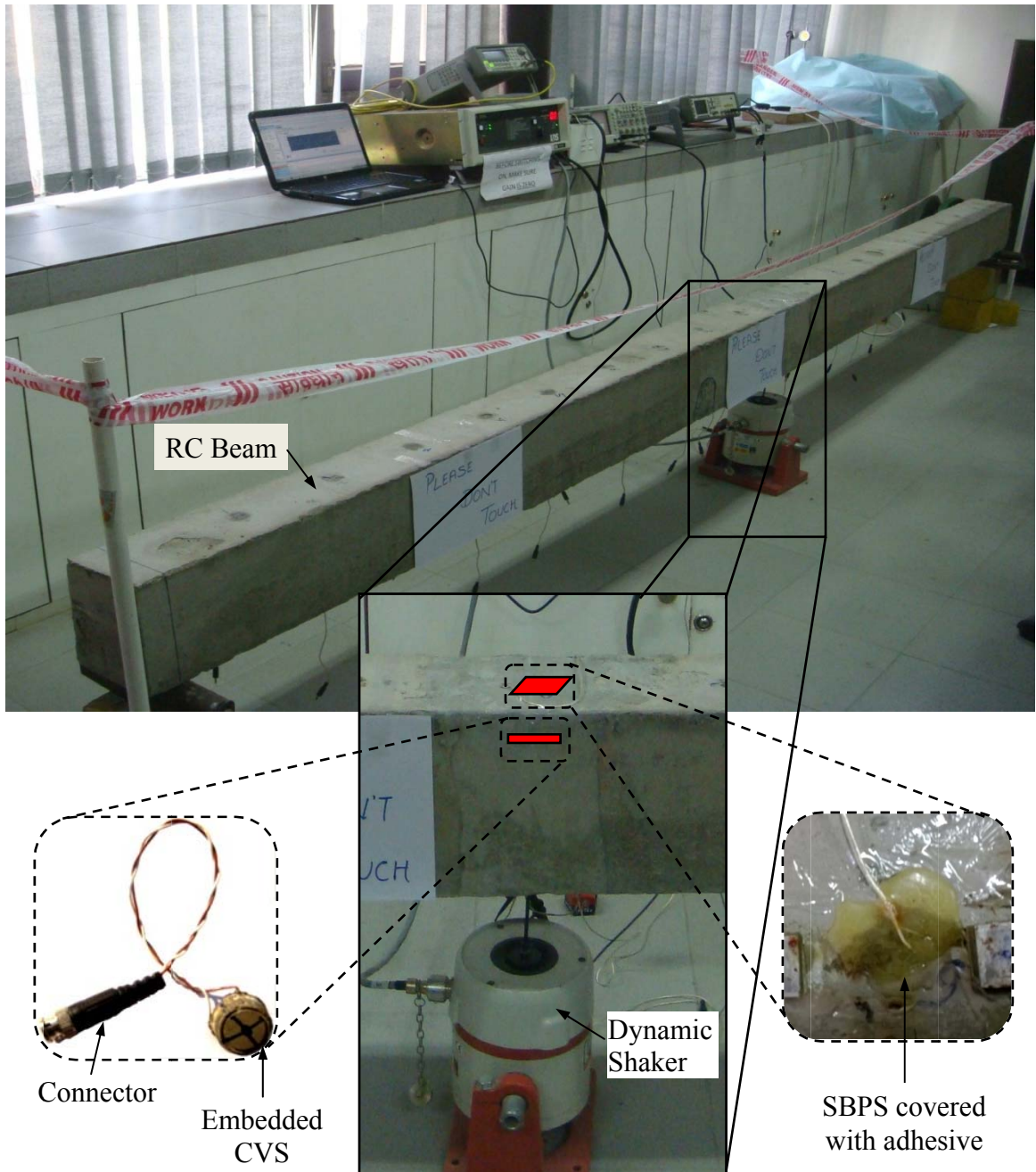


**Figure 7.1:** Experimental set-up showing RC beam considered in present study with embedded CVS and SBPS (covered with adhesive) at its mid point.

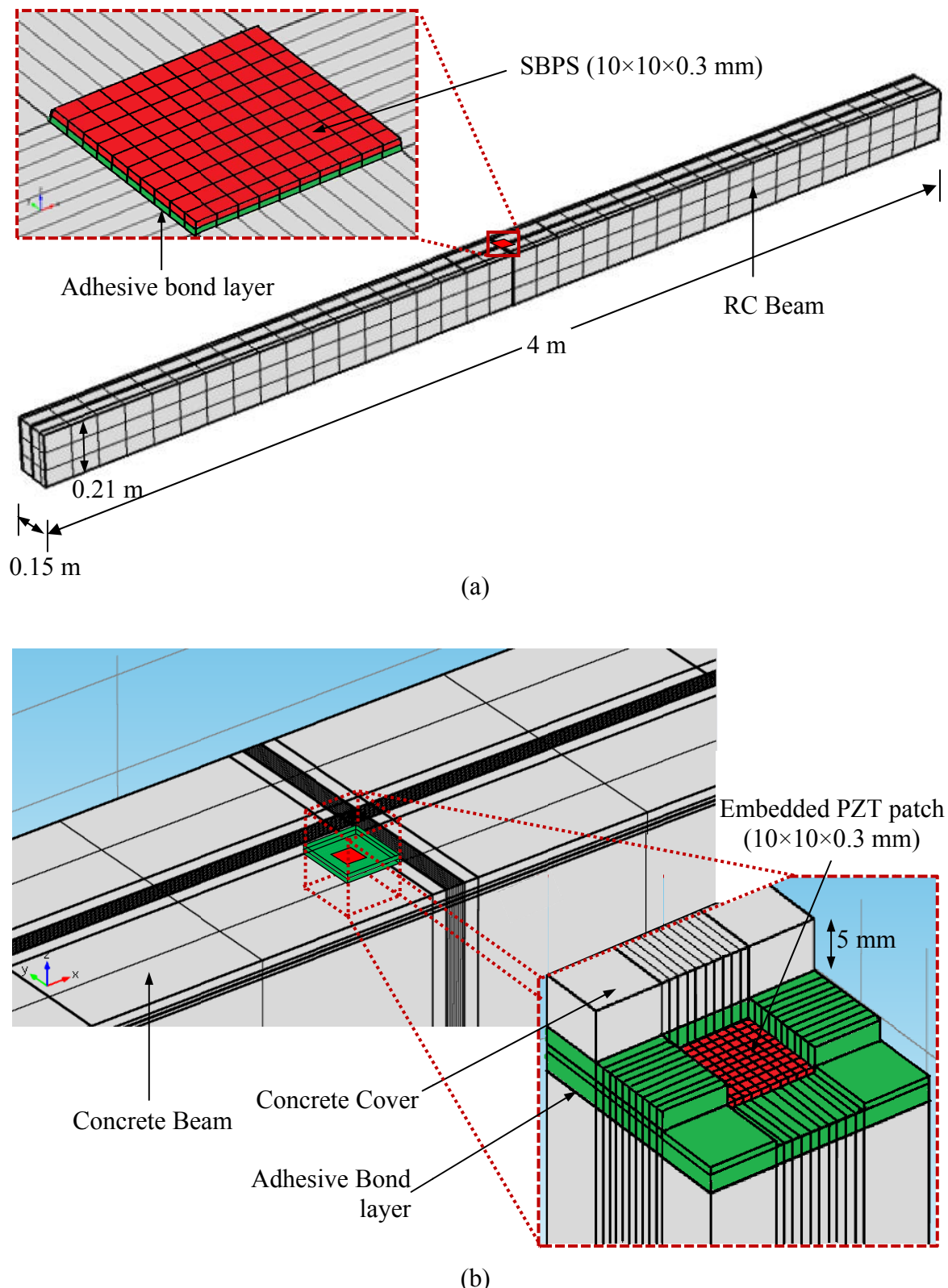


**Figure 7.2:** (a) Isometric view of RC beam with PZT patch surface bonded at midpoint.  
(b) RC beam with an enlarged view to show embedded PZT patch.

**Table 7.1:** Properties of PZT patch (PI Ceramic, 2014) and bond layer.

Property	Unit	PZT patch	Adhesive	
			SBPS	Embedded CVS
Size (Plan)	mm <sup>2</sup>	10×10	10×10	25×25
Thickness,	mm	$h = 0.3$	$(t_s)_S = 0.15$	$(t_s)_E = 2.00$ (top/bottom)
Density, $\rho$	kg/m <sup>3</sup>	7800		1000
Dielectric loss factor, $\delta$		0.02		-
Damping		Compliance Matrix Loss Factor, $\eta_{ce} = 0.02$	Structural Loss Factor, $\eta_s = 6 \times 10^{-9}$ (Moharana and Bhalla, 2012)	
Young's Modulus, $Y^E$	N/m <sup>2</sup>	$6.667 \times 10^{10}$	1000	
Shear Modulus	N/m <sup>2</sup>	-	$1 \times 10^9$	
Compliance Matrix, $[s^E]$	$(\times 10^{-12})$ m <sup>2</sup> /N	$\begin{bmatrix} 15 & -4.5 & -5.7 & 0 & 0 & 0 \\ 0 & 19 & -5.7 & 0 & 0 & 0 \\ 0 & 0 & 19 & 0 & 0 & 0 \\ 0 & 0 & 0 & 39 & 0 & 0 \\ 0 & 0 & 0 & 0 & 39 & 0 \\ 0 & 0 & 0 & 0 & 0 & 49.4 \end{bmatrix}$		

The top and the bottom surfaces of the PZT patch were individually coupled in such a way that the bottom surface was under ‘ground’ condition (i.e electric potential = 0) and the top surface under a spatially uniform electric potential across the entire surface, harmonically varying with time. A mesh convergence study was first performed, resulting in a suitable element mesh size of 1mm for the PZT patch. The COMSOL software accepts the piezo parameters directly in the IEEE format as supplied by the manufacturer (PI ceramic, 2014). A vertical dynamic force with magnitude of 75 N, as in the experimental beam (see Chapter 4) and frequency ranging of 5 Hz to 150 Hz (with a step-interval of 5 Hz), was applied over an area 150×400 mm at the midpoint of the beam. In this manner, frequency domain analysis was performed and the result, in form of

electrical quantities i.e. voltage, current and power, was obtained directly, circumventing any additional computations otherwise warranted in semi-analytical approach (Moharana and Bhalla, 2014).

### 7.3 MODEL VALIDATION

In order to validate the behaviour and the properties of the PZT patch being modelled correctly, a comparison has first been made between the experimental and the numerical admittance signature of a PZT patch in ‘free-free’ condition. A PZT patch ( $10 \times 10 \times 0.3$  mm), having physical properties listed in Table 4.2 and Table 7.1, was excited by a peak potential difference of 1 V (between top and bottom surfaces) in ‘free-free’ condition, as shown in Figure 7.3, and the admittance signatures (conductance and susceptance) were acquired for the frequency range 1 to 1000 kHz. For structural stability, one node each on the top and the bottom surfaces [see Figure 7.3] at the centre (nodal point) of the patch were restrained against translation in the poling direction (global Z) but free in the global X and Y directions. The electrical boundary conditions, as explained above, are shown in Figure 7.3(b). The real (conductance) and the imaginary (susceptance) parts of the admittance signature are compared with the experimental and the analytical results (Bhalla, 2004) in Figure 7.4. The experimental results are showing twin peak behaviour due to slight mismatch between the two edge lengths, as explained earlier by Bhalla (2004). Reasonable match (except for twin-peak behaviour) between the experimental and numerical results can be observed from the figure, which ensures the accuracy of the behaviour of the PZT patch utilized in numerical modelling. In fact, the experimental frequencies are closer to the numerical results than the analytical ones (Bhalla and Soh, 2004c, d), owing to more realistic modelling of the 2D stiffening effects otherwise ignored in the analytical model.

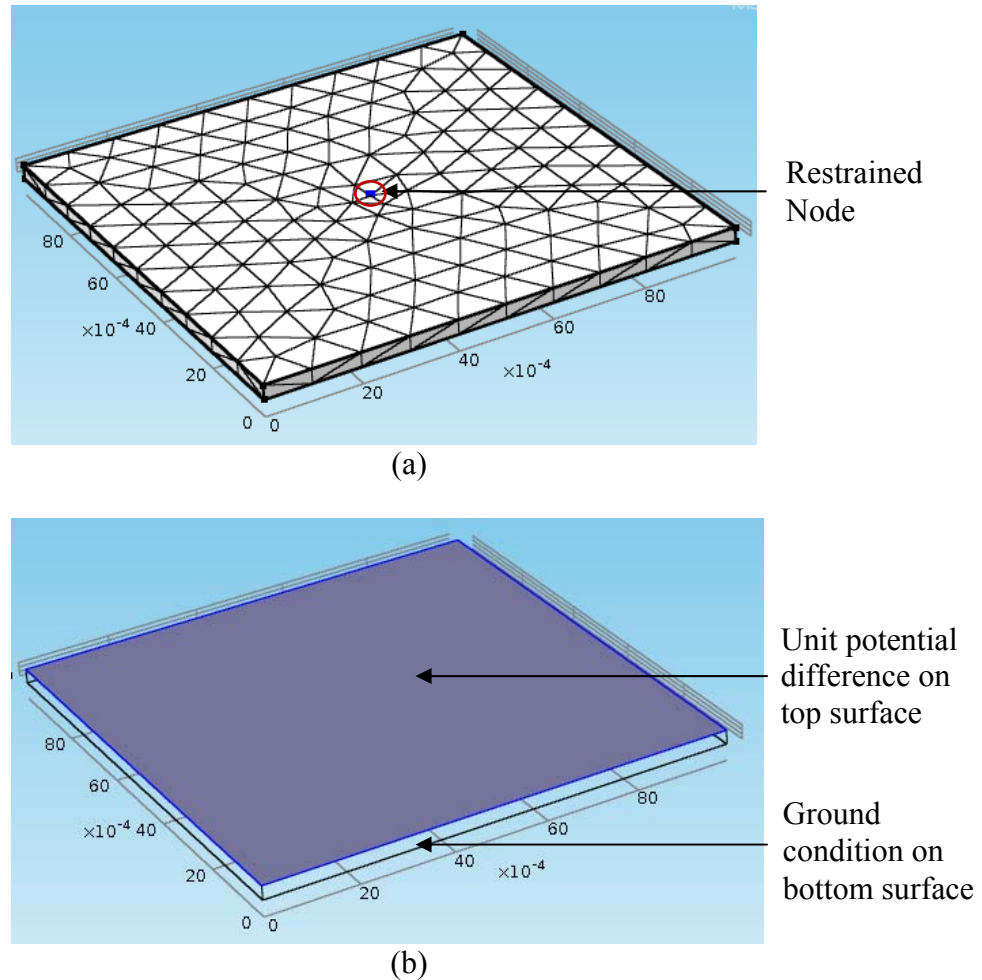


**Figure 7.3:** (a) Isometric view of free PZT patch restrained at top and bottom central node.  
(b) Electrical boundary conditions of free PZT patch.

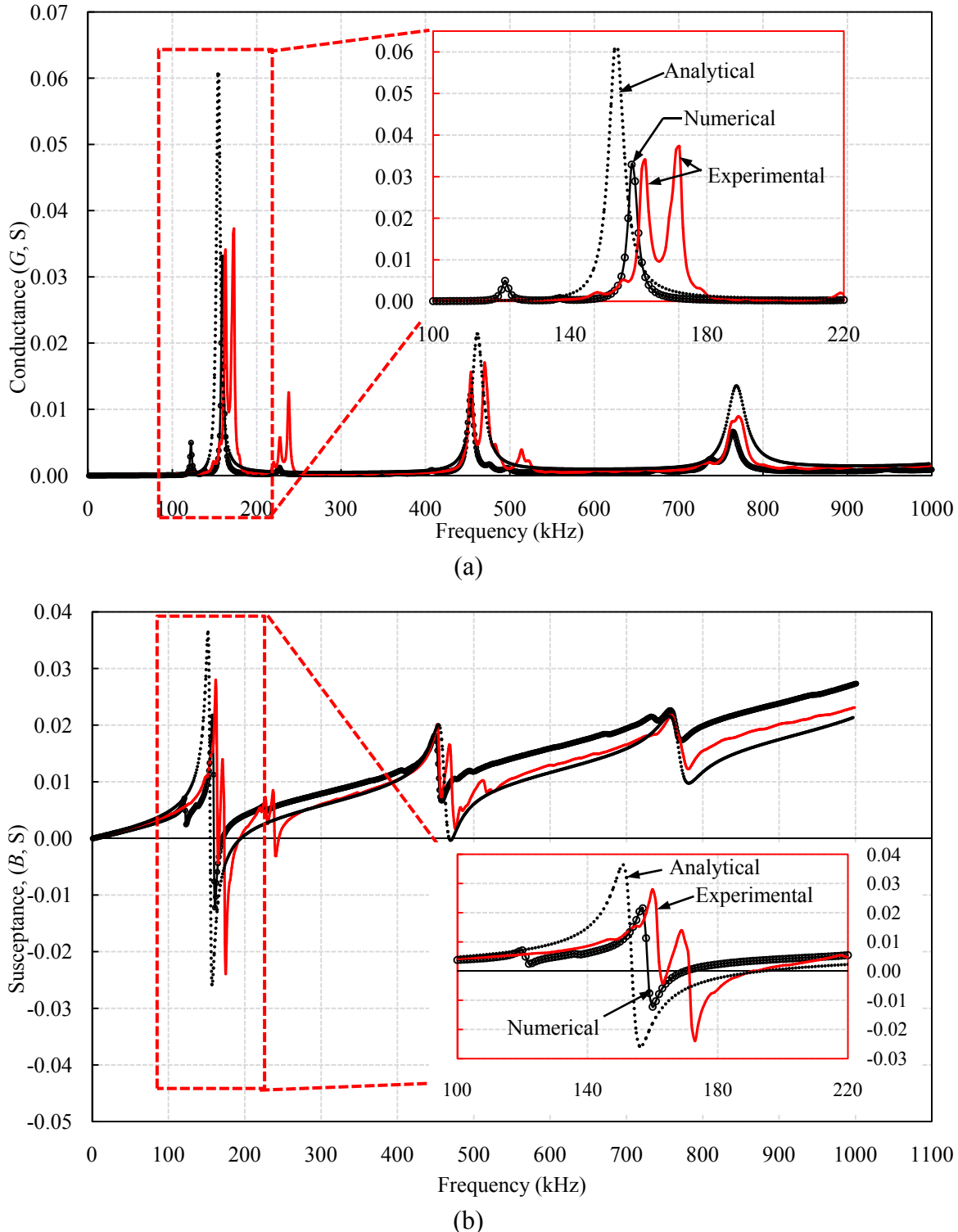


**Figure 7.4:** Comparison of numerical (a) conductance and (b) susceptance signature of a free PZT patch with analytical and experimental results.

After validation of the PZT patch's model, the model of the complete PZT-beam system was validated. For this purpose, the voltages generated by the SBPS and the embedded

CVS located at the midpoint of the beam are compared with the experimental results of Chapter 4 (Kaur and Bhalla, 2014b) in Figure 7.5. The experimental damping of the RC beam was measured to be 1.7% (see Chapter 4), hence, the equivalent Rayleigh's damping coefficients ( $\alpha$  and  $\beta$ ) were considered corresponding to a damping ratio of 1.7% for the validation purpose. The numerical results [Figure 7.5(a)] correspond to load of magnitude 75 N (applied over an area 150×400 mm) at the midpoint of the beam, with the frequency varying from 5 to 45 Hz at an interval of 5 Hz, augmented by a finer interval in the peak region, that is between 20 to 25 Hz (0.1 Hz between 22 to 23 Hz and 1 Hz elsewhere). The experimental results [Figure 7.5(b)] have been obtained using impact hammer test on the 20<sup>th</sup> day after casting of the beam (see Chapter 4, Kaur and Bhalla, 2014b), through Fast Fourier Transform (FFT) of the voltage response acquired first in the time domain for the two patches. From Figure 7.5, the numerical and the experimental maximum values of the Root Mean Square (RMS = Peak value × 0.707) voltage generated by the SBPS and the embedded CVS can be observed to occur at frequencies of 22.7 Hz and 22.49 Hz, respectively which are very agreeable. Since the experimental plot is based on impact excitation and then FFT, the absolute magnitude of the voltage may not be comparable to that of the numerical model, which is based on harmonic analysis. It can also be observed that the voltage generated by the SBPS is higher than the embedded CVS, in the numerical as well as the experimental case. The numerical and experimental value of ratio of voltage generated by embedded CVS to SBPS  $[(V_p)_E / (V_p)_S]$  was calculated to be 0.80 and 0.61 respectively, against 0.79 obtained analytically (Chapter 4, Kaur and Bhalla, 2014b). Hence, a reasonable match between the experimental, analytical and numerical results can be observed, which motivated the author to proceed further for detailed parametric studies using the FE model generated for the concrete beam with SBPS and embedded CVS. The detailed results are covered in the following sections.

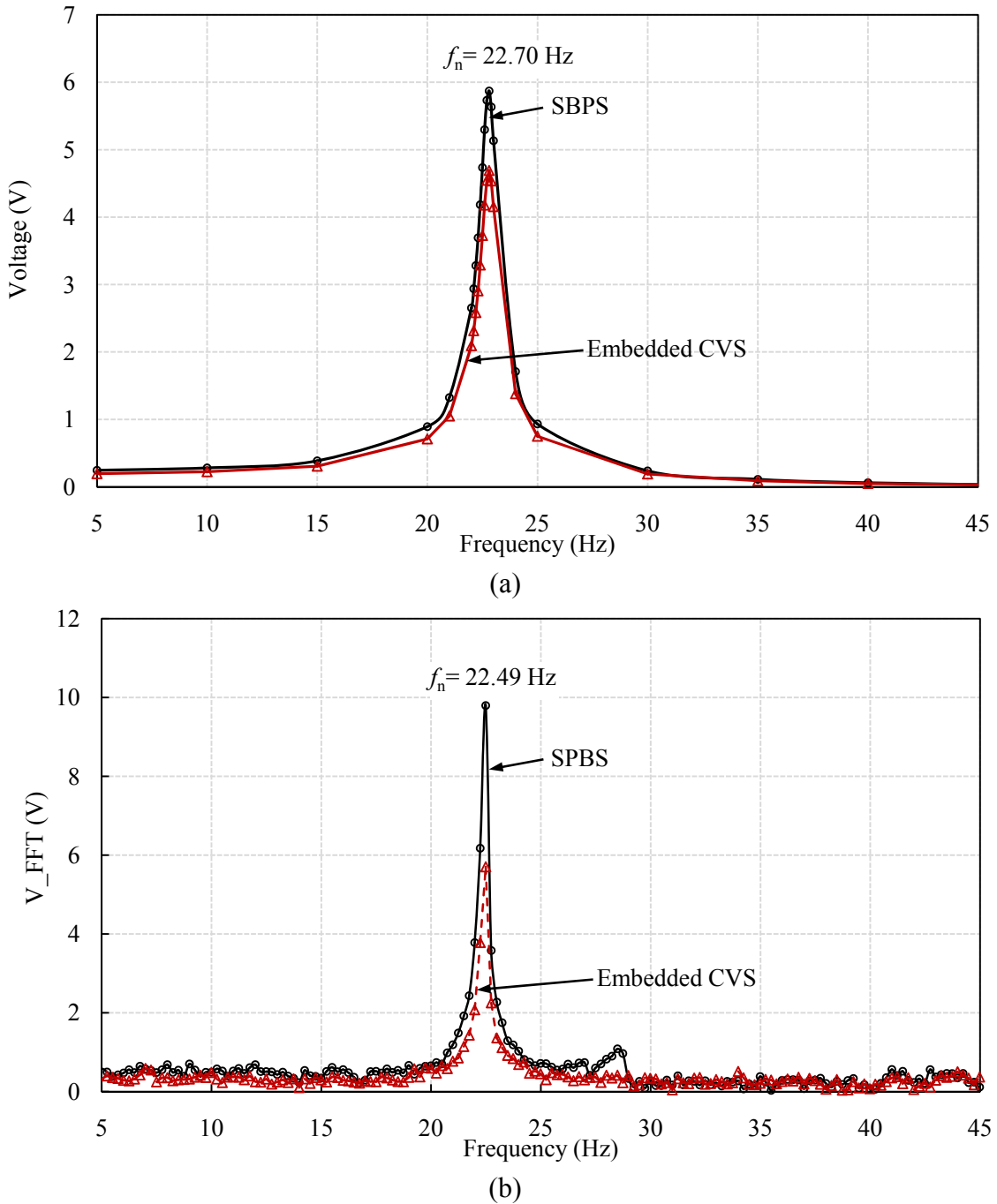


**Figure 7.5:** Comparison of (a) numerical and (b) experimental voltage generated by SBPS and embedded CVS in the RC beam.

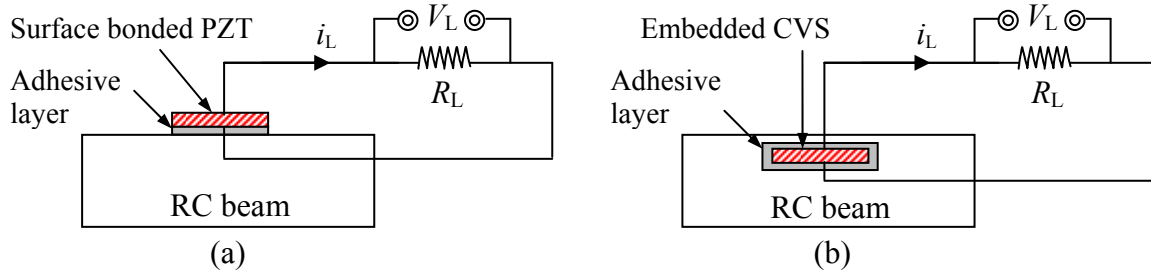
## 7.4 NUMERICAL ENERGY HARVESTING INVESTIGATIONS

The two separate numerical models of the RC beam, instrumented with SBPS and embedded CVS described above, were utilized to carry out detailed investigations related

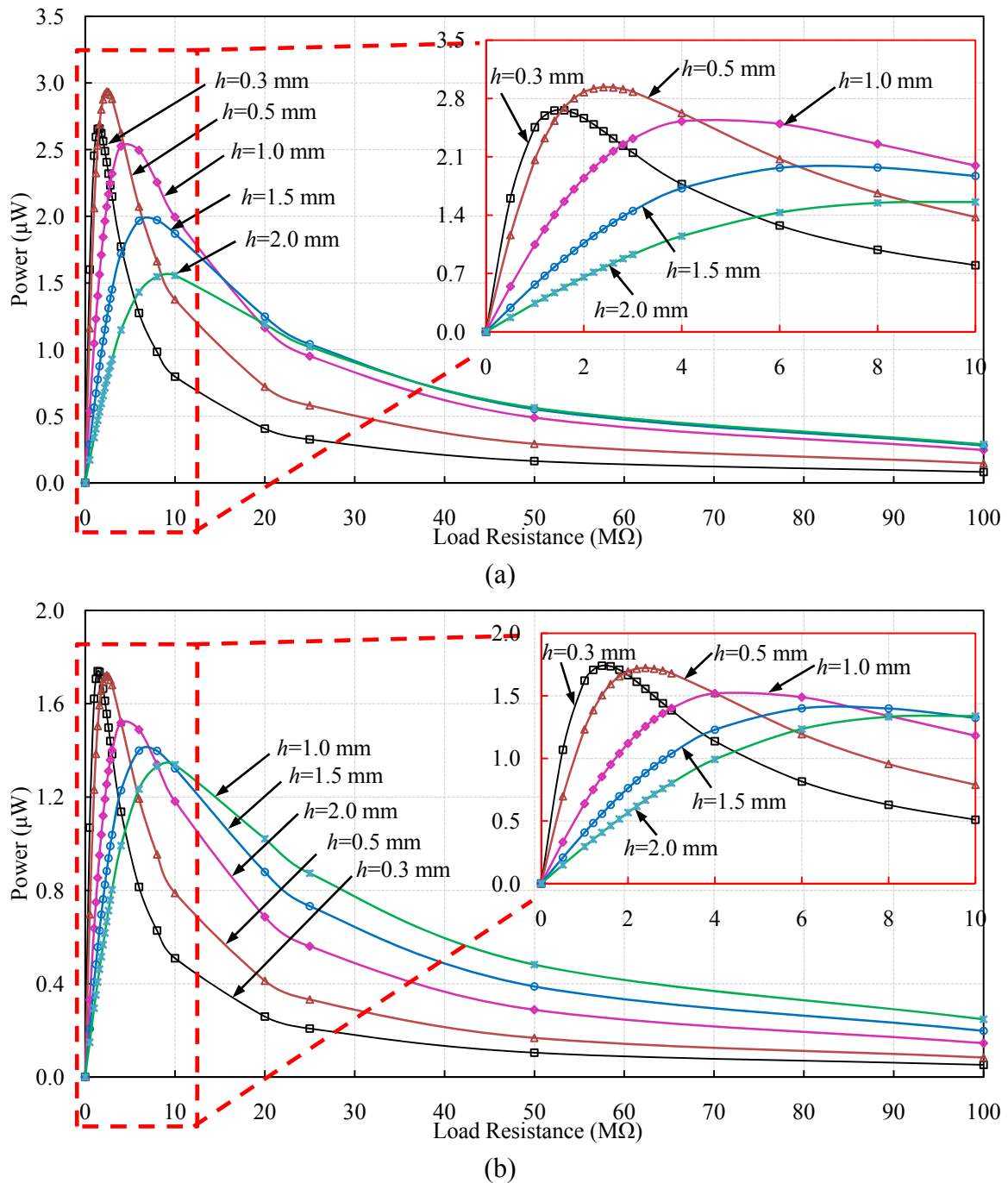
to energy harvesting to study the effect of external electrical load, thickness/ stiffness of the bond layer and the patch's size. The numerical results correspond to a sinusoidal load of magnitude 75 N acting at the natural frequency (22.7 Hz) of the RC beam, applied over an area  $150 \times 400$  m at its centre, as stated earlier. The experimental acceleration at the top of the beam was measured to be  $3.14 \text{ m/s}^2$  and the one resulting from the simulation to be  $4.724 \text{ m/s}^2$ . Detailed results are presented in the following sub sections.

#### 7.4.1 Effect of External Load Resistance

The variation of the close circuit power generated by the SBPS and the embedded CVS located at the midpoint of the RC beam was studied by attaching a load resistance ( $R_L$ ) across the PZT patch in each configuration, as shown in Figure 7.6. Table 7.1 may be referred for dimensional and material parameters of the PZT patches. The variation of the close circuit RMS power, the voltage and the current with increasing the load resistance for different piezo thickness ( $h$ ) for the SBPS and the embedded CVS are shown in Figure 7.7(a) and (b), respectively. From the figures, it can be observed that both the SBPS and the CVS exhibit similar trends, with the power output from the CVS being less (upto nearly 60%) of that of the SBPS. The value of optimum load resistance for which the RMS power attains maximum value can be observed to increase with the piezo thickness ( $h$ ) for both the SBPS and the embedded CVS, manifest as the shifting of the peak towards right. Due to the fact that the PZT patch has very high impedance, the values of optimum load resistance lie between a range of  $1 \text{ M}\Omega$  to  $10 \text{ M}\Omega$  for both the SBPS and the embedded CVS, typically very close to the electrical impedance of the PZT patch determined at 22.7 Hz (operating frequency) from the numerical analysis, signifying impedance matching.

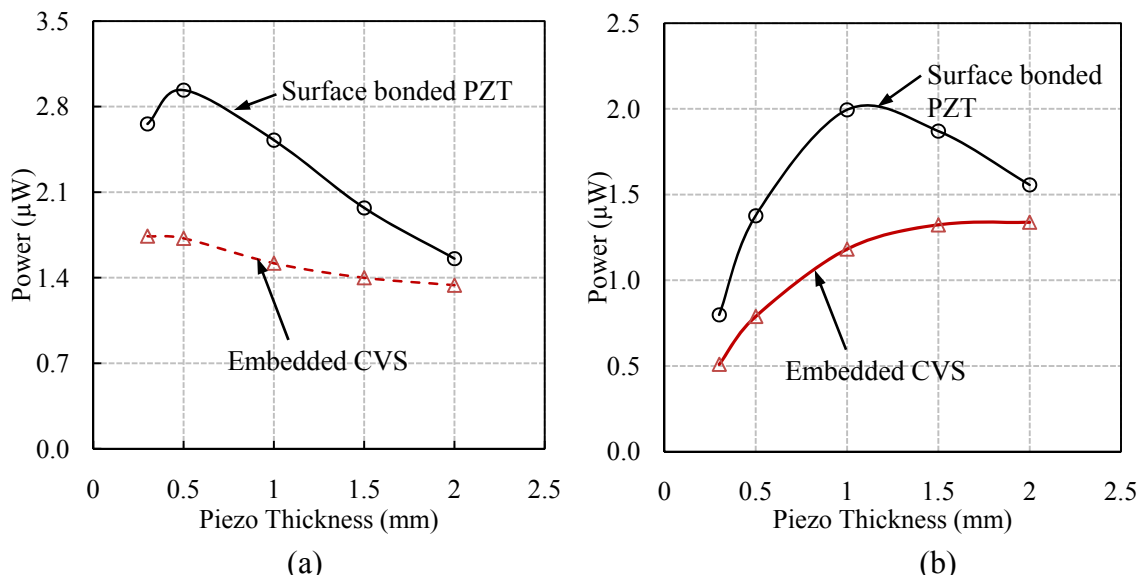


**Figure 7.6:** Load resistance attached across the (a) SBPS and (b) embedded CVS.



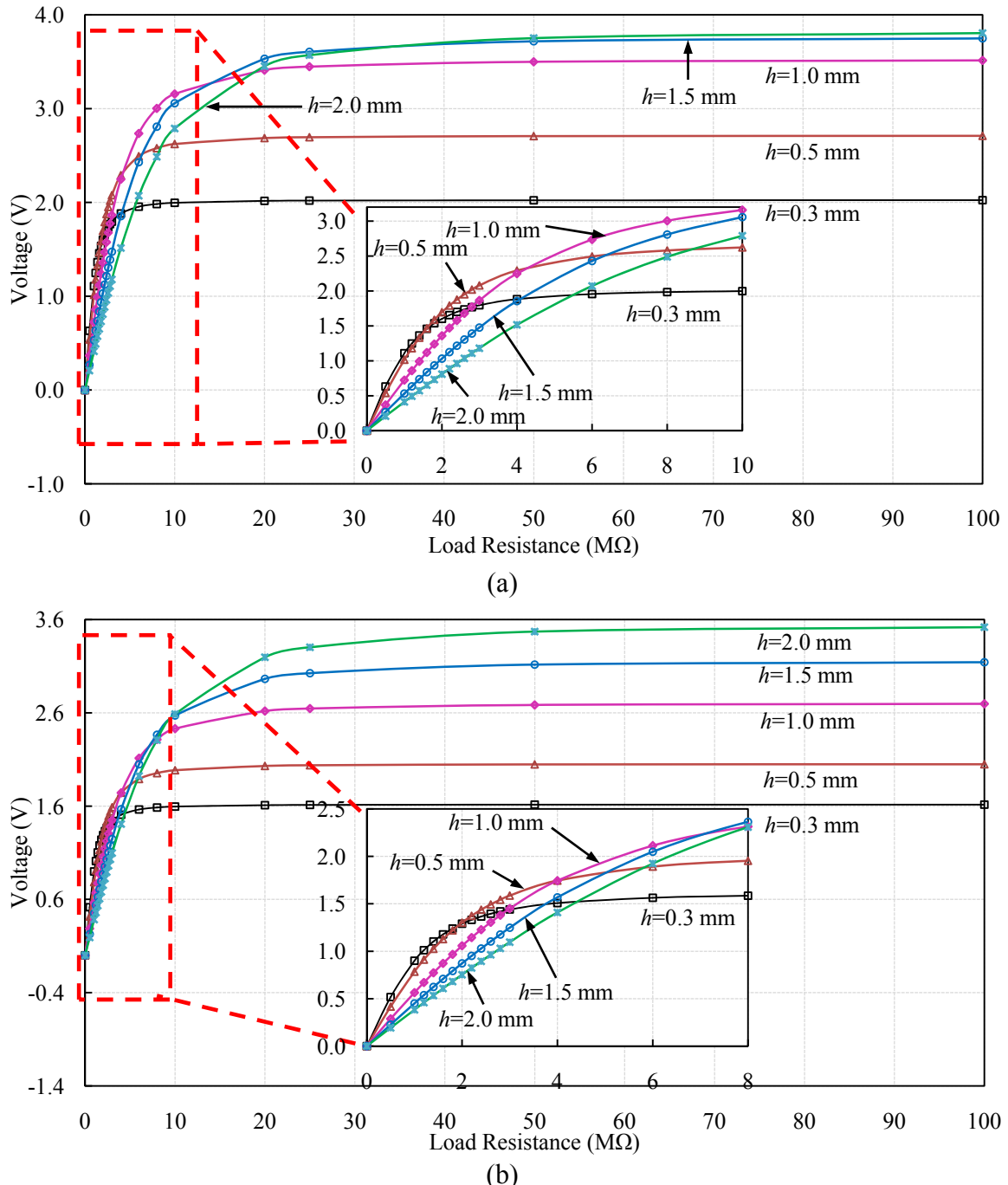
**Figure 7.7:** RMS power for varying load resistance across  
 (a) SBPS and (b) embedded CVS.

The peak values of the close circuit RMS power generated by the SBPS and the embedded CVS for varying piezo thickness ( $h$ ) are shown in Figure 7.8(a). It can be observed that with increase in the piezo thickness ( $h$ ), the close circuit RMS power initially increases, attains a maximum value for  $h=0.5$  mm, and then reduces for SBPS. However, the close circuit RMS power generated by the embedded CVS reduces monotonically with increase in the piezo thickness (tends to be asymptotic to  $1.4 \mu\text{W}$ ). Also, it can again be noted that the close circuit RMS power generated by the SBPS is higher than the embedded CVS, with the gap reducing with increase in PZT patch's thickness. Figure 7.8(b) shows the RMS power corresponding to a fixed load  $R_L=10 \text{ M}\Omega$ . Here, it can be observed that the power output is higher for thicker piezos, both for the SBPS and the embedded CVS, up to 1mm thickness. Thereafter, it is decreasing for the SBPS and asymptotic to  $1.3 \mu\text{W}$  for the embedded CVS. It can be concluded that for sufficiently high load resistance, increasing piezo thickness is somewhat beneficial with regard to power output, especially for the CVS.



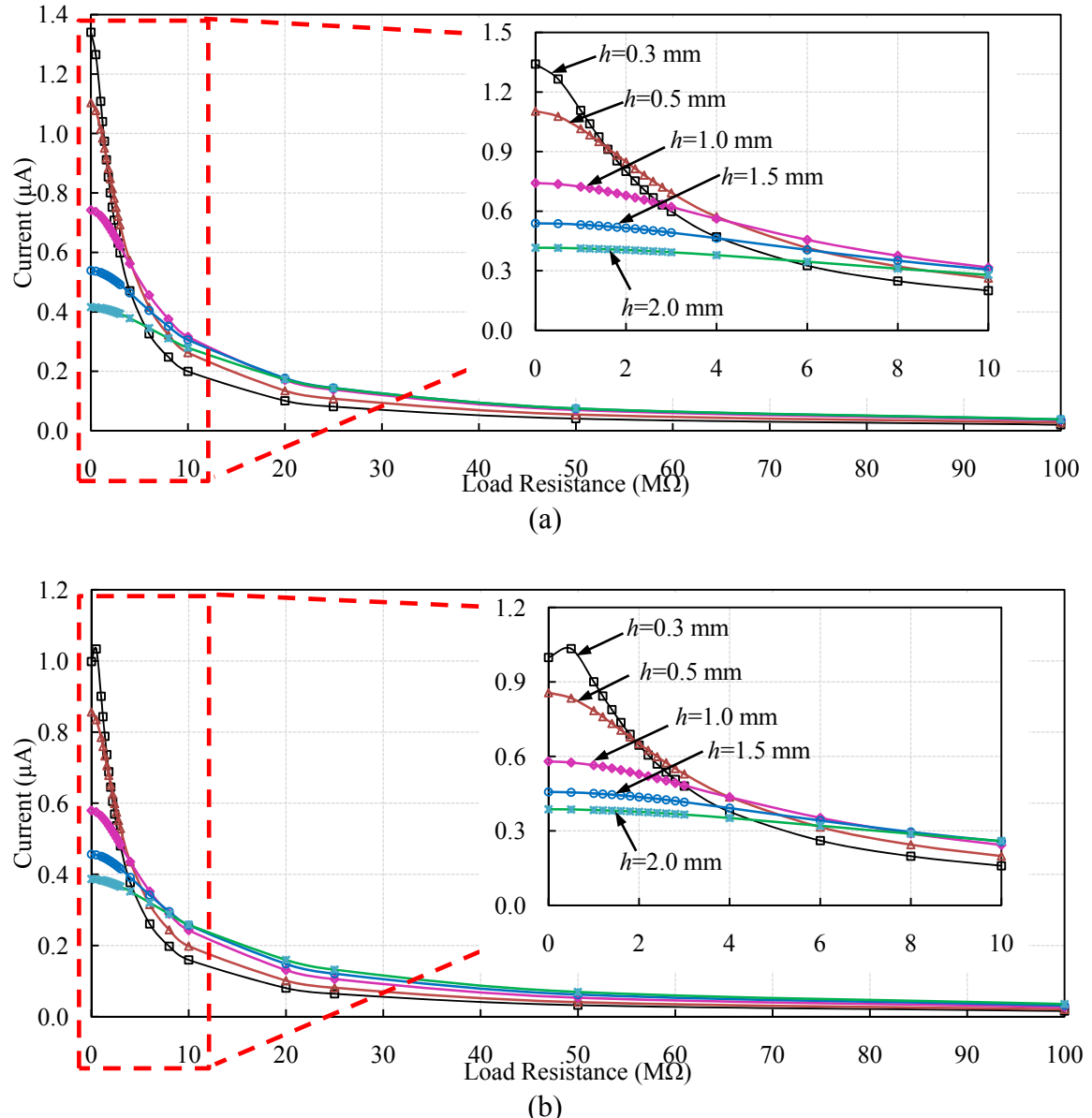
**Figure 7.8:** Variation of (a) maximum power and (b) power corresponding to load resistance,  $R_L = 10 \text{ M}\Omega$  generated by SBPS and embedded CVS with varying piezo thickness.

Figure 7.9 shows the variation of the open circuit RMS voltage across the SBPS and the embedded CVS with the external load resistance. The voltage can be observed to asymptotically increase with load resistance, the maximum value being higher for thicker PZT patches. At sufficiently high value of the load resistance, the difference in the open circuit voltages generated by the SBPS and the embedded CVS is only marginal.



**Figure 7.9:** RMS voltage varying with load resistance across  
(a) SBPS and (b) embedded CVS.

Figure 7.10 compares the RMS current flowing in the circuit, the value of which sharply declines with increase in the load, finally reaching an asymptotic value of zero, which is obvious. This decrease is responsible for the post peak behaviour of power output observed in Figure 7.7.



**Figure 7.10:** RMS current varying with load resistance across  
 (a) SBPS and (b) embedded CVS.

### 7.4.2 Effect of Piezo and Bond Thicknesses

The next parametric study has been performed to study the effect of varying piezo thickness ( $h$ ), for different adhesive bond layer thickness ( $t_s$ ), on the RMS voltage generated by the SBPS and the embedded CVS. The results are shown in Figure 7.11. Here, the perfect bonding case represents an ideal situation, where there is no bond layer and hence no strain differential between the PZT patch and the host structure (RC beam). From Figure 7.11(a), the RMS voltage generated by the SBPS for different adhesive thicknesses ( $t_s$ ) can be observed to increase with piezo thickness ( $h$ ) upto 2 mm, and becoming asymptotical thereafter. Lesser the adhesive thickness, the higher the RMS voltage generated by the SBPS, with the case of perfect bonding representing the upper bound. The observed behaviour can be explained from the fact that the induced strain transmission from the structure to the sensor takes place via the bond layer through shear lag mechanism (Bhalla, 2004). This reduces with bond thickness, hence the observed trend of lower voltage with increasing  $t_s$ . Further, the adhesively bonded SBPS has force transmission from one face (lower one) only. Therefore, the beneficial effect of larger piezo thickness tends to saturate beyond a certain piezo thickness ( $h= 2$  mm here). Hence, it can be concluded that for the SBPS, the thickness of the patch may be chosen less than 2 mm and that of the adhesive be kept minimum possible from practical considerations.

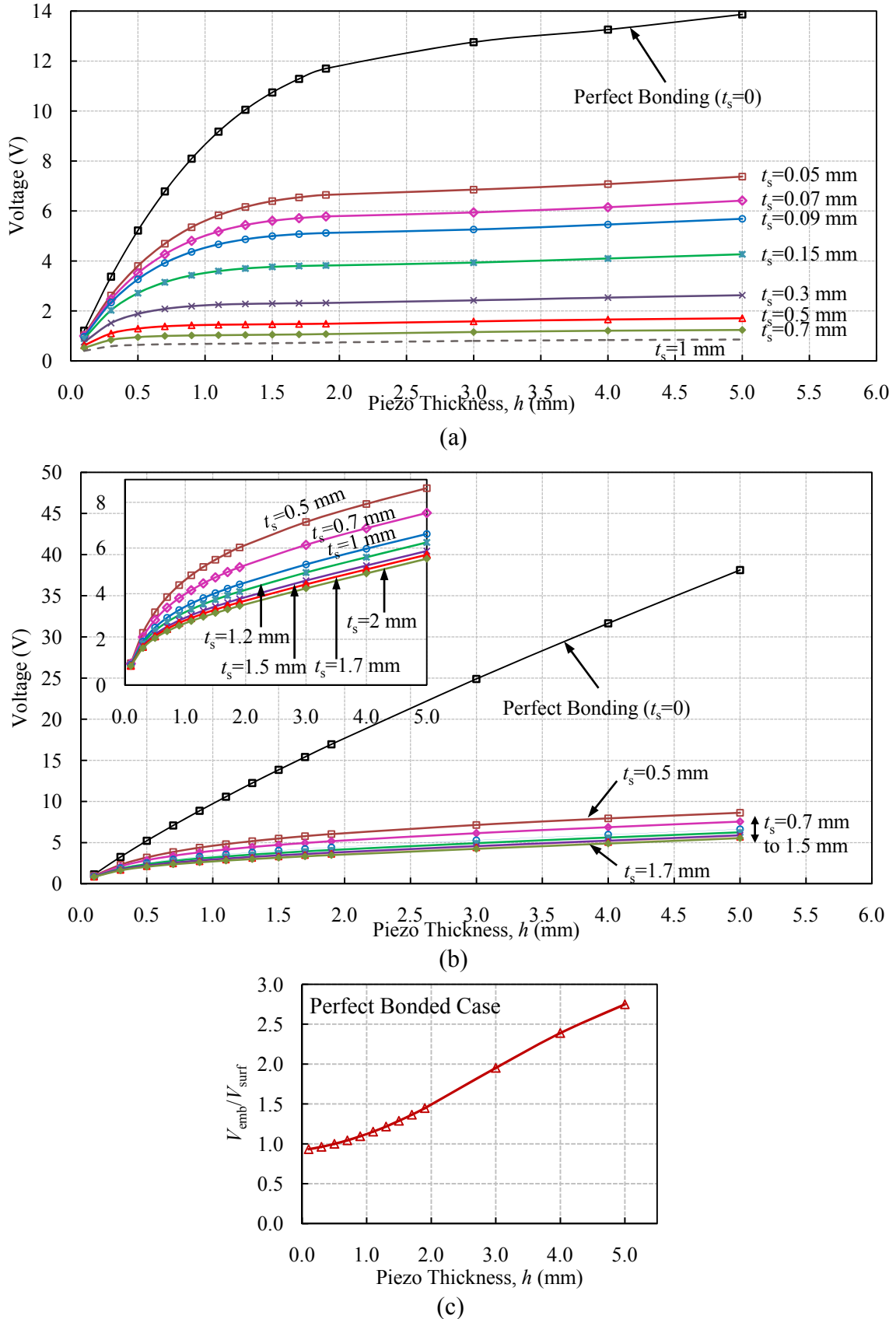


**Figure 7.11:** Voltage generated by (a) SBPS (b) embedded CVS, with constant adhesive bond layer thickness ( $t_s$ ); and (c) ratio of voltage generated by perfectly bonded embedded CVS and SBPS for varying piezo thickness ( $h$ ).

Figure 7.11(b) shows the corresponding trend for the embedded CVS. On contrary to the SBPS, the RMS voltage generated by the embedded CVS is somewhat more sensitive to piezo thickness, which clearly imposes a pronounced beneficial effect. For further clarity, the perfect bonded case has been suppressed to observe the effect of different adhesive layers in a separate plot within Figure 7.11(b). The RMS voltage can be seen to increase with increase in the piezo thickness for the entire selected range even up to  $h= 5$  mm. The better behaviour as compared to SBPS results from the fact that the strain is transferred from the structure to the PZT patch from both sides (top and bottom). However, the slope of the curve reduces with increasing bond thickness ( $t_s$ ), becoming almost constant after  $t_s = 1.5$  mm. The effect of increasing adhesive thickness can be observed to be similar to that of SBPS [Figure 7.11(a)], that i.e. reducing voltage, for reasons similar to the SBPS. The effect of increasing adhesive thickness on the RMS voltage generated by the embedded CVS becomes less and less dominant as the adhesive thickness approaches a value of 1.5 mm. The reason is lesser and lesser force transmission to the sensor from top and bottom via the thick adhesive bond layer, with predominant force transmission occurring from the two side edges of the patch only. The ratio of the RMS voltage generated by the SBPS and the embedded CVS  $\left[ \left( V_p \right)_E / \left( V_p \right)_S \right]$  for perfectly bonded case with varying piezo thickness ( $h$ ) is shown in Figure 7.11(c). It can be observed that the ratio is less than unity till  $h=0.5$  mm and thereafter, it becomes greater than unity. Hence, it can be concluded that the RMS voltage generated by the embedded CVS will be lesser than that of SBPS till  $h= 0.5$  mm and will become higher afterwards.

The variation of the RMS voltage generated by the SBPS and the embedded CVS with varying piezo thickness considering the adhesive thickness in various fractions of the piezo thickness is shown in Figure 7.12. It should be noted that here, the adhesive

thickness is considered as a fixed fraction of piezo thickness (instead of constant value as considered above) while analyzing the effect of increasing piezo thickness.

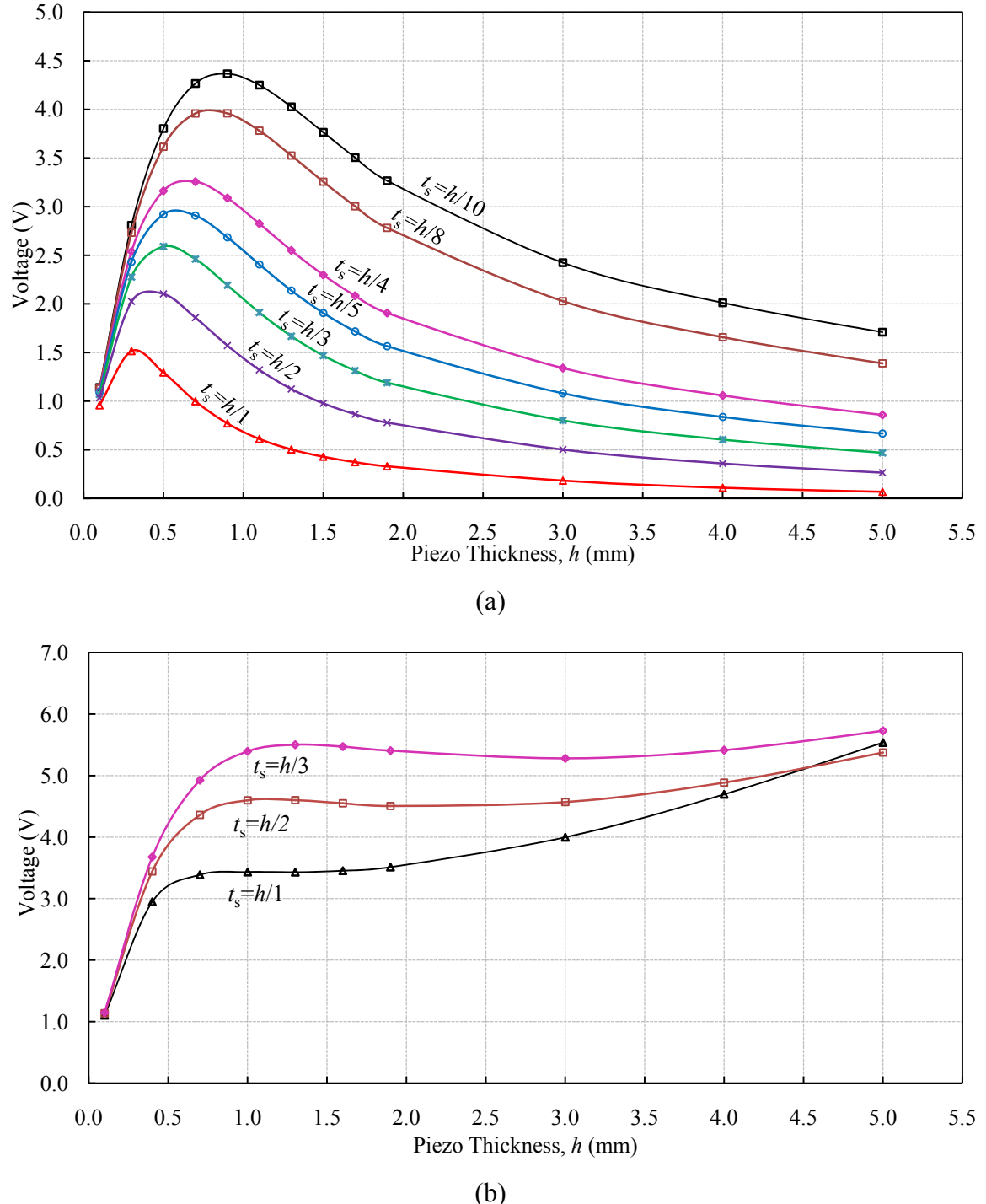


**Figure 7.12:** Voltage generated by (a) SBPS and (b) embedded CVS, with varying piezo thickness ( $h$ ) for adhesive bond layer thickness ( $t_s$ ) in a fixed ratio of ' $h$ '.

It is observed from the figure that with increasing piezo thickness, the RMS voltage generated by the SBPS [Figure 7.12(a)] initially increases, attains a maximum value, and then starts reducing. An optimum value of the piezo thickness for which maximum RMS voltage is generated (for all the adhesive thicknesses considered here) lies between 0.3 mm to 1 mm. It can again be concluded that lesser the adhesive thickness, higher the RMS voltage generated by SBPS, resulting in the most appropriate adhesive thickness ( $t_s$ ) to be minimum possible (here  $t_s=h/10$ ). For embedded CVS, the thickness of adhesive was varied between  $h/3$  to  $h/1$ , because reducing the adhesive thickness beyond  $h/3$  was not practical due to FE modelling limitations. Contrary to SBPS, the RMS voltage generated by the embedded CVS (for different adhesive thickness in fraction of ' $h$ ') increases with increasing piezo thickness and then became almost uniform [Figure 7.12(b)]. The maximum RMS voltage generated by embedded CVS is again for minimum possible adhesive thickness (here  $t_s=h/3$ ). It should be noted that unlike the SBPS, the embedded CVS shows somewhat higher consistency, uniformity and stability with regard to the voltage generated over the range of thicknesses considered. In general, thickness above 1 mm for PZT patch is found to be optimal, resulting in higher voltage output than the SBPS.

#### 7.4.3 Effect of Piezo's Plan Dimensions

The effect of increasing the size ( $L_p \times L_p$ ) of the square PZT patch on the voltage generated by it has also been investigated. The variation of the RMS voltage generated by the SBPS and the embedded CVS with varying piezo size ( $L_p \times L_p$ ) for different piezo thicknesses ( $h$ ) is shown in Figure 7.13(a) and (b), respectively. The adhesive bond layer thickness ( $t_s$ ) has been considered to be a constant value of 0.15 mm. The investigation was done for five different sizes of PZT patch: 10 × 10 mm, 13×13 mm, 15×15 mm,

18×18 mm and 20×20 mm, for various piezo thicknesses from 0.1mm to 3mm. From the figures, it is apparent that increasing the size of the PZT patch results in an increase of the RMS voltage generated by both the SBPS and the embedded CVS. This is because larger surface area implies higher average strain transmitted to the patch, the maximum strain lag being restricted near the ends of the patch. Though the increase in surface area increases the RMS voltage, its overall sensitivity for damage may reduce due to reduction in the net sensing zone. Hence, the plan area of the patch has to be decided upon as per the particular application. In case of the SBPS [Figure 7.13(a)], the voltage gradient can be observed to increase with increasing the piezo thickness initially and then reduce. This happens due to the fact that the mechanism of force transmission in the SBPS is via only one contact surface area (bottom surface of the patch), with the top surface remaining stress free. Hence, increasing the PZT patch's thickness beyond certain value (here  $h= 3$  mm) is not helpful from the point of view of the voltage output. On the other hand, for the embedded CVS [Figure 7.13(b)], increasing the PZT patch's thickness can be observed to consistently result in higher RMS voltage generated by it. This is because the force transfer from the structure to the PZT patch occurs from both top and bottom surfaces. Similar plots [Figure 7.13(c) and (d)] of the RMS voltage generated by the SBPS and the embedded CVS have been drawn to observe the effect of increasing piezo size ( $L_p \times L_p$ ) and thickness ( $h$ ) together, when the adhesive thickness ( $t_s$ ) was fixed as a fraction of ( $h$ ), i.e.  $t_s=h/10$  and  $h/3$  for SBPS and embedded CVS, respectively. The RMS voltage can be observed to increase with increasing surface area of the PZT patch. The main difference here is that the RMS voltage starts reducing with increasing piezo thickness for SBPS beyond a certain value of  $h$  [Figure 7.13(c)], which, on the contrary, tends to reach a limiting value when the epoxy thickness is maintained a fixed value (instead of a fraction of  $h$ ) [Figure 7.13(a)]. This trend is very similar to the one observed in Figure 7.12(a). For

the embedded CVS [Figure 7.13(d)], the RMS voltage tends to reach an asymptotic value with increasing PZT thickness, especially for areas larger than  $15 \times 15\text{mm}$ . This is again similar to the earlier observed trend in Figure 7.12(b). To observe the effect of increasing PZT thickness and size more clearly, Figure 7.14 has been plotted in a different manner, by changing its abscissa to PZT size so as to clearly distinguish the effect of  $h$ .

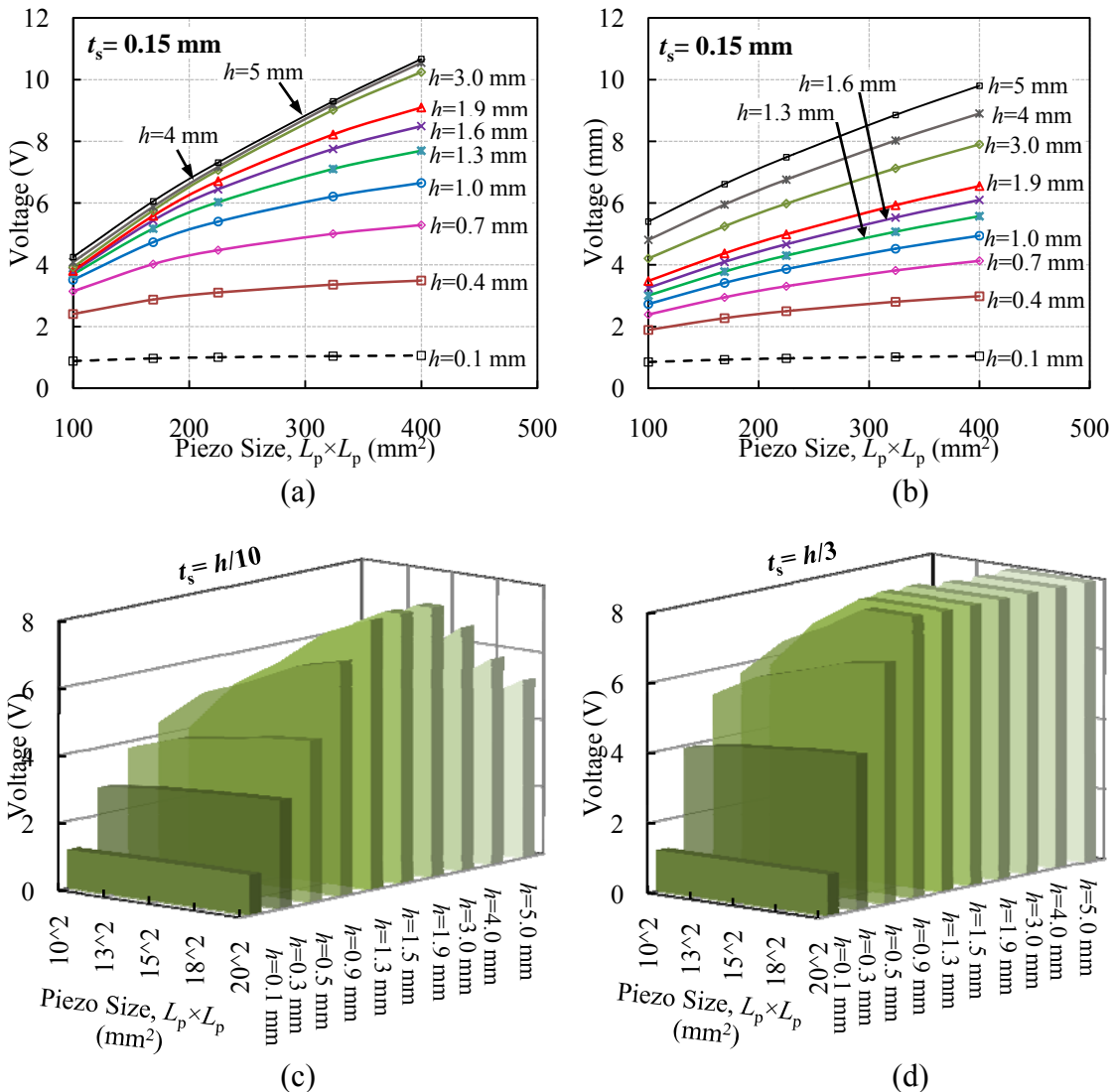


**Figure 7.13:** (a) Voltage generated by SBPS with varying piezo size ( $L_p \times L_p$ ) for different piezo thickness ( $h$ ), [*adhesive thickness*,  $t_s = 0.15\text{ mm}$ ].  
 (b) Voltage generated by embedded CVS with varying piezo size ( $L_p \times L_p$ ) for different piezo thickness ( $h$ ), [ $t_s = 0.15\text{ mm}$ ].  
 (c) Voltage generated by SBPS with varying piezo size ( $L_p \times L_p$ ) for different piezo thickness ( $h$ ), [ $t_s = h/10$ ].  
 (d) Voltage generated by embedded CVS with varying piezo size ( $L_p \times L_p$ ) for different piezo thickness ( $h$ ), [ $t_s = h/3$ ].

Comparison of Figure 7.14(a) with Figure 7.14(b) and Figure 7.14(c) with Figure 7.14(d) clearly indicates the beneficial and stability effect (voltage reaching a constant value), respectively, of both the piezo-thickness as well as the overall area, on the voltage output for the embedded CVS in comparison to the SBPS.

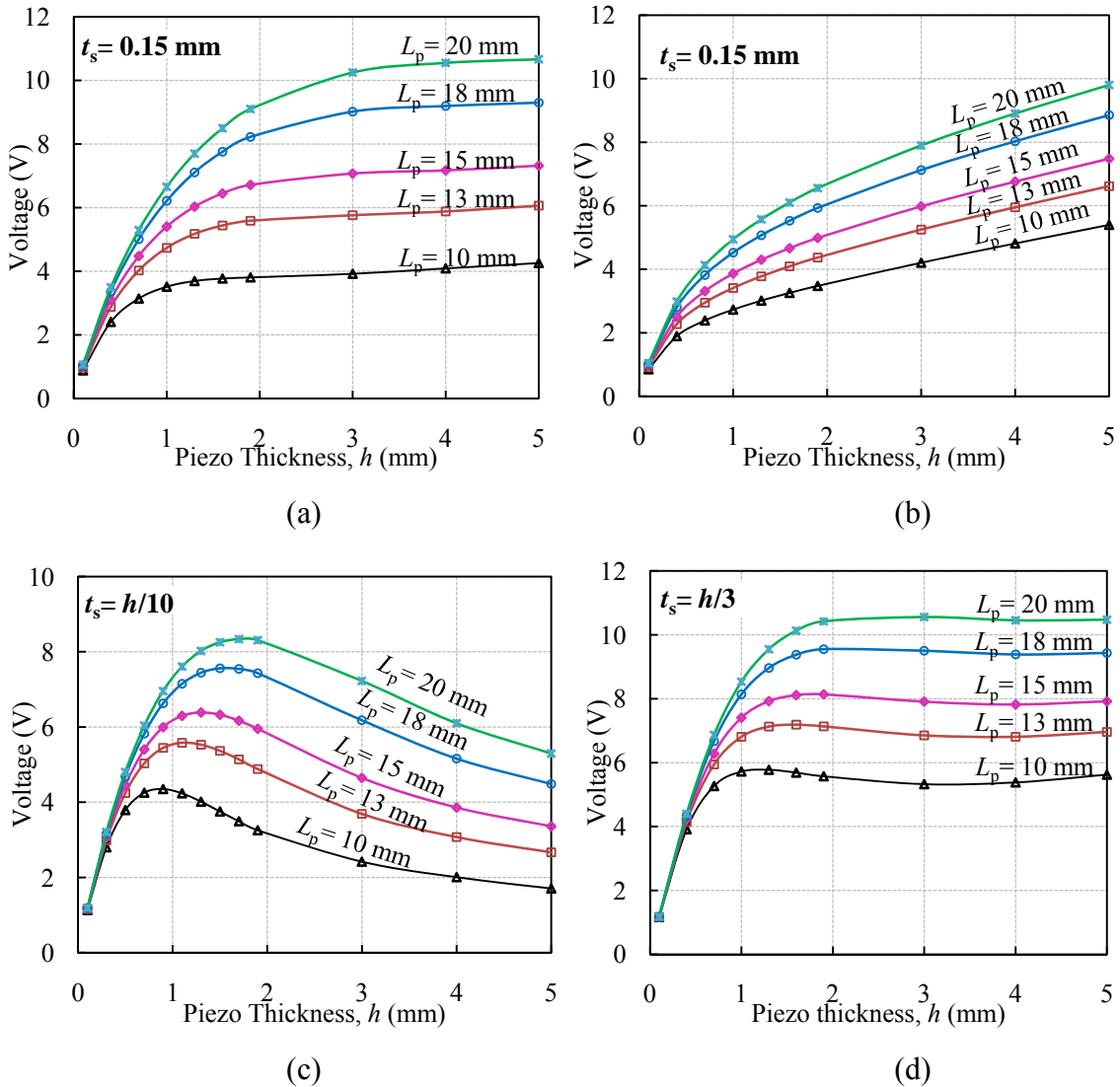


**Figure 7.14:** (a) Voltage generated by SBPS with varying piezo thickness ( $h$ ) for different areas of PZT patch ( $L_p \times L_p$ ), [adhesive thickness,  $t_s = 0.15 \text{ mm}$ ].  
 (b) Voltage generated by embedded CVS with varying piezo thickness ( $h$ ) for different areas of PZT patch ( $L_p \times L_p$ ), [ $t_s = 0.15 \text{ mm}$ ].  
 (c) Voltage generated by SBPS with varying piezo thickness ( $h$ ) for different areas of PZT patch ( $L_p \times L_p$ ), [ $t_s = h/10$ ].  
 (d) Voltage generated by embedded CVS with varying piezo thickness ( $h$ ) for different areas of PZT patch ( $L_p \times L_p$ ), [ $t_s = h/3$ ].

#### 7.4.4 Effect of Shear Modulus of Adhesive

The shear modulus ( $G_s$ ) of the adhesive layer also plays an important role in PZT-structure interaction and hence the voltage generated by both the SBPS and the embedded CVS (Bhalla and Soh, 2004e). So, an investigative study has been done to analyze the effect of increasing shear modulus by considering  $G_s = 0.05$  GPa, 0.5 GPa, 1.0 GPa and 1.5 GPa, along with different adhesive thicknesses. The piezo thickness ( $h$ ) has been kept same as 0.3 mm for both the SBPS and the embedded CVS. The results are shown in Figure 7.15. It can be observed that with increase in the shear modulus of the adhesive bond layer, the RMS voltage increases for both the SBPS and the embedded CVS. This is because a higher shear modulus implies better bonding of the PZT patch with the host structure and consequently higher strain transfer to the patch. The perfect bonded case, which has the RMS voltage equal to 3.4 V and 3.2 V respectively, for the SBPS and the embedded CVS, serves as the upper bound. It can be noted that the initial gradient of the plot increases sharply with reduction in adhesive thickness and then tends to become zero, especially for the SBPS [Figure 7.15(a)]. For higher adhesive thickness, somewhat linear increase in the RMS voltage can be observed. In overall, the effect of higher shear modulus is much more pronounced for the SBPS as compared to the embedded CVS.

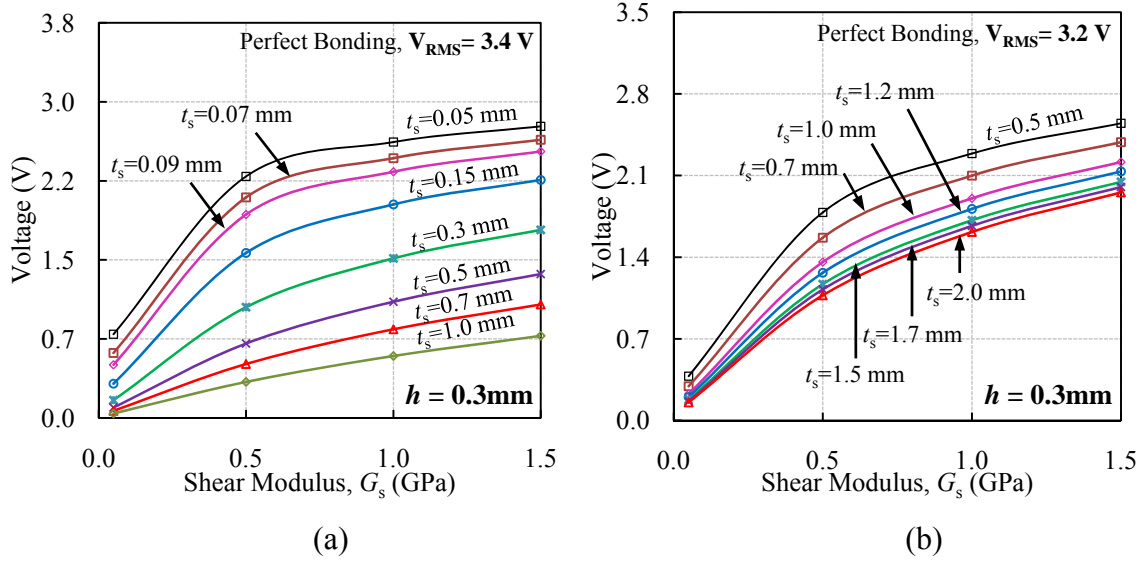


**Figure 7.15:** (a) Voltage generated by SBPS with varying shear modulus ( $G_s$ ) of adhesive for different adhesive thickness, [piezo thickness,  $h = 0.3 \text{ mm}$ ].  
 (b) Voltage generated by embedded CVS with varying shear modulus ( $G_s$ ) of adhesive for different adhesive thickness, [ $h = 0.3 \text{ mm}$ ].

#### 7.4.5 Effect of Adhesive Covering on Surface Bonded PZT Sensor

The PZT patches, whether employed for SHM or energy harvesting, are bound to be influenced by environmental effects, such as temperature fluctuations and humidity, when bonded on the real-life structures. Hence, they need a protection layer especially when they are surface bonded on a structure. As compared to the embedded CVS, the SBPS is susceptible to environmental exposure and hence the associated degradation. This can be effectively checked by covering the SBPS with a layer of epoxy adhesive as protection. Effect of covering the SBPS with a layer of adhesive of 2 mm has been investigated here. The adhesive layer thickness ( $t_s$ ) for bonding the PZT patch with the host structure (RC beam) has been fixed as 0.15 mm. In this study, the results of the bare and the covered SBPS have been compared with the embedded CVS for varying piezo thickness. The variation of the RMS voltage with increasing piezo thickness for the bare and the covered SBPS is shown in Figure 7.16(a). It can be observed that covering the SBPS with adhesive appreciably increases the RMS voltage generated by it. This is because in the

bare PZT patch, the top surface of the patch is unrestrained and strain transfer occurs from the bottom face only. However, it gets suitably restrained when covered with an additional layer of adhesive on its top, resulting in better transfer of forces from all the sides. Also, it can be observed that for the bare SBPS, the RMS voltage initially increases and then became almost constant with increase in piezo thickness. However, for the adhesive covered SBPS, the RMS voltage increases throughout the whole range of the piezo thickness. Its behaviour starts resembling that of the embedded CVS, in which the voltage increases with increase in piezo thickness, as observed earlier in Figure 7.11(b). The ratio of the voltage generated by the embedded CVS and the SBPS with varying piezo thickness when the surface PZT is bare and covered is shown in Figure 7.16(b). Since, the voltage attains a constant value after the piezo thickness of 2 mm for bare SBPS [see Figure 7.11(a)], whereas the voltage for the embedded CVS keeps increasing with piezo thickness [see Figure 7.11(b)], the ratio  $\left[ \left( V_p \right)_E / \left( V_p \right)_S \right]$  became greater than unity when the piezo thickness is increased beyond 2 mm. For the covered SBPS, the ratio  $\left[ \left( V_p \right)_E / \left( V_p \right)_S \right]$  is always less than unity, due to the higher voltage generated by the covered SBPS.

This study shows that the beneficial effects of embedding can be partially achieved by covering the PZT patch with an adhesive layer. From practical point of view, the embedded CVS is ready to use and packaged in nature, hence, it does not warrant a high installation skill from the user. The SBPS, on the other hand, requires skilled hands for installation so as to achieve derived results.

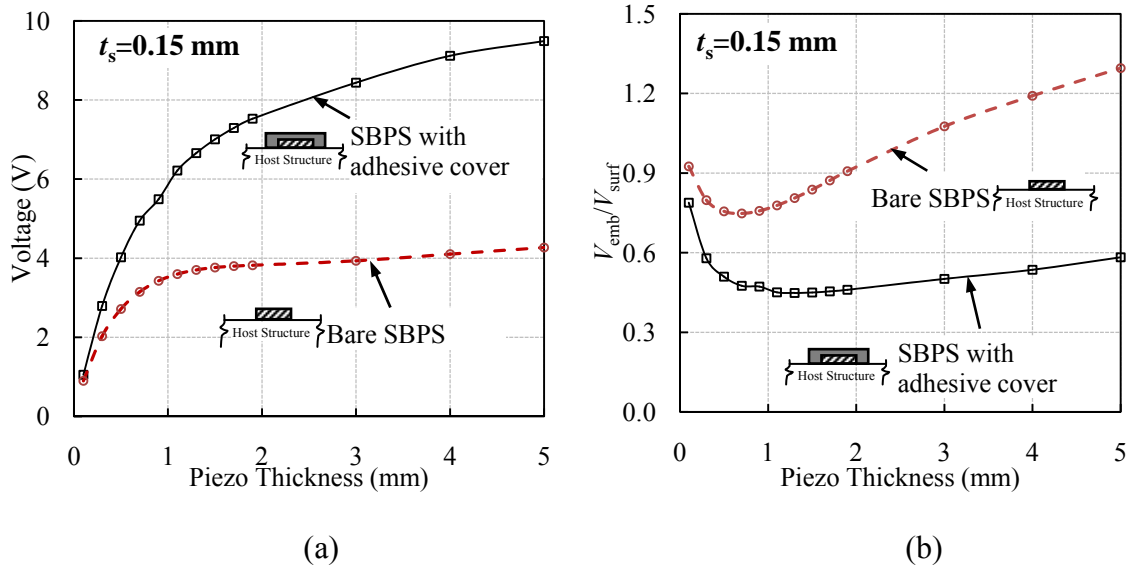


**Figure 7.16:** (a) Voltage generated by SBPS for varying piezo thickness with and without cover of adhesive layer over its top.  
 (b) Ratio of voltage generated by embedded CVS and SBPS for varying piezo thickness with and without cover of adhesive layer over its top.

#### 7.4.6 Effect of Adhesive Covering on EMI signature

The effect of covering the SBPS with a protective layer on its EMI signature has been investigated experimentally. A two part Araldite epoxy adhesive with shear modulus of elasticity of 1 GPa (Moharana and Bhalla, 2012) was used as a protective layer over the surface bonded PZT patches. The complete set-up for the experiment is shown in Figure 7.17. Three PZT patches were bonded on the surface of the RC beam at CVS location 9, 10 and 11 (refer Figure 4.6 for details). The thickness of the protective layer was maintained between 1.5 and 2 mm. The protective layer was kept undisturbed for a period of 24 hours to ensure its complete setting. The conductance and susceptance signatures of the PZT patches were acquired using conventional LCR meter (Agilent E4980A) (Agilent Technologies, 2014) for a frequency range of 50 kHz to 400 kHz at an RMS voltage of 1 V for both the cases i.e. bare PZT patch and when it was covered with protective layer. The comparison of the conductance and the susceptance signatures with and without

protective layer over the surface bonded PZT patch at (a) location 9 (b) location 10 and (c) location 11 are shown in Figure 7.18.

From these figures it can be observed that with addition of the protective adhesive layer, an increase in the slope of conductance signature occurs for all the sensors throughout the frequency range. Significant increase of conductance slope can be especially observed in the frequency range of 110 Hz to 150 Hz, with the effect being similar to that caused by an overall increase in the electric permittivity of the PZT bond combination. However, the susceptance plots exhibit opposite trend with addition of protective layer over the sensors. The slope of the susceptance plots tends to reduce throughout the frequency range, and somewhat appreciably in the frequency range of 110 Hz to 150 Hz.

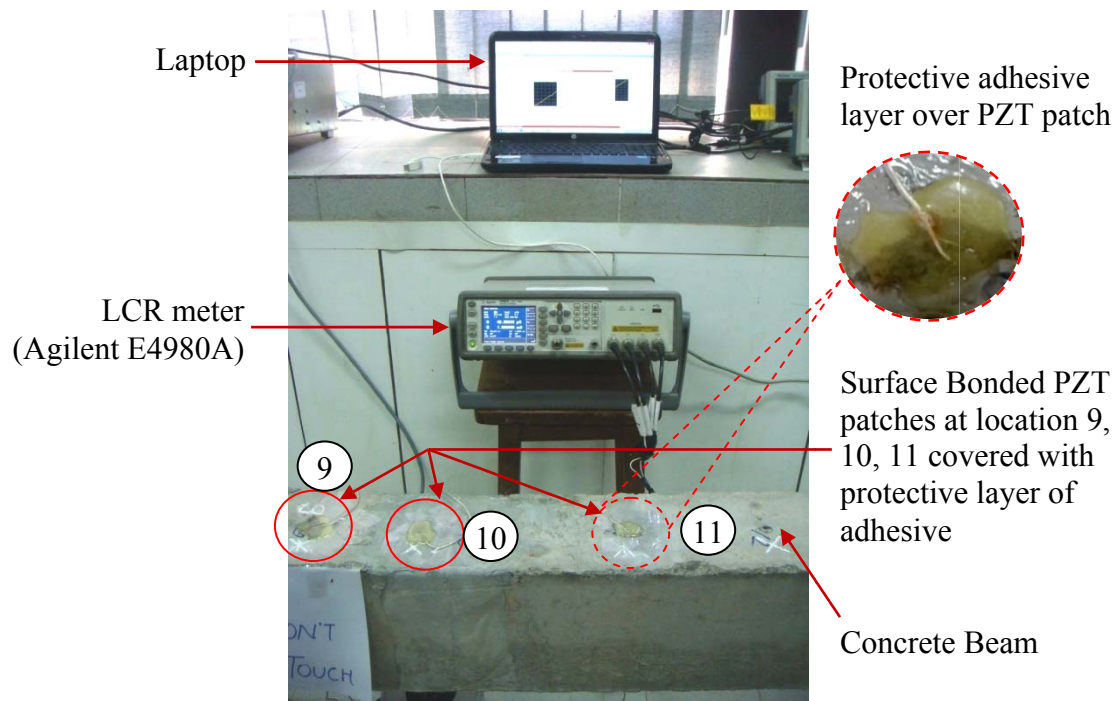


**Figure 7.17:** Experimental set-up for acquiring EMI signatures of surface bonded PZT patches.

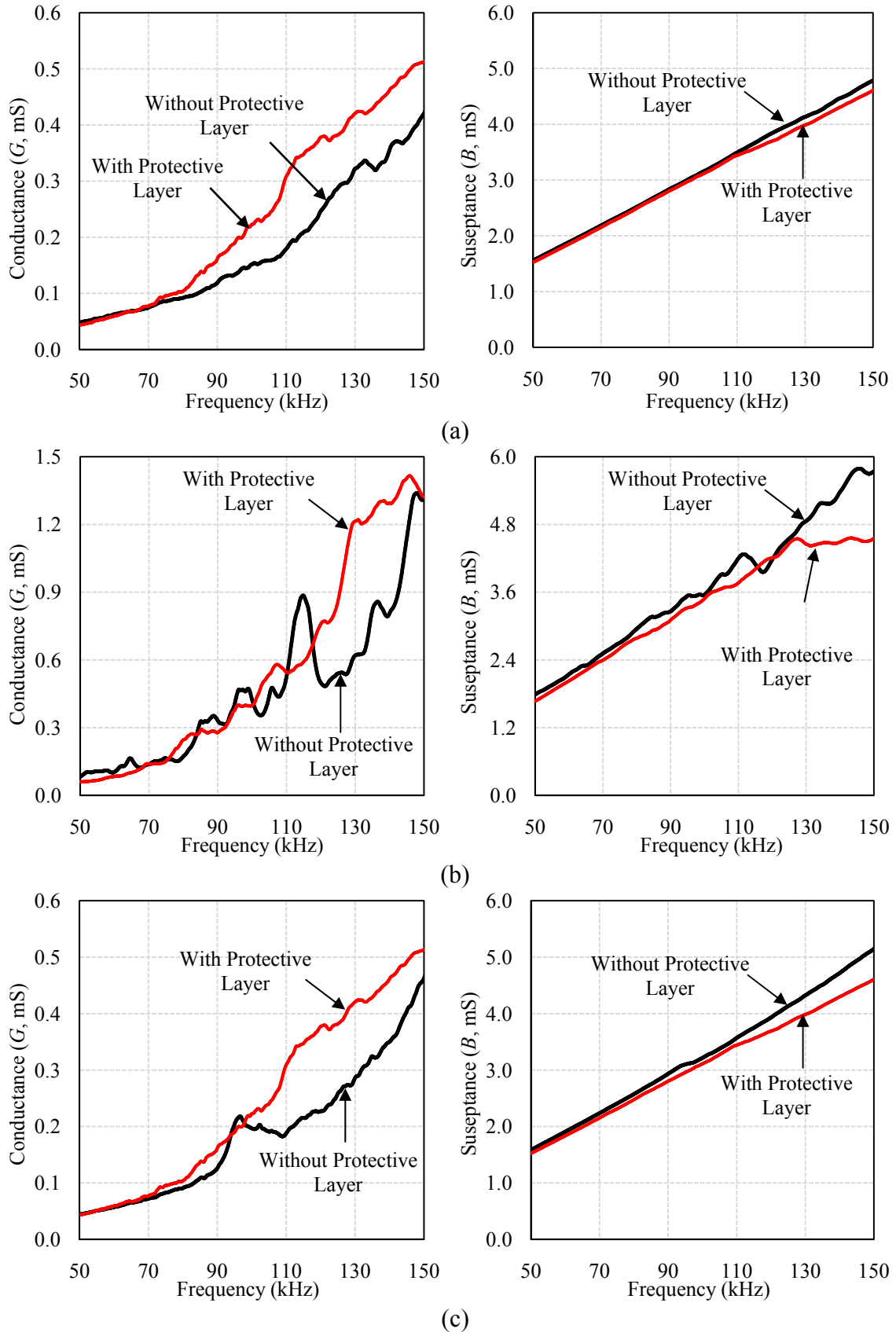


**Figure 7.18:** Comparison of conductance and susceptance signatures with and without protective layer over the sensors for surface bonded PZT patch at (a) location 9, (b) location 10 and (c) location 11.

This experiment suggests that since a protection layer is necessary to protect the PZT patches against external environmental conditions in the actual field applications, due importance should be given to its effect on the signature of the PZT patch. Also, the change in the slope of conductance and susceptance should not be interpreted as damage indication.

## 7.5 SUMMARY AND CONCLUDING REMARKS

In this chapter, the quantum of energy harvestable by the SBPS and the embedded CVS has been determined for a typical real-life sized structure, a 4 m long RC beam using finite element (FE) method and comparisons made. This chapter has presented a numerical approach to perform a parametric study to study the effect of various parameters, including PZT patch's geometric parameters, the adhesive layer's thickness and the stiffness on the power generated by it. Two configurations- conventional SBPS and embedded CVS have been considered. The conductance and susceptance signatures of a free PZT patch have been compared with the analytical and experimental results to validate the FE modelling. In addition, the voltages generated by the SBPS and the embedded CVS have been compared with the experimental results (Chapter 4) and found acceptably close. The power generated by the SBPS and embedded CVS for varying load resistance across the PZT patch has been investigated for different patch thicknesses. Due to the fact that the PZT patch has very high impedance, the values of optimum load resistance lie in a range of  $1 \text{ M}\Omega$  to  $10 \text{ M}\Omega$  for both the SBPS as well as the embedded CVS, typically equal to the electrical impedance of the bonded patch. It has been found that with increase in the piezo thickness, the close circuit RMS power initially increases and then reduces for the SBPS. For embedded CVS, it exhibits increasing trend. Also, it can be noted that the close circuit RMS power generated by the SBPS is higher than the

embedded CVS. Effect of increasing the PZT patch's thickness and the adhesive bond layer thickness has also been studied for the SBPS and the embedded CVS and compared with the perfect bonded case. For the SBPS, the thickness of the patch and the adhesive bond layer should be chosen less than 2 mm and 0.15 mm (or lowest practical value), respectively. The RMS voltage increases with increase in the piezo thickness for the entire selected range for the embedded CVS, showing a stable trend. The advantageous effect of the increasing the piezo thickness on the RMS voltage generated by the SBPS becomes lesser and lesser after a piezo thickness of 1.5 mm. An optimum value of the piezo thickness for which maximum RMS voltage is generated by the SBPS (for all the adhesive thickness considered) lies between 0.3 mm to 1 mm. Thickness above 1 mm is found to be optimal for embedded CVS, resulting in higher voltage output than the SBPS. The RMS voltage increases by reducing the adhesive bond layer thickness for both SBPS and CVS. For both the SBPS and the embedded CVS, increasing the size of PZT results in increase of the RMS voltage for all piezo thicknesses. Covering the SBPS with an adhesive layer is beneficial not only from the point of view of protection of the patch but also from power considerations. Increase in the shear modulus of the adhesive bond layer is beneficial for both the SBPS and the embedded CVS in terms of higher voltage.

Although embedded configuration results in smaller power output, it offers advantage in form of the beneficial effects of the higher piezo thickness, besides practical advantages. Increasing the PZT thickness beyond certain value (here  $h= 1.5$  mm) is not beneficial for the RMS voltage generated by SBPS. On the other hand, increasing thickness consistently increases the RMS voltage for the embedded CVS. Hence, using PZT patch in the form of CVS both for SHM and energy has good practical potential. This piezo will act as energy harvester when not in use and shall carry out SHM utilizing its own harvested energy

later. The results of the study will be beneficial in optimizing energy harvesting from thin PZT patches in surface bonded or embedded configurations.

The next chapter will provide the conclusions and the future recommendations derived from this thesis.

## **Chapter 8**

# **CONCLUSIONS AND RECOMMENDATIONS**

### **8.1 INTRODUCTION**

This thesis embodies findings from the research carried out for combined energy harvesting and SHM potential of thin PZT patches on civil infrastructure. Specifically, a major objective of the research was to explore the energy harvesting capabilities of a simple low-cost PZT patch bonded for SHM and operating in the simple  $d_{31}$ -mode. The energy harvesting potential has also been explored on several real-life bridges, ideal candidates for this purpose, based on the reported vibration measurements and the electro-mechanical formulations developed in this thesis. The previous studies, on the other hand, have considered the piezo sensors in special configurations (such as stack and bimorph), which are somewhat expensive for energy harvesting. The research presented in this thesis has considered axial strain actuation, which is the most natural form of excitation for energy harvesting in addition to SHM. The major novelty in the present research is that for the first time, proof-of-concept experimental demonstration has been provided to employ the same PZT patch for SHM as well as energy harvesting in  $d_{31}$ -mode. Both surface-bonded as well as embedded configurations have been considered. This dual functioning piezo acts as energy harvester when not in use and carries out SHM whenever necessary utilizing its own harvested energy. Hence, energy harvesting has been explored and successfully demonstrated through simplest structural configuration, without any secondary structure, which has been avoided in order to circumvent any extra burden on the structure in terms of cost, functionality and performance.

The following sections outline the major contributions, conclusions and recommendations stemming out from this research.

## 8.2 RESEARCH CONCLUSIONS AND CONTRIBUTIONS

Major research conclusions and contributions are summarized below:

- (i) The proof-of-concept feasibility of energy harvesting using a thin surface-bonded PZT patch operating in the  $d_{31}$ -mode has been explored experimentally and successfully demonstrated in laboratory set up. A coupled electro-mechanical model, considering the losses associated with the PZT patch and the bond layer, has been derived and validated with experimental measurements. The model has been extended to embedded configuration employing CVS, duly considering the piezo-bond-structure interaction, which is much different in this configuration.
- (ii) The feasibility of combined SHM and energy harvesting using specially designed embedded PZT patch (CVS) operating in the axial mode has also been explored and experimentally established on a prototype RC beam emulating a real-life structure.
- (iii) Comparison of the power generated by the surface bonded PZT patch and the embedded CVS has been investigated analytically and validated experimentally. Typically, the CVS is found to be capable of generating about 60% power as compared to its counterpart bonded in a steel structure subjected to same order of magnitude of acceleration. Proof-of-concept experimental demonstration has been provided for CVS to be able to identify and localize damage ranging from incipient to severe nature using a combination of global dynamic and local EMI techniques based on its own harvestable energy.

- (iv) The coupled electro-mechanical model has been first extended to a typical real-life city flyover, modelled through FEM, to estimate the energy harvesting capability in the real-life structures. It is estimated that two day operation of the PZT patch for energy extraction is sufficient enough to enable one time operation of AD5933 (Analog Device, 2014) for acquisition of SHM related data in surface-bonded configuration. As CVS, the scavenging time would be approximately two and half days. Hence, using the PZT patch both for SHM and energy harvesting in real-life structures is certainly feasible.
- (v) The coupled electro-mechanical models for surface-bonded and embedded patches have been extended to eight real-life bridges across the world. It has been estimated that Low power consuming circuits like typical A/D convertor, such as TMP 112 (Texas Instruments, 2014) would warrant energy harvesting for 1 second and 2.5 minutes when powered by a surface bonded PZT patch on steel bridge and an embedded CVS in a RC bridge, respectively. It is further estimated that on an average, a period of less than 21 minutes for steel bridges and about 2.2 days for RC bridges (as CVS) will be needed for the thin piezo based harvester to harvest sufficient energy so as to enable one signature acquisition of AD5933. With the ongoing developments in electronics, as lesser power consuming circuits are emerging, it is believed that the energy scavenging time will drastically come down.
- (vi) A numerical study has been undertaken to carry out a detailed parametric investigation to study the effect of various parameters, including PZT geometric parameters and the adhesive layer's thickness and stiffness, on the power generated by the piezo patch. An optimum value of piezo thickness for which maximum RMS voltage is generated by the SBPS (for all the adhesive thickness

considered) lies between 0.3 mm to 1 mm. Thickness above 1 mm is found to be optimal for embedded CVS, resulting in higher voltage output than the SBPS. The results of the study will be beneficial in optimizing energy harvesting from thin PZT patches in surface bonded or embedded configurations. For the SBPS, the thickness of patch and adhesive bond layer should be chosen less than 2 mm and 0.15 mm (or lowest practical value), respectively. The RMS voltage increases with increase in the piezo thickness for the entire selected range for the embedded CVS, showing a stable trend. The advantageous effect of the increasing the piezo thickness on the RMS voltage generated by the SBPS becomes lesser and lesser after a piezo thickness of 1.5 mm.

- (vii) The effect of covering the SBPS with a protective layer on its energy harvesting capability and EMI signature has been investigated experimentally. Covering the SBPS with an adhesive layer is beneficial not only form the point of view of protection of the patch but also from power considerations. Hence, due importance should be given to its effect on the signature of the PZT patch and the change in the slope of conductance and susceptance on account of covering should not be interpreted as damage indication.
- (viii) The strength gain and fatigue characteristics of a real-life sized RC simply supported beam have been monitored using the embedded CVS. The monitoring was done by investigating two aspects of the beam, the global parameters (natural frequency) and the local parameters (piezo identified equivalent stiffness), while the beam was subjected to continuous vibrations, totalling  $9.303 \times 10^6$  cycles. Embedded CVS, owing to its unique packaging, was able to detect the reduction in the strength of the RC beam due to the development of fatigue induced micro cracks and possible rebar-concrete debonding, based on

both the global and the local parameters. This is a first of its kind proof-of-concept demonstration of long term monitoring by CVS in addition to energy harvesting.

- (ix) This study has focused on using the normal piezos in place of commercial expensive transducers for energy harvesting in the strain mode. This piezo will act as energy harvester when not in use and shall carry out SHM utilizing its own energy harvesting. Hence, successful demonstration of simple type PZT patch both for SHM and energy harvesting in real-life structures is the major new and original contribution of this thesis.

### **8.3 RECOMMENDATIONS FOR FUTURE WORK**

The author believes that the following areas can be explored further in future in this research field:

- (i) The present study has only provided a proof-of-concept demonstration of energy storage. Storage of the energy generated by PZT patch is an important issue due to very small value of the current (typically microamperes) generated by the PZT patches. Further research can be possibly extended in this area, especially from electronics point of view.
- (ii) Research can be carried out to enhance the energy generated by PZT patches. This could be possible with development of piezo materials with higher  $d_{31}$  and lower  $\varepsilon_{33}$ . In addition, optimum configurations need to be explored so as to minimize shear lag losses, by either highly stiff adhesives or some geometrical configurations.

- (iii) In the present work, the embedded sensors are tested in a position resting at an angle  $0^\circ$  with the ground in the present research. Different angles ( $45^\circ$  and  $90^\circ$ ) can be explored for maximizing its utility for both SHM and energy harvesting.  $45^\circ$  orientation could enable excitation of both  $d_{31}$  and  $d_{33}$  modes.  $90^\circ$  orientation will imply manifestation of the  $d_{33}$  mode.
- (iv) Fatigue phenomenon in RC structures is presently a very little explored area. The initial fatigue experiments conducted in this research clearly establish the high potential of CVS as long term fatigue monitoring sensor on bridges and other infrastructure. This calls for more lab as well as field experiments for establishing suitable fatigue assessment model based on CVS.
- (v) The present research work has basically extrapolated the lab benchmark studies and the electro-mechanical formulation on real-life bridges. Future studies could focus on instrumenting of actual structures and carrying out field measurements of actual harvestable power.

It is believed that the findings of this thesis will aid the future researchers and also enable the industry to develop standard SHM cum energy scavenging modules utilizing  $d_{31}$ -mode.

## **AUTHOR'S PUBLICATIONS**

### **INVENTION DISCLOSURE:**

**Kaur**, N. and Bhalla, S. (2014), "A novel energy harvesting solution for reinforced concrete structures", *Invention disclosure, Foundation for Innovation and Technology Transfer (FITT)*, IIT Delhi, (*under process of filing*, submitted on 30<sup>th</sup> October, 2014, approved for filing patent on February 25<sup>th</sup>, 2015). This invention disclosure is byproduct of thesis, refer Appendix E.

### **INTERNATIONAL JOURNALS:**

1. **Kaur**, N. and Bhalla, S. (2014), "Feasibility of energy harvesting from thin piezo sensor patches via axial strain actuation mode", **Journal of Civil Structural Health Monitoring**, Vol. 4, pp 1-15. (*Based on Chapter 3 of thesis*). [\[link\]](#)
2. **Kaur**, N. and Bhalla, S. (2014), "Combined energy harvesting and structural health monitoring potential of embedded piezo concrete vibration sensors", **Journal of Energy Engineering, American Society of Civil Engineers (ASCE)**, accepted on July 7<sup>th</sup>, 2014, published online, DOI: [10.1061/\(ASCE\)EY.1943-7897.0000224](https://doi.org/10.1061/(ASCE)EY.1943-7897.0000224). **8<sup>th</sup> 'Most Read Article'** as on 5<sup>th</sup> May, 2015 (*Based on Chapter 4 of thesis*).
3. Suresh, R., Bhalla, S., Singh, C., **Kaur**, N., Hao, J. and Anand, S. (2014), "Integrated use of PZT and FBG sensors for improved plantar pressure monitoring", **Technology and Health Care**, Vol. 23, pp. 47-61, DOI: [10.3233/THC-140867](https://doi.org/10.3233/THC-140867). (*This paper is a byproduct of thesis*)
4. **Kaur**, N., Bhalla, S., Panigrahi, R. and Shanker, R. (2015), "Evaluation of miniature impedance chip for structural health monitoring of prototype steel/ RC structures based on EMI technique", **Experimental Techniques**, accepted on Jan 20<sup>th</sup>, 2015, *in press*. (*Based on Chapter 4 of thesis*).

5. Kaur, N. and Bhalla, S. (2014), "Numerical investigations on energy harvesting from adhesively bonded thin PZT patches in surface bonded/ embedded configurations", **Sensors and Actuators A: Physical**, *under review*. (*Based on Chapter 7 of thesis*).
6. Kaur, N., Matsagar, V.A. and Nagpal, A.K. (2012), "Earthquake response of mid-rise to high-rise buildings with friction dampers", **International Journal of High-Rise Buildings, CTBUH**, Vol. 1(4), pp. 311-332. (*Based on author's M. Tech. thesis*). [\[link\]](#)
7. Negi, P., Kaur N., Bhalla, S. and Chakraborty, T. (2015) "Experimental Strain Sensitivity Investigations on Embedded PZT Patches in Varying Orientations", **The Indian Concrete Journal**, Vol. 89(1), pp. 87-90. (*This paper was originally part of the Proceedings of Structural Engineering Convention, December 22-24<sup>th</sup>, 2014*) [\[link\]](#)
8. Kaur, N. and Bhalla, S. "Fatigue damage assessment and monitoring curing of RC structures using embedded PZT sensors", **Strain: An International Journal for Experimental Mechanics**, *under preparation*. (*Based on Chapter 6 of thesis*).
9. Kaur, N., Singamsetty, S., Dasari, M. and Bhalla, S. "New paradigms in energy harvesting from structural vibrations and wind using piezo transducers", **Journal of Intelligent Materials and Smart Structures**, *under preparation*.

#### INTERNATIONAL CONFERENCE:

1. Bhalla, S., Srivastava, S., Suresh, R., Moharana, S., Kaur, N. and Gupta, A. (2015), "Application of Structural Health Monitoring Technologies to Bio-Systems: Current Status and Path Forward", **SPIE International Conference on Smart Structures NDE**, March 8<sup>th</sup>-12<sup>th</sup>, San Diego, California.
2. Bhalla, S., Suresh, R., Moharana, S., Visalakshi, T., Kaur, N. and Naskar, S. (2015), "Multi-Disciplinary Applications Of Piezo-Sensors: Structural Health

Monitoring, Bio-Mechanics And Energy Harvesting”, **SPIE International Conference on Smart Structures NDE**, March 8<sup>th</sup>-12<sup>th</sup>, San Diego, California.

3. Kaur, N. and Bhalla, S. (2014), “New Paradigms in Piezoelectric Energy Harvesting from Civil Structures”, **9<sup>th</sup> Biennial International Workshop on Structural Engineering Convention (SEC)**, Indian Association for Structural Engineering (IASE), December 20<sup>th</sup>-21<sup>st</sup>, IIT Delhi, India, pp. 2601-2614. [[link](#)]
4. Negi, P., Kaur, N., Bhalla, S. and Chakraborty, T. (2014), “Experimental Strain Sensitivity Investigations on Embedded PZT Patches in varying orientations”, **9<sup>th</sup> Biennial International Workshop on Structural Engineering Convention (SEC)**, Indian Association for Structural Engineering (IASE), December 20<sup>th</sup>-21<sup>st</sup>, IIT Delhi, India, pp. 2615-2620. [[link](#)]
5. Kaur, N. and Bhalla, S. (2014), “Monitoring Strength Gain and Fatigue Damage of RC Structure Using Embedded PZT Sensors”, **7<sup>th</sup> ISSS International Conference on Smart Materials, Structures and Systems**, July 8<sup>th</sup>-11<sup>th</sup>, Indian Institute of Science (IISc.) Bangalore, India.
6. Singamsetty, S., Kaur, N., and Bhalla, S. (2014), “Energy Harvesting from Structural Vibrations Using Piezo transducers: A Parametric Study”, **3<sup>rd</sup> International Conference on Sustainable Innovative Techniques In Architecture, Civil and Environmental Engineering (SITACEE - 2014)** organized by "Krishi Sanskriti", April 26<sup>th</sup>-27<sup>th</sup>, Jawaharlal Nehru University, New Delhi, India, pp. 331-334.
7. Kaur, K., Singmasetty, S., Dasari M. and Bhalla, S. (2014), “Piezoelectric Energy Harvesting Potential through Built Up and Simple Configurations under Mechanical Vibrations”, **9<sup>th</sup> International Symposium on Advanced science and Technology in Experimental Mechanics (9th ISEM)**, November 1<sup>st</sup>-6<sup>th</sup>, Hotel Jaypee Siddharth, New Delhi, India.

8. Bhalla, S., **Kaur, N.**, Naskar, S. (2014), "Virtual Smart Structures and Dynamics Lab: Towards Teaching Advanced Concepts Online", **9<sup>th</sup> International Symposium on Advanced science and Technology in Experimental Mechanics (9th ISEM)**, November 1<sup>st</sup>-6<sup>th</sup>, Hotel Jaypee Siddharth, New Delhi, India.
9. **Kaur, N.**, Bhalla, S., Gupta, N. and Jain, N. (2013), "Integrated Global Vibration and Low Cost EMI Technique for Structural Health Monitoring of RC Structures using Embedded PZT Patches", **UK-India Education and Research Initiative, UKIERI Concrete Congress, Innovations in Concrete Construction**, March 5<sup>th</sup>-8<sup>th</sup>, NIT Jalandhar, Punjab, India, pp. 1620-1629.
10. **Kaur, N.** and Bhalla, S. (2013), "Feasibility for Energy Harvesting from Surface Bonded/Embedded Piezo-Patches in Addition to Structural Health Monitoring", **9<sup>th</sup> IWSHM International Workshop on Structural Health Monitoring**, September 10<sup>th</sup>-12<sup>th</sup>, Stanford University, Stanford, CA – USA, pp. 2600-2605. [link]
11. Talakokula, V., Dhawan, S.K., Srivastava, S., **Kaur, N.**, Moharana, S., Bhalla, S., Bhattacharjee, B. and Gupta, A. (2013), "Recent Advances in Structural Health Monitoring based on EMI technique at IIT Delhi", **International Conference on Trends and Challenges in Concrete Structures (TRACCS)**, December 19<sup>th</sup>-21<sup>st</sup>, CPWD Training Institute, Ghaziabad, UP, India.
12. **Kaur, N.**, Matsagar, V.A. and Nagpal, A.K. (2011), "Earthquake Response of Medium-Rise to High-Rise Buildings with Friction Dampers", **18<sup>th</sup> ICSV International Congress on Sound and Vibration**, July 10<sup>th</sup>-14<sup>th</sup>, Rio de Janeiro, Brazil.
13. **Kaur, N.**, Matsagar, V.A. and Nagpal, A.K. (2011), "Tuned Mass Damper on Base-Isolated Building under Near-Fault Earthquakes", **21<sup>st</sup> SMiRT International Conference on Structural Mechanics in Reactor Technology**, November 6<sup>th</sup>-11<sup>th</sup>, Indian Habitat Centre, New Delhi, India, pp. 2535-2542.

---

## **INVITED LECTURES**

1. **Delivered a lecture** on “Integrated Structural Health Monitoring and Energy Harvesting Potential of Thin Piezo Patch” at IIT Delhi during Research Scholar’s Day, **awarded for ‘Best Oral Presentation’** among all research scholars at IIT Delhi, April 10<sup>th</sup>, 2015.
  
2. **Delivered a lecture** on “Introduction to Virtual Smart Structures and Dynamic Lab at IIT Delhi”, **The School of Engineering and Technology (SoET)-IGNOU**, **broadcasted on National Television Channel**, ‘Gyan Darshan’, **Indira Gandhi National Open University (IGNOU)**, April 20<sup>th</sup>, 2014.
  
3. **Delivered a lecture** on “Virtual Smart Structures and Dynamic Lab”, QEEE pilot program sponsored by **Ministry of Human Recourse and Development (MHRD), Govt. of India, IIT Delhi**, March 25<sup>th</sup>, 2014.
  
4. **Delivered a lecture** on “Integrated Structural Health Monitoring and Energy Harvesting from Thin Piezo Sensor Patch via Axial Strain Actuation Mode”, **Workshop on Quality Control of Concrete and Construction Materials Through Testing and Experimental Structural Dynamics, Structural Health Monitoring and Non-Destructive Evaluation using Smart Materials, IIT Delhi**, June 14<sup>th</sup>, 2013.
  
5. **Delivered a lecture** on “Integrated Structural Health Monitoring and Energy Harvesting from Thin Piezo Sensor Patch via Axial Strain Actuation Mode”, **Workshop on Experimental Structural Dynamics, Structural Health Monitoring and Non-Destructive Evaluation using Smart Materials, IETE, New Delhi**, October 26<sup>th</sup>, 2013.



## REFERENCES

1. Abdessemed, M., Kenai, S., Bali, A., and Kibboua, A. (2011), “Dynamic analysis of a bridge repaired by CFRP: experimental and numerical modeling”, *Construction and Building Materials*, Vol. 25, pp. 1270-1276.
2. Aggarwal, R. (2009), “Development of piezo-based low-cost dynamic force sensor”, *B.Tech. Thesis*, Department of Civil Engineering, Indian Institute of Technology (IIT) Delhi, India, <http://web.iitd.ac.in/~sbhalla/btechfinalstudent.html>.
3. Agilent Technologies (2014), *Test and Measurement Catalogue*, USA, <http://www.home.agilent.com/>. (Date of access: 01 Nov, 2014)
4. Aktan, A.E., Catbas, F. N., Grimmelmann, K. A. and Tsikos, C. J. (2000), “Issues in infrastructure health monitoring for management”, *Journal of Engineering Mechanics*, Vol. 126, No.7, pp. 711-724.
5. Analog Devices (2014), AD5933 Tech note. [www.analog.com](http://www.analog.com). (Date of access: 07 Oct, 2014)
6. Anamdas, V.G.M. and Yang, Y.W. (2012), “Practical implementation of piezo-impedance sensors in monitoring of excavation support structures”, *Structural Control and Health Monitoring*, Vol. 19, pp. 231-245.
7. Anton, S.R. and Sodano, H.A. (2007), “A review of power harvesting using piezoelectric materials (2003–2006)”, *Smart Materials Structures*, Vol. 16, pp. R1-R21.
8. Artfuldodger (2014), “Piezoelectric energy harvesting” [www.hubpages.com/artfuldodger](http://www.hubpages.com/artfuldodger). (Date of access: 10 Sept, 2014)
9. Asheboa, D.B., Chana, T.H.T., and Yua, L. (2007), “Evaluation of dynamic loads on a skew box girder continuous bridge Part II: Parametric study and dynamic load factor”, *Engineering Structures*, Vol. 29, pp. 1064-1073.
10. Atmel (2014), Products, <http://www.atmel.com/>. (Date of access: 12 Nov, 2014)
11. Avitabile, P. (2001), “Experimental modal analysis-A simple non-mathematical presentation”, *Lecture Notes*, University of Massachusetts Lowell, USA,

[http://innomet.ttu.ee/martin/MER0070/WB/WS9/WS9\\_Bell/Modal\\_Analysis.pdf](http://innomet.ttu.ee/martin/MER0070/WB/WS9/WS9_Bell/Modal_Analysis.pdf).

(Date of access: 24 Nov, 2014)

12. Baker, J., Roundy, S. and Wright, P. (2005), "Alternative geometries for increasing power density in vibration energy scavenging for wireless sensor networks", *Proceedings of the 3<sup>rd</sup> International Energy Conversion Engineering Conference*, San Francisco, CA, USA, August, Vol. 2, pp. 959-970.
13. Banan, M.R., Banan, M.R. and Hjelmstad, K.D. (1994), "Parameter estimation of structures from static response I: Computational aspects", *Journal of Structural Engineering*, ASCE, Vol. 120, No. 11, pp. 3243-3258.
14. Beeby, S.P., Tudor, M.J. and White, N.M. (2006), "Energy harvesting vibration sources for micro systems applications", *Measurement Science and Technology*, Vol. 17, pp. R175-R195.
15. Bhalla, S. and Soh, C.K. (2003), "Structural impedance based damage diagnosis by piezo transducers", *Earthquake Engineering and Structural Dynamics*, Vol. 32, No. 12, pp. 1897-1916.
16. Bhalla, S., (2004), "A mechanical impedance approach for structural identification, health monitoring and non-destructive evaluation using piezo-impedance transducers", *Ph.D. Thesis*, School of Civil and Environmental Engineering, Nanyang Technological University, Singapore.
17. Bhalla, S. and Soh, C.K. (2004a), "High frequency piezoelectric signatures for diagnosis of seismic/blast induced structural damages", *NDT&E International*, Vol. 37, No. 1, pp. 23-33.
18. Bhalla, S and Soh, C.K. (2004b), "Electro-mechanical impedance modeling for adhesively bonded piezo-transducers", *Journal of Intelligent Material Systems and Structures*, Vol. 15, No. 12, pp. 955-972.
19. Bhalla, S. and Soh, C.K. (2004c), "Structural health monitoring by piezo-impedance transducers: modeling", *Journal of Aerospace Engineering*, ASCE, Vol. 17, No. 4, pp. 154-165.

20. Bhalla, S. and Soh, C.K. (2004d), “Structural health monitoring by piezo-impedance transducers: applications”, *Journal of Aerospace Engineering*, ASCE, Vol. 17, No. 4, pp. 166-175.
21. Bhalla, S. and Soh, C.K. (2004e), “Impedance based modelling for adhesively bonded piezo-transducers,” *Journal of Intelligent Material Systems and Structures*, Vol. 15, No. 12, pp. 955-972.
22. Bhalla, S. and Gupta, A. (2007), “A novel vibration sensor for concrete structures.” *Invention disclosure* (FT/IPR/CE/SB/2007/0570), *Foundation for Innovation and Technology Transfer (FITT)*, IIT Delhi, Patent application no. 1011/DEL/2011.
23. Bhalla, S., Kumar, P., Gupta, A. and Datta, T.K. (2009), “Simplified impedance model for adhesively bonded piezo-impedance transducer”, *Journal of Aerospace Engineering* , Vol. 22, No. 4, pp. 373-382.
24. Bhalla, S. and Deb, S.K. (2011), “A cost-effective approach for traffic monitoring using piezo-transducers”, *Experimental Techniques*, pp. 30-34.
25. Bhalla, S. and Moharana, S. (2012), “A refined shear lag model for adhesively bonded piezo-impedance transducers”, *Journal of Intelligent Material Systems and Structures*, Vol. 24, No. 1, pp. 33-48.
26. Bhalla, S., Vittal, A.P.R. and Veljkovic, M. (2012), “Piezo-impedance transducers for residual fatigue life assessment of bolted steel joints”, *Structural Health Monitoring, An International Journal*, Vol. 11, No. 6, pp. 733-750.
27. Boller, C. and Buderath. M. (2007), “Fatigue in aerostructures-where structural health monitoring can contribute to a complex subject”, *Philosophical Transactions in the Royal Society A*, Vol. 365, pp. 561-587.
28. Bressers, S., Avirovik, D., Lallart, M., Inman, D.J. and Priya, S. (2011), “Contactless wind turbine utilizing piezoelectric bimorphs with magnetic actuation”, *Structural Dynamics*, Vol. 3, pp. 233-243.
29. Brownjohn, J.M.W, Moyo, P., Omenzetter, P. and Yong, L. (2003), “Assessment of highway bridge upgrading by dynamic testing and finite element model updating”, *ASCE Journal of Bridge Engineering*, Vol. 8, No. 3, pp. 162-172.

30. Brownjohn, J.M.W., Moyo, P., Omenzetter, P. and Chakraborty, S. (2005), “Lessons from monitoring the performance of highway bridges”, *Structural Control and Health Monitoring*, Vol. 12, pp. 227-244.
31. Calio, R., Rongala, U.B., Camboni, D., Milazzo, M., Stefanini, C., Petris, G. and Oddo, C.M. (2014), “Piezoelectric energy harvesting solutions”, *Sensors*, Vol. 14, pp. 4755-4790.
32. COMSOL (2014), COMSOL Multiphysics Pvt. Ltd. <http://www.comsol.co.in>. (Date of access: 11 Nov, 2014)
33. Cornwell, P.J., Goethal, J., Kowko, J. and Damianakis, M. (2005), “Enhancing power harvesting using a tuned auxiliary structure”, *Journal of Intelligent Material Systems and Structures*, Vol. 16, pp. 825-834.
34. Chao B. (2012), “Making low-voltage energy harvesting practical: Part 1-The history of energy harvesting”, *Electronic Products*, <http://www.electronicproducts.com/>.(Date of access: 11 Oct, 2014)
35. Cheng, B.L. and Reece, R.J. (2001), “Stress relaxation and estimation of activation volume in a commercial hard PZT piezoelectric ceramic”, *Bulletin of Material Science, Indian Academy of Sciences*, Vol. 24, No. 2, pp. 165-167.
36. Chopra, A.K. (2007), “Dynamics of structures”, *Prentice Hall of India Limited*, New Delhi.
37. Churchill, D.L., Hamel, M.J., Townsend, C.P. and Arms, S.W. (2003), “Strain energy harvesting for wireless sensors networks”, *Proceedings of the SPIE Conference on Smart Structures and Materials*, Vol. 5055, pp. 319-327.
38. Dagdeviren, C., Yang, B.D., Su, Y., Tran, P.L., Joe, P., Anderson, E., Xia, J., Doraiswamy, V., Dehdashti, B., Feng, X., Lub, B., Postone, R., Khalpeye, Z., Ghaffarig, R., Huangc, Y., Slepian, M.J. and Rogers, J.A. (2014), “Conformal piezoelectric energy harvesting and storage from motions of the heart, lung, and diaphragm”, *Proceedings of National Academy of Sciences of the United States of America*, Vol. 111, pp. 1927-1932.
39. Das, R. (2014), “Piezoelectric energy harvesting 2013-2023: Forecasts, Technologies, Players”, *Report published by IDTechEx*.

40. duToit, N.E., Wardle, B.L. and Kim, S.G. (2005), “Design considerations for MEMS-scale piezoelectric mechanical vibration energy harvesters”, *Integrated Ferroelectrics*, Vol. 71, pp. 21-160.
41. Delebarre, C., Sainthuile, T., Grondel, S. and Paget, C. (2012), “Power harvesting capabilities of SHM ultrasonic sensors”, *Smart Materials Research*, Vol. 2012, pp. 1-7.
42. Eichhorn, C., Tchagsim, R., Wilhelm, N., Woias, P. (2011), “A smart and self-sufficient frequency tunable vibration energy harvester”, *Journal of Micromechanics and Microengineering*, Vol. 21, pp. 1-11.
43. Erturk, A. and Inman, D.J. (2008), “Issues in mathematical modeling of piezoelectric energy harvesters”, *Smart Materials and Structures*, Vol. 17, Article No. 065016.
44. Ferrari, M., Ferrari, V., Guizzetti, M., Marioli, D. and Taroni, A. (2008) “Piezoelectric multi frequency energy converter for power harvesting in autonomous microsystems”, *Sensors and Actuators A Physical*, Vol. 142, pp. 329-335.
45. Farrar, C.R. and Worden, K. (2007), “An introduction to structural health monitoring”, *Philosophical Transactions of the Royal Society A*, Vol. 365, pp. 303-315.
46. Fox, S. (2014), “French City Plans To Harness Pedestrian Power for Street Lights”. <http://www.sustainabledanceclub.com>. (Date of access: 15 Sep, 2014)
47. Gasch R. and Twele J. (2012), “Wind Power Plants: Fundamentals, Design, Construction and Operation”, DOI: 10.1007/978-3-642-22938-1\_2, © Springer-Verlag Berlin Heidelberg.
48. Giurgiutiu, V., Zagrai, A.N. and Bao, J.J. (2002), “Embedded active sensors for in-situ structural health monitoring of thin-wall structures”, *Journal of Pressure Vessel Technology, ASME*, Vol. 124, pp. 293-302.
49. Goldfarb, M. and Jones, L.D. (1999), “On the efficiency of electric power generation with piezoelectric ceramic”, *ASME Journal of Dynamic Systems, Measurement, and Control*, Vol. 121, pp. 566-571.

50. Goldschmidtboeing, F., Woias, P. (2008), “Characterization of different beam shapes for piezoelectric energy harvesting”, *Journal of Micromechanics and Microengineering*, Vol. 18, No. 104013, pp. 1-7.
51. Gu, L. and Livermore, C. (2012), “Compact passively self-tuning energy harvesting for rotating applications”, *Smart Materials and Structures*, Vol. 21, No. 015002.
52. Halliday, D., Resnick, R. and Walker, J. (2008), Fundamentals of Physics, 8<sup>th</sup> ed., Wiley, New York, pp. 768-800.
53. Hausler, E. and Stein, L. (1984), “Implantable physiological power supply with PVDF film”, *Ferroelectrics*, Vol. 60, pp. 277-282.
54. Hey, F., Bhalla, S. and Soh, C.K. (2006), “Optical parallel interrogation and protection of piezo-transducers in electromechanical impedance technique”, *Journal of Intelligent Material Systems and Structures*, Vol. 17, pp. 457-468.
55. Hoja, J. and Lentka, G. (2009), “Portable analyzer for impedance spectroscopy”, 19<sup>th</sup> IMEKO World Congress on Fundamental and Applied Metrology, September 6<sup>th</sup> -11<sup>th</sup>, Lisbon, Portugal.
56. Ikeda, T. (1990), “Fundamentals of Piezoelectricity”, *Oxford University Press*, Oxford.
57. IRC-6 (2000), “Standard specifications and code of practice for road bridges: Loads and Stresses”, *Indian Road Congress*, Section II, 4<sup>th</sup> Revision.
58. Karami, M.A., Farmer, J.R. and Inman, D.J. (2013), “Parametrically excited nonlinear piezoelectric compact wind turbine”, *Renewable Energy*, Vol. 50, pp. 977-987.
59. Kaur, N. and Bhalla, S. (2014a), “Feasibility of energy harvesting from thin piezo patches via axial strain actuation mode”, *Journal of Civil Structural Health Monitoring*, Vol. 4, pp. 1-15.
60. Kaur, N. and Bhalla, S. (2014b), “Combined energy harvesting and structural health monitoring potential of embedded piezo concrete vibration sensors”, *Journal of Energy Engineering, American Society of Civil Engineers ASCE*, (accepted, in press).

61. Khaligh, A., Zeng, P. and Zheng, C (2010), “Kinetic energy harvesting using piezoelectric and electromagnetic technologies—state of the art”, *IEEE Transactions on Industrial Electronics*, Vol. 57, pp. 850–860.
62. Khameneifar, F., Moallem, M. and Arzanpour, S. (2011), “Modeling and analysis of a piezoelectric energy scavenger for rotary motion applications”, *Journal of Vibration and Acoustics ASME*, Vol. 133, No. 011005.
63. Khameneifar, F., Arzanpour, S. and Moallem, M. (2013) “A piezoelectric energy harvester for rotary motion applications: Design and experiments”, *IEEE/ASME Transactions on Mechatronics*, Vol. 18, pp. 1527-1534.
64. Kim, C.W., Kawatani, M. and Hwang, W.S. (2004), “Reduction of traffic-induced vibration of two-girder steel bridge seated on elastomeric bearings”, *Engineering Structures*, Vol. 26, pp. 2185–2195.
65. Kim, S., Clark, W.W. and Wang, Q.M. (2005), “Piezoelectric energy harvesting with a clamped circular plate: Analysis”, *Journal of Intelligent Material Systems and Structures*, Vol. 16, pp. 847-854.
66. Kim, S.H., Ahn, J.H., Chungb, H.M. and Kang, H.W. (2011), “Analysis of piezoelectric effects on various loading conditions for energy harvesting in a bridge system”, *Sensors and Actuators A: Physical*, Vol. 167, pp. 468-483.
67. Kim, G.W. and Kim, J. (2013), “Compliant bistable mechanism for low frequency vibration energy harvester inspired by auditory hair bundle structures”, *Smart Materials and Structures*, Vol. 22, No. 014005.
68. König, F.V. (1976), “Windenergie in praktischer Nutzung (Practical application of wind energy)”, *Udo Pfriemer Verlag*, München.
69. Kuphaldt, T.R. (2007), “Lessons In Electric Circuits, Volume II - AC”, Sixth Edition, *Design Science License*.
70. Kymissis, J., Kendall, C., Paradiso, J. and Gershenfeld, N. (1998), “Parasitic power harvesting in shoes”, *Proceedings of 2<sup>nd</sup> IEEE International Symposium on Wearable Computers*, October 19–20<sup>th</sup>, Pittsburg, PA, pp. 132-139.

71. Lee, S.Y., and Yhim, S.S. (2005), “Dynamic behaviour of long-span box girder bridges subjected to moving loads: Numerical analysis and experimental verification”, *International Journal of Solids and Structures*, 42, pp. 5021–5035.
72. Lefevre, E., Badel, A., Richard, C., Petit, L. and Guyomar, D. (2006), “A comparison between several vibration-powered piezoelectric generators for standalone systems”, *Sensors and Actuators A Physical* Vol. 126, pp. 405-416.
73. Liang, C., Sun, F.P. and Rogers, C.A. (1994), “Coupled electro-mechanical analysis of adaptive material systems: determination of the actuator power consumption and system energy transfer”, *Journal of Intelligent Materials Systems and Structures*, Vol. 5, pp. 12-20.
74. Lim, Y.Y., Bhalla, S. and Soh, C.K. (2006), “Structural identification and damage diagnosis using self-sensing piezo-impedance transducers”, *Smart Materials and Structures*, Vol. 15, No. 3, pp. 987-995.
75. Lu, F., Lee, H.P. and Lim, S.P. (2004), “Modelling and analysis of micro piezoelectric power generators for micro electromechanical systems applications”, *Smart Materials and Structures*, Vol. 13, pp. 57-63.
76. Majcher, K. (2011), “10 technologies to watch”, Aviation Week.
77. Margo, C., Katrib, J., Nadi, M. and Rouane, A. (2013), “A four-electrode low frequency impedance spectroscopy measurement system using the AD5933 measurement chip”, *Physiological Measurement*, Vol. 34, pp. 391-405.
78. Mark, W. and George, D. (2000-2003), “A brief description of NDT techniques”, *Insight NDT Equipment Ltd.*
79. Marzencki, M., Ammar, Y. and Basrour, S. (2007), “Integrated power harvesting system including a MEMS generator and a power management circuit”, *Sensors and Actuators A: Physical*, Vol. 145–146, pp. 887-890.
80. Mateu, L. and Moll, F. (2005a), “Optimum piezoelectric bending beam structures for energy harvesting using shoe inserts”, *Journal of Intelligent Material Systems and Structures*, Vol. 16, pp. 835-845.

81. Mateu, L. and Moll, F. (2005b), “Review of energy harvesting techniques and applications for microelectronics”, *Proceedings of SPIE*, Vol. 5837, pp. 359-373.
82. McCann, D.M. and Forde, M.C. (2001), “Review of NDT methods in the assessment of concrete and masonry structures”, *NDT & E International*, Vol. 34, pp. 71-84.
83. Microstrain Inc., <http://www.microstrain.com>. (Date of access: 13 July, 2014)
84. Microchip Technology, (2014) [www.microchip.com](http://www.microchip.com). (Date of access: 12 Sep, 2014)
85. Mitcheson, P.D., Yeatman, E.M., Rao, G.K., Holmes, A.S., Green, T.C. (2008), “Energy harvesting from human and machine motion for wireless electronic devices”, *Proceedings of IEEE*, Vol. 96, pp. 1457-1486.
86. Moghimi, H., and Ronagh, H. R. (2008), “Development of a numerical model for bridge-vehicle interaction and human response to traffic-induced vibration”, *Engineering Structures*, Vol. 30, pp. 3808-3819.
87. Mohammadi, F., Khan, A. and Cass, R.B. (2003), “Power generation from piezoelectric Lead Zirconate Titanate fiber composites”, *Proceedings of Material Research Symposium*, Vol. 736, pp. D5.5.1.
88. Moharana, S. and Bhalla, S. (2012), “Numerical investigation of shear lag effect on PZT –Structure integration: Review and applications”, *Current Science*, Vol. 103, No. 6, pp. 685-696.
89. Moharana, S. and Bhalla, S. (2014), “A continuum based modelling approach for adhesively bonded piezo-transducers for EMI technique”, *International Journal of Solids and Structures*, Vol. 51, No. 6, pp. 1299-1310.
90. Moyo, P., Brownjohn, J.M.W. and Omenzetter, P. (2004), “Highway bridge live loading assessment and load carrying capacity estimation using a health monitoring system”, *Structural Engineering and Mechanics, An International Journal*, Vol. 18, No. 5, pp. 609-626.
91. Myers, R., Vickers, M., Kim, H. and Priya, S. (2007), “Small scale windmill”, *Applied Physics Letters*, Vol. 90, Article No. 054106.

92. Nayfeh, A.H. and Mook, D.T. (1995), *Handbook on Nonlinear Oscillations*, Wiley Interscience Publication, New York.
93. Nchibvute, A., Akande, A.R. and Luhanga, P.V.C. (2011), “Modelling of PZT beam for voltage generation”, *Pertanika Journal of Science and Technology*, Vol. 19, No. 2, pp. 259-271.
94. Niitsu, Y. and Iizuka, T. (2014), “Real time displacement measurement of bridge with image correlation method”, *9<sup>th</sup> International Symposium on Advanced Science and Technology in Experimental Mechanics*, November, 1<sup>st</sup>-6<sup>th</sup>, New Delhi, India.
95. Ocean Power Technologies Inc. (2014), <http://www.oceanpowertechnologies.com/>. (Date of access: 12 June, 2014)
96. Oliver, J.R., Neurgaonkar, R.R., Moffatt, A.P., Khoshnevisan, M. and Nelson, J.G. (2002), “Piezoelectric energy harvester and method”, U.S. Patent 6,407,484, 18 June.
97. Overly, Park, G., Kevin, Farinholt, M., Timothy, G. S., and Farrar, C.R. (2008), “Development of an extremely compact impedance-based wireless sensing device”, *The Engineering Institute, Los Alamos National Laboratory*, Los Alamos, NM 87545, USA.
98. Pal, A. (2013), “Damage assessment using curvature mode shape”, *M.Tech. thesis*, Department of Civil Engineering, Indian Institute of Technology (IIT) Delhi, India.
99. Pandey, A.K., Biswas, M. and Samman, M.M. (1991), “Damage detection from changes in curvature mode shapes”, *Journal of Sound and Vibration*, Vol. 145, pp. 331-332.
100. Pandey, A.K. and Biswas, M. (1994), “Damage detection in structures using changes in flexibility”, *Journal of Sound and Vibration*, Vol. 169, pp. 3-17.
101. Paradiso, J.A. and Starner, T. (2005), “Energy scavenging for mobile and wireless electronics,” *Pervasive Computing*, IEEE, Vol. 4, pp. 18-27.
102. Park, G., Cudney, H.H. and Inman, D.J. (2000), “Impedance-based health monitoring of civil structural components”, *Journal of Infrastructure Systems*, ASCE, Vol. 6, pp. 153-60.

103. Park, G., Cudney, H.H. and Inman, D.J. (2001), “Feasibility of using impedance-based damage assessment for pipeline structures”, *Earthquake Engineering and Structural Dynamics*, Vol. 30, pp. 1463-1474.
104. Park, G., Farrar, C.R., Todd, M.D., Hodgkiss, W. and Rosing T. (2008), “Energy harvesting for structural health monitoring sensor networks”, *Journal of Infrastructure Systems*, Vol. 14, No. 1, pp. 64-79, DOI: 10.1061/(ASCE)1076-0342(2008)14:1(64).
105. Peigney, M. and Siegert, D. (2013), “Piezoelectric energy harvesting from traffic-induced bridge vibrations”, *Smart Materials and Structures*, Vol. 22, pp. 1-11, Article No.-095019.
106. PI Ceramic (2014), *Product Information Catalogue*, Lindenstrabe, Germany, <http://www.picерamic.de>. (Date of access: 12 March, 2014)
107. Pillatsch, P., Yeatman, E.M. and Holmes, A.S. (2013), “A wearable piezoelectric rotational energy harvester”, *Proceedings of the IEEE International Conference on Body Sensor Networks (BSN)*, Cambridge, MA, USA, 6<sup>th</sup>-9<sup>th</sup> May, pp. 1-9.
108. Platus, D.L. (1991), “Negetive-stiffnes-mechanism vibration isolation systems”, *SPIE Vibration control in Microelectronics, Optics and Metrology*, Vol. 1619, pp. 44-54.
109. Priya, S. (2007), “Advances in energy harvesting using low profile piezoelectric transducers”, *Journal of Electroceramics*, Vol. 19, pp. 165-182.
110. Priya, S. and Inman, D.J. (2009), *Handbook on Energy Harvesting Technologies*, New York, USA, Springer Science + Business Media Publications.
111. Poulin, G., Sarraute, E. and Costa, F. (2004), “Generation of electrical energy for portable devices comparative study of an electromagnetic and piezoelectric system”, *Sensors and Actuators A*, Vol. 116, pp. 461-471.
112. Quazar Technologies (2014), *Data Acquisition Systems*, India <http://www.quazartech.com>. (Date of access: 10 Nov, 2014)

113. Ramsey, M.J. and Clark, W.W. (2001), “Piezoelectric Energy harvesting for bio MEMS applications”, *Proceedings of SPIE*, Vol. 4332, Newport Beach, CA, pp. 29-438.
114. Ratnasari, D. (2014), “Electrical power generation using piezoelectric ceramic tile prototype design”, *Proposed Activity*, published in <http://www.researchgate.net>. (Date of access: 25 Nov, 2014)
115. Ren, W.L. and Peng, X.L. (2005), “Baseline finite element modeling of a large span cable-stayed bridge through field ambient vibration tests”, *Computers and Structures*, Vol. 83, pp. 536–550.
116. Roundy, S. and Wright, P.K. (2004), “A piezoelectric vibration based generator for wireless electronics”, *Smart Materials and Structures*, Vol. 13, pp. 1131-1142.
117. Roundy, S. (2003), “Energy scavenging for wireless sensor nodes with a focus on vibration to electricity conversion”, *Ph.D. Dissertation*, Department of Mechanical Engineering, University of California, Berkeley.
118. Roundy, S., Wright, P.K. and Rabaey, J. (2003), “A study of low level vibrations as a power source for wireless sensor nodes”, *Computer Communication*, Vol. 26, No. 11, pp. 1131-1144.
119. Roundy, S., Leland, E.S., Baker, J., Carleton, E., Reilly, E., Lai, E., Otis, B., Rabaey, J.M., Wright, P.K. and Sundararajan, V. (2005), “Improving power output for vibration-based energy scavengers”, *Pervasive Computing, IEEE*, Vol. 4, No. 1, pp. 28-36.
120. Sanayei, M. and Saletnik, M.J. (1996), “Parameter estimation of structures from static strain measurements II: Formulation”, *Journal of Structural Engineering*, ASCE, Vol. 122, No. 5, pp. 555-562.
121. Seiko Instruments Inc. (2014), <http://www.sii.co.jp/components/battery/topEN.jsp>.
122. Shankar, R. (2013), “Damage assessment using curvature mode shape”, *M.Tech. Thesis*, Department of Civil Engineering, Indian Institute of Technology (IIT) Delhi, India.

123. Shanker, R., Bhalla, S. and Gupta, A. (2010), "Integration of electro-mechanical impedance and global dynamic technique for improved structural health monitoring", *Journal of Intelligent Material Systems and Structures*, Vol. 21, No. 2, pp. 285-295.
124. Shanker, R., Bhalla, S. and Gupta, A. (2011), "Dual use of PZT patches as sensors in global dynamic and local EMI techniques for structural health monitoring", *Journal of Intelligent Material Systems and Structures*, Vol. 22, No. 16, pp. 1841-1856.
125. Sirohi, J. and Chopra, I. (2000), "Fundamental understanding of piezoelectric strain sensors", *Journal of Intelligent Material Systems and Structures*, Vol. 11, No. 4, pp. 246-257.
126. Sodano, H., Inman, D.J. and Park, G. (2004a), "A review of power harvesting from vibration using piezoelectric materials", *Shock and Vibration Digest*, Vol. 36, pp. 197-205.
127. Sodano, H.A., Park, G. and Inman, D.J. (2004b), "Estimation of electric charge output for piezoelectric energy harvesting", *Strain*, Vol. 40, pp. 49-58.
128. Sodano, H., Inman, D.J. and Park, G. (2005), "Comparison of piezoelectric energy harvesting devices for recharging batteries", *Journal of Intelligent Material Systems and Structures*, Vol. 16, pp. 799-807.
129. Soh, C.K., Tseng, K.K-H., Bhalla, S., Gupta, A. (2000), "Performance of smart piezoceramic patches in health monitoring of a RC bridge", *Smart Material and Structures*, Vol. 9, pp. 533-542.
130. Sohn, J.W., Choi, S.B. and Lee, D.Y. (2005), "An investigation on piezoelectric energy harvesting for MEMS power sources", *Proceedings of the Institution of Mechanical Engineers, Part C—Journal of Mechanical Engineering Science*, Vol. 219, pp. 429-436.
131. Srinivasulu, P. and Vaidyanathan, C. (2004), "Handbook of Machine Foundation", Mc Graw Hill.
132. SSDL (2013), "Smart Structures and Dynamic Laboratory", Department of Civil Engineering, IIT Delhi, <<http://ssdl.iitd.ac.in/>>. (Date of access: 24 Nov, 2014)

133. Starner, T. (1996), "Human-powered wearable computing", *IBM Systems Journal*, Vol. 35, pp. 18-628.
134. Stordeur, M. and Stark, I. (1997), "Low power thermoelectric generator–self-sufficient energy supply for micro systems", *Proceedings of 16<sup>th</sup> International Conference on Thermoelectrics*, Dresden, Germany, pp. 575-577.
135. Stubbs, N. and Kim, J.T. (1994), "Field verification of a non-destructive damage localization and severity estimation algorithm", *Texas A and M University Report*, New Mexico State University.
136. Sun, F.P., Chaudhry, Z., Rogers, C.A., Majmundar, M. and Liang, C. (1995), "Automated real-time structure health monitoring via signature pattern recognition", *Proceedings of the SPIE Conference on Smart Structures and Materials*, San Diego, California, Vol. 2443, pp.236-247.
137. Talakokula, V., Bhalla, S., and Gupta, A. (2014), "Corrosion assessment of RC structures based on equivalent structural parameters using EMI technique", *Journal of Intelligent Materials System and Structures*, Vol. 25, pp. 484-500.
138. Talwar, G. (2010), "Development of low-cost SHM system for defense structures: Algorithm Development", *M.Tech. Thesis*, Department of Civil Engineering, Indian Institute of Technology (IIT) Delhi, India
139. Tektronix Inc. (2013). <http://www.tek.com/oscilloscope/tds2000-digital-storage-oscilloscope>. (Date of access: 24 Oct, 2014)
140. Texas Instrument (2014), [www.ti.com](http://www.ti.com). (Date of access: 04 July, 2014)
141. Tien, C.M.T. and Goo, N.S. (2010), "Use of a piezo-composite generating element for harvesting wind energy in an urban region", *Aircraft Engineering and Aerospace Technology*, Vol. 82, pp. 376–381.
142. Tomlinson, R.A. (1976), "The Perachora Waterworks: Addenda", *The Annual of the British School at Athens*, Vol. 71, pp. 147-148.
143. Twiefel, J., Richter, B., Hemsel, T. and Wallaschek, J. (2006), "Model-based design of piezoelectric energy harvesting systems", *Proceedings of SPIE*, SanDiego, California, USA, Vol. 6169, pp. 09.1-09.10.

144. Umeda, M., Nakamura, K. and Ueha, S. (1996), “Analysis of transformation of mechanical impact energy to electrical energy using a piezoelectric vibrator”, *Japanese Journal of Applied Physics*, Vol. 35, pp. 3267-3273.
145. Vries, J.A. (2005), “Short history of piezoelectricity”, *Applied Piezo*, [www.applied-piezo.com/](http://www.applied-piezo.com/).
146. Williams, C. and Yates, R.B. (1996) “Analysis of a micro-electric generator for microsystems” *Sensors and Actuators A Physical*, Vol. 52, pp. 8-11.
147. Wray, P. (2008), “Good vibrations lead to ’smart’ roads and energy”, *American Ceramic Society Bulletin*, Vol. 88, No. 1, pp. 16.
148. Yang, Y., Lim, Y.Y. and Soh, C.K. (2008), “Practical issue related to the application of the electro-mechanical impedance technique in structural civil health monitoring of the structures: II. Numerical verification”, *Smart Material and Structures*, Vol. 17, No. 3, pp. 1-12.
149. Zimmerman, D.C. and Kaouk, M. (1994), “Structural damage detection using minimum rank update theory”, *Journal of Vibration and Acoustics*, Vol. 116, pp. 222-231.
150. Zuo, D., Hua, J., and Landuyt, D. V. (2012), “A model of pedestrian-induced bridge vibration based on full-scale measurement”, *Engineering Structures*, 45, pp. 117–126.



**APPENDIX (A)**


---

**MATLAB Program for determination of amplitude of vibration of simply supported beam under sinusoidally varying concentrated load. This is based on mode superposition theory (Chopra, 2007), Eq. 3.21 of Chapter 3.**

---

**'Description of Symbols'**

f1=Forcing frequency  
 W=Angular forcing frequency  
 w=Natural frequency  
 K=Generalized stiffness  
 P0=Amplitude of generalized external force  
 p0=Amplitude of external force  
 q=Generalized displacement  
 u=Amplitude of vibration  
 Mode=Mode Shape

**'Main Program'**

```
clear all;
display('Hello');

L=input('Enter the length (L) of the beam = ');
EI=input('Enter the flexural rigidity of the beam = ');
m=input('Enter the mass per unit length(m) of the beam = ');
po=input('Enter the magnitude of external force = ');
%W=input('Enter the operating frequency of force = ');
N=input('Enter the number of modes to be used = ');
Zeta=input('Enter the damping ratio = ');

for f=1:10000;
    u(f)=0;
end;
for n=1:N;
    for f=1:10000;
        f1=0.01*f;
        W=2*pi*(f1);
        w(n)=((n*3.14/L)^2)*(EI/m)^0.5;
        Po=po*sin(n*pi/2);
        K=(m*L*w(n)^2)/2;
        usto=Po/K;
        A=1-(W/w(n))^2;
        B=2*Zeta*(W/w(n));
        Rd=1/(A^2+B^2)^0.5;
        Phai=atan(B/A);
        q=usto*Rd;
```

```
Mode=sin(n*pi/2);
u(f)=u(f)+Mode*q;
F(f)=f1;
end;
U=u';
plot(F,u)
```

---

## APPENDIX (B)

---

### **Design calculations for determination of ultimate moment carrying capacity, $M_u$ , of RC beam (This has been used in Chapter 4).**

---

For a rectangular RC section, with depth ( $D$ ), width ( $b$ ), tension reinforcement area ( $A_{st}$ ) and characteristic strength of reinforcement and concrete as  $f_y$  and  $f_{ck}$ , respectively, ultimate load carrying capacity,  $M_u$  is given by

$$M_u = 0.87f_y A_{st}(D - 0.416d') \quad (\text{B.1})$$

where,  $d'$  represents the depth of neutral axis of the section and is given by,

$$d' = \frac{0.87f_y A_{st}}{0.36f_{ck}b} \quad (\text{B.2})$$

Using the above mentioned equations and input parameters as mentioned in Table 4.1 and Figure 4.5, the depth of neutral axis ( $d'$ ) and ultimate load carrying capacity ( $M_u$ ) of concrete beam was determined to be 66.055 mm and 10.86 KN-m, respectively.

The inertial shaker especially fabricated in lab will result in adding a point load on the beam in addition to its self weight. Hence, before proceeding further, it becomes essential to determine the maximum static point load ( $P_{max}$ ) which the beam can withstand at its centre. It was determined using the following equation,

$$M_u = \frac{wL^2}{8} + \frac{P_{max}L}{4} \quad (\text{B.3})$$

Here,  $w$  represents the weight per unit length of the RC beam and  $L$  represents the length of the RC beam. Using the  $M_u$  value as calculated above and the input parameters mentioned in Table 4.1, the point load ( $P_{max}$ ) which the beam can carry was determined to be 9650 N which is much greater than the total weight of inertial shaker (800 N approx.).



---

## APPENDIX (C)

---

**Design calculations for determination of stiffness of spring used in inertial-type shaker (This has been used in Chapter 4).**

---

### **C.1 REQUIRED STIFFNESS ( $K_{req}$ ) OF SPRING:**

The stiffness of the spring in inertial shaker was based two characteristics of the LDS V406 shaker, (a) stroke value ( $s = 8.8$  mm), which is its maximum peak to peak displacement, and (b) the maximum force ( $F_s$ ) generated by it. The permissible value of displacement which was allowed for the vertical movement of the shaker was considered as one third of the stroke value, i.e. 2.933 mm and maximum sine force generated by shaker as 98 N. Four springs were used in inertial shaker to transfer the force to the RC beam. The required stiffness ( $K_{req}$ ) of spring in inertial shaker was determined using,

$$(4K_{req}) \times (s/3) \leq F_s \quad (\text{C.1})$$

$$K_{req} \leq 8353.2 \text{ N/m} \quad (\text{C.2})$$

### **C.2 ACTUAL STIFFNESS OF SPRING:**

The actual stiffness of the spring was determined both experimentally ( $K_{exp}$ ) and analytically ( $K_{an}$ ). Analytical stiffness is given by (Srinivasulu and Vaidyanathan, 2004)

$$K_{an} = \frac{1}{n_{sp}} \left( \frac{Gd_{sp}^4}{8D_{sp}^3} \right) \quad (\text{C.3})$$

Here,  $d_{sp}$  (=7 mm) represents the diameter of the wire used for spring,  $D_{sp}$  (=50 mm) represents the mean diameter of the ring of spring,  $n_{sp}$  (=24) represents the number of turns and  $L_{sp}$  (= 392 mm) represents the free length of the spring. The bulk modulus of the

---

material constituting the spring was  $G_{sp} = 8.077 \times 10^{10}$  N/m. Using Eq. (C.3), the analytical of stiffness of the spring used in the inertial shaker was calculated as 7622.887 N/m.

The experimental determination of stiffness is based on the fundamental approach in which a single degree of system vibrates in its natural frequency in the vertical direction as shown in Figure C.1. The bottom of the spring was fixed to the floor and a known mass ( $m_{sp} = 0.963$  kg) was attached on the top of the spring. The spring-mass system was excited in vertical direction to vibrate freely in its first mode. The frequency of vibration ( $f_{sp}$ ) was determined using accelerometer attached on the top of the mass. The mass of the spring was assumed negligible as compared to the mass ( $m_{sp}$ ) attached on its top. The natural frequency of vibration ( $f_{sp}$ ) of spring was determined as 14.46 Hz using accelerometer (refer Figure C.2). The experimental stiffness of spring ( $K_{exp}$ ) was determined to be 7941.127 N/m using,

$$f_{sp} = \frac{1}{2\pi} \sqrt{\frac{K_{exp}}{m_{sp}}} \quad (C.4)$$

The experimental (7941.127 N/m) and analytical stiffness (7622.887 N/m) of spring are in a good match and both satisfy the limit established on stiffness value given by Eq. (C.2).

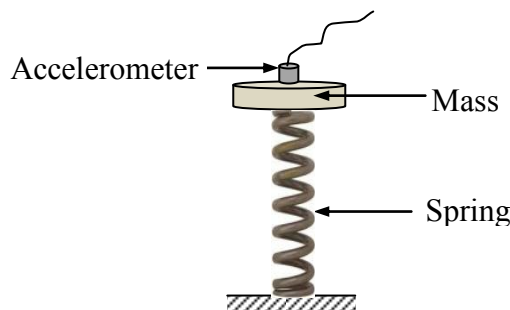


**Figure C.1:** Mass-spring configuration as single degree of freedom system.

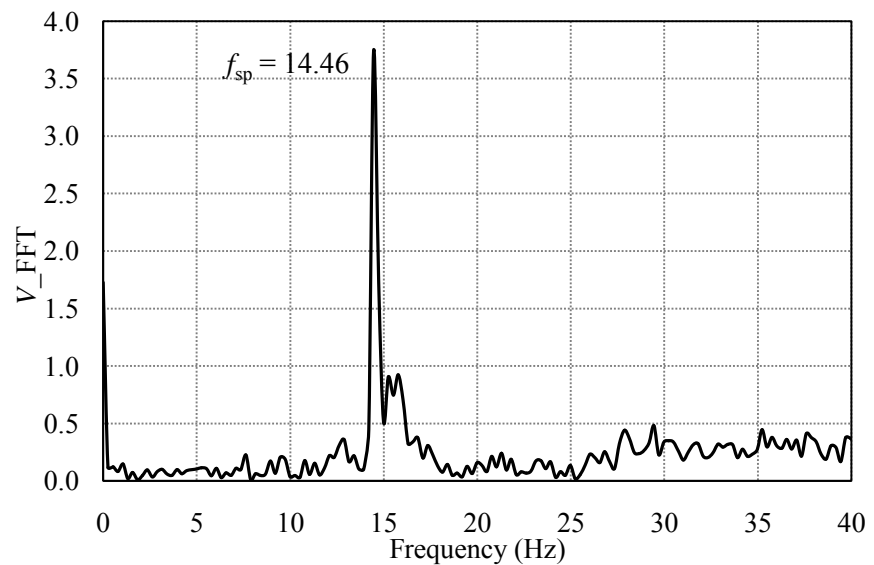


**Figure C.2:** FFT voltage of accelerometer versus frequency, giving the natural frequency of spring.



**APPENDIX (D)****Design calculations for compensating effect of temperature on PZT parameters (This has been used in Chapter 7).**

The properties of the PZT materials are very much sensitive to temperature. From Figure D.1(a), it can be concluded that the piezoelectric charge constant ( $d_{31}$ ) is only marginally affected by the temperature within the operating range ( $10^{\circ}\text{C}$  to  $40^{\circ}\text{C}$ ) considered in the study. Hence, its variation can be neglected. Variation of the coupling coefficient  $k_{31}$  is shown in Figure D.1(b) (PI Ceramic, 2014). The variation of  $k_{31}$  can be approximated by the following equation (for  $10^{\circ}\text{C} \leq T \leq 40^{\circ}\text{C}$ ), which relate the values of the coupling coefficient at any temperature ( $T^{\circ}\text{C}$ ) to its corresponding values at  $20^{\circ}\text{C}$ .

$$k_{31}(T^{\circ}\text{C}) = k_{31}(20^{\circ}\text{C})[1 - 0.0008(T - 20)] \quad (\text{D.1})$$

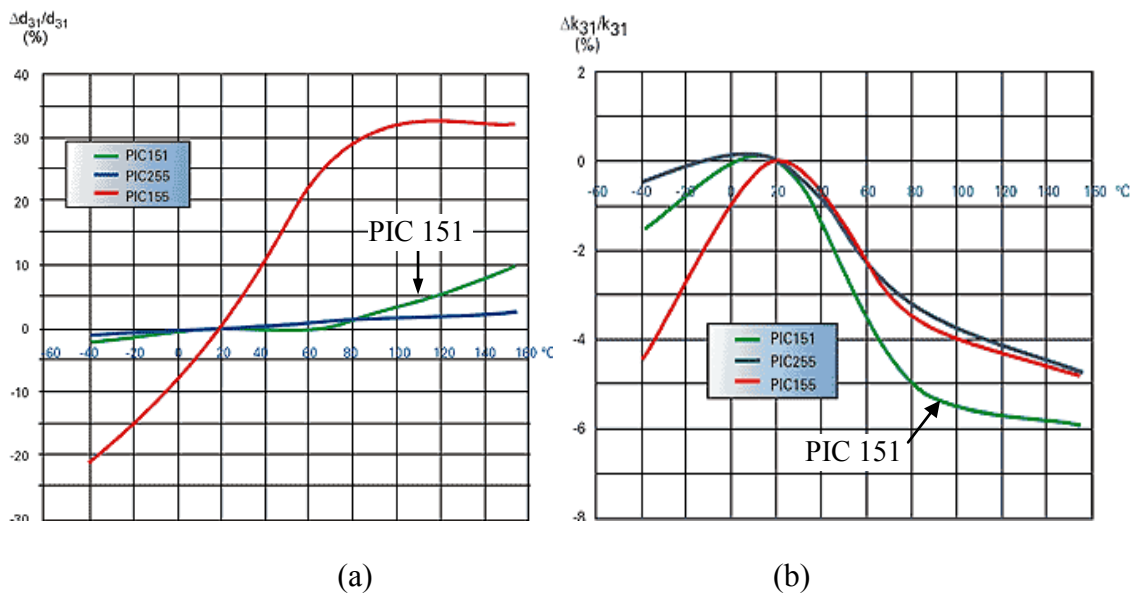


**Figure D.1:** Temperature dependence of (a) piezoelectric charge constant  $d_{31}$  and (b) transverse oscillation coupling factor  $k_{31}$  (PI Ceramic, 2014) [The PZT patches employed in study here conform to PIC151].

Using above equation and following relation (Ikeda, 1990), one can determine the variation in electric permittivity,  $\varepsilon_{33}^T$ .

$$\varepsilon_{33}^T = \frac{1}{s_{11}^E} \left( \frac{d_{31}}{k_{31}} \right)^2 \quad (D.2)$$

where,  $s_{11}^E$  is the compliance (inverse of Young's Modulus) of the PZT material at constant electric field. Assuming that the Young's Modulus of the PZT material is negligibly effected by temperature. Substituting the values in Eq. (D.2) from Table 4.2, which are at  $T=23^\circ\text{C}$ ,  $k_{31}(23^\circ\text{C})$  was worked as 0.372046. Further, substituting the value of  $k_{31}(23^\circ\text{C})$  in Eq. (D.1), at  $T=23^\circ\text{C}$ , value of  $k_{31}(20^\circ\text{C})$  was determined to be 0.372941. Table D.1 compiles the values of  $\varepsilon_{33}^T$ , determined using Eq. (D.1) and Eq. (D.2), for the specific days, along with the average temperature on the corresponding days.

**Table D.1:** Values of  $\varepsilon_{33}^T$  on the specific dates during study, along with measured average temperature.

Date	Day after casting	Temperature ( $^\circ\text{C}$ )	Permittivity, $\varepsilon_{33}^T$ (F/m)
17 <sup>th</sup> Jan, 2013	6 <sup>th</sup>	13	$2.091 \times 10^{-8}$
8 <sup>th</sup> Feb, 2013	28 <sup>th</sup>	15	$2.097 \times 10^{-8}$
28 <sup>th</sup> Feb, 2013	48 <sup>th</sup>	20	$2.114 \times 10^{-8}$
20 <sup>th</sup> March, 2013	68 <sup>th</sup>	23	$2.124 \times 10^{-8}$
8 <sup>th</sup> April, 2013	87 <sup>th</sup>	27	$2.138 \times 10^{-8}$
29 <sup>th</sup> April, 2013	108 <sup>th</sup>	30	$2.148 \times 10^{-8}$

---

**APPENDIX (E)**

---

**INVENTION DISCLOSURE: ABSTRACT**

---

**A NOVEL ENERGY HARVESTING SOLUTION FOR REINFORCED CONCRETE STRUCTURES****CONCRETE VIBRATION ENERGY HARVESTER (CVEH)**

**Concrete Vibration Energy Harvester (CVEH)** is a novel and practical solution for harvesting renewable energy from reinforced concrete (RC)/composite structures under ambient vibrations. It is different from the existing harvesters in sense that it does not warrant an additional secondary structure. CVEH, when embedded inside the RC structures, can facilitate the conversion of the mechanical vibrations experienced by them into electric energy using the piezoelectric effect. *Piezoelectric effect* is the property of any ceramic material to convert mechanical strain into voltage and vice versa. Typically, the harvester can harvest power or the order of microwatt to milliwatt (depending upon the structure and its own configuration), suitable to power basic structural health monitoring sensors.

Exact design details of the proposed device are omitted owing to IP issues in accordance with the IIT Delhi norms.



**NAVEET KAUR**  
[naveet.kaur1985@gmail.com](mailto:naveet.kaur1985@gmail.com)

---

## SUMMARY

Sr. Project Scientist at the Indian Institute of Technology (IIT) Delhi. Rich experience in the research area of piezoelectric energy harvesting during PhD at IIT Delhi. Secured first rank among all M.E Programmes in the Department of Civil Engineering in 2011. Research areas of interest include piezo-electric energy harvesting (PEH), structural health monitoring (SHM), earthquake engineering, vibration control devices, bio-mechanics and concrete fatigue.

## RESEARCH ACCOMPLISHMENTS

- Publications: 9 International Journal & 13 International Conference (*Page 179*) 2011-'15
  - Invited Lectures: Delivered five lectures (*Page 183*) 2010-'14
  - Peer Review Activities: In Review Board of Journal of Institute of Smart Structures and Systems 2014
  - Invention Disclosure/Patent: A novel energy harvesting solution for reinforced concrete structure 2014
- 

## EDUCATIONAL QUALIFICATION

### **Indian Institute of Technology (IIT) Delhi, India**

- PhD in Structures: Thesis Submitted 2011-'15  
 M.Tech. in Structures: 1<sup>st</sup> Rank out of 77 (CGPA: 9.3/10) 2008-'11

### **Thapar University, Patiala India**

- B.Tech. in Civil Engineering: 5<sup>th</sup> Rank out of 27 (CGPA: 8.42/10) 2003-2007
- 

## R & D PROJECTS

- IIT Delhi** 2014  
*Project 1:* Experimentation for investigation of behaviour of UV coated cement fibre board under wind load  
*Project 2:* Contribution in employing low-cost impedance analyser for different structures using piezos  
*Project 3:* Experimental investigation, data analysis for excessive vibrations in ASF building, Gurgaon  
*Project 4:* Identifying cause and remedy measures for excessive vibrations in PNB building, Delhi
- 

## RESEARCH EXPERIENCE

- PhD, (Integrated SHM and energy harvesting using thin piezo patches in  $d_{31}$  mode )** 2011-'15  
 ▪ Feasibility of same PZT patch in  $d_{31}$  mode for integrated SHM & PEH, circumventing secondary structures  
 ▪ Analytical power estimation model for adhesively embedded/ surface bonded PZT patches  
 ▪ Detailed numerical investigations for parametric study to maximize piezoelectric energy  
 ▪ Demonstration of feasibility of combined energy harvesting & SHM on real-life steel/ RC bridges  
 ▪ Determination of fatigue characteristics of concrete using PZT patches

**M.Tech., (Structures)** 2011

- Project 1:* Friction Dampers, High-Rise Buildings  
 ▪ Investigation of earthquake response of the medium-rise to high-rise shear-type buildings  
 ▪ Time history analyses of high-rise buildings with friction dampers in SAP2000 software  
 ▪ Optimizing damping parameters by developing FORTRAN program based on Newmark's Beta method

- Project 2:* Tuned Mass Damper (TMD), Base-Isolated Building, Near-Fault Earthquakes 2011  
 ▪ Investigation of effectiveness of TMD in base-isolated building in a near field earthquake scenario

**B. Tech. Project, (Analysis & Design of Industrial Structures)**

2006

- Design of 80 m long tunnel for the Wagon Tippler Complex for Duro Felguera Industries, South Africa
  - Analysis of 100 Mega Ton RCC silo using STAAD.Pro – 2005
- 

**WORK EXPERIENCE**

▪ **Structural Engineer, (Desein Pvt. Ltd., New Delhi)**

2008-2011

*Project 1:* Reviewing of TG foundation & ID, PA fan foundation for 2×800 MW thermal power plant (TPP)

*Project 2:* Analysis & design of cooling tower blow-down pump house for 2×507.5 MW TPP

*Project 3:* Analysis & design of critical pipe supports framing plan & thrust block for CW piping line

*Project 4:* Designed TG foundation, crane girder & low/high pressure heater beams under moving loads for 2×250 MW TPP

▪ **Engineer, (Laing O'Rourke's, Eigen Tech. Services Pvt. Ltd., Gurgaon, India)**

2007-2008

*Project 1:* Analysis & design of building using STAAD.Pro – 2007 for DLF project, Cyber City, Gurgaon

*Project 2:* Analysis & design of underground water tanks, Extended Basement Area for Accenture, Gurgaon

---

**AWARDS & RECOGNITIONS**

- **NBCC Prize of Excellence:** For securing 1<sup>st</sup> rank (among 77) in Civil Engineering M.Tech. batch 2011
  - **Best Oral Presentation Award:** Among research scholars at IIT Delhi on Research Scholars' Day 2015
  - **Guest Faculty, IGNOU:** Lecture broadcasted all over India on National Television Channel, 'Gyan Darshan'
  - **Team Leader, Virtual Smart Structures Dynamic Lab:** Delivered video demonstrations for explaining the experiments; contributed in experiment improvement 2013-'14
  - **Stanford Uni., USA:** 9<sup>th</sup> International Workshop on SHM (9-IWSHM) 2012
    - Delivered a talk on 'Feasibility of energy harvesting from piezo-patches in addition to SHM'
    - *SHM in Action:* The video demonstration of my research work has been *selected among the 19 best across the world* for the event in 9-IWSHM, 12<sup>th</sup> September
  - **Honoured as Guest Faculty, MHRD, Govt. of India** sponsored QEEE Pilot Program 2014
  - **Won financial sponsorship for Asia Pacific Summer School:** Interacted and shared ideas with 50 international participants 2012
  - **Presenter, UK India Educational & Research Initiative:** Presented my work at Bath University 2014
  - **MHRD Scholarship:** Received Ministry of Human Resource & Development (MHRD) 2011-'15 scholarship for Ph.D.
  - **Winner, HELIX'05 (Inter-College Tech-Fest):** Technical paper presentation & bridge model making 2005
  - **Rashtrapati Guide:** Highest award for Bharat Scouts & Guides awarded by President of India 2002
- 

**SOFTWARE SKILLS**

STAAD Pro - 2008, COMSOL, SAP 2000, ANSYS, NISA, ABAQUS, MATLAB, FORTRAN

---

**HOBBIES**

Calligraphy, Running, Cycling, Yoga, Games including badminton & lawn tennis.